13th Numerical Towing Tank Symposium

10-12 October 2010

Duisburg/Germany

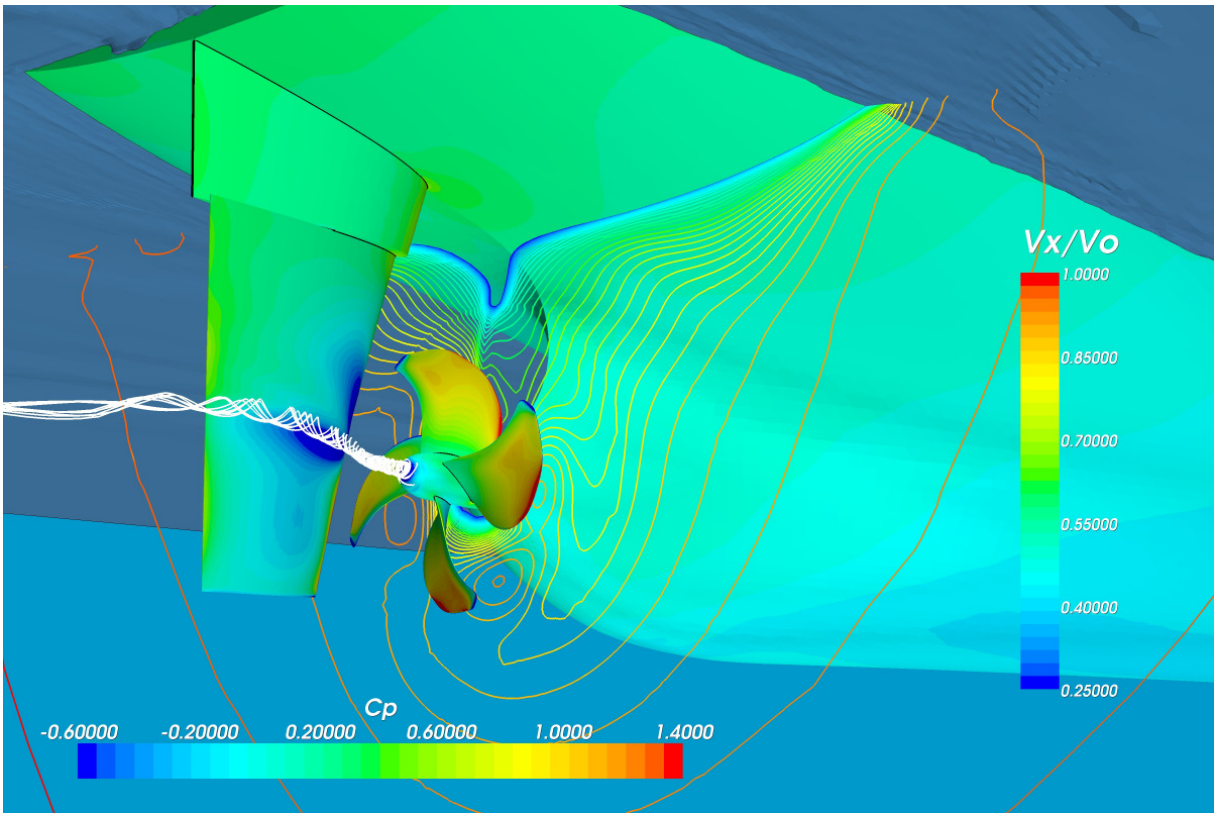

Volker Bertram, Ould El Moctar (Eds.)

ISMT
Institut für Schiffstechnik, Meerestechnik und Transportsysteme
Universität Duisburg-Essen

UNIVERSITÄT DUISBURG ESSEN

Sponsored by

Voith Turbo
www.voithturbo.com

CD-Adapco
www.cd-adapco.com

Germanischer Lloyd
www.gl-group.org

Joe Banks, A. Phillips, Stephen Turnock
Free-surface CFD Prediction of Components of Ship Resistance for KCS

Silvan Brändli
Sloshing Simulations with Fluid-Structure-Interaction using OpenFOAM

Alejandro Caldas, Marcos Meis, Adrián Sarasquete
CFD Validation of Different Propeller Ducts on Open-Water Condition.

Giuseppina Colicchio, Daniele Righetti, Claudio Lugni
Theoretical and Numerical Evaluation of a Sail Deformation close to the Wind

SeyadReza Djeddi, Mohammed Saeed Seif
Comparison of New Interface Capturing Schemes for Free Surface Flow Modeling

Pawel Dymarski
Numerical Modelling of Cavitation and Erosion on Rudder

Pawel Dymarski, Marek Kraskowski
CFD Optimization of Vortex Generators Forming the Wake Flow of Large Ships

Arash Eslamdoost, Rickard Bensow, Lars Larsson
Waterjet Hull Interaction

Benjamin Friedhof, Rainer Kaiser, Roland Vilsmeier
Simulation of Ship to Ship Interactions in Passing Manoeuvres using Overlapping Grids from the CFD Package MOUSE

Alexander von Graefe, Vladimir Shigunov, Tobias Zorn
Squat Computation for a Containership with Potential and Viscous Methods

Marilena Greco, Giuseppina Colicchio, Claudio Lugni
A 3D Domain-Decomposition Strategy for Violent Wave-Vessel Interactions

Tobias Huuva, Magnus Pettersson
Using Automated Optimization Routines for Designing High Efficiency Nozzle Profiles.

Nikolai Kornev, Andrey Taranov, Evgeny Shchukin, Lutz Kleinsorge
Development of Hybrid URANS-LES Methods for Flow Simulation in the Ship Stern Area

Jean-Marc Laurens, Jean-Baptiste Leroux, B. Pengam
Sheet Cavitation Model Implementation within a RANSE Solver

Simon G. Lewis, Marek Skrzynski, Stephen R. Turnock , Alexander M. Wright
Free Surface CFD for Integrated Design of High Speed Craft Stern Gear and Propeller

Dimitrios Nikolakis, Nikolai Kornev, Daniel Schmode, Volker Bertram
Combining CFD and Autonomic Control to Simulate Autonomous Surface Vessel Operation

Jan Oberhagemann, Ould El Moctar
Fluid-Structure Interaction using Free-Surface RANSE for Springing and Whipping

Michael Palm, Dirk Jürgens, D. Bendl
CFD Study on the Propeller-Hull-Interaction of Steerable Thrusters

Roozbeh Panahi, Mehdi Shafieefar
Using Overlapping Mesh System to Develop a General Wavemaker

Auke van der Ploeg, Karl Chao, Jochen Marzi, Jeroen Wackers
Computation of Scale Effects in Free-Surface Flows near a Ship's Transom

Mahdi Pourmostafa, Mohammad Saeed Seif, SeyadReza Djeddi
Multigrid Method in Free-Surface Flow Simulation

Nobuaki Sakamoto, Takanori Hino
Unsteady Flow Simulations for Dynamically-Moving 2d and 3d Geometries by Unstructured Grid Based RANS Solver

Jochen Schoop-Zipfel, Moustafa Abdel-Maksoud, Thomas Rung
Numerical Investigation of the Influence of Water Depth on Ship Manoeuvring Behaviour

Claus D. Simonsen, Christian Klimt Nielsen, Zdravko Kishev
Using CFD for Simulation of Ships with Different Fuel Saving Rudder-Propeller Devices

Florian Vesting, Daniel Knutsson, Rickard Bensow, Lars Larsson
Propeller Optimisation in behind Condition considering Sheet Cavitation

Jeroen Wackers, Gaubo Deng, Michel Visonneau
Tensor-Based Grid Refinement Criteria for Ship Flow Simulation

Christian D Wood, Dominic A Hudson, Mingyi Tan
CFD Simulation of Orifice Flow for the Flooding of Damaged Ships

Tobias Zorn, Justus Heimann, Volker Bertram
CFD Analysis of a Duct's Effectiveness for Model Scale and Full Scale

Free-surface CFD Prediction of Components of Ship Resistance for KCS

Joe Banks*, A.B. Phillips, Stephen R. Turnock, Southampton University
*jb105@soton.ac.uk

1. Introduction

Towing tank experiments are commonly used to determine the resistance components of new hull forms (ITTC, 2008). As the presence of a propeller at the stern of a ship significantly changes the flow field compared to that of a towed hull, self propelled resistance tests are also conducted. These procedures are often very expensive and there is an increasing drive to assess the resistance components numerically.

The computational cost of fully resolving the flow around a propeller geometry and hull inhibits the use of numerical simulations for commercial use. However, several groups have implemented simplified body force propeller models, as described in (Phillips et al, 2010), which accurately induce the accelerations produced by a propeller into the fluid. It is intended to use a similar body force propeller model to investigate its impact on resistance and the free surface around the stern of a self propelled ship.

Initially it is essential to develop and validate a numerical method for evaluating the resistance components on a towed hull. This requires a free surface model that will allow the wave pattern and therefore wave resistance to be assessed. The accurate modelling of the boundary layer growth is required to capture the frictional resistance and the form drag. Extensive research has been conducted in this area and is well documented in the proceedings of the CFD workshop conducted in Gothenburg and Tokyo (Larsson et al, 2000)(Hino, 2005). One of the commonly used hull geometries is the KRISO container ship (KCS), which is used in this study.

2. Theoretical approach

To numerically capture the free surface fluid motions a finite volume method, using a Volume of Fluid (VOF) approach was used. This method is derived from the surface integration of the conservative form of Navier Stokes' equations over a control volume. Equations (1) and (2) are the incompressible Reynolds averaged Navier-Stokes (RANS) equations in tensor form and Equation (3) is the volume fraction transport equation (Peric and Ferziger, 2002).

$$\frac{\partial(\rho U_i)}{\partial t}+\frac{\partial(\rho U_i U_j)}{\partial x_j}=-\frac{\partial P}{\partial x_i}+\frac{\partial}{\partial x_j}\left[\mu\left(\frac{\partial U_i}{\partial x_j}+\frac{\partial U_j}{\partial x_j}\right)\right]-\frac{\partial}{\partial x_j}\left(\rho\overline{u'_i u'_j}\right)+f_i \quad (1)$$

$$\frac{\partial U_i}{\partial x_i}=0 \quad (2) \qquad \frac{\partial c}{\partial t}+\frac{\partial(cU_j)}{\partial x_j}=0 \quad (3)$$

The volume fraction c is defined as (V_{air}/V_{total}) and the fluid density, ρ, and viscosity, μ, are calculated as $\rho=\rho_{air}c+\rho_{water}(1-c)$ and $\mu=\mu_{air}c+\mu_{water}(1-c)$.

External forces applied to the fluid are represented as f_i, which include buoyancy forces due to differences in density and momentum sources representing the influence of the propeller. The effect of turbulence on the flow is represented in Equation (2) by the Reynolds stress tensor $\rho\overline{u'_i u'_j}$ and is modelled using a turbulence model.

In this investigation both a Shear Stress Transport (SST) eddy viscosity model and a Baseline (BSL) Reynolds stress model (ANSYS, 2009) were used to evaluate the Reynolds stress tensor. The SST model blends a variant of the k-ω model in the inner boundary layer and a transformed version of the k-ε model in the outer boundary layer and the free stream (Menter, 1994). This has been shown to be better at replicating the flow around the stern of a ship, than simpler models such as k-ε, single and zero equation models (Larsson et al, 2000)(Hino, 2005). The BSL Reynolds stress model includes transport equations for each component of the Reynolds stress tensor. This allows anisotropic turbulence effects to be modelled helping to model complex flow features such as separation off curved surfaces (Peric and Ferziger, 2002). The BSL model is blend of a Reynolds stress-ω

and ε model depending on the fluid regions (ANSYS, 2009).

3. Experimental data

Total resistance and wave field data for the KRISO Container Ship (KCS), were obtained through towing tank tests (Kim et al, 2001), and are used for validating the CFD simulations. The experiments were conducted in the KRISO towing tank (200m x 16m x 7m) on a 1/31.6 scale model of the KCS hull (full scale dimensions L=230m, B=22.2m, D=19m, with a draught of 10.8m). A Froude number of 0.26 was maintained providing a model scale Reynolds number of 1.4×10^7. The model was fixed in heave and pitch at the full scale static draught with zero trim.

4. Numerical model

Table 1 - Numerical simulation properties

Property	Fine Mesh (half hull)
Type of mesh	Structured (Hexahedral)
No. of elements	Approximately 10M
y^+ on the hull	Approximately = 1 (max value 1.2)
Domain Physics	Homogeneous Water/Air multiphase, SST or BSL turbulence model, Automatic wall function, Buoyancy model –density difference, Standard free surface model
Boundary physics:	
Inlet	Inlet with defined volume fraction, flow speed = 2.1966 m/s, turbulence intensity 0.05
Outlet	Opening with entrainment with relative pressure = hydrostatic pressure
Bottom/side wall	Wall with free slip condition
Top	Opening with entrainment with relative pressure 0 Pa
Hull	Wall with no slip condition
Symmetry plane	Along centreline of the hull
Solver settings:	
Advection scheme	High Resolution (ANSYS, 2009)
Timescale control	Physical timescale function: 0.01[s] + 0.09[s]*step(atstep-20)+ 0.1[s]*step(atstep-200)
Convergence criteria	Residuary type: RMS, Target: 0.00001
Multiphase control	Volume fraction coupling
Processing Parameters:	
Computing System	Iridis 3 Linux Cluster (University of Southampton)
Run type	Parallel (24 Partitions run on 3x8 core nodes each with 16 Gb RAM)

Simulations are performed using ANSYS CFX V12 (ANSYS, 2009). This is a commercial finite volume code, which uses collocated (nonstaggered) grids for all transport equations, coupling pressure and velocity using an interpolation scheme. The physical parameters and solver settings used to define the numerical solution are provided in Table 1, along with details of the computing resources used for the largest mesh.

5. Structured Meshing Technique

A structured mesh was built using ANSYS ICEM around the full scale KCS hull geometry. The domain width and depth matched the dimensions of one half of the KRISO towing tank. The length was selected to allow one ship length in front of the hull and two behind. This was then converted to model scale dimensions each time a mesh was generated.

A blocking structure was developed that allowed a good quality surface mesh to be created over the hull (see Figure 1). It was found that collapsing the blocks under the stern down to a point provided the best overall mesh structure in this region. This approach also allowed extra mesh density to be added in this localised area where large surface curvatures needed to be captured. Elements were also clustered within the region of the free surface to allow a sharp interface to be captured.

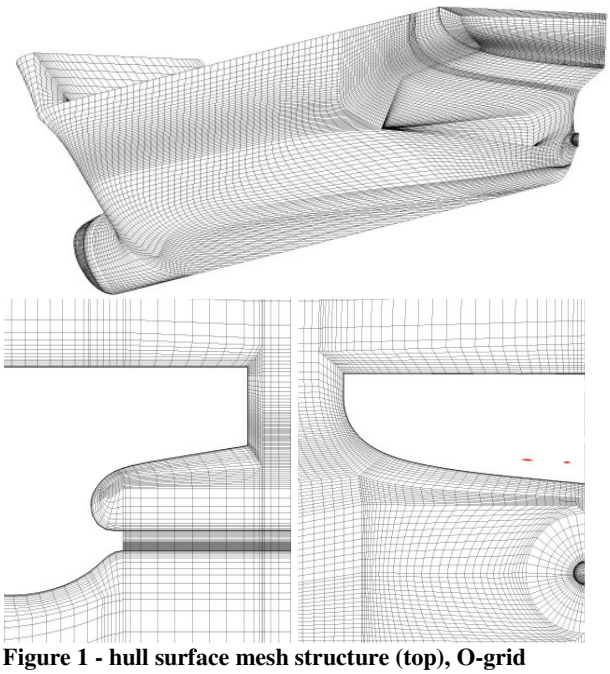

Figure 1 - hull surface mesh structure (top), O-grid structure at stern from the side (left) and from the stern (right), for the initial mesh containing 0.8M elements.

Once satisfied with the surface mesh structure an O-grid blocking structure was grown out from the surface of the hull. This effectively encircles the hull with a set of blocks that maintain the surface mesh structure. The depth of the inner O-grid was matched to approximately that of the maximum expected boundary layer. This provides a great deal of control over the near wall mesh density. Another outer O-grid of the same depth was placed about the hull and manipulated so as to provide a smooth transition between the near wall radial mesh and the far field Cartesian structure. Another key feature is the continuation of the O-grids about the propeller axis, towards the outlet of the domain. The outer O-grid was expanded to match the diameter of the propeller allowing a circular propeller model to be easily added at a later date (see Figure 1).

6. Free surface deformation and mesh refinement

The initial mesh created contained 0.8M elements, with a y^+ on the hull of 30-60. The mesh density was then increased to 7M elements and the y^+ reduced to approximately 1 so as to resolve right through the boundary layer. The wave pattern captured by both these meshes, and a comparison made to the experimental data, can be seen in Figure 2. The increased mesh density has a significant impact on capturing the free surface deformation close to the hull. As the wave pattern propagates away from the hull the resolution of the free surface reduces significantly. On closer inspection of the mesh, it was found that the blocking structure adopted towards the stern of the vessel actually placed the areas of high mesh density above the free surface away from the hull. To solve this problem additional splits were placed within the far field blocks, alongside and astern of the hull. The region of high mesh density, correctly positioned on the parallel mid body, could then be forced to the correct height over the rest of the domain. This was combined with increasing the number of elements within this free surface region to provide a half body mesh of approximately 10M elements. The increased resolution of the far field free surface can be seen in Figure 2.

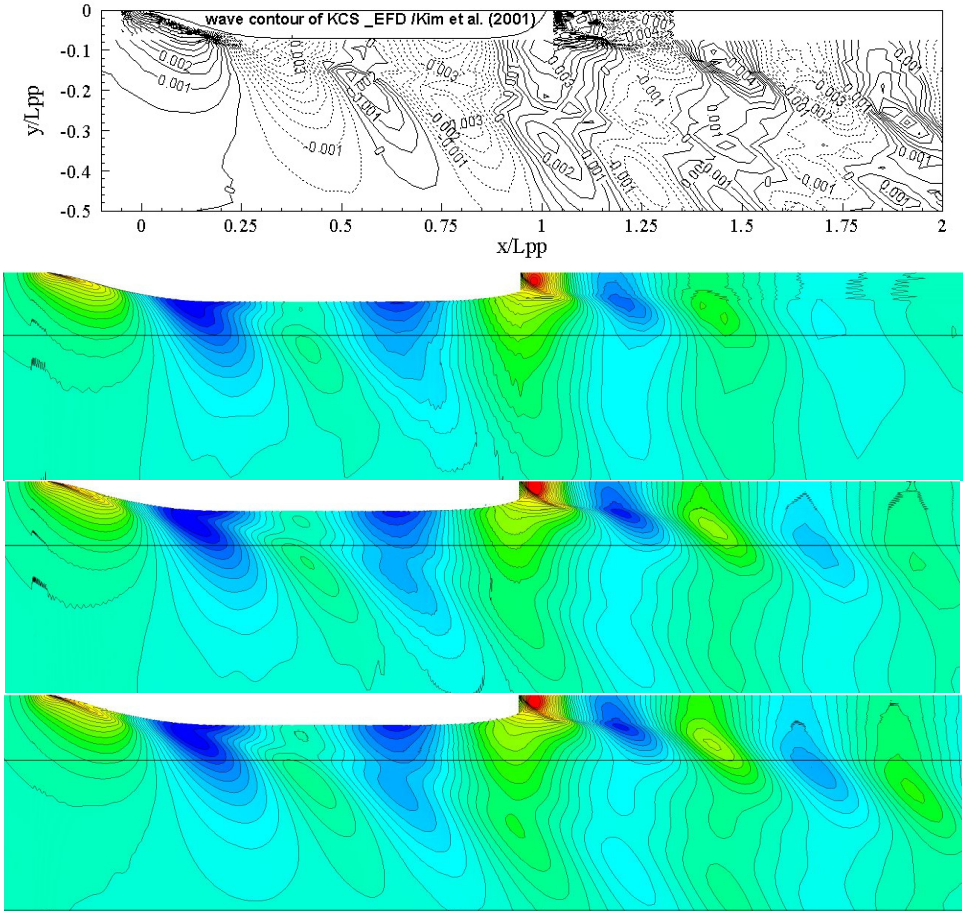

Figure 2 – Free surface elevation, z/Lpp, of global wave pattern for (Top Down) Experimental data, CFD results for 0.8M, 7M and 10M element meshes. Contours range from z/Lpp = -0.005 to 0.010 in steps of 0.0005. The straight lines represent the positions of the wave cuts.

Comparisons between the free surface elevation from experimental and CFD data can also be seen in Figure 3. This provides the wave height seen along the surface of, and at a fixed distance away from, the hull. The position of the wave cuts are shown as straight lines in Figure 2.

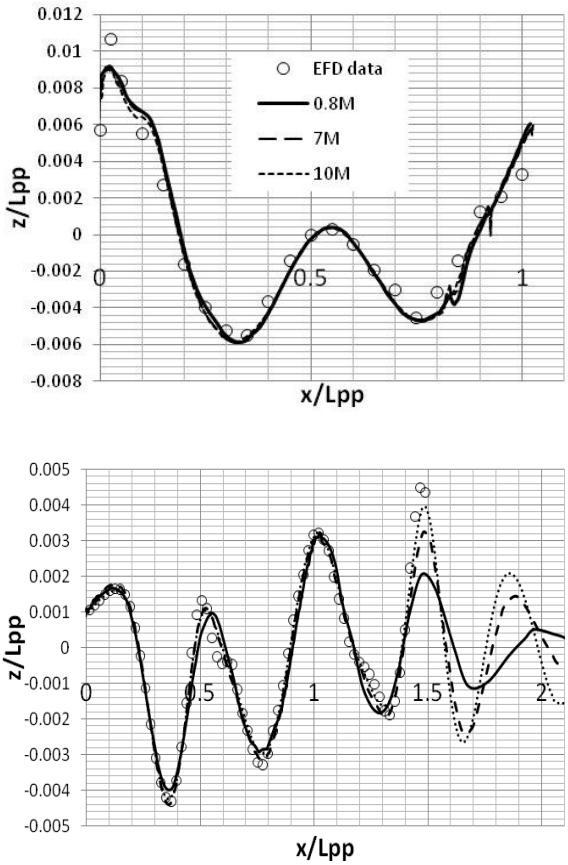

Figure 3 - Comparison between experimental (EFD) and CFD wave elevation on the surface of the hull (top) and at a distance of y/Lpp=0.15 from the ship centerline (bottom)

It can be seen that all the CFD data agrees well with the experimental data along the majority of the surface of the hull. Some differences are observed at the bow and stern, however it should be noted that the experimental data was obtained through photo analysis (Kim et al, 2001) and therefore is subject to increased error compared to wave probe data. Another discrepancy is observed as a dip in the free surface as it starts rising towards the stern. This was found to occur over a slight discontinuity in the surface mesh structure which is believed to be the cause. Interestingly alterations to the mesh had almost no impact on the free surface on the hull, however did have a significant impact on the wave cut traces. It can be seen in Figure 3 that the 7M mesh was sufficient to accurately capture the magnitude and position of the wave crests and peaks up until the stern (x/Lpp=1), however, beyond this the 10M mesh was required to obtain the correct wave amplitudes. Based on the comparisons made with the experimental data, displayed in Figures 2 and 3, it was decided that the 10M mesh structure and element distribution would be adopted as the basis mesh.

7. Mesh sensitivity study

To evaluate how the number of elements within the mesh affected the solution the 10M mesh was subjected to two $\sqrt{2}$ global element distribution reductions, creating 4M and 1.5M element meshes. Both these maintained a y^+ value of approximately 1 on the surface of the hull and were only modified so as to provide smooth mesh expansion ratios. To evaluate the impact this had on the free surface three different wave cuts were compared, see Figure 4. It is clear that the mesh density has the greatest impact astern of the hull and closest to the centre line. However, some slight differences in wave amplitude can be seen further forward. This would indicate that to accurately capture the wave pattern, and therefore the wave resistance of a model hull, the 4M element mesh could be used with added mesh density astern of the hull. This should help to minimise the computing power required for the simulation.

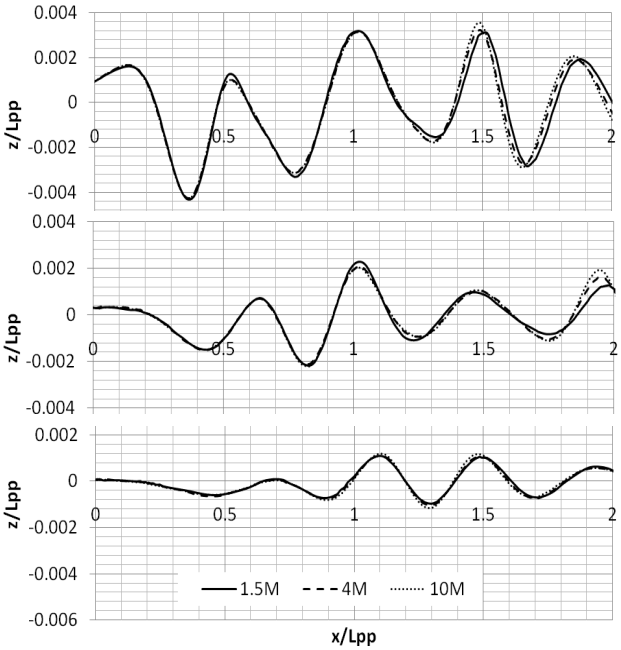

Figure 4 - Influence of mesh density on free surface elevation at wave cuts positioned at y/Lpp = 1.5 (top), 3 (middle) and 4.5 (bottom) from the ship centreline

8. Resistance components and influence of turbulence model

Once confidence had been gained that the wave pattern was accurately being captured it was important to verify that the hull resistance was being correctly obtained.

During the experiments conducted by (Kim et al, 2001) the coefficient of total resistance C_T was calculated to be 3.557×10^{-3}. To evaluate this from the CFD results the total force acting on the hull in the x-direction was evaluated and non-dimensionalised using equation 4, where A_W is the static wetted surface area of the model (9.5121 m^2) and U_0 is the tow velocity (2.196 m/s).

$$C_T = \frac{R_T}{0.5 \rho A_w U_0^2} \qquad (4)$$

The total resistance obtained from all three meshes (1.5, 4 and 10M) was significantly higher than the experimental findings. To understand the cause of this the individual components of resistance were evaluated. In (Kim et al, 2001) the coefficient of frictional resistance, C_F, was calculated using the ITTC correlation line (ITTC, 2008) to be 2.832×10^{-3}. By subtracting this, the coefficient of residuary resistance, or pressure resistance, C_P, was calculated to be 0.725×10^{-3}. Within CFX-Post the frictional resistance acting on a body can be calculated by performing an area integral of the wall shear in the x-direction. This was evaluated for both the hydrodynamic and aerodynamic frictional resistance and presented in coefficient form. The aero and hydrodynamic pressure drag was similarly calculated by integrating the x-component of the pressure over the relevant areas of the hull through using the volume fraction. The force components obtained by the different meshes can be seen in Table 2

Up until this point all the simulations had been conducted using the SST turbulence model. However the results clearly indicate that both the frictional and pressure resistance components were being over estimated. It is also apparent that although increasing mesh density seems to have some impact on improving the hydrodynamic pressure component, it doesn't seem to have any impact on the frictional component of resistance.

To establish if these discrepancies were linked to the use of the SST turbulence model a BSL Reynolds stress model was compared. It was hoped that through modelling the anisotropic turbulence in the flow a more accurate representation of the boundary layer would be obtained, especially towards the stern of the ship where separation is most likely to occur. The resistance components obtained from these simulations are also presented in Table 2. Immediately it can be seen that both resistance components have been reduced compared to the SST model. It is also apparent that the BSL model is far more sensitive to mesh density than the SST model, with all components of resistance varying significantly. Interestingly, as the mesh density increased both aerodynamic and hydrodynamic C_F rose whilst the hydrodynamic C_P dropped significantly. In contrast to this the aerodynamic C_P increased to the same magnitude as the hydrodynamic C_P. Therefore the net result of increasing mesh density was to increase the total resistance acting on the hull whilst actually reducing the hydrodynamic resistance.

Table 2 - Components of resistance for the model hull simulations

Mesh	Turbulence model	Cf		Cp		Ct	
		Hydro	Aero	Hydro	Aero	Combined	Hydro
1.5M	SST	2.968E-03	3.824E-05	1.006E-03	-2.766E-05	3.985E-03	3.975E-03
4M	SST	2.999E-03	2.849E-05	9.348E-04	-7.944E-07	3.962E-03	3.934E-03
10M	SST	3.010E-03	3.215E-05	8.615E-04	5.662E-05	3.960E-03	3.871E-03
1.5M	BSL	2.648E-03	7.318E-05	8.208E-04	2.204E-05	3.564E-03	3.469E-03
4M	BSL	2.700E-03	6.699E-05	6.430E-04	1.447E-04	3.554E-03	3.343E-03
10M	BSL	2.916E-03	9.779E-05	3.819E-04	3.957E-04	3.791E-03	3.298E-03
Experimental		(ITTC) 2.832E-03		7.250E-04		3.557E-03	

If we try and compare these results with the experimental data we are posed with an interesting dilemma, we do not know what the components of air resistance are for the model tests. The experimental components of resistance are determined purely using the ITTC correlation line which is an empirical relationship, used for effectively scaling model data. The recommended procedures for towing tank resistance tests, outlined in (ITTC, 2008), make no allowances for the air resistance for models up to a Froude number of 0.45. Therefore models do not necessarily have the correct freeboard or bow configurations, or a deck. This is because at low Froude numbers the aerodynamic component of resistance is considered small. However if we look at the BSL results from Table 2 we can see that the aerodynamic component of resistance varies from 2.6 to over 10%. It should be remembered however that the mesh structure was not focused on accurate aerodynamic modelling so these values could be subject to large errors.

The key point still remains, however, to fully asses the validity of the CFD resistance components more detail of the above water model configuration is required. It could be that significant changes from the full scale hull geometry, along with the addition of a towpost etc could significantly alter the total resistance measured. Due to the use of the ITTC correlation line these changes are represented in the residuary/pressure resistance component, despite containing aerodynamic frictional and pressure components. This means that direct comparison of experimental results could be misleading.

Another important point that should be mentioned is that if the aerodynamic components of resistance are significant then more focus should be placed on accurately modelling the aerodynamic flow features around the hull.

In general, it seems that the BSL Reynolds stress turbulence model provided a closer match to the experimental results indicating that maybe the different components of resistance can be successfully modelled using this methodology. However more work is undoubtedly required to investigate the impact of mesh density on the different components of resistance, especially aerodynamic.

9. Conclusions

A numerical methodology has been developed to accurately simulate the flow around a towed hull. A mesh structure has been developed that efficiently captures the free surface wave pattern, whilst allowing for easy implementation of a propeller model in the future. The numerical wave pattern generated has been validated against experimental data showing good correlation.

An assessment of the aero and hydrodynamic components of drag highlighted the need for more detailed information about the 'above water' experimental set up from towing tank experiments, if accurate validation is to be achieved.

The impact of two different turbulence models on the components of resistance has been evaluated, concluding that the Baseline (BSL) Reynolds stress model provided the best comparison to experimental data. It is therefore now envisaged that this numerical methodology can be used to evaluate the impact a propeller model has on the free surface near the stern and how this affects the resistance components of a self propelled ship.

References

ANSYS. (2009) ANSYS CFX, Release 12.0. ANSYS.

Hino T. (2005) CFD Workshop Tokyo 2005. In: The Proceedings of CFD Workshop Tokyo.

ITTC. (2008) International Towing Tank Conference-Recommended Procedures and Guidelines – Testing and Data Analysis Methods Resistance Test, 7.5-02-02-01.

Kim, W.J., Van, D.H. and Kim, D.H., (2001), " Measurement of flows around modern commercial ship models", Exp. in Fluids, Vol. 31, pp 567-578

Larsson L, Stern F, Bertram V. (2003) Benchmarking of Computational Fluid Dynamics for Ship Flows: The Gothenburg 2000 Workshop. Journal of Ship Research 2003;47:63–81(19).

Menter, F.R., (1994) Two-equation eddy-viscosity turbulence models for engineering applications. AIAA Journal 32(8):1598 –605.

Peric, M., Ferziger, J.H., (2002) Computational Methods for Fluid Dynamics, Springer, 3rd edition.

Phillips, A.B., Turnock, S.R. and Furlong, M.E. (2010) Accurate capture of rudder-propeller interaction using a coupled blade element momentum-RANS approach. *Ship Technology Research (Schiffstechnik)*, 57, (2), 128-139.

Sloshing Simulations with Fluid-Structure-Interaction using OpenFOAM

Silvan Brändli, TU Hamburg-Harburg, Hamburg/Germany, silvan.braendli@tu-harburg.de

Fluid-structure-interaction (FSI) stands for the coupled simulation of a fluid and a structural problem. FSI has to be taken into account if the deformations, caused by fluid forces, are big enough to influence the fluid flow significantly. Typical FSI problems are springing and whipping of ships in waves and impact problems such as slamming and sloshing. In the scope of this project, a RANSE solver from the OpenFOAM package (interDyMFoam) was coupled with finite-element (FE) models from Ansys and Poseidon. The aim was to work with only one solver during runtime and therefore to calculate the structural deformations within the original fluid solver. Therefore, the mass and stiffness matrix are exported from the FE model and read by the FSI solver at the beginning of a calculation.

To determine the deformations at the nodes of the FE model, the equation of motion has to be solved:

$$\mathbf{K}\cdot\mathbf{d} + \mathbf{D}\cdot\mathbf{v} + \mathbf{M}\cdot\mathbf{a} = \mathbf{f}$$

K, **D** and **M** are the stiffness, damping and mass matrix of the FE model, respectively. **d**, **v** and **a** are the deformation, velocity and acceleration of the FE nodes, respectively. They are expressed in a local coordinate system of the structure. The accelerations are relative to the origin of the local coordinate system. **f** describes the nodal load on the FE model. It consists of the fluid forces $\mathbf{f}_f$ and acceleration forces.

$$\mathbf{f} = \mathbf{f}_f + \mathbf{M}\cdot\mathbf{a}_{outer}$$

The nodal accelerations in $\mathbf{a}_{outer}$ contain gravity as well as accelerations resulting from the relative motion between the local coordinate of the structure and the earth-fixed coordinate system.

The solver interDyMFoam solves viscous two-phase flows on a dynamic mesh. With the above equation of motion, the mesh update shall be modified to deform the fluid mesh according to the deformations of the structure. Fig.1 shows the flowchart of the developed FSI solver. The black boxes represent components from interDyMFoam, blue boxes represent added parts which were developed in this project. The new FSI solver works as follows:

1. Read case data: Same as interDyMFoam. Additionally mass and stiffness matrix of the FE model are read as well as its node positions and a matrix to map forces and displacements between the FE model and the fluid mesh.

2. Initialize equation of motion: The equation of motion is set up and arranged to be solved for the deformations.

   Hereafter the loop over the time steps starts.

   Within every time step, an iteration is performed to assure the compatibility of the solutions of the fluid flow and the structural problem.

3. Solve structural problem: Determine the load vector for the equation of motion. In the first iteration cycle, the fluid forces are guessed, based on the forces from previous time steps. Later cycles use the fluid forces from the fluid solution of the previous iteration cycle.

4. Update fluid mesh: The structural deformations are applied to the boundaries of the unmodified grid. By using the grid solver displacementLaplacian the inner grid is adapted to the new boundaries. Hereafter the whole grid is transformed according to the outer motion (e.g. in case of a sloshing simulation).

5. Solve fluid problem: Same as interDyMFoam

6. Check convergence

    a) End of the iteration step: In case the iteration is not converged: Advance to the next iteration cycle. The new fluid forces will be applied to the structure in the next cycle.
    b) End of the time step: In case the iteration is converged: Advance to the next time step. Fluid forces for the next time step are guessed.

To obtain good convergence behaviour within a time step, the fluid forces are relaxed dynamically. Every component of the vector of fluid forces is relaxed with a specific relaxation parameter. At the beginning of the simulation, all relaxation parameters have the same value. During the calculation, every relaxation parameter is adapted to the convergence behaviour of its fluid force. If the fluid force is oscillating over the iteration cycles, the relaxation parameter is reduced to suppress the oscillation; otherwise the relaxation parameter is increased. Furthermore there are upper and lower bounds for the relaxation parameters.

The convergence criterion for the iteration is based on the thought that (in case of convergence) the structural problem shall show no more relevant changes between two iteration cycles. Therefore a residual vector **r** is computed using the load vector **f** of the structural problem. According to the equation below, a residual in time step i equals the change of the load vector between the current iteration cycle j and the previous iteration cycle j-1 divided by the change relative to the past time step i-1:

$$\mathbf{r}[k] = (\mathbf{f}_j^i[k]-\mathbf{f}_{j-1}^i[k])/(\mathbf{f}_j^i[k]-\mathbf{f}_{end}^{i-1}[k]) = \Delta \text{ per iteration} / \Delta \text{ per time step}$$

A time step is considered as converged if the biggest residual multiplied with the average of all residuals is smaller than a specified value. In order to load the FE model with reasonable forces in the first iteration cycle of a new time step, the fluid forces are extrapolated to the new time step. Basically every fluid force is extrapolated linearly based on the values from the two previous time steps. If a fluid force oscillates in time, this extrapolation would be far from the converged result. Hence, in this case, the value from the previous time step is used directly. These guessed forces have no influence on the converged solution of the time step. However, if it lies near the converged force, convergence is achieved faster.

The numerical behaviour of the FSI solver was tested. Following experience was gained:

- By the correct choice of the parameters influencing the dynamic relaxation the simulation time can be reduced by up to 17 %.
- The strictness of the convergence criterion has only a minor influence on the result. However, very loose criteria lead to numerical instability.
- The correction of grid fluxes, usually applied by OpenFOAM after updating a mesh, can be deactivated because of the iteration inside the time step. The resulting decrease in simulation time was 18 % for the test case.

The average amount of iteration cycles per time step was approximately 7 for the test case.

Finally a sloshing simulation on a complex tank geometry was performed. Therefore a fluid mesh with 550000 cells and an FE model with about 73000 degrees of freedom were used. The tank performs periodic movements, which excite the free surface. At the ends of the tank the tank top is hit by the liquid, whereat high pressures occur. Fig.2 illustrates a pressure peak for two simulations. The simulation taking FSI into account shows a significantly lower pressure peak than the simulation on the rigid structure. This is as expected; the yielding of the structure should reduce pressure peaks.

Details on the project can be found in my diploma thesis “Entwicklung eines Simulationsmodells für Fluid-Struktur-Interaktion” (in German).

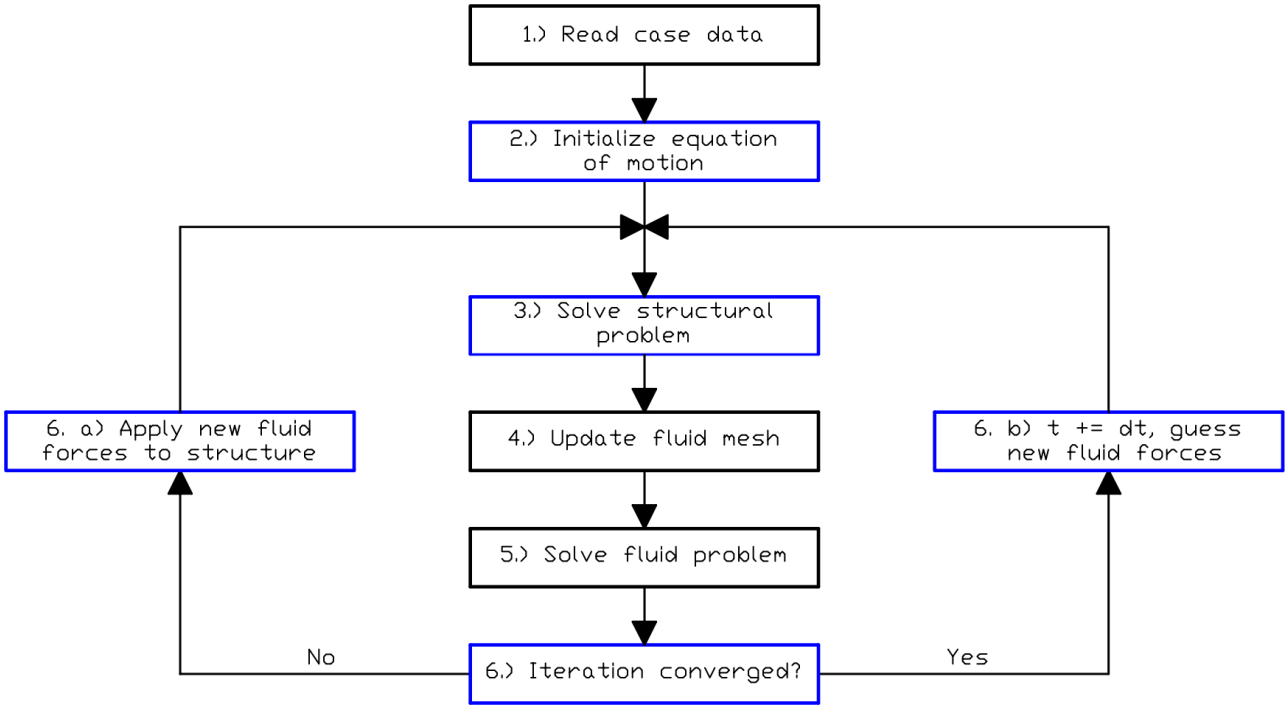

Fig.1: Flowchart of the FSI solver. Black items mark components from interDyMFoam

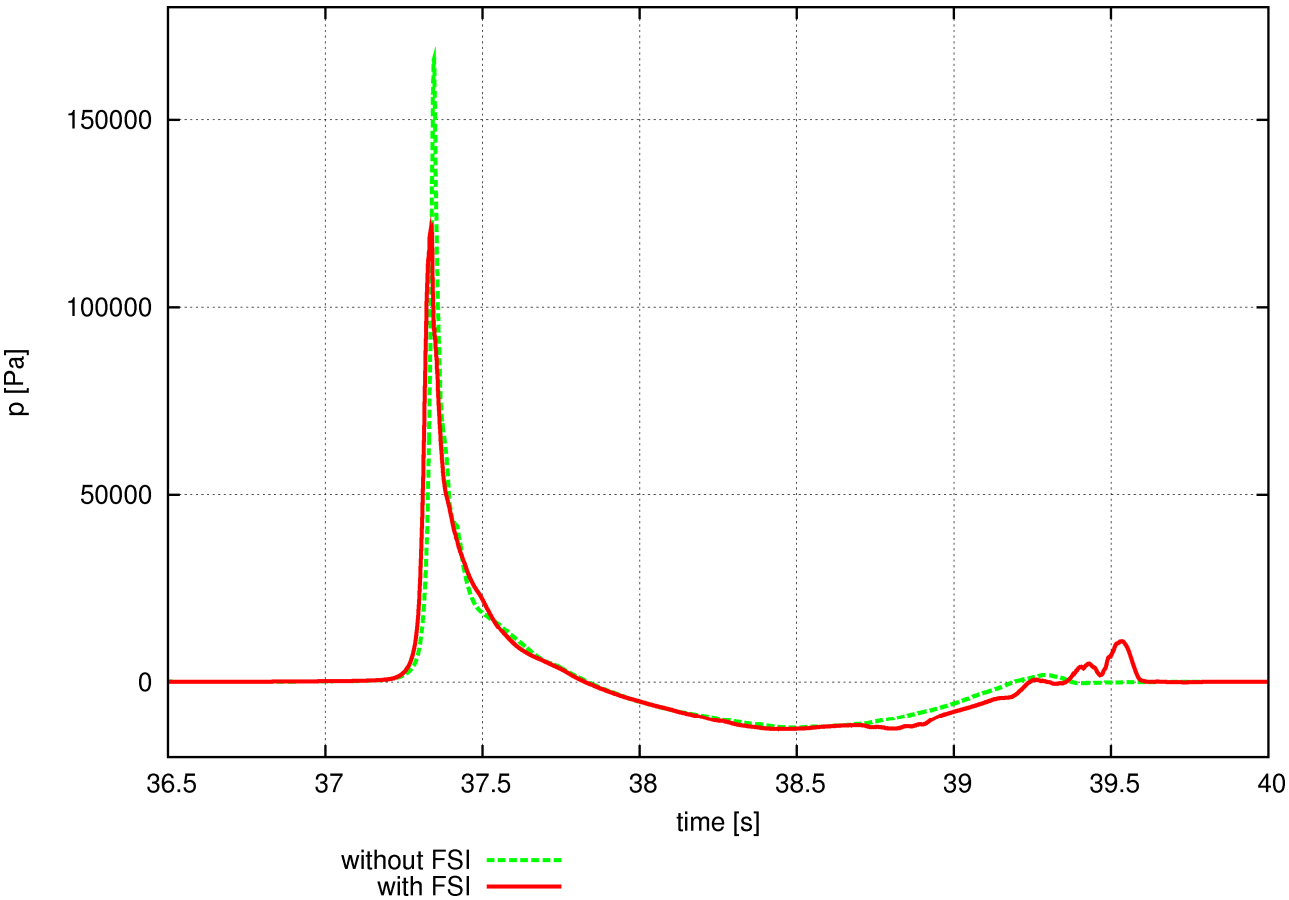

Fig.2: Pressure during sloshing calculation with and without FSI.

CFD validation of different propeller ducts on open water condition.

Alejandro Caldas, Marcos Meis and Adrián Sarasquete
Vicus Desarrollos Tecnológicos, Vigo

a.caldas@vicusdt.com
m.meis@vicusdt.com
a.sarasquete@vicusdt.com

Intro

Trawlers account for the largest percentage of fishing vessels in Galicia. This kind of ships needs to provide high thrust at low advance ratios (it's usual operating velocities are around 3.5kn when the ship is towing the fishing net); because of this fact generally their propulsion units consist on ducted propellers. This paper summarizes some of the CFD calculations performed as starting point for trawler ducted propeller studies and highlights the capabilities of CFD as a valuable tool for the prediction of propulsive factors for ducted propellers. The calculations have been performed for a controllable pitch propeller with two different nozzle geometries. For all the calculations the mathematical model employed is Reynolds Averaged Navier Stokes based, coupled with wall laws and a two equations turbulence model. A Finite Volume method has been employed for the solution of the model.

Geometries description

As it has been said before a controllable pitch propeller of 200 mm diameter was employed for the calculations. In *Fig. 1* it can be seen the propeller geometry and in *Table 1* geometry parameters are presented.

EAR	Skew	0.7 Pitch	P/D	Pm	Pm/D	Profile
0.55	6º	200 mm	1	188.46 mm	0.9423	NACA 16

Table 1. General propeller parameters

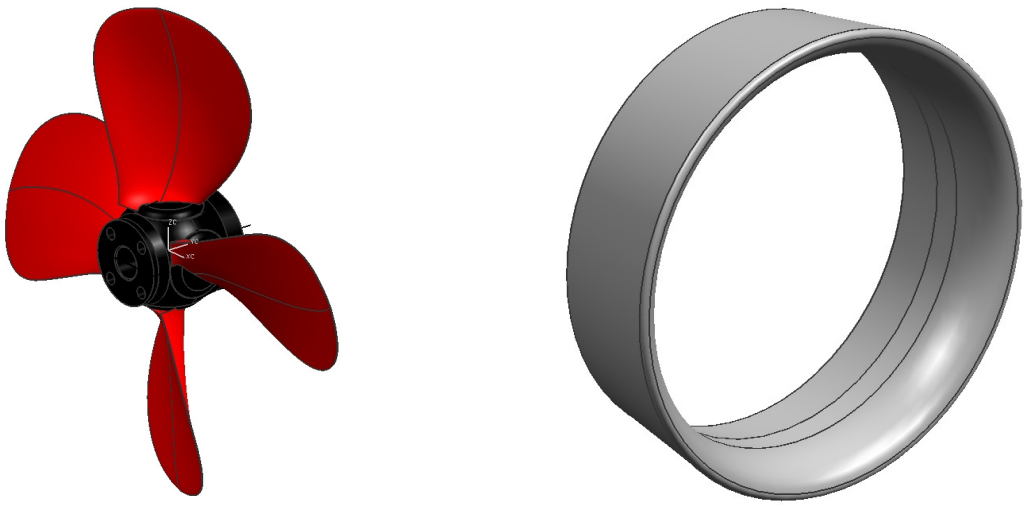

Fig. 1. Virtual propeller model

We have employed two different nozzles; both of them are 19A based but with different chord length. The first one (Nozzle 1) is 100 mm length and the second one (Nozzle 2) is 75 mm length, which corresponds with 50% and 37.5% of the propeller diameter. The internal nozzle diameter is the same for both cases, 202 mm which corresponds with a diametrical clearance of 1% of the propeller diameter.

Experimental data

The propeller model was manufactured at the Ship Design and Research Centre S.A. located in Poland (CTO). An image of the manufactured model can be seen on *Fig. 2*.

Fig. 2. Propeller model

The experiments were carried out at the CEHINAV, from the Madrid Polytechnic University in Spain; CEHINAV facilities includes a 56 m length, 3.8 m wide and 2.2 m depth tank. A calibration of the measurement instruments was carried out employing propeller nº 3297 from The National Physical Laboratory (United Kingdom). The deviation in the thrust and torque measurements were below 3% and 4% respectively. These deviations are within expectations about the usually errors in this towing tank.

Numerical simulation description

The computations were performed employing a Reynolds Averaged Navier Stokes Equations model solved in integral form and employing the Finite Volume based code Star CCM+.

As we are performing open water calculations with a uniform inflow, we have chosen a steady state temporal approximation treating the rotating propeller movement with a moving reference frame approach.

For the spatial discretization, second order schemes for both convective and viscous terms were employed and as pressure and velocities are treated in a segregated manner, the coupling between them is done by means of SIMPLE Method.

For the closure problem a two equations model were employed coupled with a wall law; for this case the k-ε turbulence model with an all Y+ wall treatment was employed.

For the domain discretization three polyhedral meshes were employed to asses the spatial convergence.

Numerical Results

The employed domain in the calculations is a cylinder which takes 5*D upstream the propeller, 10*D downstream the propeller and 5*D to the far field. Three unstructured polyhedral meshes were employed for the assessment of the spatial discretization convergence; Fig. 3 corresponds to the intermediate one (Mesh 1).

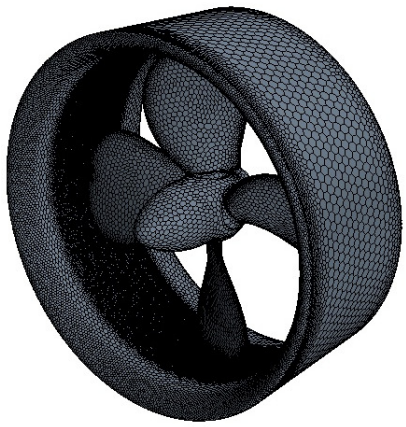

Fig. 3. Propeller mesh

Torque [N*m]	Mesh 1	Mesh 2	Iterative Error	Spatial Discretisation Error
3.01	*2.99*	*2.96*	*1.17E-06*	*0.9%*
Thrust [N]	**Mesh 1**	**Mesh 2**	**Iterative Error**	**Spatial Discretisation Error**
139.03	*133.58*	*133.77*	*6.23E-07*	*-0.1%*

Table 2. Convergence study

Before the performance of all the calculations, a spatial sensitivity analysis were carried out for J=0.2 and Nozzle 1 (*Table 2*). As we are employing unstructured grids, the mesh selection is carried out according to integral values of thrust and torque by an error. This error is computed as the difference between integral values for a mesh respect to the finest one. Theses errors estimations are shown in *Table 2* for the selected configuration. The results of spatial discretization error show us that the Mesh 1 can be used for all the simulations since the values of these ones are under 1% (we can disregard iterative errors for all cases since the magnitude order is too low).

The validation of the CFD results for the different ducted propellers against the results of towing tank test are carried out by the comparison of the different figures of merit. These figures of merit are: thrust and torque.

The validations of numerical results for Nozzle 1 are discussed in the following lines. The torque and thrust values versus the advance coefficient (J) are shown on *Fig. 4* and *5* respectively. It must be said that the presented curves for CFD calculations were interpolated from three calculation points (J=0.1, J=0.2 and J=0.5).

Agreement between the experimental data and the calculated torque is very good over the complete range of advance coefficient (the deviation is below 2% for all cases).

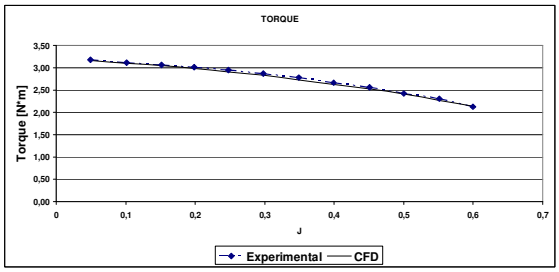

Fig. 4. Torque for Nozzle 1

The agreement between calculated and measured thrust is also good (the deviation is below 4% for all cases). Although the error for thrust is slightly higher than for torque, the curve shape is recovered.

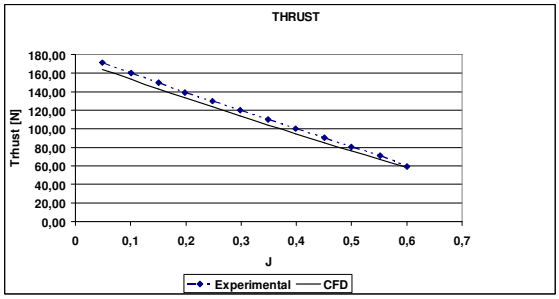

Fig. 5. Thrust for Nozzle 1

Non dimensional thrust, Kt (for propeller, nozzle and the total one), non dimensional torque, Kq, and the efficiency (η) from the CFD are visualized on *Fig. 6*. If we define a thrust distribution percentage between propeller and nozzle as Ktp/Kt, it can be seen that for low J this percentage presents values around 0.5. This means that the delivered thrust provided by nozzle and propeller is almost the same. As J increases its values our percentage value is increased too, since the Kt nozzle decrease faster than Kt propeller reaching negative values once the maximum efficiency has been reached.

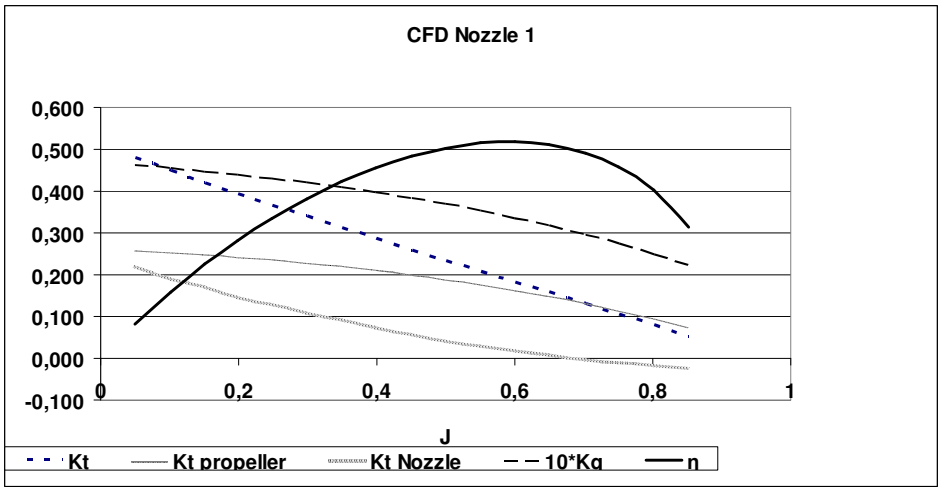

Fig. 6. CFD Results for Nozzle 1

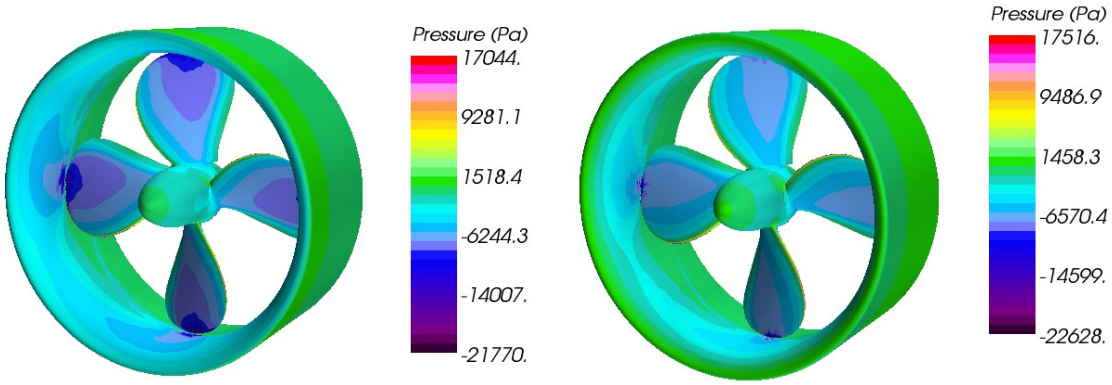

Fig. 7. Pressure distribution for J=0.2 and J=0.5

In *Fig. 7* the pressure distribution on propeller and nozzle surfaces are represented. As it can be seen for lower advance ratios the load of the propulsion system is higher (lower pressures on the suction side of the propeller and on the nozzle). It is easy to understand the importance of the gap tip length seeing the pressure distribution as it is the point of highest interaction between propeller and nozzle (a good mesh resolution is required). For lower advance ratios, the percentage of thrust from the nozzle is higher as the load of the propeller is displaced to the tip and this generates higher velocities (lower pressures) on the interior nozzle surface.

Fig. 8 and *9* represent torque and thrust calculations versus experimental data for Nozzle 2. It could be seen that discrepancies are in the same order as for Nozzle 1. *Fig. 10* represents the propulsive characteristics (Kt, 10*Kq and η) in the whole operating range for the propeller with Nozzle 2.

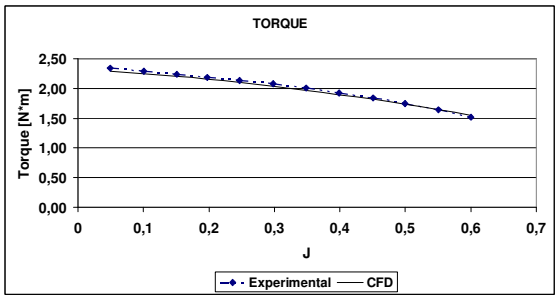

Fig. 8. Torque for Nozzle 2

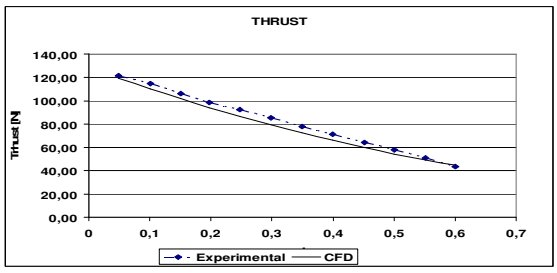

Fig. 9. Thrust for Nozzle 2

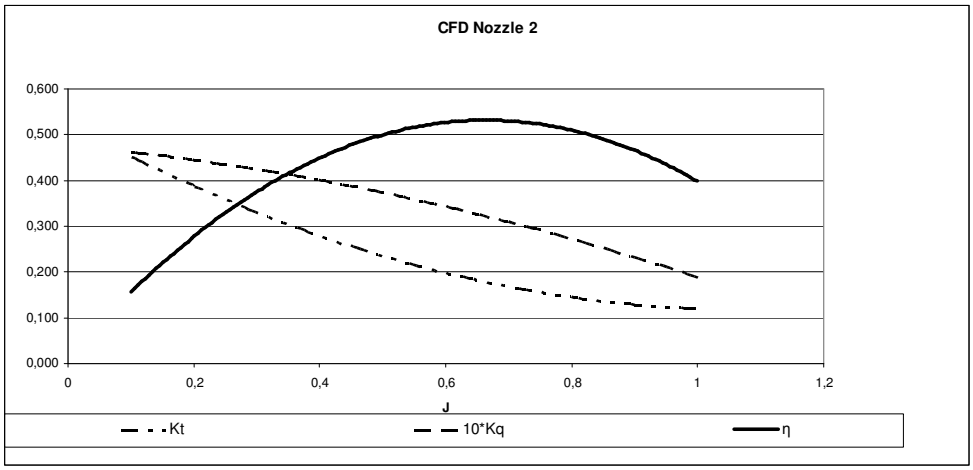

Fig. 10. CFD Results for Nozzle 2

Concluding remarks

A validation process for ducted propellers in open water condition is presented in this article. For this purpose a controllable pitch propeller was employed with two different nozzle geometries. The CFD calculations were performed employing a RANSE model solved with a Finite Volume Method. The results were compared with towing tank data and as it could be seen the agreement is good enough for design purposes.

As final conclusion it could be set that the CFD numerical model can be employed as a design tool for trawler propulsion systems.

Current and future works

The fact of locating a rudder downstream the propeller will vary the propulsive characteristics of the propulsion system [ref 2]; as a consequence the rudder must be included as an active element of the propulsion system. It is a common practice for deep sea trawlers to locate a group of three rudders with high aspect ratios downstream the propeller. At first this is a bad choice from the point of view of energy recovery for several reasons; a reduced sectional profile thickness on the blade leads to lower levels of energy recovery, furthermore, the fact of locating two of the rudders decentred from the propeller shaft results a worse working condition for rudders as the axial inflow is higher and the availability of energy recovery is lower.

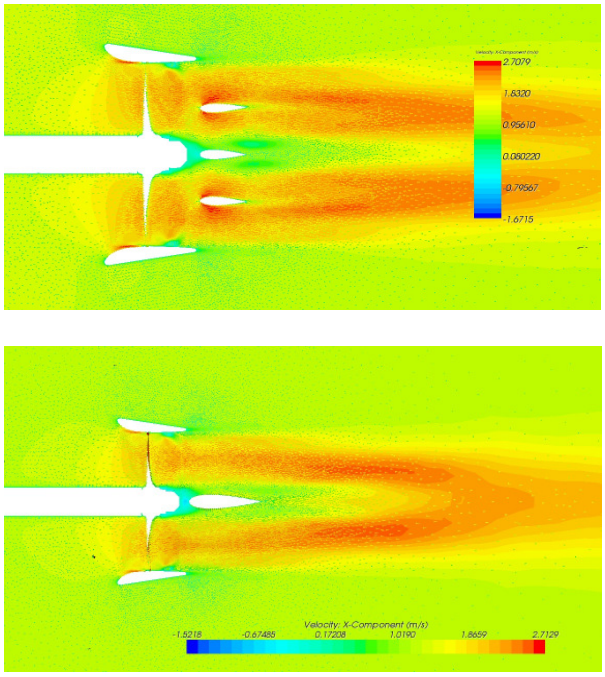

Fig. 11. Velocities profiles

	Without Rudder	Three Rudders	One Rudder
Propeller + Nozzle [N]	58.32	62.6	63.34
Propeller + Nozzle +Rudder [N]		59.4	62.36
Torque [N*m]	1.73	1.82	1.83
η	44.35%	42.81%	44.98%

Table 3. Preliminary results

In *Fig. 11* it can be seen the velocity field downstream a ducted propeller for a conventional three rudders arrangement and the same field for a single rudder. It seems, from preliminary studies, that for energy purposes it could be better to employ only one rudder aligned with the propeller hub with a higher aspect ratio than the employed one (three rudder arrangement).

The results of these preliminary calculations are presented on *Table 3*. It can be seen that for energy purposes the use of one rudder instead of three is much better and without any special modification on the rudder geometry such as Costa bulb, additional lifting surfaces, or special profile design of the rudder surface (indeed these solutions must be checked).

In addition to energy considerations, manoeuvrability aspects should be taken into account in future works as this could be an important issue for the control of the fishing operation while trawling in bad weather and reduced sailing speed.

Bibliography

[1]Carlton, J. *Marine propellers and Propulsion*. 2nd Edition. Butterworth-Heinemann 2007

[2]Sánchez Caja, A., Pylkkänen, J. V. and Spilä, Tuomas P. *Simulation of the incompressible Viscous Flow around Ducted Propellers with Rudders Using a RANSE Solver*. 27th Symposium on Naval Hydrodynamics Seoul, Korea, 5-10 October 2008

[3]Ferziger, J.H., Perić, M. *Computational Methods for fluid dynamics*. Springer. 2000

[4] Harvald, SV.AA., *Resistance and Propulsion of Ships*, Krieger Publishing Company, Malabar, Florida, 1991

[5] ITTC- *Recommended Procedures and Guidelines - CFD General Uncertainty Analysis in CFD Verification and Validation Methodology and Procedures*

[6] User guide STAR-CCM+ (Version 4.0.6)

Theoretical and numerical evaluation of a sail deformation close to the wind

Giuseppina Colicchio, Daniele Righetti, Claudio Lugni
g.colicchio@insean.it, INSEAN, Rome/Italy.

1 Introduction

Here we propose both an analytical and a numerical tool for the design of the sail plan in upwind conditions. It is a very simplified model that considers the sail plan as a set of 2D sections. Nonetheless it couples the structural deformation of the sail with the aerodynamic field in stationary conditions, allowing also the evaluation of the tension acting on the mast and on the boom. The flow field around the sail is described both with an analytical Glauert theory and with the CFD solver OpenFOAM. The deformation of the sail section is calculated using a cable model.

Even though the theoretical model can be used only in simplified conditions, *i.e.* when sailing close to the wind, it can be considered a valid tool both to verify more sophisticated numerical models and in the design stage, where applicable, when quick results are necessary. Finally, evaluating the effects of the excess length of the sail on the lift coefficients, it allows the identification of the proper camber depth and position from luff.

The work presented does not pretend to be complete, it represents a preliminary view of the potential use of the model. For actual applications to sail boats, a 3D validation as well as a coupling with the hull is necessary.

2 Models

2.1 Structural model: the cable

Some basic assumptions have to be formulated for the structural model. Here we consider that: a sail section can be considered inextensible, *i.e.* the elasticity of the sail can be disregarded; the curvature in the longitudinal direction is usually much higher then the curvature of the leech, so that, once the boom length has been fixed, the extremes of each section can be considered fixed. These assumptions allow the use of a cable representation of each sail section. In particular, if $\boldsymbol{T}(s)$ is the tension at the curvilinear coordinate s and $\boldsymbol{f}(s)$ the force acting in that position, the equilibrium in stationary conditions can be written as

$$\frac{d\boldsymbol{T}(\boldsymbol{s})}{ds} + \boldsymbol{f}(\boldsymbol{s}) = 0\,. \tag{1}$$

According to [1] the rope is represented as a series of N segments of length l_i inclined with an angle θ_i with respect to the vertical direction in the plane, see figure (1). Each node of the cable has the coordinates:

$$x_i = x_{i-1} + h_i \sin(\theta_i) \tag{2}$$

$$y_i = y_{i-1} + h_i \cos(\theta_i) \tag{3}$$

So that the θ_i are the unknowns of the problem. Figure (1) shows the distribution of the internal T_i and external actions A_i^N and C_i^N on the nodes of the segmented cable nodes as well as a representation of the segmented sail with fixed extremes.

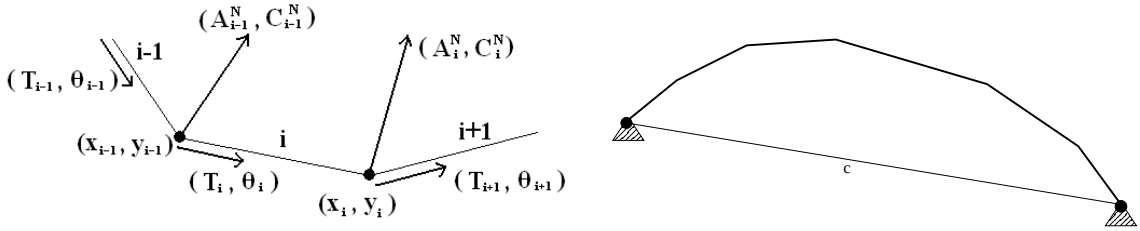

Figure 1: Distribution of the internal and external actions on the segmented cable nodes. Example of the segmented sail section with the constraints on the position of its extremes.

The discrete representation of equation 1 is given by

$$\begin{cases} T_{i+1}\sin\theta_{i+1} - T_i\sin\theta_i + A_i^N = 0 \\ T_{i+1}\cos\theta_{i+1} - T_i\cos\theta_i + C_i^N = 0 \end{cases} \tag{4}$$

With algebraic operations, it is possible to get the following $N-2$ equations

$$\begin{aligned} &(-C_{i-1}^N\sin\theta_{i-1} + A_{i-1}^N\cos\theta_{i-1})\sin(\theta_i - \theta_{i+1}) = \\ &(-C_i^N\sin\theta_{i+1} + A_i^N\cos\theta_{i+1})\sin(\theta_{i-1} - \theta_i) \end{aligned} \tag{5}$$

completed by the boundary conditions on the last node:

$$\sum_{i=1}^{N} h_i\sin\theta_i = x_{end} - x_{begin} \tag{6}$$

$$\sum_{i=1}^{N} h_i\cos\theta_i = y_{end} - y_{begin} \tag{7}$$

The system (5) and (6) can be solved through a Newton-Raphson method. Once θ_i are determined, the tension action on each segments can be calculated by the equation (4)

2.2 Aerodynamic theoretical model: Glauert

The thickness of the sail section can be considered null, so that the Glauert theory can be applied in the windward sailing conditions. In fact for a close hauled sail, the angle of attack α with respect to the apparent wind is smaller than 15^o and the Reynolds number is usually higher than $1.5\cdot 10^5$ so that the theoretical results can be considered reliable ([5]). Assuming that the thin foil of equation $y(x)$ can produce a distribution of vorticity $\gamma(x)$, from the Biot-Savart law, the vertical flow can be written as

$$v(x) = \frac{1}{2\pi}\int_0^c \frac{\gamma(r)}{x-r}dr \tag{8}$$

where c is the chord. As the foil is locally inclined by an angle $\alpha - dy/dx$ the free slip condition becomes

$$V_\infty(\alpha - dy/dx) = v(x) = \frac{1}{2\pi}\int_0^c \frac{\gamma(r)}{x-r}dr \tag{9}$$

where V_∞ is the inflow velocity. Substituting

$$x = \frac{c}{2}(1-\cos(\theta)) \tag{10}$$

in (9) and solving the integral as a Fourier series in $A_n \sin(n\theta)$ the local vorticity is expressed as

$$\gamma(\theta) = 2V_\infty \left[A_0 \frac{1+\cos(\theta)}{\sin(\theta)} + \sum_{n=1}^{\infty} A_n \sin(n\theta) \right] \tag{11}$$

where the coefficients A_n are

$$A_0 = \alpha - \frac{1}{\pi} \int_0^\pi \frac{dz}{dx} d\theta \tag{12}$$

$$A_n = \frac{2}{\pi} \int_0^\pi \frac{dz}{dx} \cos(n\theta) d\theta \tag{13}$$

with $n = 1, \ldots, \infty$. From the Bernoulli equations, the force acting at the abscissa x of the foil perpendicularly to the camber line is equal to $\Delta p(x) = \rho V_\infty \gamma(x)$.

2.3 Aerodynamic numerical model: OpenFOAM

The same forces can be calculated with more sophisticated tools. In particular, here the open source code OpenFOAM has been used. Among its many utilities the following have been chosen: 1) incompressible single fluid solver, 2) with Spalart-Almaras turbulence model ($y+ = 30$ and wall function) resulting in the code *rasInterFoam* and 3) an in house code to move the mesh according to the results of structural analysis.

2.4 Iterative solution of the coupled solvers

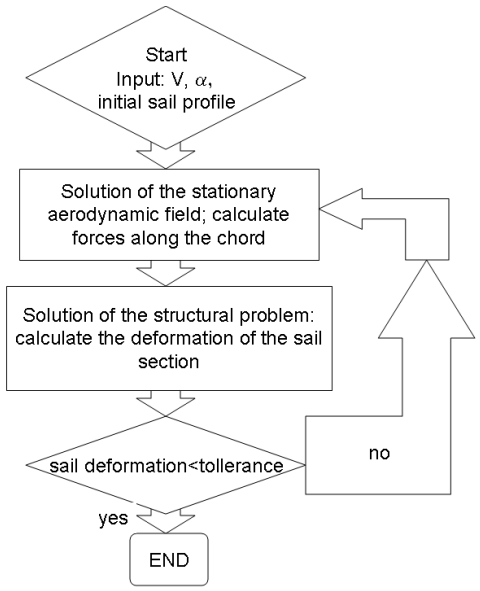

Figure 2: Flow chart of the iterative procedure.

Figure (2) shows the iterative coupling between the structural solver and the aerodynamic problem. Once the velocity of the sail section and its angle of attack have been stated, it is necessary to give an initial shape to the sail. Given the length of the sail $L = c + \epsilon c$, where ϵ is the excess length, here we adopted a NACA00** profile for the initial shape of the sail, but the convergence solution is not affected by the initial profile.

The fluid dynamic solver, either the Glauert theory or the OpenFOAM solver, gives the forces acting on each point of the sail section in stationary conditions. These are input to the structural solver that calculates the deformation of the profile. If the maximum deformation is smaller than the tolerance, here stated to $0.0001c$, the solution has been found, otherwise the two steps are repeated to convergence.

3 Validation

The first validation case refers to a common camber depth of sails around 25% of the chord, corresponding to $\epsilon = 1.14\%$. The results shown in the following are obtained using the theoretical Glauert model, because it allows a fast calculation of the sail shape in several condition, only in the end some results with the openFOAM solver will be shown and compared with the theoretical one. Figure (3) shows the sail shape and the position of the centre of pressure at different angles of attack. For large values of angle of attack, the profile shape and the centre of pressure do not change much. Most of the differences happen around the critical angle, *i.e.* the stall angle, where the lift at the leading edge decreases, and eventually becomes negative causing the luff of the sail. Further steering to windward will cause the sail stall. At the same time the centre of pressure of the sail plane move backward.

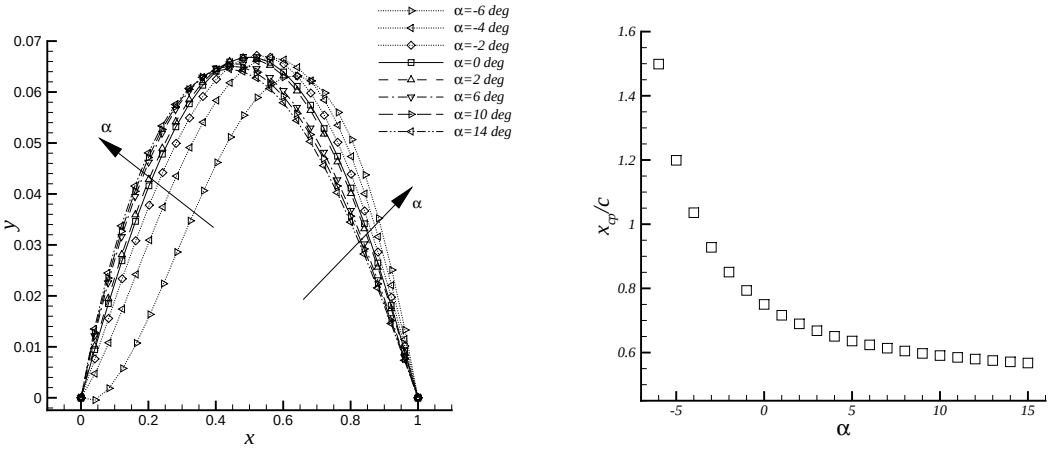

Figure 3: $\epsilon = 1.14$: equilibrium profiles and centre of pressure of the sail versus angle of attack.

Figure (4) shows the lift and tension coefficient versus the angle of attack. For large angle of attack the sail generates high lift, as the angle decreases and eventually becomes negative the lift decreases up to the stall. Further slights decrease in the angle of attack causes the sail to become soon again largely lifting. This is what happens when changing the direction of the wind, the lift decreases up to the sail stalling, the inertia in the yawing causes further slight decrease in the angle of attack, leading the sail profile to become lifting in the other direction and the boom to rotate.

The lift of the sail is transmitted to the mast and to the boom that constrain its deformation as a tension. The lift and the tension action can be evaluated through and empirical relation, see [2]. The comparisons between the numerical and empirical data show a good agreement, testifying the reliability of the model. This is also confirmed by the comparison with [3] and [4] in figure (5) for the same variable but different angle of attack. The data are, respectively, numerical and experimental data that are only slightly overestimated by the theoretical model

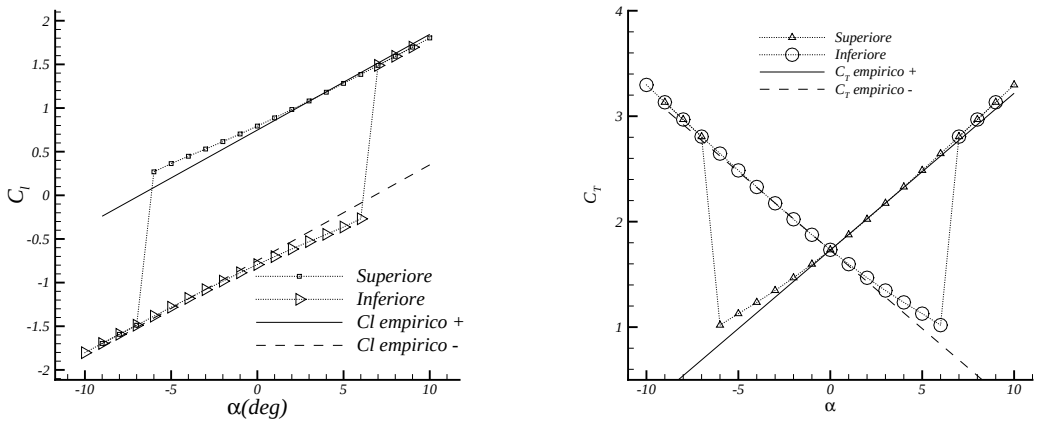

Figure 4: $\epsilon = 1.14$: Lift and Tension coefficient versus angle of attack.

here used.

The difference is due to the viscous effects disregarded in the theoretical approach. In fact, the

Coefficients	OpenFOAM	Glauert	Experiments
C_l	0.757576	0.793256	0.747395
C_m	0.380121	0.396643	//
C_d	0.00703436	//	//
C_T	1.723	1.823	1.73

Table 1: Aerodynamic coefficients in the equilibrium condition for $\epsilon = 1\%$ and $\alpha = 0$.

same conditions reproduced with the Navier-Stokes solver at $\alpha = 0^o$ give the differences in lift and tension shown in table 1. The CFD Solution shows smaller values as in the experiments. However, we would like to underline that the six iterations necessary to get a convergent solution in the CFD solver have taken 18 hours of calculation on a Xeon 3.00GH compared with the few minutes used for the theoretical solution. The top-left side of figure (6) shows the comparison

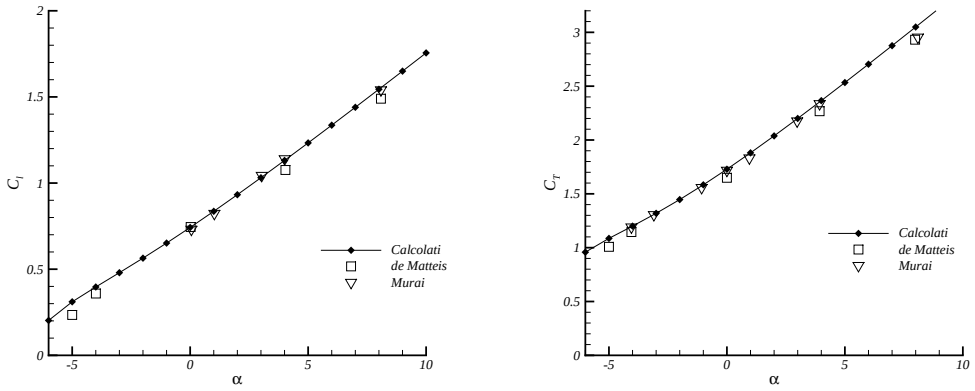

Figure 5: $\epsilon = 1.1$: Lift and Tension coefficient versus angle of attack, comparison with [3] and [4].

between theoretical and numerical final shapes for the same sailing conditions and set up. The two results are practically superimposed, confirming that the effect of viscosity is so small that

it can be disregarded in the design stage of the sail for windward sailing.

In the bottom part of the same figure there is the comparison between the theoretical results (continuous line) and the experimental data (triangles) for another case available in literature. Once again the comparison is promising.

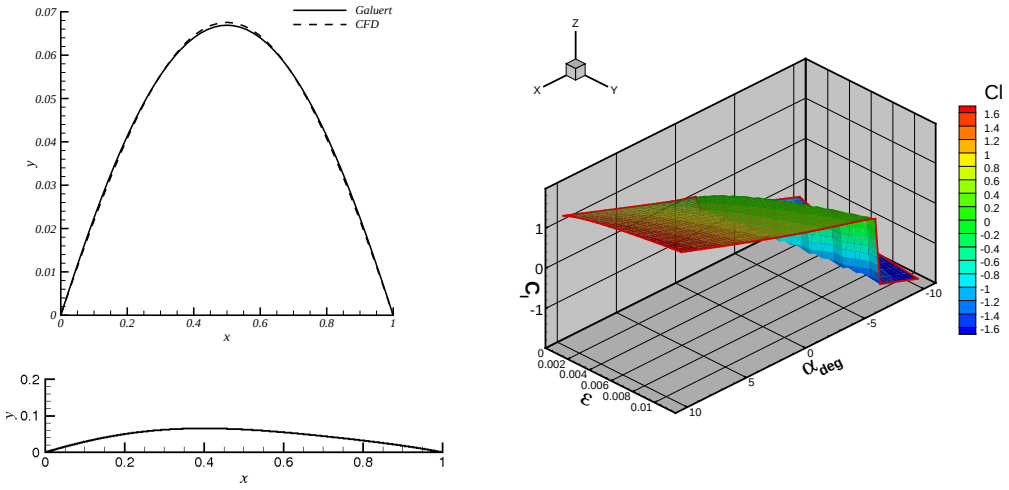

Figure 6: Left: $\epsilon = 1\%$, $\alpha = 0^o$ comparison of the final sail shape with the CFD solution (top); $\epsilon = 0.45\%$, $\alpha = 5^o$ comparison of the final sail shape with experimental data in [2] (bottom). Right: Lift coefficient as function of α and ϵ.

4 Discussion and future works

The right part of figure (6) depicts dependence of the lift coefficient from the angle of attack and the excess length of the sail section. It shows that, with larger excess length, it is possible to sail closer to the wind. It also shows that for values of $\epsilon > 1$ the increase in the lift and the angles where the sail is trusting are very limited and the effectiveness should be evaluated in other wind conditions.

The obtained results are promising but still miss the 3D integration over all the sail sections, taking into account the wind variation with the boundary layer and also the coupling with a hull to determine the actual sailing condition deriving from the sail trust. Moreover the application of the CFD solver coupled with the structural deformation should be evaluated in other wind directions.

References

[1] Dreyer, T.P. and Murray, D.M. (1984) The numerical solution of the pre-elimination model of cable configurations. Journal of Computational and Applied Mathematics, 10: 81-91.

[2] Greemhalghr, S., Curtiss, H.C. and Smith, B. (1984) Aerodynamic properties of a two-dimensional inextensible flexile airfoil. AIAA Journal, 22(7):865-870

[3] de Matteis, G., and de Socio, L. (1986) Nonlinear aerodynamics of a two-dimensional membrane airfoil with separation, Journal of Aircraft, 23(11).

[4] Murai, H. and Maruyama S., (1980) Theoretical investigation of the aerodynamics o double membrane sailing airfoil sections. Journal of Aircraft, 17:445-462.

[5] Anderson, J, Fundamentals of Aerodynamics. McGraw-hill

Comparison of new interface capturing schemes for free surface flow modeling

SeyedReza Djeddi, Sharif University of Technology, jeddi@mech.sharif.edu
MohammadSaeed Seif, Sharif University of Technology, seif@sharif.edu

1: Introduction

Two fluids flows with interface have always been of significant importance to the engineering applications such as marine sciences, hydrodynamics, biochemistry, casting, injection process and many more. In the numerical simulation of these flows, one of the most important subjects is the modeling of the advancing front or the interface between the two fluids. On the other hand, the accuracy and resolution of the interface should be seriously taken into consideration. Methods which have been used during the past decades can be generally divided into two main categories: (1) Lagrangian (2) Eulerian. In the Lagrangian framework, the flow field of the considered fluid is covered by a mesh moving with the fluid. This method is not suited for flows undergoing large distortions because the mesh will be greatly deformed which degrades the accuracy of the solution and causes instability of the solution procedure [1]. In the category of Eulerian methods, the grids used for fluid flow calculations are fixed without motion. There are two main methods in this category. In the front-tracking method, the interface is represented by a connected set of points, which forms a moving boundary, whereas a stationary grid is constructed for the solution of the Navier–Stokes equations [2, 3]. This method is somehow difficult to implement due to the interaction between the interface grid and the Eulerian grid. An alternative to front-tracking is volume-tracking. In volume tracking methods, different fluids must be marked by different indicators. A common way to mark the fluid is the use of an indicator function, generally known as the volume fraction. This function represents the fraction of a local cell volume occupied by one of the fluids and the indicator function is then transported through the domain using a hyperbolic equation. This approach is generally referred to as the VOF method. In the past, a variety of techniques have been developed to maintain a well defined interface within the frame of the VOF method [1]. In one class of such schemes, the exact location of the front is discarded and the interface is reconstructed in an approximate manner using information of local fluid volumes. After the interface is approximately reconstructed, new fluid fraction values are computed by moving the fluid volume according to the local velocity field [4, 5]. In application of the above VOF methods, the computational cells adopted are usually rectangular mainly due to the difficulty of interface reconstruction for irregular meshes. Another approach, requiring no explicit interface reconstruction, is to capture the sharp interface by directly solving the hyperbolic equation of the indicator function [1]. This method needs to overcome the problem of numerical diffusion, which smoothes out the sharp gradient of the interface, and that of numerical dispersion, which may cause the volume fraction unbounded. Among the techniques in this framework are the high-resolution schemes of TVD (total variation diminishing) and NVD (normalized variable diagram). However, direct use of these schemes cannot eliminate the numerical diffusion and unboundedness of the interface. An effective way to remedy these problems is to blend high-resolution schemes and compressive schemes together. These blending schemes switch in a continuous manner from the high-resolution scheme to the compressive scheme, depending on the angle between the interface and the grid lines [1]. Several such schemes have been introduced, such as the CICSAM (compressive interface capturing scheme for arbitrary meshes) of Ubbink and Issa [6], the HRIC (high resolution interface capturing) of Muzaferija and Peric [7], and the STACS (switching technique for advection and capturing of surfaces) of Darwish and Moukalled [8].

Similarly, the new method of Flux Blending Interface Capturing Scheme of Tsui et al. [1] in which the transport flux through each face of the computational cell is controlled by the flux limiters is studied and presented. This method is one of the new and improved techniques based on the Normalized Variable Diagram (NVD) which has a good accuracy on the unstructured grids in compare to the other methods of CICSAM, HRIC and STACS.

In the current study the mentioned methods have been implemented inside an in-house computational fluid dynamic computer code (NUMELS) [10] at Sharif University of Technology. According to the unstructured grids algorithms and methods of solving the governing equations, different hydrodynamic tests has been analyzed in order to validate and measure the accuracy of the techniques for the

modeling of the free surface. Finally the results are compared and studied thoroughly. It seems that the FBICS technique has better accuracy in compare to the other methods in the courant number range of 0 to 1 as a result of its less dependency on the local cell courant numeral and the use of the flux limiter functions. Also the accuracy and efficiency of the computational fluid dynamics computer code has been increased by using an adaptive time stepping algorithm based on a predefined cell courant number and CFL criterion.

2: Mathematical Model

Flows for both fluids having a common interface are assumed to be incompressible and the governing equations are the mass and momentum conservation as follows:

(1) $$\frac{\partial U_j}{\partial x_j} = 0$$

(2) $$\frac{\partial \rho U_i}{\partial t} + \frac{\partial}{\partial x_j}\left(\rho U_j U_i\right) = -\frac{\partial P}{\partial x_i} + \frac{\partial \tau_{ij}}{\partial x_j} + \rho g_i$$

in which U_j is the velocity, ρ density, P pressure, τ_{ij} viscous stress tensor and g_i gravitational acceleration. The mixture of fluids is considered as a single continuum. The volume fraction α is advected as a Lagrangian invariant and has zero material derivative:

(3) $$\frac{D\alpha}{Dt} = \frac{\partial \alpha}{\partial t} + U_j \frac{\partial \alpha}{\partial x_j} = 0$$

Using conservation equation, the transport equation can be expressed in the divergence form. For discretization, the differential equations are integrated on the controlled volume. According to the divergence theorem, the divergence terms of the above equation can be changed into surface integrals. Fluxes through computational cell faces can be approximated using the mean value theorem. As a result the equation for the volume fraction can be expressed approximately as follows:

(4) $$\frac{\partial U}{\partial t}(\alpha_P^{n+1} - \alpha_P^n) + \sum_{faces} F_f \alpha_f = 0$$

In which n and $n+1$ superscripts show the old and new times respectively and subscripts P and f show the values at the center of the control volume and their surrounding faces. Also F_f is the volumetric flux through a face. To complete discretization, the volume fraction at each face requires estimate from neighboring nodes:

(5) $$\alpha_f = \alpha_U + \frac{\gamma_{(r)}}{2}(\alpha_D - \alpha_U)$$

where the subscript U denotes the node upstream of the considered face and the subscript D is the one downstream. The function $\gamma_{(r)}$ is the flux limiter depending on the gradient ratio [1]:

(6) $$r = \frac{\alpha_U - \alpha_{UU}}{\alpha_D - \alpha_U}$$

It is obvious that the expression represents the upwind difference scheme for $\gamma = 0$, the central difference scheme for $\gamma = 1$ and the downwind difference scheme for $\gamma = 2$. Thus the second term on the right of Eq. (5) represents anti-diffusion to the upwind scheme. In solving the advection equation, the upwind part of the convection flow is treated by the Crank–Nicolson scheme whereas the anti-diffusion part in the explicit manner [1]. As a result, it is obtained

(7) $$\frac{\Delta U}{\Delta t}(\alpha_P^{n+1} - \alpha_P^n) + \sum_{faces} F_f \left[\tfrac{1}{2}(\alpha_U^{n+1} + \alpha_U^n) + \frac{\gamma_{(r)}}{2}(\alpha_D^n - \alpha_U^n)\right] = 0$$

The limiters for linear difference schemes can be expressed as simple linear functions of the gradient ratio. Nonlinear schemes like TVD and NVD schemes can also be easily implemented by expressing the limiting functions in terms of r [9]. Tests of a variety of such schemes on model problems had shown that the smear of interface is serious even with the use of the SUPERBEE [8] which was regarded as the most non-diffusive among the TVD schemes. It was recognized that in contrast to the upwind differencing, the downwind scheme could cause significant oscillations and, thus, instability of the solution due to the fact the sign of its artificial viscosity is negative. This anti-diffusion feature makes it capable to compress a smooth function into a step profile [1]. To take advantage of this compression nature, a strategy is to blend slightly diffusive high-resolution schemes (HR) with bounded downwind schemes (BD):

(8) $$\gamma = [1 - \omega(\theta)]\gamma^{HR} + \omega(\theta)\gamma^{BD}$$

The weighting factor ω depends on the angle θ between the grid lines and the interface. A rule of thumb is that the bounded downwind scheme is used when the interface is parallel with the considered face and it is gradually switched to the high-resolution scheme until the interface becomes orthogonal to the face [1]. In the previous studies [19–21], schemes in the NVD form were blended in the manner

similar to Eq. (8) with various expressions for ω. The different functions have been tested using the present blending scheme. It was found that the results are not sensitive to the choices of ω. In the following, the form $\omega = cos^4(\theta)$ [8] is employed.

The flux limiters can be more easily understood using the normalized variables formulation (NVF).

(9) $$\tilde{\alpha} = \frac{\alpha - \alpha_{UU}}{\alpha_D - \alpha_{UU}}$$

Eq. (5) can then be rewritten as

(10) $$\widetilde{\alpha_f} = \widetilde{\alpha_U} + \frac{\gamma(r)}{2}(1 - \widetilde{\alpha_U})$$

NVD schemes must satisfy the convection boundedness criteria (CBC) which can be represented by the combination of the upper triangle bounded by the lines $\widetilde{\alpha_U} = 0$ and $\widetilde{\alpha_f} = 1$, and the diagonal line $\widetilde{\alpha_f} = \widetilde{\alpha_U}$ in Fig. 1a. The constraints on TVD schemes are more stringent, which is bounded by an oblique line $\widetilde{\alpha_f} = 2\,\widetilde{\alpha_U}$ instead of the vertical line $\widetilde{\alpha_U} = 0$ in the NVD schemes as shown in Fig. 1a.

The FBICS scheme can be interpreted using the NVF as [1]

(11a) $$HR \qquad \widetilde{\alpha_f} = \begin{cases} 3\widetilde{\alpha_U} & 0 < \widetilde{\alpha_U} < \frac{1}{8} \\ \widetilde{\alpha_U} + \frac{1}{4} & \frac{1}{8} < \widetilde{\alpha_U} \le \frac{3}{4} \quad (FDS) \\ 1 & \frac{3}{4} < \widetilde{\alpha_U} \le 1 \quad (DDS) \\ \widetilde{\alpha_U} & \widetilde{\alpha_U} \le 0 \ or \ \widetilde{\alpha_U} \ge 1 \quad (UDS) \end{cases}$$

(11b) $$BD \qquad \widetilde{\alpha_f} = \begin{cases} 3\widetilde{\alpha_U} & 0 < \widetilde{\alpha_U} \le \frac{1}{3} \\ 1 & \frac{1}{3} < \widetilde{\alpha_U} \le 1 \quad (DDS) \\ \widetilde{\alpha_U} & \widetilde{\alpha_U} \le 0 \ or \ \widetilde{\alpha_U} \ge 1 \quad (UDS) \end{cases}$$

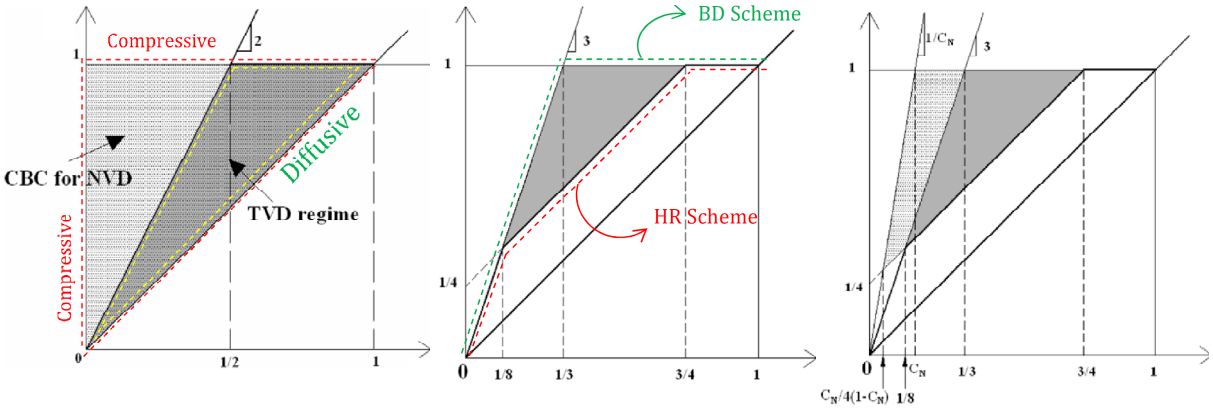

Fig 1: (a) CBC and TVD regions on NVD (b) FBICS technique, the initial scheme, (c) adding the C_N criteria

These schemes are drawn on the normalized variable diagram in Fig. 1b. Note that for schemes in the NVD range, but out of the TVD regime, which is bounded by the line $\widetilde{\alpha_f} = 2\,\widetilde{\alpha_U}$ as shown in Fig. 1a, are less diffusive. It is readily seen that both schemes represented by Eqs. (11a) and (11b) fall out of the TVD range for small values of $\widetilde{\alpha_U}$ because of the higher slope $\widetilde{\alpha_f} = 3\,\widetilde{\alpha_U}$, equivalent to $\gamma = 4r$ in the flux limiter [1]. It is emphasized that in the sketch of NVD, the diagonal represents the upwind scheme and the upper bound represents the downwind scheme. Therefore, scheme curves closer to the diagonal line have the character of higher diffusion and those closer to the upper line and the vertical line $\widetilde{\alpha_U} = 0$ are more compressive. The line $\widetilde{\alpha_f} = \frac{\widetilde{\alpha_U}}{C_N}$ is adopted as the left boundary in the NVD diagram in the CICSAM scheme of Ubbink and Issa [6], where C_N is the local Courant number in the considered cell. When the Courant number approaches zero, it becomes the vertical line $\widetilde{\alpha_U} = 0$ and the CICSAM scheme is compressive. However, for C_N close to one it degenerates into the diagonal line and results in significant diffusion. To allow the present scheme to be more compressive for small Courant numbers, the above schemes shown in Eqs. (11a) and (11b) are modified and in the NVD form, they become (Fig. 1c) [1]:

(12a) $$HR \qquad \widetilde{\alpha_f} = \begin{cases} \max\left(\frac{1}{C_N}, 3\right)3\widetilde{\alpha_U} & 0 < \widetilde{\alpha_U} < \min\left(\frac{C_N}{4(1-C_N)}, \frac{1}{8}\right) \\ \widetilde{\alpha_U} + \frac{1}{4} & \min\left(\frac{C_N}{4(1-C_N)}, \frac{1}{8}\right) < \widetilde{\alpha_U} \leq \frac{3}{4} \quad (FDS) \\ 1 & \frac{3}{4} < \widetilde{\alpha_U} \leq 1 \quad (DDS) \\ \widetilde{\alpha_U} & \widetilde{\alpha_U} \leq 0 \ or \ \widetilde{\alpha_U} \geq 1 \quad (UDS) \end{cases}$$

(12b) $$BD \qquad \widetilde{\alpha_f} = \begin{cases} \max\left(\frac{1}{C_N}, 3\right)\widetilde{\alpha_U} & 0 < \widetilde{\alpha_U} \leq \min\left(C_N, \frac{1}{3}\right) \\ 1 & \min\left(C_N, \frac{1}{3}\right) < \widetilde{\alpha_U} \leq 1 \quad (DDS) \\ \widetilde{\alpha_U} & \widetilde{\alpha_U} \leq 0 \ or \ \widetilde{\alpha_U} \geq 1 \quad (UDS) \end{cases}$$

3: Results and Discussion

The new and improved technique of FBICS [1] has been compared with the well known and commonly used methods of interface capturing such as CICSAM, HRIC and STACS. Classical problems which have been chosen to validate the accuracy of the methods are as follows: (1) Advection of a hollow square and hollow circle in a uniform velocity field (2) advection of a circle (drop) in a shear flow field. In all these tests, velocities are pre-defined at the start of the solution and there is no coupling between volume fraction scalar and the velocity field during the solution procedure. Therefore in all these cases the transport problem of the volume fraction scalar and the accuracy of the solution of the governing equation are being analyzed.

3 – 1: Advection of the hollow square and hollow circle in the uniform velocity field

It is assumed that the velocity field has a uniform distribution of $\vec{U} = 2\vec{\imath} + \vec{\jmath}$. The computational domain is rectangle of 4 x 4 divided into 100 x 100 rectangular cells. The hollow square and the hollow circle have the outer length/diameter of 0.8 and inner length/diameter of 0.4 and both are centered at (0.8, 0.8) at the initial time. Initial distributions will be transported for 1 second [1].

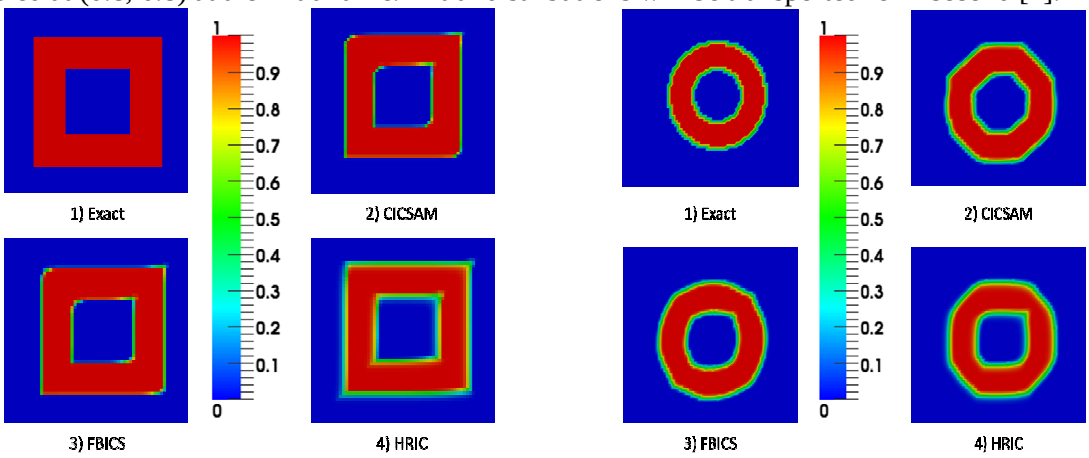

Fig. 2: Volume fraction distribution for (a) the hollow square (b) the hollow circle at C_N = 0.25 after 1 sceond advection with uniform velocity field

The volume fraction distribution for the hollow square and the hollow circle for C_N = 0.25 are shown in Fig. 2a and b. The schemes adopted for comparison are the CICSAM of Ubbink and Issa [6], the HRIC of Muzaferija et al. [7], STACS of Darwish and Moukalled [8] and finally the new method of FBICS of Tsui et al. [1]. By testing the same problem in different courant numbers (changing the solution time step) it is revealed that the results obtained by the CICSAM and HRIC are not acceptable for C_N = 0.75. It was mentioned in the last section that the CICSAM scheme is limited by a bound $\widetilde{\alpha_f} = \frac{\widetilde{\alpha_U}}{C_N}$. It is reduced to the upwind scheme as C_N approaches 1. Thus, it is highly diffusive at Courant numbers close to 1. Even higher diffusive phenomenon can be found in the HRIC as a result of the use of upwind scheme for C_N greater than 0.7 in this scheme. The HRIC scheme blends the upwind difference and a bounded downwind difference for C_N < 0.3 [7]. As a consequence of the effects of the embedded upwind difference, smear of the interface is still visible. Both the predictions by the CICSAM and FBICS are very satisfactory. Similar observations can be found for the case with circular cylinder. However, the circle tends to transform into an octagon for C_N = 0.1 due to the large compression effects of the downwind difference. This is especially true for the CICSAM and HRIC

schemes. The effects of Courant number on the prediction accuracy for the considered schemes are shown in Fig. 3a and b for the square cylinder and the circular cylinder, respectively. Due to the use of upwind difference in the flux blending in the HRIC, the numerical errors are much greater than the other schemes even at low Courant numbers. The sharp increase of the errors at high Courant numbers for both the HRIC and CICSAM is owing to the approach to the upwind difference scheme. In general, the CICSAM is accurate for $C_N < 0.4$. It can be identified that FBICS perform satisfactorily, regardless of the Courant numbers. For small Courant numbers FBICS is slightly inferior to the CICSAM scheme.

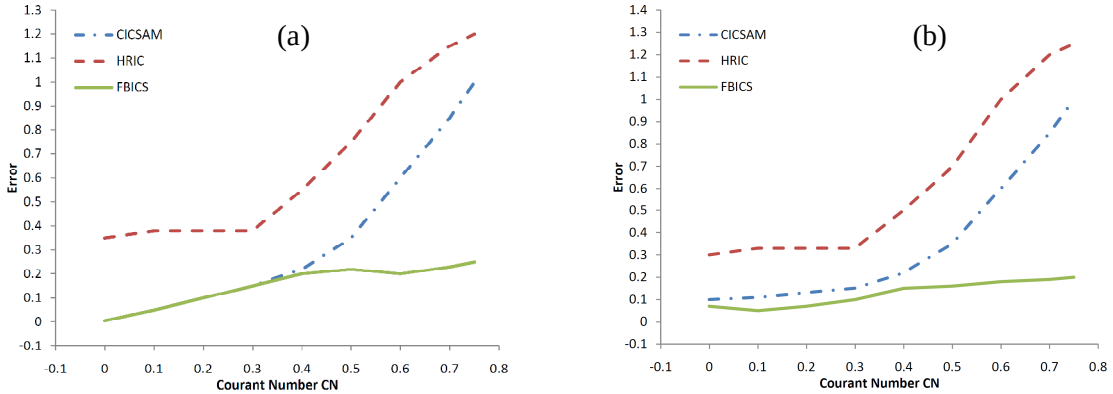

Fig. 3: Numerical errors against Courant number for (a) hollow square (b) hollow circle in uniform flow field

3 – 2: Advection of a circle in a shear flow

In the above case, the cylinders are transported by the uniform velocity field without changing its shape. In realistic problems, the interface is subject to flow straining and deforms continuously. To mimic this situation, the following velocities are assumed.

(13) $$\vec{V} = \sin x \cdot \cos y\vec{i} - \cos x \cdot \sin y\vec{j}$$

with $(x, y) \in (0, \pi)$. The initial condition is a circle of diameter 0.4π with its center located at $(\pi/2, (1 + \pi)/5)$ [1]. The time marching of the computation is carried out over N units of time. It is followed by another N units of time in which the velocity field is reversed. The circle will be stretched by the velocity straining in the forward step and recovers its original shape by the end of the backward step. Selected results for the CICSAM and FBICS at $C_N = 0.25$ and 0.75 for N = 8 and 16 are shown in Fig. 4. For $C_N = 0.25$ the FBICS is slightly better than the CICSAM by comparing the final circles after the backward step. As the Courant number is increased to 0.75, the wide spread of the contours lines for the CICSAM indicates the smear caused by the numerical diffusion. Fig. 5 presents the solution error against the Courant number for the case with N = 16. As expected, the errors for the HRIC increases sharply for $C_N > 0.3$ whereas the corresponding point for the CICSAM occurs at $C_N = 0.5$. The FBICS is not sensitive to the Courant number and it has less error throughout the entire range considered.

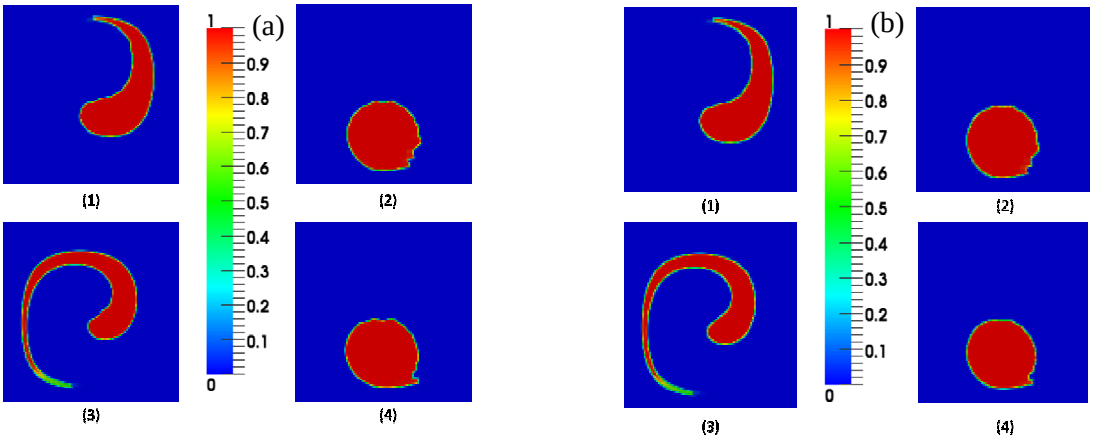

Fig. 4: Advection of a drop in the shear flow field using (a) CICSAM scheme, (b) FBICS scheme

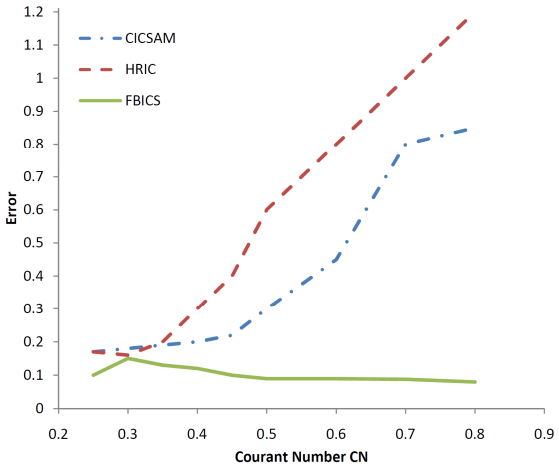

Fig. 5: Numerical errors against Courant number for the advection in the shear flow field

4: Conclusions

Different algorithms were used for the modeling of the two phase flow with the free surface. Inside the finite volume framework and using unstructured grids with arbitrary geometries the classical problems have been analyzed. In the new method of FBICS with the aid of the flux limiters, the combination of two high resolution and compressive schemes are used to determine the flux through each face of the computational cell. The blending factor is a function of the angle between the interface and the grid orientation. Different tests and problems have been done using CICSAM, HRIC and STACS techniques and the results have been compared with the ones from the new and improved FBICS strategy. Results show that FBICS has better behavior in compare to the commonly used CICSAM and HRIC schemes especially for the high courant numbers. In order to decrease the numerical diffusion effects it is better to keep the cell courant number below 0.3, but at the same time it can be seen that the FBICS has good accuracy for the range of $0 < C_N < 1$. This shows its better capability in modeling and simulation of the hydrodynamic problems in marine engineering applications.

References

[1] Y.-Y. Tsui, S.-W. Lin, T.-T. Cheng, T.-C. Wu, Flux-blending schemes for interface capture in two-fluid flows, Int. Journal of Heat and Mass Transfer 52 (2009) 5547-5556.
[2] S.O. Unverdi, G. Tryggvason, A front-tracking method for viscous, incompressible, multi-fluid flows, J. Comput. Phys. 100 (1992) 25–37.
[3] G. Tryggvasson, B. Bunner, A. Esmaeeli, D. Juric, N. Al-Rawahi, W. Tauber, J. Han, S. Nas, Y.-J. Jan, A front-tracking method for the computations of multiphase flow, J. Comput. Phys. 169 (2001) 708–759.
[4] W.J. Rider, D.B. Kothe, Reconstructing volume tracking, J. Comput. Phys. 141 (1998) 112–152.
[5] M.R. Davidson, M. Rudman, Volume-of-fluid calculation of heat or mass transfer across deforming interfaces in two-fluid flow, Numer. Heat Transf. B: Fund. 41 (2002) 291–308.
[6] O. Ubbink, R.I. Issa, A method for capturing sharp fluid interfaces on arbitrary meshes, J. Comput. Phys. 153 (1999) 26–50.
[7] S. Muzaferija, M. Peric, P. Sames, T. Schellin, A two-fluid Navier–Stokes solver to simulate water entry, in: Proceeding of Twenty-Second Symposium On Naval Hydrodynamics, Washington, DC, 1998, pp.638–649.
[8] M. Darwish, F. Moukalled, Convective schemes for capturing interfaces of freesurface flows on unstructured grids, Numer. Heat Transf. B: Fund. 49 (2006) 19–42.
[9] Y.-Y. Tsui, T.-C. Wu, A pressure-based unstructured-grid algorithm using highresolution schemes for all-speed flows, Numer. Heat Transf. B: Fund. 53 (2008) 75–96.
[10] E. Jahanbakhsh, R. Panahi, M.S. Seif, Development of a VoF-fractional step solver for floating body motion simulation, Applied Ocean Research 28 (2006) 171–181.

Numerical modelling of cavitation and erosion on rudder

Paweł Dymarski

CENTRUM TECHNIKI OKRĘTOWEJ S.A. (CTO S.A.)
e-mail: pawel.dymarski@cto.gda.pl

1. INTRODUCTION

The main target of the project, which results are presented in the article, was to develop computational method for modelling of cavitation phenomenon on rudder behind a propeller.
The model was developed in order to enable prediction of cavitation and the secondary effect of the phenomenon – erosion on the surface of rudder. Two types of rudder have been taken into consideration: conventional (symmetrical) rudder and flow adapted twisted rudder. The results of CFD analyses are compared with results obtained from model tests realized with the use of High Speed Video camera. Additionally, the results of soft paint tests of erosion on rudders are presented.

2. MATHEMATICAL MODEL

2.1. GOVERNING EQUATIONS OF THE RANSE MODEL

The closed system of motion equations, derived for incompressible fluid, is based on the momentum and mass conservation laws. An integral form of mass conservation equation formulated for control volume Ω with a surface S reads [3]:

$$\int_S \rho \boldsymbol{v}\cdot\boldsymbol{n}\, dS \quad , \tag{1}$$

and the conservation equation of i-th momentum component has the following form:

$$\frac{\partial}{\partial t}\int_\Omega \rho \boldsymbol{v}\, d\Omega + \int_S \rho \boldsymbol{v}\,\boldsymbol{v}\cdot\boldsymbol{n}\, dS = \int_S \boldsymbol{T}\cdot\boldsymbol{n}\, dS + \int_\Omega \rho \boldsymbol{b}\, d\Omega \quad , \tag{2}$$

where $\boldsymbol{v}$ is velocity vector, p - pressure, ρ - density, $\boldsymbol{n}$ - unit vector normal to *S* surface, $\boldsymbol{T}$ is a stress tensor and $\boldsymbol{b}$ is a vector of volume forces.
When the flow is turbulent, $\boldsymbol{v}$ refer to mean velocity vector, p is a mean value of pressure. The word "mean" denotes average in a time period, which is long compared to the period of turbulent oscillations [5].
The viscous stress tensor $\boldsymbol{T}$ is specified by Boussinesq approximation [1],[5]:

$$T = -p\boldsymbol{I} + 2\left(\mu + \mu_t\right)\boldsymbol{D} \quad , \tag{3}$$

where μ is a molecular viscosity, μ_t is the turbulent viscosity and $\boldsymbol{D}$ is the mean strain-rate (deformation) tensor. The turbulent viscosity is calculated with the use of Spalart-Allmaras turbulence model [1],[5].

2.2. NUMERICAL MODEL OF PROPELLER

Within the introduced model the screw propeller is being modelled in the simplified way, using unsteady function of volume forces. In order to define the distribution of volume forces one should implement the geometry of the contour of the propeller's blade and the field of axial and tangential forces on the blade. The implemented field of volume forces is being normalised in order to get specified total values of the thrust and the torque. Defined force field is rotating with the determined angular speed around the specified propeller's axis, inducing the unsteady, periodic field of velocity.
The pressure distribution on the blade, which is needed for modelling of the propeller, can be evaluated from codes based on potential methods (for example solvers based on Boundary Element Method), as well as it can be approximated using simplified functions of pressure distribution. The latter method was used for computations of test cases presented in this paper.

2.3. MODEL OF CAVITATION

The cavitation model is based on travelling bubble method [4],[2]. It is assumed in the model, that a large number of micro gas nuclei is present in the liquid. When pressure value decreases below a specified critical level, the radius of nucleus starts to grow rapidly and – according to the model – this is the inception of cavitation.
To determine behaviour of a single bubble, the pressure field, velocity field (or bubble trajectory) and initial size of nucleus have to be given.
The single bubble dynamic is described by Rayleigh-Plasset equation [4]:

$$R\frac{d^2R}{dt^2}+\frac{3}{2}\left(\frac{dR}{dt}\right)^2+4\frac{\mu}{\rho R}\frac{dR}{dt}=-\frac{p_\infty+\frac{2A}{R}-p_v-p_g}{\rho} \quad , \tag{4}$$

where: R is a radius of the bubble, t is time, p is the water pressure acting on the bubble, p_v - vapour pressure, p_g - pressure of the gas in the bubble, A denotes the surface tension coefficient.
The value of p is evaluated as a mean value at the surface of bubble:

$$p_{mean}=\frac{1}{S}\int_S p(x,y,z)dS \quad , \tag{5}$$

where S is a bubble surface.
The pressure of gas inside bubble is calculated with the assumption that the process of growing and collapsing is isothermal:

$$p_g=p_{g_0}\left(\frac{R_0}{R}\right)^3 \quad , \tag{6}$$

Where p_{g_0} and R_0 is gas pressure and radius of the bubble at inlet.

The introduced model of predicting the phenomenon of cavitation is a hybrid model. The velocity field and the pressure field are being calculated with finite volume method using the grid defined in main system of coordinates, however dynamics of bubbles are being solved in local frames of reference moving with bubbles. In order to obtain the information about the volume of the gas phase inside elements of the computational mesh, an additional, fine grid is constructed. The new auxiliary grid is structural and orthogonal with cubic elements. Each of them is storing the information about the volume of gas phase and the index of the element of the main grid in which it is included. The algorithm for calculating of the gas phase volume is as follows:

1. For every bubble, the elements of the auxiliary grid, which are inside it, are being found
2. Calculating volume of the gas phase included in elements of the auxiliary grid
3. Calculating the volume of the gas phase in elements of the main grid, by adding the volume of gas from elements of the auxiliary grid.

Because capacity of elements of the auxiliary grid is limited, the algorithm prevents multiple summing up the gas volume from overlapping bubbles. When a volume of gas in a control volume of the main grid is available, then the volume fraction of gas phase α inside specified CV can be evaluated:

$$\alpha=\frac{V_g}{V_{CV}}, \tag{7}$$

Where, V_{CV} is volume of control element, $\alpha=0$ - when the volume V is fully filled with water, $\alpha=1$ - when the volume V is filled with gas.

With a view to accelerate the computational process, as well as in order to reduce the number of the required RAM, the phenomenon of the cavitation is being estimated only in the defined relatively small area inside the domain of flow computation. In case of calculations of the cavitation phenomenon on a rudder model, computational area is included inside the cuboid with a breadth about 4 cm larger than the thickness of the rudder (in the model scale) and of the height and the length of the subdomain about 20 - 50 % larger than the relevant size of the rudder. The narrow zone at the inlet into the cuboid, is an area, in which microbubbles of gas are “injected” to water. Initial position of microbubbles is determined by random process, the amount and sizes of bubbles are being selected on the basis of statistical data.

2.4 MODELLING OF CAVITATION EROSION

The model of erosion is based on kinetic energy of a water around collapsing bubble. When bubble is collapsing (or growing) the velocity field around it is described by the following formula [4]

$$u=\frac{R^2}{r^2}\frac{dR}{dt} \quad , \tag{8}$$

where : u is a radial velocity at a sphere of radius r.
The kinetic energy of the small volume of water between two spheres is:

$$\Delta E_K = \frac{1}{2} m_{\Delta V} u^2 = \frac{1}{2} \rho \Delta V u^2 \tag{9}$$

Where: $m_{\Delta V}$ is a mass of water inside volume ΔV ; $m_{\Delta V} = \rho \Delta V$
The above equation can be transformed to a differential form:

$$dE_K = \frac{1}{2} \rho \left(\frac{R^2}{r^2} \dot{R} \right)^2 dV \quad . \tag{10}$$

Hence, the total kinetic energy of water around bubble, can be expressed as an following integral:

$$E_K = \int_V \frac{1}{2} \rho \left(\frac{R^2}{r^2} \dot{R} \right)^2 dV = \frac{1}{2} \rho R^4 \dot{R}^2 \int_V \frac{1}{r^4} dV \tag{11}$$

When *dV* is a volume between two concentric spheres, it can be written as:

$$dV = 4 \pi r^2 dr \quad , \tag{12}$$

hence, the total kinetic energy of bubble is:

$$E_K = 2 \pi \rho R^4 \dot{R}^2 \int_R^\infty \frac{1}{r^2} dr = 2 \pi \rho R^3 \dot{R}^2 \quad . \tag{13}$$

The above formula describes the total value of kinetic energy of water around spherical bubble. For prediction of erosion more suitable can be used - "normalized" kinetic energy of water, which may be obtain by dividing E_K by surface of the bubble's sphere. Therefore the normalized value of E_K is:

$$E_{KS} = \frac{E_K}{4 \pi R^2} = \frac{1}{2} \rho R \dot{R}^2 \quad . \tag{14}$$

Characteristics of E_K and E_{KS} are presented at Fig 1, additionally the radius of bubble is drawn, in order to show phases of bubble's "life" as a background.

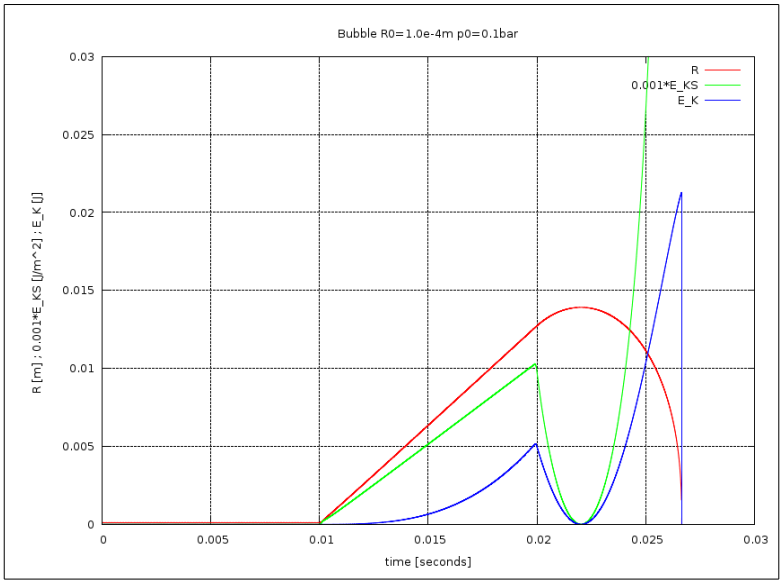

Fig. 1. Characteristics of kinetic energy of water around bubble E_K (blue) and "normalized" kinetic energy E_{KS} (green) multiplied by 0.001. The red line indicates the function of bubble's size *R*. The bubble growth has been induced by sudden drop of pressure from 0.1 bar to 0.0 at t=0.01s and then at t=0.02 s the pressure value rises to the 0.1 bar.

It is assumed in presented model, that intensity of cavitation erosion depends on amount of kinetic energy of bubbles at their moment of collapse inside unit volume (near the surface of model) in specified time period.

3. DESCRIPTION OF TEST CASES

The test cases are based on condition of real case of fast twin propeller boat, which was tested in CTO's cavitation tunnel a few years ago. The presented results correspond to half load conditions of the vessel.
In order to extend the analysis, the additional test case was prepared, a rudder with alternative geometry has been designed based on preliminary CFD results with conventional rudder (Fig. 2). The shape of the new rudder was adapted to geometry of flow behind a propeller; the peculiar shape of leading edge causes, that the pressure difference is smaller compared to the original shape, and hence the risk of the appearance of cavitation (or the scale of the phenomenon) is smaller.

The “experiment” with the new shape will allow for better testing the developed computational model. If the differences between the test cases in scale of cavitation phenomenon obtained from the the numerical model are similar to ones observed in cavitation tunnel, the model can be useful in design process.

Test conditions (in model scale):

- pressure at propeller axis: $p_0 = 10200 Pa$;
- velocity at inlet: V = 3.83 m/s;
- propeller geometry:
  D =0.250 m ; $P_{0,7}/D$ =1.174; Z = 3;
- propeller revolutions: $n_p = 16.0 \frac{1}{s}$;
- thrust and torque coefficient:
  $K_T = 0.136 ; K_Q = 0.056$;

Fig. 2. Comparing of the geometry of models of two rudders, for which experimental tests and computational analyses were performed as part of the project. On the right-hand side: rudder with conventional geometry, on the left: rudder with the leading edge twisted, adapted to the geometry of the velocity field.

4. FLOW SIMULATION WITH THE USE OF CFD

The CFD domain was a copy of geometry of the dummy-body model in cavitation tunnel. The computational grid was block-structured and hexahedral. The grid was generated with the use of ANSYS-ICEM HEXA. Fig. 3 a) shows the grid structure.

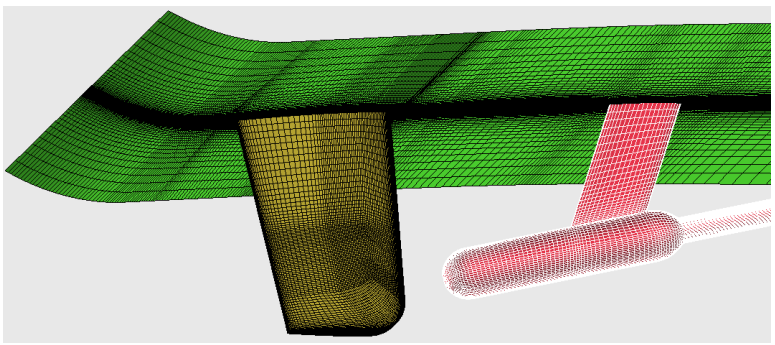

a)

b)

Fig. 3. a) The structure of grid for computations of flow around conventional rudder. Number of control volumes was about 3.7 M; b) picture of the model of propeller and rudder (behind a dummy- body) during tests in cavitation tunnel

The results of computations of cavitation phenomenon on conventional rudder are shown at Fig. 4. The results for twisted rudder are presented at Fig 5.

5. MODEL TESTS RESULTS

The model configuration in test section of cavitation tunnel is shown at Fig. 3 b). The results of model tests for conventional rudder are presented at Fig. 6, however tests results for twisted rudder are shown at Fig. 7.
In order to predict an area peculiarly exposed to erosion, a special type of test has been performed. The same method which is applied for prediction of erosion on propeller blade was applied to predict the phenomenon on the rudder. The model of the rudder was painted with special soft paint to assess the presence of cavitation impingement. After 120 minutes in specified constant conditions in cavitation tunnel the rudder was subjected to detailed inspection. The defect of soft coat on the surface of model of conventional rudder has been noticed. In order to make sure that the received result isn't accidental, the erosion test has been repeated. The results from the second test were almost the same. Twisted rudder has been tested according to the same procedure, but no defect of the coat was identified.

6. CONCLUSIONS AND REMARKS:

- the presented computational model seems to be sufficient to predict “more significant” structures of cavitation on rudder,
- the difference between cavitation on conventional and twisted rudder has been captured by the model, however some forms of cavitation were underestimated (or just omitted),
- the evolution of main cavitation structures due to non-steady periodic flow obtained from computation was

very similar to the cavitation evolution recorded by HSV camera,

- some structures of cavitation were strongly underestimated, for example the cavitation behind a sharp leading edge near the bottom of the rudder at Fig. 6 a) and Fig 4 a),
- some weak structures of cavitation were not predicted by the model, for example cavitation at the starboard side on the twisted rudder – Fig. 7 b),
- the soft paint test, which is usually applied for prediction of cavitation erosion on propeller's blade seems to be applicable for investigation of erosion on rudder (will be presented at Symposium),

7. ACKNOWLEDGEMENT

The research presented in this paper has been financially supported by the Polish Ministry of Science and Higher Education Grant No. N504 489134. The author would like to express his gratitude for this support.

REFERENCES:

[1] Blazek J.: *Computational Fluid Dynamics: Principles and Applications*, ELSEVIER 2001
[2] Dymarski P.: *Predictions of the open water propeller cavitation using the SOLAGA solver 9th Numerical Towing Tank Symposium*, 23-25 September 2007 Hamburg-Germany
[3] Ferziger J.H, Peric M.: *Computational Methods for Fluid Dynamics*, 2nd ed., Berlin, Springer 1999
[4] Lecoffre Y.: *Cavitation. Bubble Trackers*, A.A. Balkema/Rotterdam/Brookfield 1999
[5] Wilcox D.C.: *Turbulence Modeling for CFD*, DCW Industries 2002

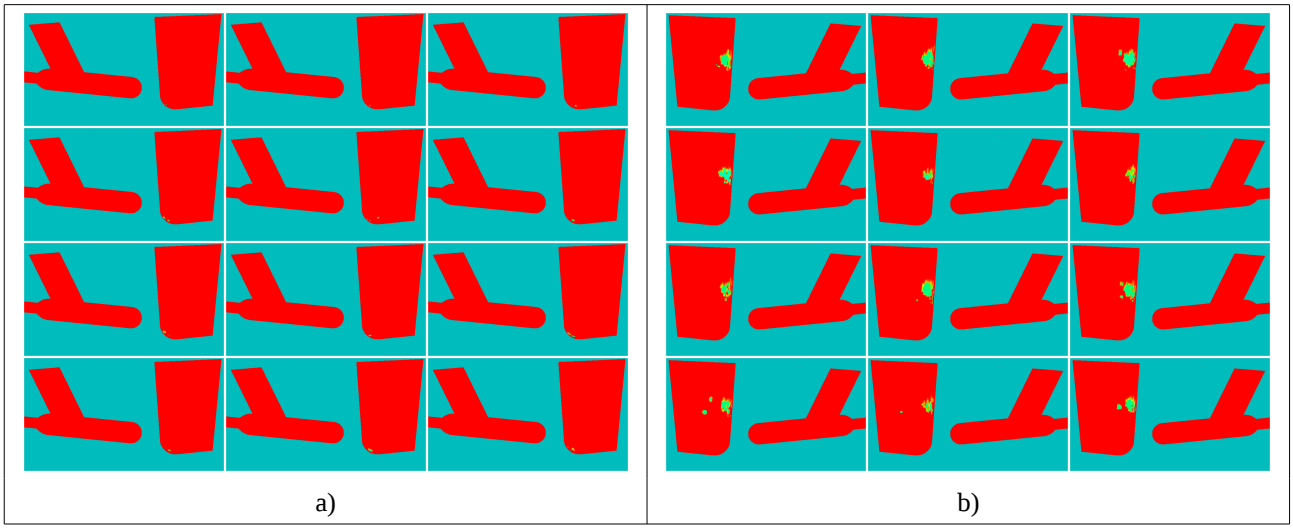

Fig. 4. Results of computations of cavitation on **conventional rudder** (behind a propeller). The time interval between successive frames is (in the model scale) 0.004 s , a) portside, b) starboard view.

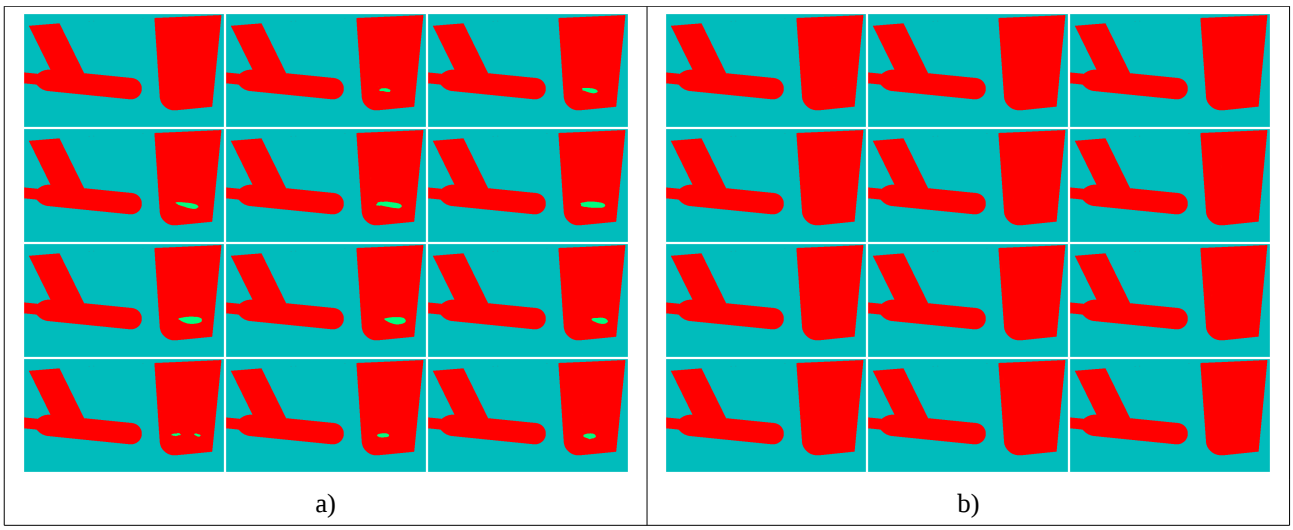

Fig. 5. Results of computations of cavitation on **twisted rudder** (behind a propeller), a) starboard view. No cavitation has been observed at portside b).

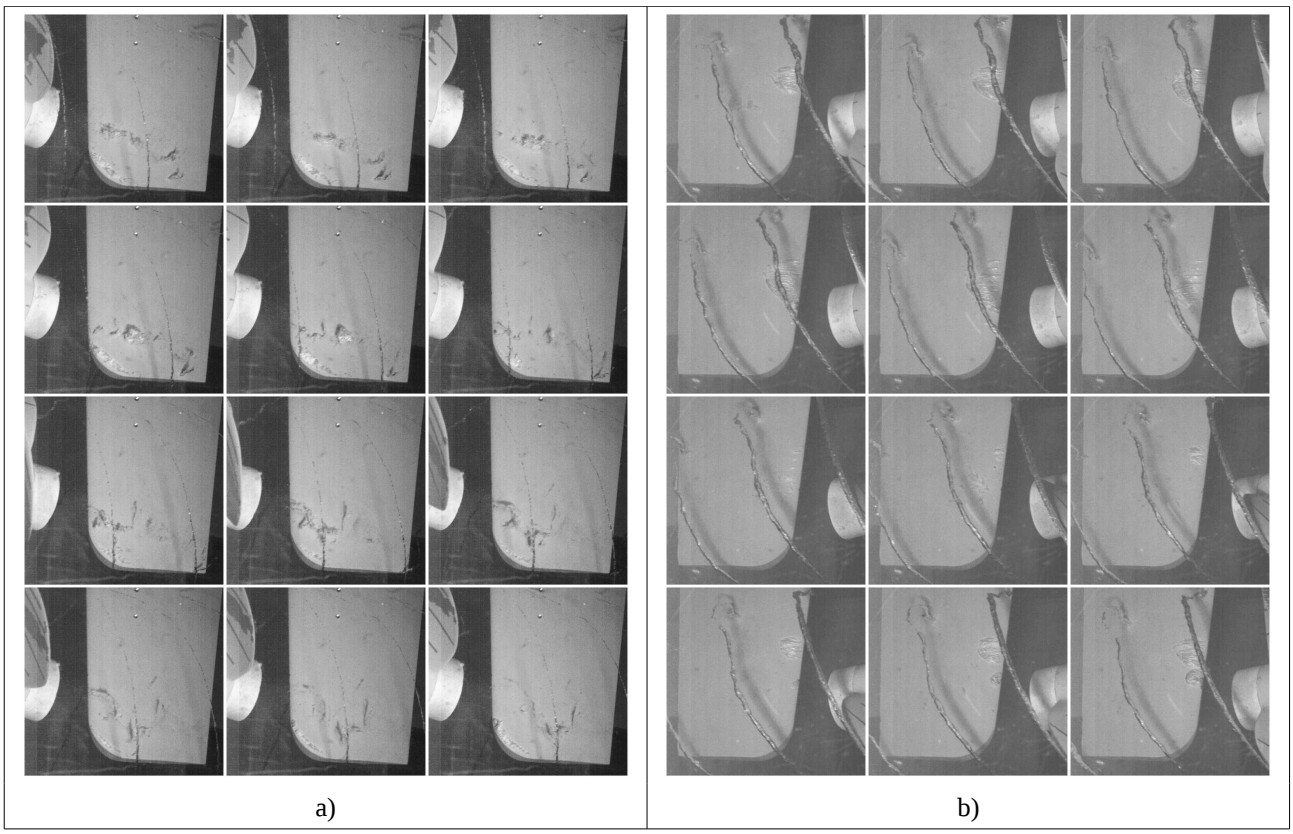

a) b)

Fig. 6. Model tests results: cavitation on the **conventional rudder.** Snapshots from High Speed Video recording. The time interval between frames is 0.002 s. a) View from the port side; b)View from the starboard

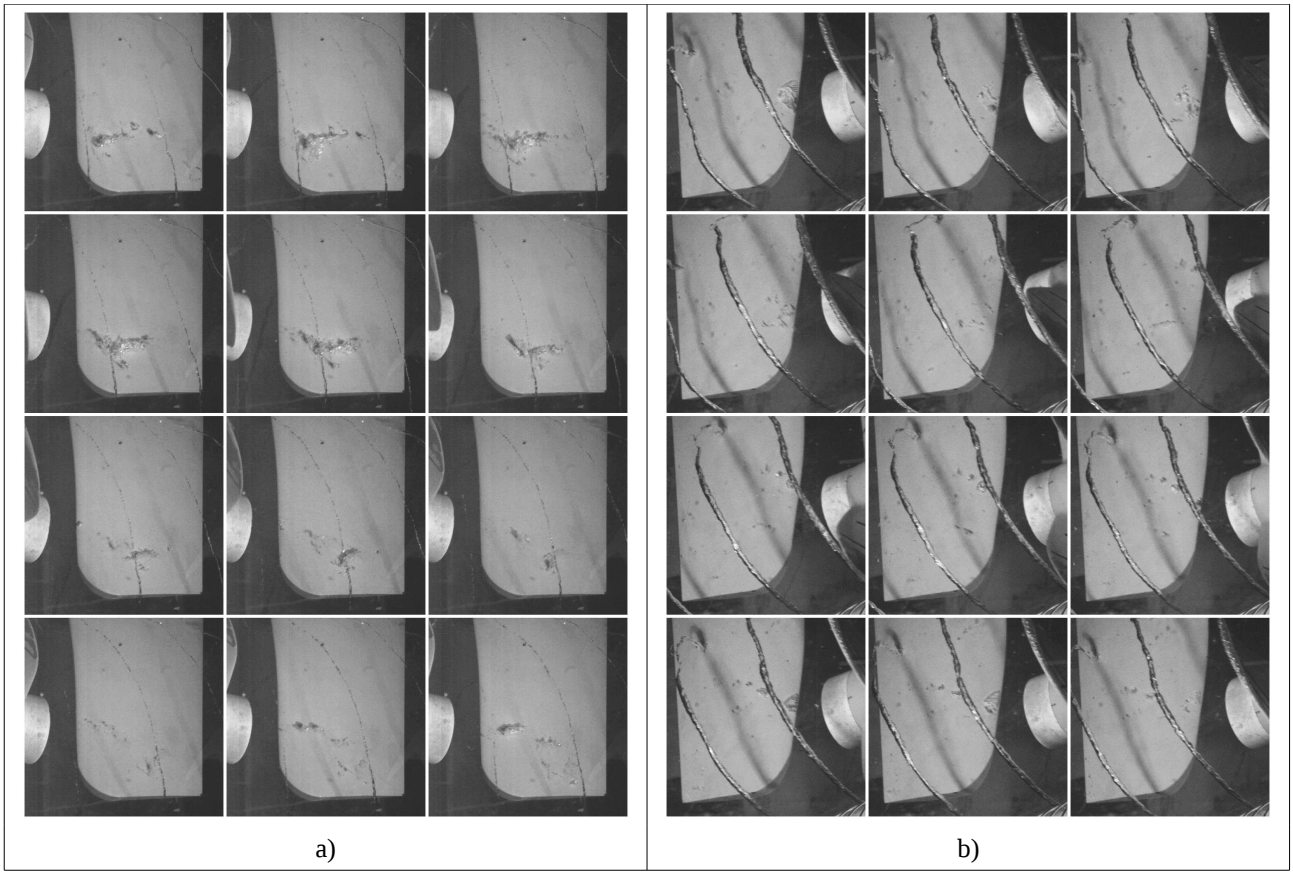

a) b)

Fig. 7. Model tests results: cavitation on the **twisted rudder**. Snapshots from High Speed Video recording. The time interval between frames is 0.002 s. a)View from the port side; b)View from the starboard

CFD optimization of vortex generators forming the wake flow of large ships

Pawel Dymarski, Marek Kraskowski

Ship Design and Research Centre S.A., Poland
pawel.dymarski@cto.gda.pl marek.kraskowski@cto.gda.pl

The paper presents the results of preliminary investigation of the effectiveness of using the vortex generators for improving the wake flow of large merchant ships.

The idea of vortex generators is based on that from aerospace industry, where the vortex generators are used to prevent the flow separation on the suction side of the airplane's wing – the vortices introduced to the boundary layer are attaching to the wing surface. It is expected that it is also possible to take advantage of this effect in ship design, by reducing the boundary layer thickness and reducing the areas of separated flows in the propeller disc region. Some promising results were already published (Schmode, 2008)

The vortex generators are just small winglets, located (in case of a ship) in the aft part of the hull, e.g. on the skeg, as presented in Figure 1. It is important that these winglets do not exceed the basic line and maximum breadth of the hull, to minimize the damage risk.

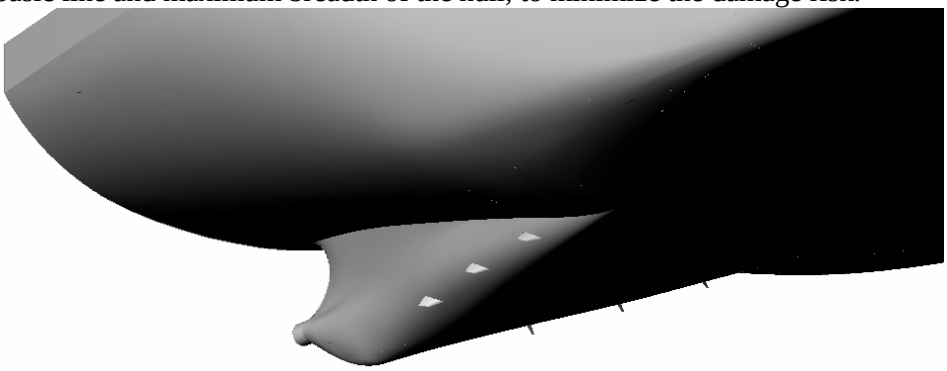

Figure 1 Aft part of the hull appended with vortex generators

The purpose of vortex generators is to improve the propulsion efficiency of the hull and reducing the propeller vibration and cavitation, by reducing the suction coefficient and improving the uniformity of the wake flow. The presence of vortex generators introduce some additional resistance, however, the total resistance of the hull with generators is not necessarily increased, because in some cases the generators improve the pressure distribution on the aft part (e.g. by reducing the flow separation area).

The results of CFD analyses for two large merchant vessels with vortex generators in different configurations are presented in the paper. The computations were carried out at model scale, to enable direct comparison of the CFD results with the experimental results.

The vessels, for which the analyses were realized, are presented in figure 2. The first one is a car carrier (left), the second one – a bulk carrier (right)

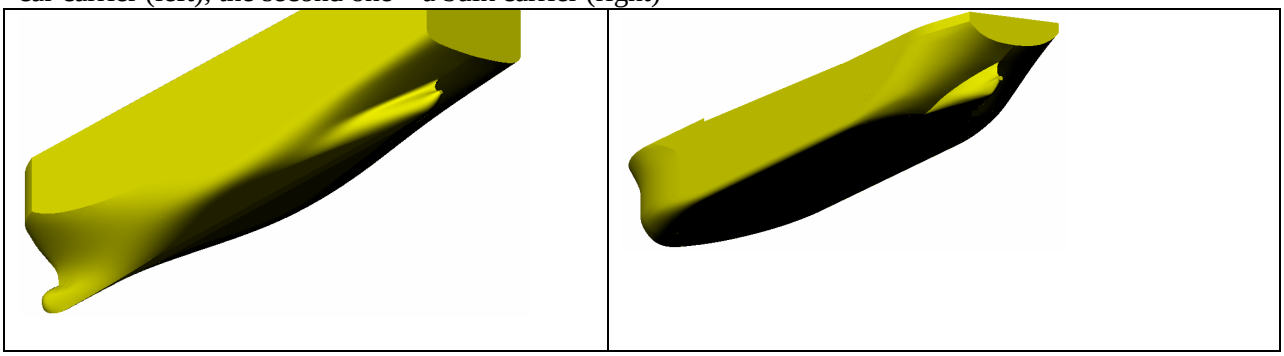

Figure 2 Hull shapes – car carrier (left) and bulk carrier (right)

Main parameters of the vessels are listed in the table below.

Tab. 1 Main parameters of the hulls

Vessel	Car carrier	Bulk carrier
Length b.p. [m]	188.00	250.80
Breadth [m]	32.23	44.40
Draught [m]	9.00	13.00
Block coefficient [-]	0.582	0.836
Speed [kn]	20.0	15.0
Model scale	26.6	38

Both vessels are characterized with complex wake flow, troublesome in respect of the propeller design (high non-uniformity, strong vortices and low average axial velocity). It was expected that there is a large area for improvement for both of them.

The following procedure was applied for the analysis:

- For both vessels, few configurations of vortex generators were proposed, basing mainly on intuition and CFD results for bare hull;
- Simplified criteria were used to evaluate the quality of the computed wake field: average value of the axial velocity in the propeller disc (required to be as large as possible) and total resistance of the hull with vortex generators.
- The configuration of vortex generators, for which the best results were obtained (for only one vessel), underwent further optimization.

The criterion of the average axial velocity in the propeller disc was applied basing on the assumption that faster wake flow reduces the suction coefficient and that the total hydrodynamic efficiency of the hull is higher.

The initial configurations of the vortex generators for both vessels are presented in figures 3 and 4

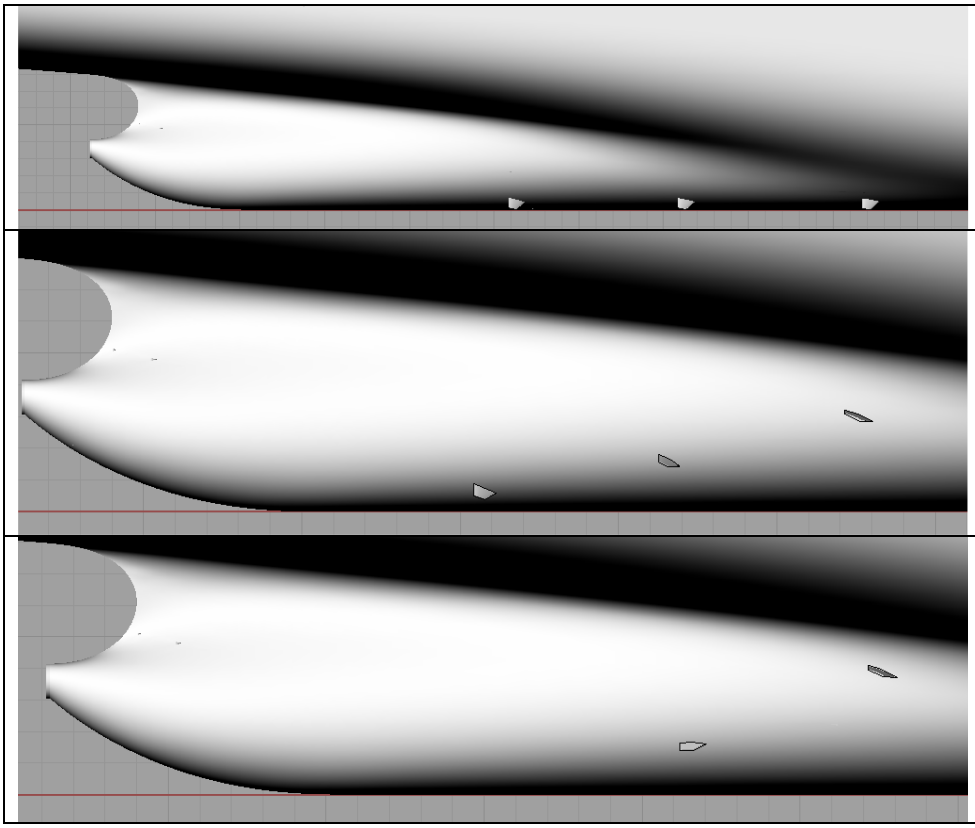

Car carrier - Configuration 1

Car carrier - Configuration 2

Car carrier - Configuration 3

Figure 3 Initial configurations of vortex generators – car carrier

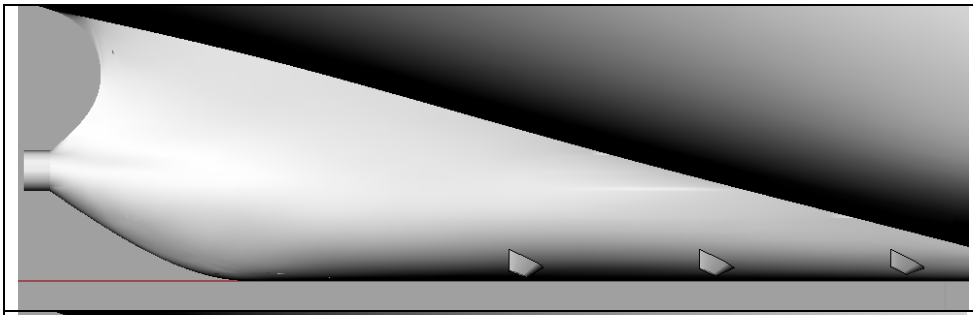

Bulk carrier -

Configuration 1

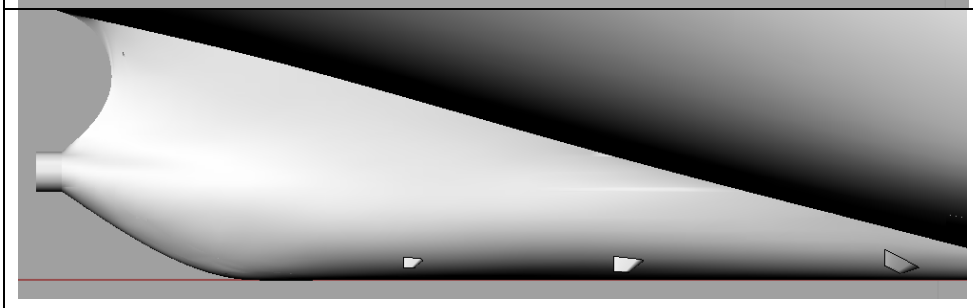

Bulk carrier -

Configuration 2

Figure 4 Initial configurations of vortex generators – bulk carrier

The angle of attack of the vortex generators was set basing on the streamlines evaluated for bare hull. For the initial configurations, the angle of attack relative to the streamlines was +15deg in most cases (positive value means that the streamlines are deflected upwards). Only in one configuration for the bulk carrier, the angle of attack of two vortex generators was set to -15 deg.

The CFD computations of the flow around the ship hulls with vortex generators were carried out with the use of RANSE flow model, implemented in STAR CCM+ solver. The basic assumptions for the simulation were as follows:

- The free surface was neglected in order to reduce the convergence time;
- The dynamic trim and sinkage of the hulls were also neglected; these simplifications are justified by low or moderate Froude numbers of the vessels (0.16 for the bulk carrier and 0.24 for the car carrier);
- Only the nominal wake field was computed – the propeller operation was not modelled.

The unstructured computational mesh of hexahedral cells was used for the computations. The number of cells was varying between 2 and 4 millions of cells, depending on the variant. The visualizations of mesh details are presented in figure 5.

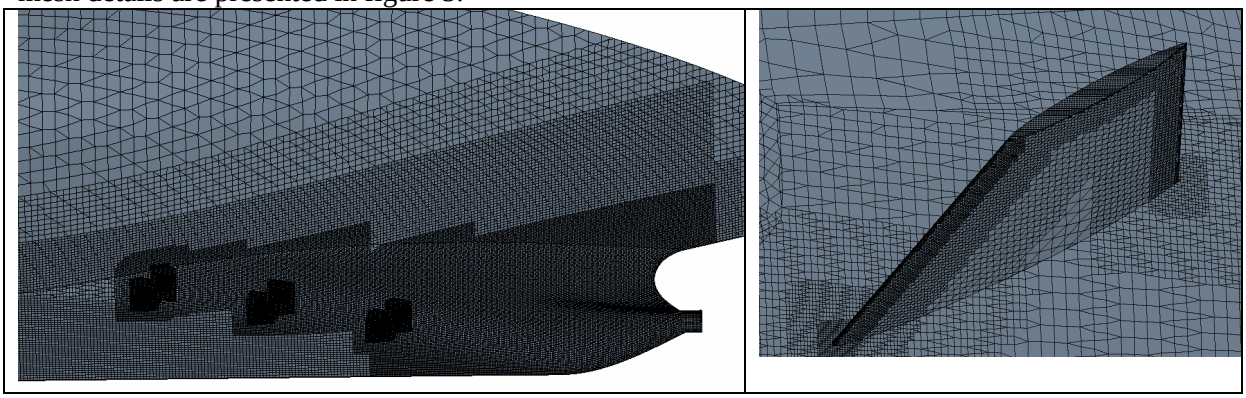

Figure 5 Numerical mesh – aft part of the hull and vortex generator

The CFD analyses were started with computation of the wake field for bare hull, for which the experimental data were available, which allowed for estimation of the numerical model accuracy. Figure 6 shows the computed wake fields for bare hulls, compared with the measured wake fields. Considerably better accuracy of the numerical model was achieved for the car carrier, however, for both cases the accuracy of CFD can be considered sufficient for comparative studies.

Car carrier		Bulk carrier	
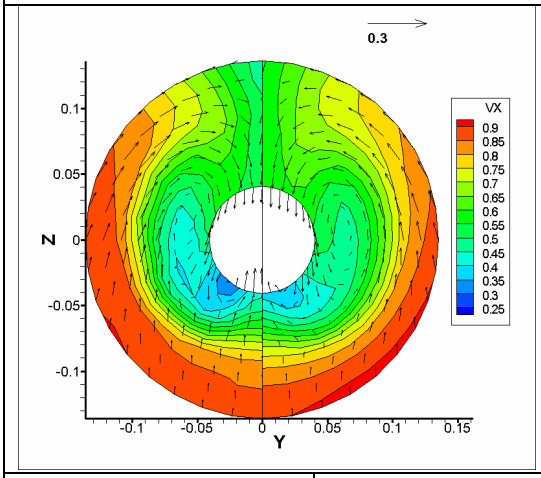		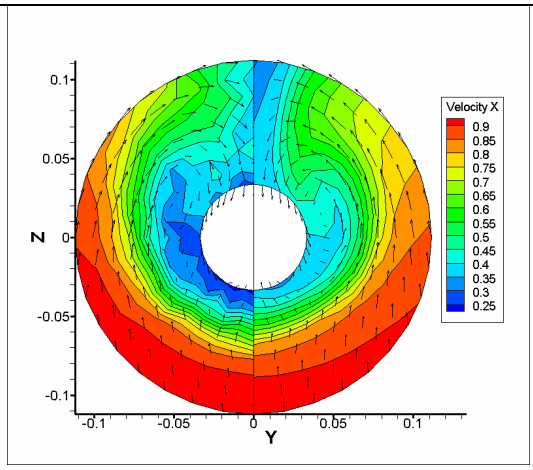	
Experiment	CFD	Experiment	CFD

Figure 6 Comparison of CFD results and model test results for bare hulls

The results of the preliminary analyses are summarized in the tables 2 and 3; the values of wake fraction and total resistance of the hulls with vortex generators are compared with corresponding values for bare hull and given as relative values.

Tab. 2 Results for car carrier with vortex generators

Configuration No.	Wake fraction [-]	Resistance (relative to bare hull) [%]
0 – bare hull	0.360	100
1	0.314	107.1
2	0.297	102.5
3	0.346	100.9

Tab. 3 Results for bulk carrier with vortex generators

Configuration No.	Wake fraction [-]	Resistance (relative to bare hull) [%]
0 - bare hull	0.380	100
1	0.322	88.8
2	0.338	91.3

For the car carrier, the best results were obtained for configuration No. 2, for bulk carrier – configuration No.1. Visualization of the wake fields for these configuration is presented in Figure 7

Car carrier		Bulk carrier	
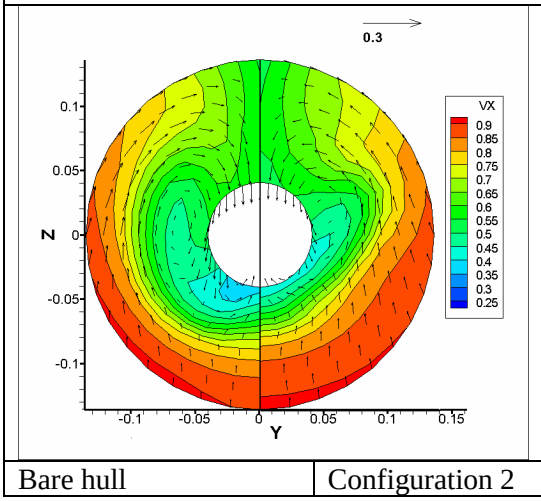		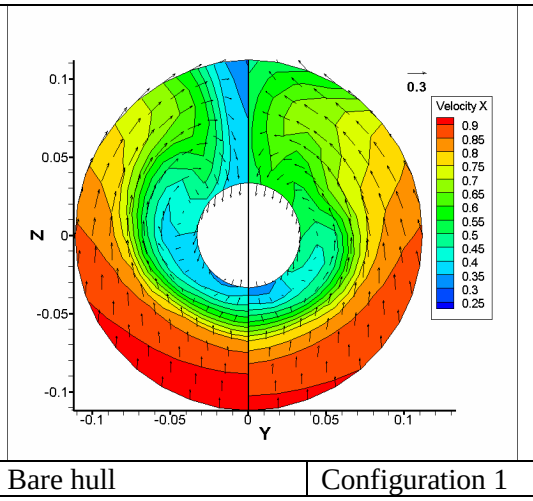	
Bare hull	Configuration 2	Bare hull	Configuration 1

Figure 7 Comparison of CFD results for bare hulls and hulls with vortex generators

The most promising results were obtained for the bulk carrier, for which the average axial velocity in the propeller disc was increased by 9.4%, and simultaneously the resistance was reduced by 11.2%. The differences in computed resistance are estimative only, as no wave resistance is considered, however, such large difference in CFD results allows expecting that the flow around the aft part of the hull was considerably improved and some reduction of the resistance will really occur.
An analysis of the streamlines in the aft part gives some explanation of this reduction of resistance: (Figure 8): in the flow around the bare hull, large area of separation is visible, and strong vortex is detaching from the skeg; introducing the vortex generators largely reduces these effects.

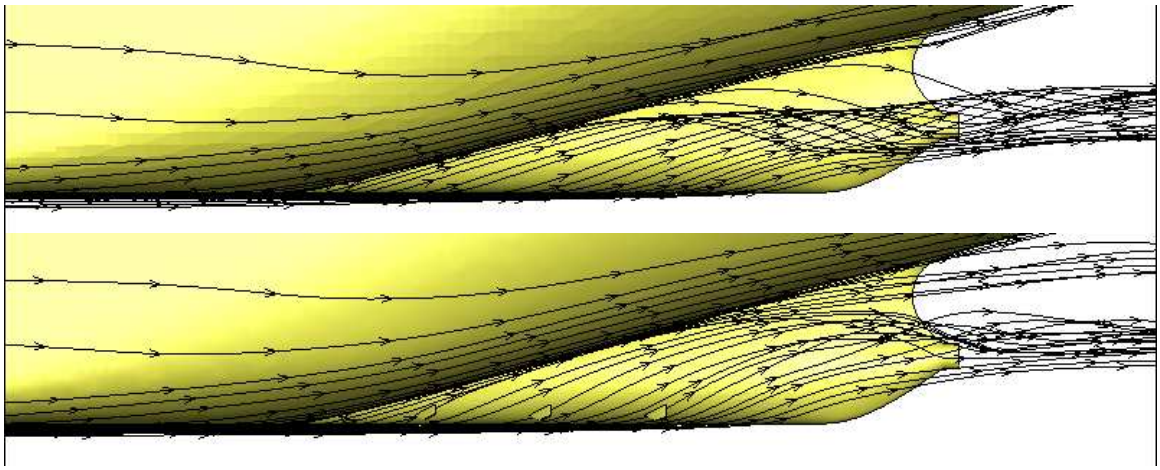

Figure 8 Streamlines for bulk carrier

For the car carrier, some increase of the average axial velocity is also visible, but it was obtained at the cost of increased resistance. Further analyses and optimization of the configuration of vortex generators was then carried out for the bulk carrier.

For the optimization of the configuration of vortex generators, the following parameters of it were used as "variables":

- Number of vortex generators;
- Size (the shape of each vortex generator used in this analysis is the same, but they vary in size; the characteristic dimension of the winglet is the maximum span, which varies from 20 to 40 mm in model scale);
- Angle of attack.

The initial configuration of the vortex generators, which underwent the optimization, consists of three winglets of maximum span 40 mm, fixed to the hull at the angle of attack 15 deg relative to the streamlines. Few modifications of this configuration were analysed, and the results for two of them are presented here, as they are most interesting:

- First modification consisted in reducing the size of two winglets to 30 mm (these located closer to the propeller) – it will be referred to as "Configuration No. 3"
- Second modification consisted in reducing the size of all winglets to 30 mm and increasing the angle of attack to 30 deg ("Configuration No. 4")

The quantitative results are presented in table 4, and visualizations – in figure 9.

Tab. 4 Results for bulk carrier with vortex generators – optimized configurations

	Wake fraction [-]	Resistance (relative to bare hull) [%]
Bare hull	0.380	100
Configuration No.1	0.322	88.8
Modification No.3	0.318	87.8
Modification No.4	0.302	102.5

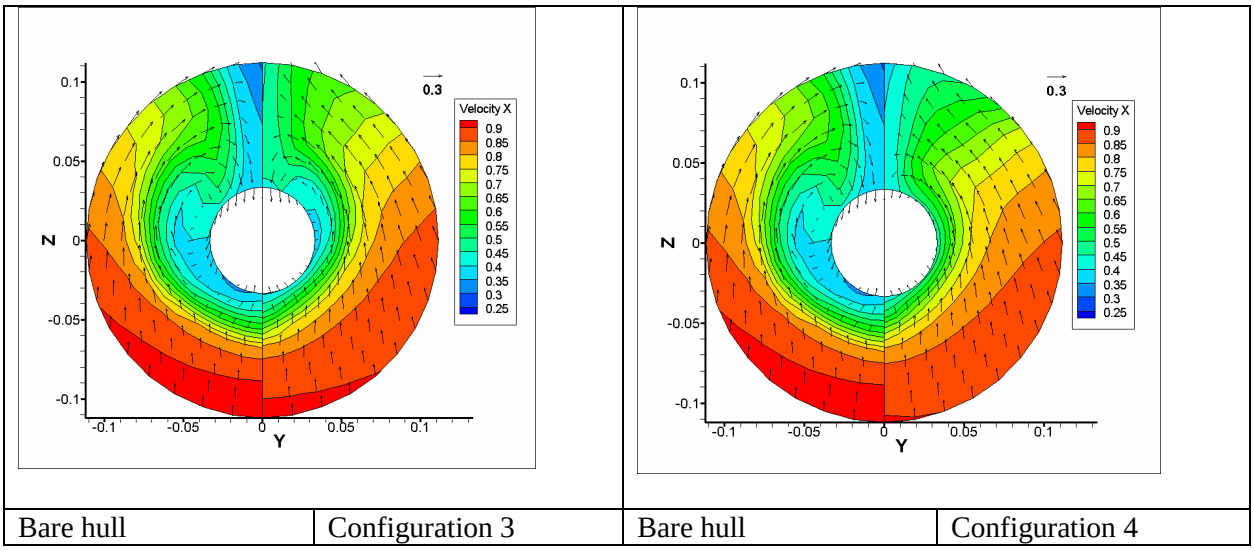

Bare hull	Configuration 3	Bare hull	Configuration 4

Figure 9 Comparison of CFD results for bare hulls and hulls with optimized vortex generators

Configuration No.3 is so far the most successful compromise in respect of assumed criteria – it provides high velocity in the propeller disc and lowest resistance.

For configuration No.4 the velocity in the propeller disc is the highest, but such effect was achieved at the cost of slight increase of resistance. However, the results for this configuration reveals that the vortex generators provide really large possibility of forming the wake flow for large vessels.

The study presented in this paper can be then summarized as follows:

- The possibility of forming the wake flow by using the vortex generators was investigated by means of CFD, for two large merchant vessels and few initial configurations of vortex generators;
- For both vessels, considerable influence of the vortex generators on the wake flow was observed; more promising results were obtained for the bulk carrier;
- The most succesful initial configuration of vortex generators for the bulk carrier was further optimized.

Further work on this topic will include:

- Experimental wake measurements for the hull with vortex generators – validation of the CFD results;
- Self-propulsion model tests, allowing for estimation of the influence of vortex generators on the propulsion efficiency; in fact, the criterion assumed here (high average axial velocity) is strongly simplified and does not really give an estimation of the influence on propulsion efficiency;
- Numerical analyses of the propeller operation (shaft forces, cavitation and pressure pulses) in the measured wake fields; the potential code based on lifting surface will be used for these analyses.

Acknowledgement
The research presented in this paper has been financially supported by The Polish National Centre for Research and Development (NCBiR), Grant No. N R10 0040 06/2009. The authors would like to express their gratitude for this support.

References:

Schmode D., (2008), *RANS computations for wake improving vortex generators*, Proceedings of 11th Numerical Towing Tank Symposium (NuTTS), Brest, France.

WATERJET HULL INTERACTION

Arash Eslamdoost, Rickard Bensow, Lars Larsson
arash.eslamdoost@chalmers.se

Hydrodynamics Group, Department of Shipping and Marine Technology
Chalmers University of Technology, Gothenburg, Sweden

Introduction

Waterjet propulsion systems are widely used on high-speed crafts (30-35 Knots) during the recent decades. The principle of operation of the present-day waterjet is that in which water is drawn through a ducting system by an internal pump which adds energy after which the water is expelled aft at high velocity. The unit's thrust is primarily generated as a result of momentum increase imparted to the water [1]. Elements and general definitions applied in waterjet system are presented in Figure 1.

There have been lots of experimental and numerical investigations to predict the performance curves of these propulsive systems and their optimization. But despite these various studies which mostly are focused on a confined package of waterjet intake, inlet ducting, impeller and nozzle, still there are some questions which cannot be answered unless the whole system including the waterjet propulsion system, hull and free-surface is taken into consideration all together; but investigating the existing interaction effects is not trivial for waterjet and hull system assembly. The main difficulty is the implicit dependence of the effective parameters on each other, which makes it tricky to render the effect of each single parameter on the overall behavior of the system.

Employing a RANS simulation Park et al.[3] discussed the complicated viscous flow feature of the waterjet, such as the secondary flow inside of the inlet ducting system, the recovery of axial flow by the action of the stator, and tip vortex, etc. The performances of thrust and torque are also predicted. Park et al.[4] compared the numerical results of surface pressure distributions, velocity vectors, and streamlines with experiments. Strong suction flow through the inlet, the vortex induced by the separation along the corner of the sidewall and the flow separation on the lip are investigated. With the aid of PIV measurement the location of stagnation point on the lip is also predicted. Bulten [5] reported one of the most comprehensive and recent studies on modeling waterjet system including intake, inlet ducting, impeller and nozzle. The ducting shape and the time dependent forces acting on the impeller are studied in this work.

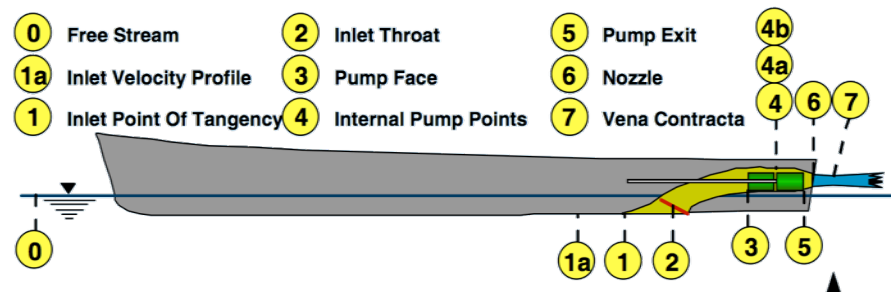

Figure 1. Definition of the waterjet system elements presented by the ITTC 23[2]

Beside lots of studies for modeling the flow inside waterjets, T. J.C. van Tervisga [6] tried to render the effect of each parameter on waterjet-hull interaction separately via some analytical, numerical and experimental analysis. He reported that in some range of Froude numbers the Thrust Deduction Fraction (t) becomes negative.

Thrust deduction fraction is defined as following (Eq.1):

$$t = 1 - \frac{R_t}{R_{sp}} \tag{1}$$

where, R_t is the bare hull resistance; R_{sp} is the resistance of the hull in self-propelled mode.

Taking the definition of thrust deduction fraction into consideration one would notice when this factor becomes negative literally there would be some gain, because the resistance of the hull in self propelled case is actually lower than the resistance of the bare hull itself. This phenomenon is caused by the interaction of the waterjet system with the hull.

The main objective of this work is to render the parameters involved in the watejet-hull interaction and finally define the weight of each of these parameters on the thrust deduction fraction. This would help to know how to control the thrust deduction fraction and try to keep this factor below zero to gain more efficiency for the hull and waterjet assembly. Aiming this goal, current paper is going to discuss some strategies for modeling waterjet-hull interaction starting with very simplified assumptions. The applied solver in this work is a potential code including a linear/none-linear free surface model which is capable of handling 6DoF simulation for calculating sinkage of a hull and its' trim angle.

Simplified Intake

The first step to start the simulations was to put two intakes on a certain hull and study the effects of these intakes and compare the final results with the results obtained from the hull without these intakes. To make the computations as simple as possible, ducting system of the waterjet was neglected and just two rectangular surfaces were fitted to the stern. Creating panels on the hull and these intakes, two different boundary conditions were employed for the existing panels based on what those panels are nominating for. Normal zero velocity boundary condition was adapted for the hull wall but for panels on the intake surface a normal velocity boundary condition was applied. These velocity vectors were set in a way to point into the inside of the hull representing flow suction beneath of it. In the present modeling, there is not any outlet jet adapted. Neglecting the jet would be a source of error during the computations but as a start point the aim of this stage is just to see the effect of a predefined suction under the hull on the generic characteristics of the system like hull's sinkage and trim angle. To capture free surface a none-linear free surface model has been applied.

Figure 2 shows pressure distribution under the hull at the stern for two cases: one without the rectangular intakes and one including the intakes. Comparing these two contours with each other one can see that the effect of intakes is rather high on the pressure distribution not only on the intake area itself but also on the vicinity of these intakes. This discrepancy in the pressure distribution, directly influences the sinkage, trim angle and the total resistance of the hull. Wave pattern caused by the hull is plotted in Figure 3. Figure 4 depicts the draft change of the hull in three various positions which are at the Bow, LPP/2 (half of the water line) and Stern. In this figure draft varies by the change of the ratio of the intake velocity to the ship speed. Taking all these three trend lines into consideration simultaneously one would notice that it implicitly represents the trim angle of the hull, which is also plotted in Figure 5. In the limited range of the calculated ratio of the intake velocity to the ship speed it is possible to see that the trim angle increases as this ratio rises. A same trend is detectable for the wave resistance coefficient of the hull as presented in Figure 6.

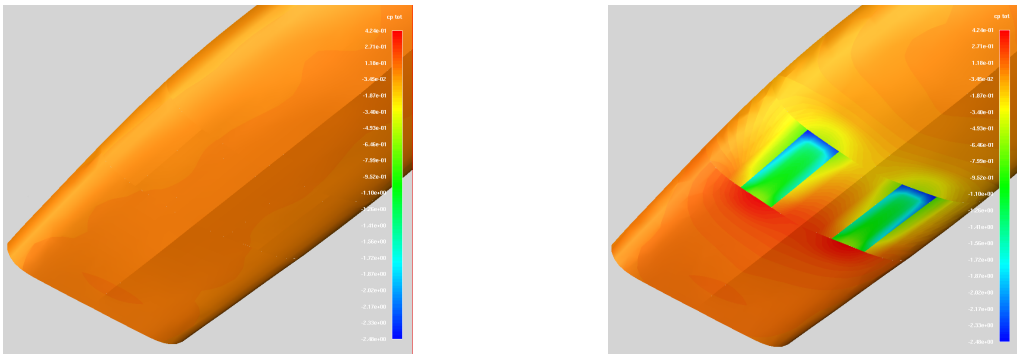

Figure 2. Comparison of the pressure distribution at the stern of the hull in two different cases. First (left) picture shows the pressure distribution at the stern on the absence of the intakes and the second (right) picture depicts the pressure distribution while there are two active intakes.

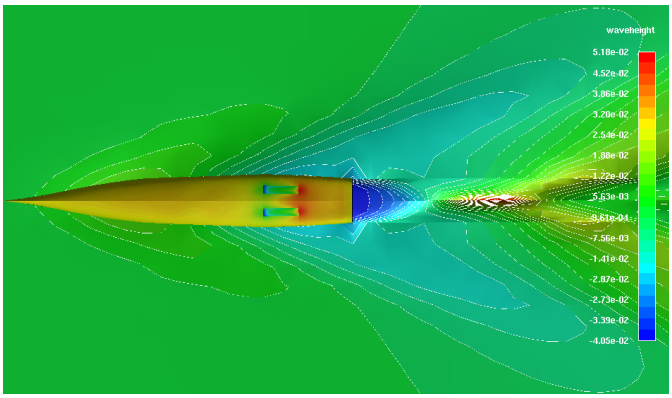

Figure 3. Free-surface wave height contour while there are two active intakes (Fn=0.5).

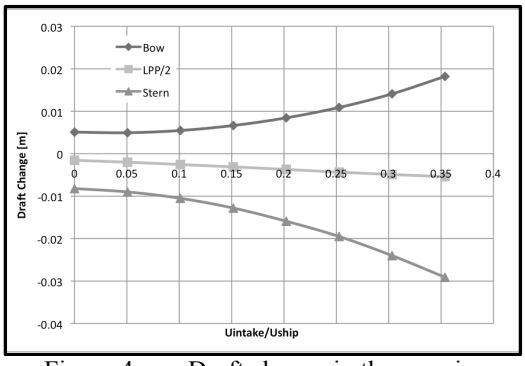

Figure 4. Draft change in three various sections of the hull against the ratio of the intake velocity to the ship speed

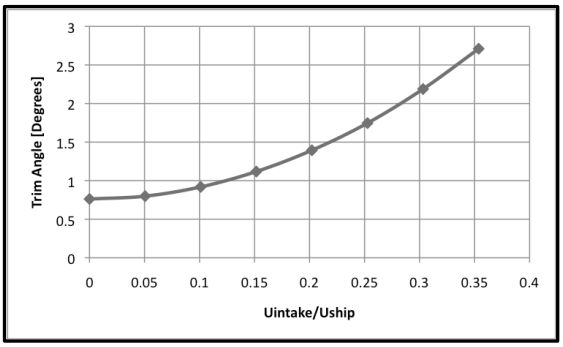

Figure 5. Trim angle of the hull against the ratio of the intake velocity to the ship speed

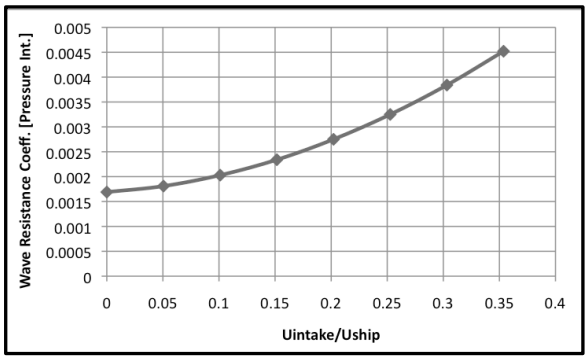

Figure 6. Wave resistance of the hull against the ratio of the intake velocity to the ship speed

All these computations are done in a confined range of Froude numbers, which the highest Froude number applied in the computations, is 0.7. Convergence of the computations is highly dependent on the applied Froude number and also the intake velocity. Increasing any of the ship velocity or the intake velocity higher than some certain values caused some numerical problems for capturing the free surface and finally ended up in divergence of the calculations. Applying a rather unphysical boundary condition on the intake area could be a reason for this outcome. Taking the whole intake geometry along with the intake ducting system into consideration can be a solution for this problem. According to this, modeling a real intake geometry is going to be discussed in the next section.

Real Intake Along with Ducting System

Beside the previous setup this step is to take the intake ducting system into consideration directly in the computations. This makes it possible to investigate the pressure distribution inside the stream tube and take the generated force on this area into account in the trim and sinkage computation. In this case a sink plane has been used just at the outlet of the stream tube. Actually, this is a model replaced by an impeller, which sucks the flow into itself and alters the pressure gradient inside the ducting. Controlling the flow rate inside the ducting is possible through changing the strength of sinks distributed on the applied actuator disk. This is done by means of propeller thrust coefficient defined as CTS [7]. Like the previous case a none-linear free surface model has been employed for capturing the free surface.

General presentation of the pressure distribution is depicted in Figure 7. The plotted vectors in Figure 7(b) shows the overall velocity distribution on the applied actuator disk at the outlet. It is clearly seen that the pressure amount on the topside of the ducting is higher comparing to the bottom side of it. Considering the flow direction and the curvature of the ducting, the overall quality of the pressure distribution seems reasonable comparing to the same existing experimental data; but still there has not been any direct comparison and validation with the existing experiments. Figure 8 shows the wave height around the hull with an active actuator disk for Fn=0.7.

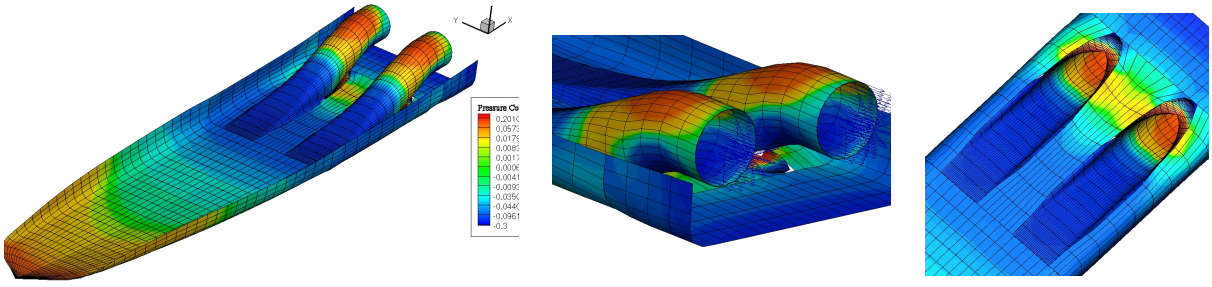

(a) (b) (c)

Figure 7. Pressure distribution on the hull and inside the ducting system. (a) General view (b) The ducting system and the overall velocity vectors on the applied actuator disk at the outlet (c) Bottom view

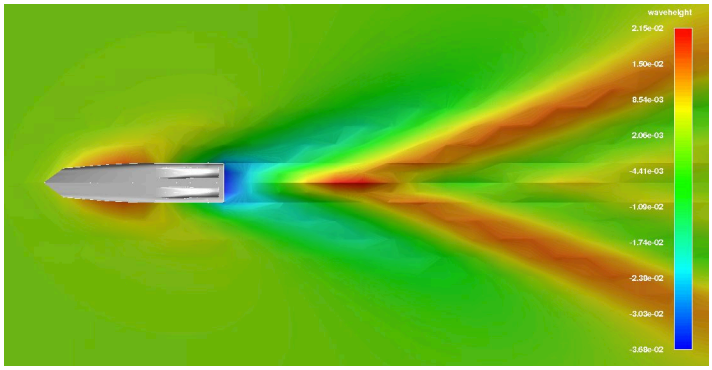

Figure 8. Free-surface wave height contour while there are two active intakes (Fn=0.7).

Figure 9 and Figure 10 respectively demonstrate the sinkage and trim angle variation against Froude number. In each of these plots two various propeller thrust coefficients is applied for the employed actuator disk. First it is supposed that there is not any suction on the disk or in other words the propeller thrust coefficient is equal to zero, CTS=0. Then CTS is set to 0.5 and a same data package is extracted. Comparison of the sinkage and trim angle is plotted in Figure 9 and Figure 10 for these two different settings. Actually, increasing the propeller thrust coefficient from 0 to 0.5 rises the flow rate inside the ducting system. This higher flow rate totally alters the behavior of the hull comparing to the case that there is not any forced suction inside the stream tube. This effect is much more stronger in higher Froude numbers.

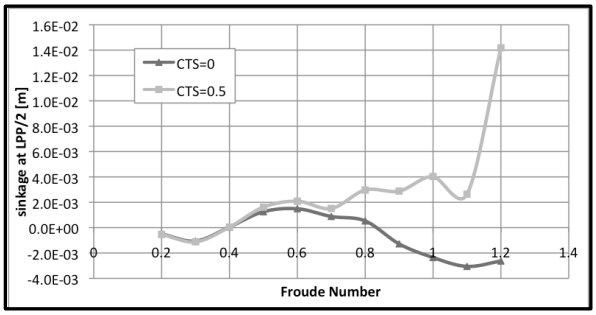

Figure 9. Sinkage at LPP/2 against Froude Number

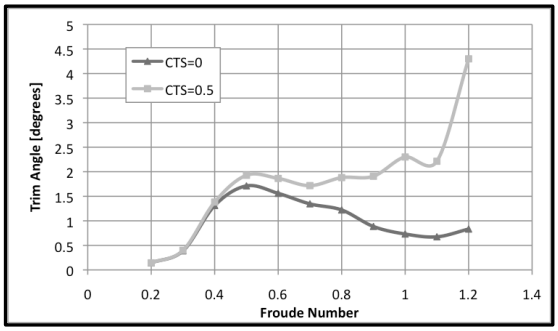

Figure 10. Trim angle against Froude Number

Conclusion and Future Work

A generic study is conducted to investigate the interaction effects of waterjet propulsion system and hull. Initial investigation of two different intake modeling shows that neglecting the stream tube of the ducting system in the computations makes it tricky to apply a proper velocity boundary condition on the intake surface and it would be more efficient to take the whole ducting system into consideration during the numerical calculations. Furthermore, one of the most important effects in modeling waterjet-hull interaction is the effect of the outgoing jet, which has not been taken into account in this study. In the next stage the jet should also be modeled. Moreover, the computation of the momentum exerted on the hull by the action of the discharged jet or in other words the propelled flow rate is of a special importance. An algorithm should be prepared for controlling the amount of the propelled flow rate through the actuator disk in order to obtain the correct required momentum from the jet action for propelling the ship in a certain Froude number.

References

1. Carlton, J. S., Marine Propellers and Propulsion, Butterworth-Heinemann, London, 1994.
2. The Specialist Committee on Validation of Waterjet Test Procedures, Proceedings of the 23rd ITTC – Volume II, 2002.
3. Warn-Gyu Park, Jin Ho Jang, Ho Hwan Chun, Moon Chan Kim, Numerical flow and performance analysis of waterjet propulsion system, Ocean Engineering, vol. 32, pp 1740–1761, 2005.
4. Warn-Gyu Park, Hyun Suk Yun, Ho Hwan Chun, Moon Chan Kim, Numerical flow simulation of flush type intake duct of waterjet, Ocean Engineering, vol. 32, pp 2107–2120, 2005.
5. Norbert Willem Herman Bulten, Numerical Analysis of a Waterjet Propulsion System, doctoral thesis, Eindhoven University of Technology, 2006.
6. Tom J.C. van Terwisga, Waterjet-Hull Interaction, doctoral thesis, Technical University of Delft, 1996.
7. Flowtech International AB, SHIPFLOW Users Manual, 2007.

Squat computation for a containership with potential and viscous methods

Alexander von Graefe, University Duisburg-Essen, Duisburg, Germany; alexander.von-graefe@uni-due.de
Vladimir Shigunov, Germanischer Lloyd AG, Hamburg, Germany
Tobias Zorn, Germanischer Lloyd AG, Hamburg, Germany

1 Introduction

Optimal exploitation of the available fairway depths becomes crucial for some internal sea ports, e.g. Hamburg, because of the growth of the size of the new built ships. Minimisation of dredging costs (for river Elbe, depth increase costs about 1.0 m$ per 1.0 cm of depth without maintenance costs) is possible if reliable squat predictions could be offered to the shipping companies and fairway authorities. The estimation of dynamic sinkage and trim due to speed in restricted waterways is a difficult task. Although many empirical formulae exists, experience shows that none of them can predict squat with sufficient accuracy for all ship sizes and forms and channel configurations, [1]. A more reliable approach is to use model tests; a cheaper alternative is using computational fluid dynamics methods.

As a classification society, Germanischer Lloyd is committed to providing reliable assessment procedures for all aspects of ship safety. In collaboration with the Technical University Hamburg-Harburg and University Duisburg-Essen, software *GL Rankine* is developed for the calculation of steady and non-steady nonlinear free-surface flows in time domain, as well as periodical flows in frequency domain, using boundary element approach. The nonlinear part is outlined in the next section; the methods for periodical flows (ship motions, loads and deformations in seaway) are described in [10] and [9].

This paper compares squat predictions of *GL Rankine* with a viscous flow solver *Comet* and with full-scale measurements for a container ship sailing on the river Elbe, [11] and [1]. *Comet* is a universal finite-volume solver of Reynolds-averaged Navier-Stokes equations (RANSE), including free-surface flows, [2] and [6].

2 Boundary element method *GL Rankine*

The nonlinear part of *GL Rankine* predicts steady and slowly varying flows using nonlinear free-surface condition. A short description of the numerical method follows. For brevity, we restrict the description to steady flows.

The fluid is assumed inviscid, incompressible and irrotational. Therefore a velocity potential ϕ exists, which has to fulfill the Laplace equation (conservation of mass) as well as kinematic and a dynamic boundary conditions on the free surface ('no flow through the surface' and 'atmospheric pressure at the surface', respectively):

$$\Delta\phi = 0 \qquad \text{within the fluid domain} \tag{1}$$

$$(\nabla\phi - \vec{U}) \cdot \vec{n} = 0 \qquad \text{on the body boundary} \tag{2}$$

$$\nabla\phi \cdot \vec{n} = 0 \qquad \text{on the channel boundary} \tag{3}$$

$$(\nabla\phi - \vec{U}) \cdot \vec{n} = 0 \qquad \text{on the free surface} \tag{4}$$

$$g\zeta = \vec{U}\nabla\phi - \frac{1}{2}|\nabla\phi|^2 \qquad \text{on the free surface .} \tag{5}$$

$\vec{U} = [u,0,0]^T$ denotes the ship velocity, $\vec{n}$ the surface normal and $\zeta = \zeta(x,y)$ the free surface elevation. In addition, a radiation condition has to be fulfilled on the free surface, so that waves created by the ship can propagate only downstream.

Following boundary element approach, only the surface of the computational domain is discretised. An unstructured triangular grid is used on the submerged ship surface and a block-structured quadrilateral grid is employed on the free surface. Rankine sources are located at points $\vec{\xi}_j$ outside the fluid slightly above centre points of each panel (desingularisation). The channel boundary can be modelled either directly, using triangular panels, or employing image sources for a rectangular channel cross section. Representing the potential

$$\phi = \phi(\vec{x}) = \sum_{j=1}^{n} q_j G(\vec{x}, \vec{\xi}_j) \tag{6}$$

as a superposition of Rankine sources $G(\vec{x}, \vec{\xi}_j) = |\vec{x} - \vec{\xi}_j|^{-1}$ of strength 4π automatically fulfills the Laplace equation; the patch method [9] is used in order to satisfy the boundary conditions. In this method, the boundary conditions are fulfilled on the average over each panel and not at discrete collocation points. Integration over each panel leads to one equation, hence the number of unknown source strengths q_j is equal to the number of equations. In order to consider boundary conditions on the body and on the free surface, the residuum (flow through the panel) on a panel τ_i is introduced,

$$r_i = \int_{\tau_i} (\nabla\phi - \vec{U}) \cdot \vec{n}\, \mathrm{d}S = \sum_{j=1}^{n} q_j \int_{\tau_i} \nabla G(\vec{x}, \vec{\xi}_j) \vec{n}\, rmdS - \int_{\tau_i} \vec{U}\vec{n}\, \mathrm{d}S = 0. \tag{7}$$

The integrals in the above equation are determined analytically; for large distances between $\vec{\xi}_j$ and τ_i they are approximated. Because the free surface boundary condition is nonlinear an iterative solution is required. Here, a Newton-like iteration for the residuum is used,

$$\sum_{j=1}^{n} \frac{dr_i}{dq_j} \Delta q_j + r_i = 0. \tag{8}$$

After each iteration step, the source strengths are updated as $q_j^* = q_j + \omega \Delta q_j$ with an relaxation parameter $0 < \omega \leq 1$. It holds that

$$\frac{dr_i}{dq_j} = \begin{cases} \frac{\partial r_i}{\partial q_j} + \frac{\partial r_i}{\partial \zeta} \frac{\partial \zeta}{\partial q_j} & \text{on the free surface} \\ \frac{\partial r_i}{\partial q_j} & \text{otherwise} \end{cases} \tag{9}$$

Since the elevation $\zeta = \zeta(x,y)$ depends on the potential ϕ, which itself depends on the q_j, changing q_j lead to changes in ζ. This has to be considered during the evaluation of $\frac{dr_i}{dq_j}$ on the free surface; in particular, one has to note that r_i is an integral over the panel τ_i, and that the shape of τ_i depends on ζ.

In order to fulfill the radiation condition, the sources above the free surface panels are shifted downstream by one panel length, [8] and [3].

In some situations it might be necessary to employ an additional wave damping on the free surface to prevent wave breaking, which cannot be modelled by this method.

After determining the potential, the forces and moments acting on the ship are computed by integration and used to determine the dynamic trim and sinkage. A small update of the ship attitude is calculated at every Newton iteration step, so that the accurate dynamic attitude is found for each time step; details can be found in [3]. After adapting the attitude of the ship, the new free surface elevation is determined using the dynamic boundary condition and the grid on the submerged ship surface is updated.

3 Finite-volume RANSE solver *Comet*

The method solves directly mass and momentum conservation equations as well as transport equations for turbulence modelling, thus allowing for accurate description of the physics without further simplifications. The fluid is assumed viscous and the flow turbulent.

Free surface evolution is modelled by solving an additional transport equation for the volume fraction of water, similarly to the Volume-of-Fluid method, thus the computational domain comprises both air and water. The fluids are handled as a mixture with variable density and viscosity, which are determined from the volume concentration of water in each finite volume. This approach allows for arbitrary deformations of the free surface including breaking waves, splashes etc.

Turbulence is modelled using the Reynolds-averaged Navier-Stokes equations (RANSE). The $k-\varepsilon$ turbulence model is used here, [4].

The motion equations are discretised with finite volumes of arbitrary form. The volume integrals over cells and surface integrals over cell faces are approximated numerically using the mid point rule with an truncation error of second order. Blended upwind-centred interpolation is used for velocities and turbulence properties. In order to resolve the sharp interface between water and air without numerical instability or excessive numerical diffusion, a high-resolution interpolation scheme (HRIC) is employed for the interpolation of the volume fraction of water, [6].

For the coupling of the pressure and velocity fields, a variant of the SIMPLE algorithm is used, [7], [2]. The equations of ship motions are solved together with the flow equations, thus allowing for accurate computation of the transient ship motions including dynamical trim and sinkage. The computations are performed as transient simulations in the time domain. In order to capture ship motions relative to the bottom, deformed grids are used. The local grid around the ship keeps unchanged and follows the ship motions dynamically over time, while the outer grid portion is fixed to the bottom and to the non-moveable outer boundary of the computational domain and remains static. The connecting grid part between the outer and the local grids is deformed over time.

This method is more accurate than the Rankine boundary-element method, but also significantly more expensive regarding both preparation and computational time.

4 Application example

A modern container ship of the class Hamburg Express with capacity of about 7500 TEU is considered, see table 1 for the main particulars. Full-scale measurements were carried out in river Elbe for three stations along the river, referred to as km630, km650 and km660. Figure 1 shows the channel topography and the cross sections of the river for the three stations. The first station features a relatively narrow cross-section with a strong influence of breadth limitation; for the two latter stations, the effect of the finite depth is also significant while the influence of the limited breadth is marginal.

T_{fp},m	T_{ap},m	L_{pp},m	L_{oa},m	B_{wl},m	C_B
12.65	12.50	ca. 300	ca. 320	ca. 42	ca. 0.64

Table 1: Main particulars of the container ship

Time histories of the ship position and attitude were derived from the data of four (two at the bow and two on the bridge) receivers of the Precise Differential Global Positioning System (PDGPS) with the error in position and attitude below 4.0 cm, [5]. The error in the measurement of the speed over ground is estimated below ± 0.08 knots, which can lead to squat error of up to ± 2.0 cm. Nautical data (rudder angle, propeller r.p.m. and wind) were taken from the voyage data recorder onboard. The bottom topography was employed from an available digital model. Due to short-term local changes of the depth, errors in depth estimation up to one metre can be expected; in general however the deviations do not exceed ± 0.2 m, which means the error in squat up to 5.0 cm.

The current and water density were measured from a support boat at 6 locations along the river before the passage of the container ship. The local level of the tide was interpolated from the measurements of gauges located on the coast along the river and verified with GPS-measurements from the support boat; the error of the water stand is estimated to be below 1.0 cm, [5].

The remaining sources of uncertainty, which may lead to errors in squat measurements are, first, the local variations of the water level, because local transient effects may be missed by the interpolation

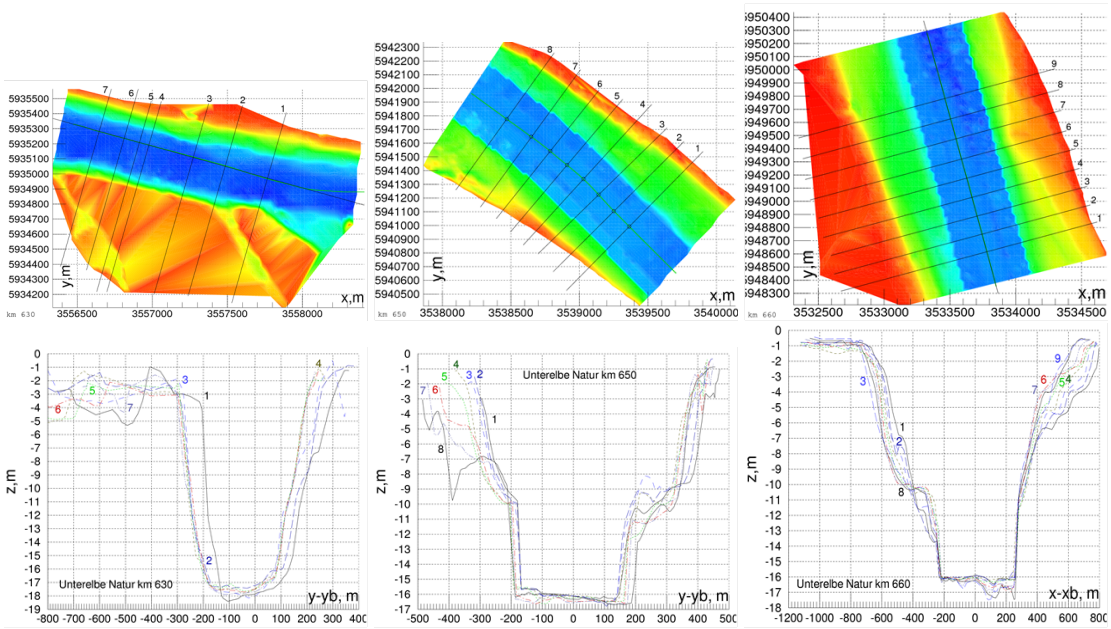

Figure 1: River Elbe at stations km630, km650 and km660 (left to right)

procedure. Secondly, the speed definition of the current and its local variations can also lead to significant uncertainty. Finally, dynamic effects of the longitudinal acceleration or deceleration significantly change the wave pattern and thus dynamic squat. Although there may also be other effects, their influence on squat and thus the resulting error are to be estimated yet, e.g. the influence of heel and calm-water ship deformations on squat.

The overall quality of squat measurement with the described procedure is estimated in [5] as ± 5.0 cm; the observed differences between the measurements for km650 and km660 suggest however that the uncertainty may be larger in some circumstances, figure 2: because the influence of side restrictions for these stations is marginal, the measurements are expected to be closer to each other. The analysis of the time histories for these two stations suggests that one of the reasons may be the influence of longitudinal acceleration of the ship.

5 Results

Figure 2 compares calculated and measured squat at forward and aft perpendiculars; figure 3 compares the wave patterns between potential and RANSE solutions. The relative velocity v_{rel} shown along the horizontal axis in figure 2 is the sum of the ship velocity over ground and the tidal current of the river.

A channel with rectangular cross section was used in *GL Rankine* computations, while RANSE used a simplified trapezoidal cross-section; comparison of RANSE simulations for a trapezoidal and a rectangular cross sections (green squares vs. red circle, respectively) shows relatively weak influence of the form of the (relatively broad) cross-section.

Comet simulations were performed only for the station km660 (green squares). The propeller of the ship was taken into account. In order to quantify the influence of the propeller, an additional simulation without propeller (brown triangle) was performed; for this example, the influence of the propeller appears not significant.

The computed squat at the forward perpendicular appears to be overestimated by both *GL Rankine* and *Comet* when compared to the measurements for km660, but is close to the measurements for km650. Squat at the aft perpendicular is underestimated by *GL Rankine* while captured well by *Comet* up to the largest speed used in the simulations when compared to km660 measurements, although the differences between the measurements for km650 and km660 do not allow for more certain conclusions.

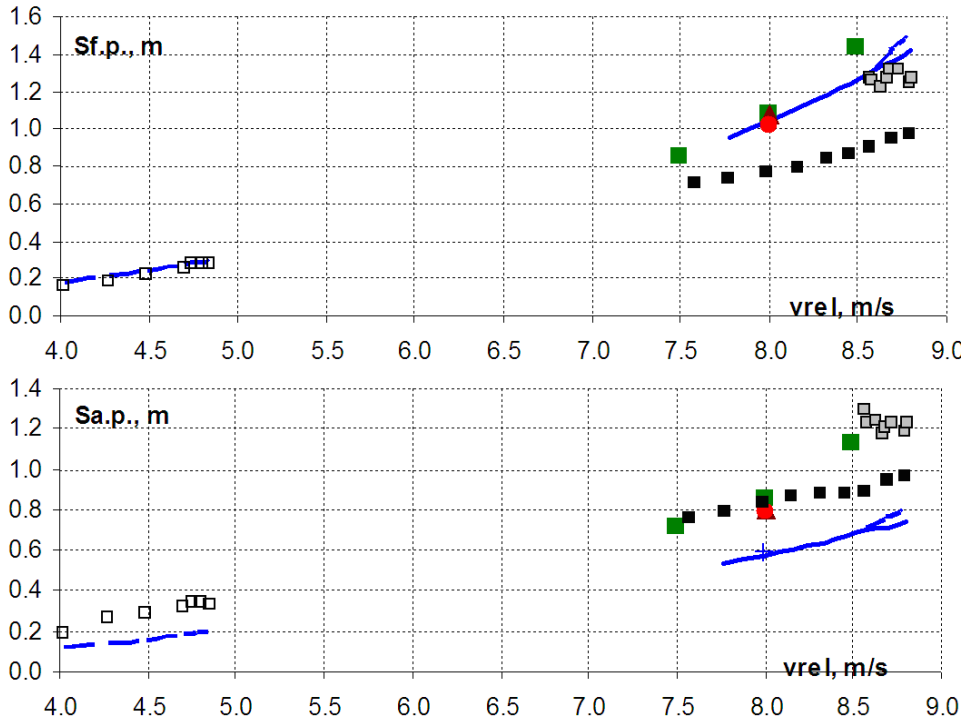

Figure 2: Results of computations with *Comet* (with propeller – green squares, without propeller – brown triangle, rectangular cross-section – red circle) and *GL Rankine* (blue lines) vs. measurements (km630 – white squares, km650 – grey squares, km660 – black squares): squat at forward (top) and aft (bottom) perpendiculars

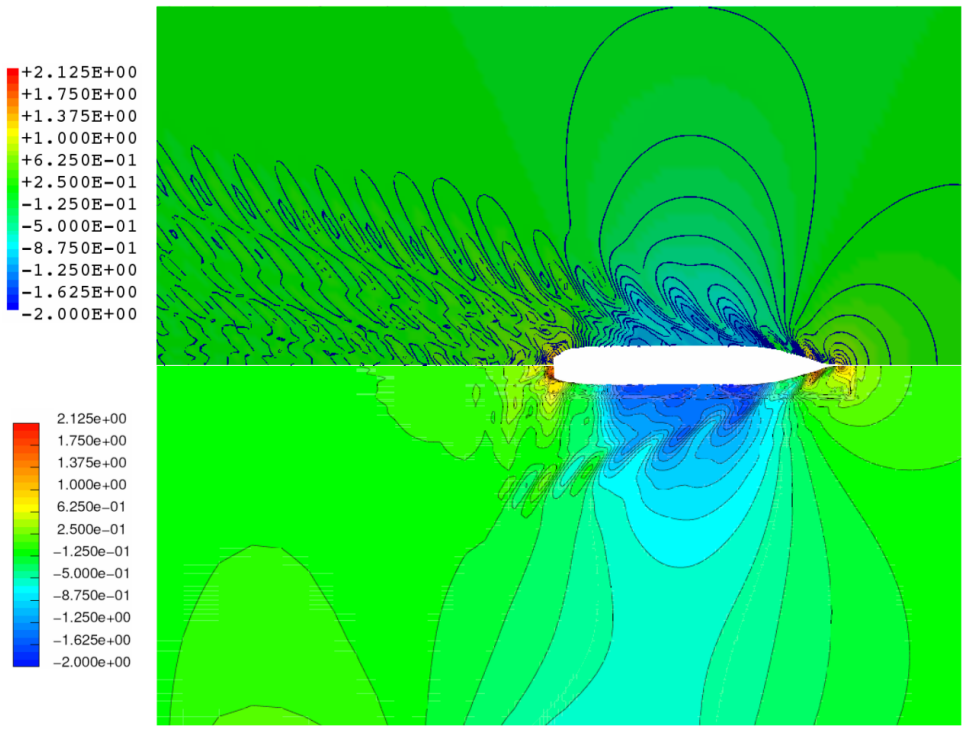

Figure 3: Wave pattern for $v_{rel} \approx 8.5$ m/s for station km660: *GL Rankine* (top) and *Comet* (bottom)

References

[1] M. Briggs, P. Debaillon, K. Uliczka, and W. Dietze. Comparison of pianc and numerical ship squat predictions for rivers elbe and weser. *3rd Squat-Workshop 2009 - Nautical Aspects of Ship Dynamics - Elsfleth (Germany)*, pages 133–154, 2009.

[2] J. H. Ferziger and M. Peric. *Computational methods for fluid dynamics*. Springer-Verlag, Berlin, 1997.

[3] G. Jensen. *Berechnung der stationären Potentialströmung um ein Schiff unter Berücksichtigung der nichtlinearen Randbedingung an der Wasseroberfläche*. PhD thesis, Institut für Schiffbau der Universität Hamburg, 1988.

[4] B. E. Launder and D. B. Spalding. The numerical computation of turbulent flows. *Computer Methods in Applied Mechanics and Engineering*, 3:269–289, 1974.

[5] C. Maushake and S. Joswig. Messung von Squat, Trimm und Krängung sehr großer Containerschiffe im Rahmen von Grundsatzuntersuchungen auf der Elbe. *Hydrographische Nachrichten*, 62(2), 2004.

[6] S. Muzaferija and M. Peric. Computation of freesurface flows using interface tracking and interface-capturing methods. In *Nonlinear Water Wave Interaction*, pages 59–100. Comp. Mech. Publ., 1998.

[7] S. V. Patankar and D. B. Spalding. A calculation procedure for heat, mass and momentum transfer in three-dimensional parabolic flows. *Int. J. Heat Mass Transfer*, 15, 1972.

[8] H. Seto. On rationalization of a staggered collocation rankine source scheme. *Transactions of The West-Japan Society of Naval Architects*, 90:253–259, 1995.

[9] H. Söding. A method for accurate force calculation in potential flow. *Ship Technology Research / Schiffstechnik*, 40:176–186, 1993.

[10] H. Söding and V. Bertram. A 3-d rankine source seakeeping method. *Ship Technology Research / Schiffstechnik*, 56:50–66, 2009.

[11] K. Uliczka and B. Kondziella. Dynamic Response of Very Large Container Ships in Extremely Shallow Water. *Proceedings 31st PIANIC Congress, Estoril, Portugal*, 2006.

A 3D domain-decomposition strategy for violent wave-vessel interactions

M. Greco, G. Colicchio, C. Lugni
NTNU, Trondheim/Norway, marilena.greco@ntnu.no
INSEAN, Rome/Italy, m.greco@insean.it

The water-on-deck is a transient nonlinear phenomenon induced by wave-vessel interactions, especially when severe incident waves and large vehicle motions happen. Green water is characterized by compact masses of liquid exceeding locally the freeboard, they enter the vessel and may flow/slosh/impact on the deck. The vessel type, its operational conditions and the incident-wave features are the major parameters of the problem, affecting the occurrence, severity and behavior of the shipped water. Green-water loads may be characterized by high localized peaks, as well as by a more persisting and global behavior. They represent a danger for safety, operations and comfort.

The present research activity focuses on Floating Production Storage and Offloading (FPSO) ships used as oil platforms in several parts of the world and is motivated by the large amount of severe accidents recorded in the years. The FPSOs' popularity is due to their suitability to operate practically at any water depth. FPSOs are moored most of the time and weather-vaning, it means that head sea waves are the most critical condition for water-shipping occurrence. The stability is not a problem, while the impact events connected with water-on-deck can be responsible for relevant damages of superstructures in the bow area. A numerical solver is under development to deal with general water shipping conditions and to provide reliable predictions of the green-water loads in a feasible time. Consistently with typical operational conditions for FPSOs, it examines head incident waves interacting with the vessel at zero forward speed. The mooring lines are not modelled, their effect on the water shipping occurrence and features should be addressed and this investigation is left for a future work. The method is based on a Domain-Decomposition (DD) strategy using two solvers: a linear (weakly nonlinear) potential-flow solver is applied in time domain to simulate the wave-vessel interactions on a global spatial scale, a Navier-Stokes free-surface flow solver is used in an inner sea-ship region to handle the nonlinear wave-vessel interactions and possible occurrence of water-on-deck phenomena.

Preliminary results of the compound solver have been published in Colicchio *et al.* (2010). Here the DD algorithm and the aspects of the solvers relevant within the coupling strategy are briefly outlined. Then the features and novelties of the inner solver are described more in detail, because they are critical in the prediction of the green-water loads. Finally the DD method is applied in its weak-coupling version to the case of water shipping caused by head regular waves on a patrol ship at rest, for which experiments have been previously carried out.

Domain-Decomposition strategy The motivation for using a DD strategy is the need of a compromise between capability, accuracy and efficiency when dealing with three-dimensional unsteady nonlinear free-surface flow problems involving violent wave-vessel interactions. The steps forward made by the CFD community for marine applications are profound and continuous along the years. However, up to now a method able to solve accurately any problem of practical interest and in a reasonable time is not available. The computational costs are progressively reducing due to the increasing computer power but are still a limiting factor. Another more important challenge is represented by the assessment of CFD solvers in terms of physical correctness, quantifiable errors and convergence, *i.e.* in terms of reliability. The second issue is affected by the first one, because for complicated unsteady problems the computational costs and memory-space requirements may represent an important limitation to properly ensure con-

vergence properties and reliable predictions with known accuracy error. A DD strategy can help in reducing the CPU-time and memory-space requirements and allow a better assessment of involved solvers. This is critical when long-time simulations are required, for example when performing statistical investigations of rare phenomena like the water on deck. In the marine field, the DD core is to split problem in space and/or time. The resulting sub-problems must be solved each by the best method and exchange information (in space and/or in time) in a coupled manner to recover the solution of the original problem.

In the present case, the problem of interest is the water-on-deck caused by head sea waves on a rigid vessel at rest. Surface tension, turbulence and air effects are neglected. Within the DD strategy the splitting is performed in space: a potential-flow solver (A), based on a Boundary-Element-Method (BEM), is used to describe the wave-body interactions from a global perspective, *i.e.* in an outer domain where large-scale breaking-wave phenomena do not occur and viscous and rotational effects are negligible. As further approximation, nonlinear effects are neglected and a first-order solution is considered, with possibility of including nonlinearities connected with the seakeeping problem within a perturbation approach in a later stage. The incident waves can be described as linear or second-order disturbances. More information on the used method can be found for instance in Greco *et al.* (2009). With this approximation, the hydrodynamic coefficients and linear excitation loads can be found in frequency domain but implemented in the rigid-motion equation system solved in time domain. This involves the estimation of the retardation matrix and the evaluation in time of convolution integrals. The latters become time consuming in the case of long-time simulations, but simplifications exist to limit the costs and allow reliable results (see *i.e.* the overview in Taghipour *et al.* 2008). These will be examined in the future as further improvement in efficiency of the solver.

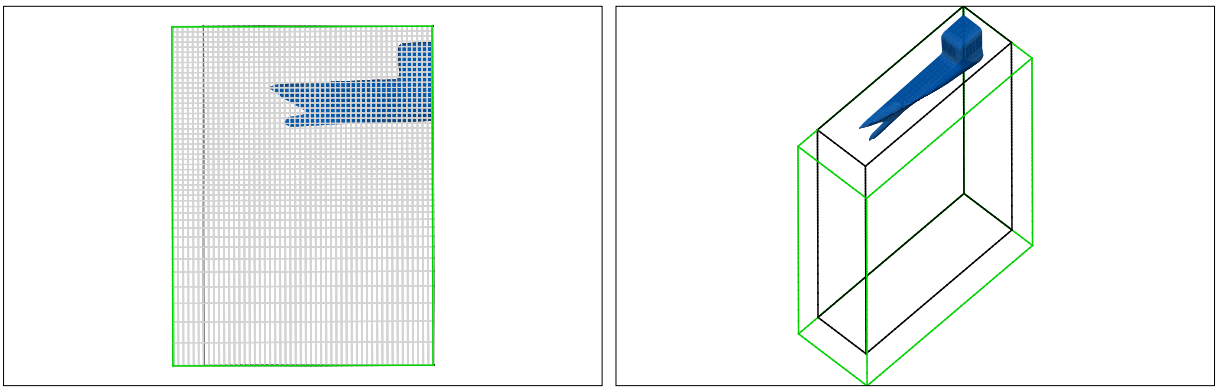

Figure 1: DD strategy: 2D (left) and 3D (right) view of the inner domain. An overlapping is used at the upstream and side boundaries, wide six times the grid size.

A Navier-Stokes (NS) method (B) for single-phase (water) problems and handling fully nonlinear free-surface flows interacting with generic moving bodies, is adopted in an inner sea region containing the forward portion of the vessel. The deck must always be inside such zone during the examined evolution. The solver is a projection method combining a finite-difference approach with additional techniques to handle the deformable and rigid moving interfaces. The basic solver is the one developed by Colicchio (2004). A sketch of the inner domain and its input data within the DD strategy is given figure 1.

Solver A provides solver B the initial and boundary conditions in terms of velocity, pressure, free-surface location and motion of the ship portion inside the inner region. Solver B handles the wave-ship interactions and water-shipping occurrence in the inner sub-domain and makes available to solver A the wave induced loads acting on the part of the vessel in its domain. They include radiation and excitation loads acting on the hull and green-water loads induced

on the deck and deck superstructures, and are estimated as fully nonlinear. Within solver A, the motion equations must be solved in time domain due to the nonlinear loads coming from the inner domain. The exchange of information described here corresponds to a strong coupling, *i.e.* solvers A and B affect each other. A weak-coupling strategy is obtained when the information travels only in one way, *i.e.* only from solver A to solver B. It implies that solution A can be pre-determined and used as input to solver B for the whole time simulation and that the effects of the nonlinear body loads estimated in the inner domain on the rigid body motions can be roughly estimated within a post-processing. The strong coupling can be performed through an iterative or an intrinsic algorithm. The former means that the two sub-problems are solved independently during any time interval and a convergence criterion is identified to ensure consistency of their solutions through iterations at the end of each time-step integration. The latter means that the two sub-problems are solved as coupled at any time step and this provides automatically the upgraded solution in time. Following Colicchio *et al.* (2006), the intrinsic approach has been chosen here, which means that the inner-domain solution and the rigid-body motions are found together in time. A simplification here is that the exchange of information involves integrated load quantities in the direction from solver B to solver A, that is the water flow evolution is not modified by the coupling. At any time instant, the ship motions are estimated and given to solver B for its time integration, the inner loads are integrated after a time interval along the wetted surface and introduced in the motion equations to predict the vessel configuration at the next time step. The schemes used by the two solvers for the time integration are accurate to the second order. The DD efficiency depends on the extension of the inner domain, the smaller the faster the solution, but it must be sufficiently large to recover the relevant nonlinear effects connected with the wave-ship interactions. The DD reliability in estimating the water-on-deck events and their consequences depends both on the capability of the linear potential-flow solver to handle the global seakeeping problem and greatly on the ability of the field method in reproducing violent water-vessel interactions and predict the water on deck occurrence and features. The adopted NS solver in its basic formulation has been comprehensively verified and validated for problems relevant for our application. One must assess the solver novelties developed within this research activity, and the numerical recopies implemented to provide the local information from solver A to solver B and to estimate the nonlinear loads that solver B must make available to solver A. These aspects are discussed next and then the solver is applied to the water-on-deck problem in its weak-coupling version.

Navier-Stokes solver and its implementation within the DD strategy Within our DD algorithm, the inner domain is bounded by the wetted surface of a rigid body whose motion is known at any time instant, a free surface region and an enclosing control surface chosen box shaped. To limit the computational costs, the symmetry of the problem in head sea waves about the longitudinal ship axis is explicitly enforced and only half of the domain is examined. The adopted approximate projection scheme combines a finite-difference spatial algorithm and a predictor-corrector time scheme, both accurate to the second order. At this stage an incompressible method is applied, but a pseudo-compressible version is under development to avoid the limitations connected with the solution of the Poisson equation for the pressure. The governing equations are solved on a Cartesian grid and the evolution of rigid and deformable interfaces is handled by means of suitable techniques. The basic method is the Eulerian Level-Set (LS) with the use of the signed distances from the free and vessel surfaces, respectively, to estimate the deformation and motion of the former and to enforce the boundary conditions on both boundaries. For the free surface: since the air is neglected, a robust way to enforce the kinematic and dynamic conditions is obtained by extending locally the liquid solution across the interface for one cell of the grid. For the body: in the case of vessel geometries with high

curvatures and/or sharp corners, the smoothing connected with the use of a LS function may lead to large errors. This problem is solved through a hybrid approach combining the Eulerian LS technique with a Lagrangian method, similarly as done by Enright *et al.* (2002). At the initial time the LS function of the vessel, say LS_B, is initialized on an uniform grid, say $g1$, four times finer than the minimum size (dx_{min}) of the computational grid, say $g0$. To limit the additional costs, $g1$ is defined across the initial body surface along a layer six times thicker than the largest size in $g0$. During the simulation, the cell centers of $g1$ become Lagrangian markers moving rigidly with the body and so keeping their LS value in time. The LS on the cell centers of $g0$ can therefore be obtained by interpolation from the body particles. This approach has great potentialities when complex vessel shapes and violent wave-body interactions are involved.

In the applications of interest the outflow condition is applied at the downstream portion of the control surface, while the linear-seakeeping solution from the outer method is enforced upstream, on the side and on the bottom parts. The upstream and side boundaries are crossed by the free-surface which represents a source of instabilities when a linear solution is enforced to a fully nonlinear method, due to their inconsistencies. A strategy able to overcome this problem introduces an overlapping from the upstream and side boundaries inward (see sketch in figure 1 and description reported in Colicchio *et al.* 2006). There, the linear pressure is directly enforced to avoid oscillations from the NS solution, while a linear interpolation forces the velocity to go smoothly from the linear to the fully nonlinear NS value. This strategy has proved to be successful in avoiding stability problems. In our applications an overlapping thickness six times the maximum cell size of the grid was found sufficient to provide robust solutions. The bottom control surface is not crossed by the free-surface so the overlapping is unnecessary and the linear solution is enforced sharply at the boundary. Care must be taken to avoid reflections from the control surfaces when radiation and/or scattering are relevant and resulting nonlinear waves generated by the body in the inner domain reach the boundaries.

The estimation of the loads (force and moments) induced on the moving vessel by its interaction with the surrounding and shipped water is challenging on a solver using an Eulerian grid. Here the loads are estimated for the vessel portion remaining always inside the inner domain during the simulation, say S_{in}, in the remaining part of the vessel forces and moments are obtained directly by the outer seakeeping solver, within its assumptions. The loads on S_{in} are obtained as weighted extrapolation of the loads on three LS_B iso-surfaces inside the fluid domain and at 0.5, 1 and 1.5 dx_{min} from S_{in}. For each of these surfaces the loads are approximated as weighed volume integrals surface with weight a Gaussian approximation of a Dirac's delta function centered at the surface and zero at a distance $\pm 1.5 dx_{min}$ from it.

The different solver features described here have been individually verified: a prescribed pitch motion was used to assess the hybrid technique for the body-boundary conditions, a pure-wave propagation not aligned to the grid axes was used to check the solver robustness and reliability when a linear-wave solution and outflow conditions are enforced at the vertical boundaries, a half-sphere with known pressure was used to verify the integration algorithm against the analytical load solution.

Validation study: water-on-deck on a patrol ship 3D water-on-deck experiments on a patrol ship have been performed by Greco *et al.* (2009) in scale 1:20. Figure 2 gives a global view of the set-up. The model was without and with forward motion and free to move in heave and pitch under the action of regular and irregular incident waves, while the remaining motions were restrained. The shipped water was partially limited on the deck by a 5cm bulwark extending for 1.02m from the front bow and by a vertical superstructure 30cm downstream of the end of the deck protection.

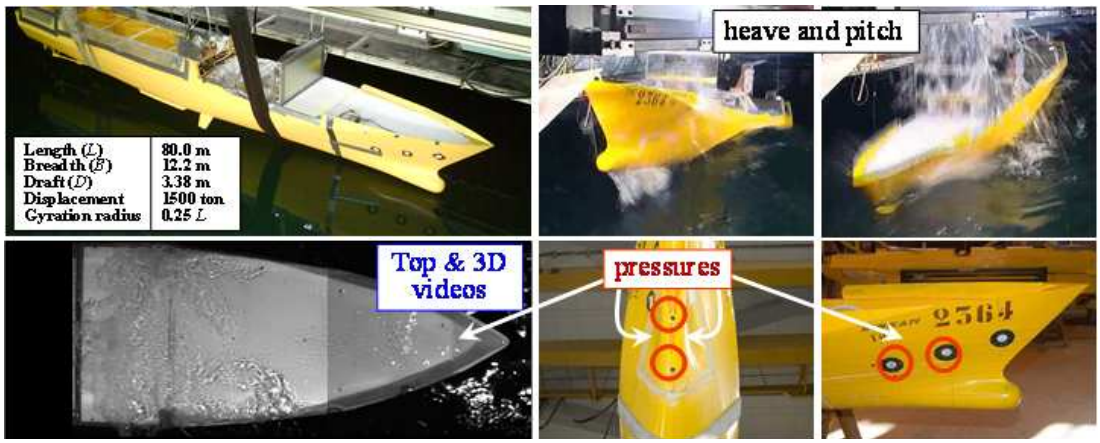

Figure 2: Set-up of the 3D water on deck experiments on a patrol-ship model in scale 1:20.

During the tests, both global and local measurements were performed: ship motions, 3D and top-view video recording of the tests, superstructure horizontal force, relative water-vessel vertical motion,wave elevation, bottom-hull, side-hull and deck pressures.

Here the model at rest in regular sea is examined. The chosen incident waves, with $\lambda/L = 1.26$ and $kA = 0.22$, are in the resonance region and caused large heave and pitch motions and the most severe water-on-deck recorded at zero forward speed. Figure 3 examines the wave-ship interaction as recorded experimentally through a 3D video and numerically. The shown snapshots refer to the main stages of the evolution during an incident-wave period: the relative wave-vessel motions are sufficiently large to cause a water-exit of the vessel, this is followed by a bottom impact with the sea surface and a water-entry phase (first plot). Later the ship bow enters the sea and the surrounding water exceeds the freeboard (second plot), the liquid invades the deck and develops toward the superstructure (third plot). Then the ship starts to exit the sea again causing the end of the water-on-deck (fourth plot) and leading to the water-off-deck phase of the shipped liquid (fifth plot). The numerical results are obtained through a weak-coupling DD strategy and involve an initial ramp function for $0.25T$, with T the incident-wave period. The comparison is globally promising and the numerics shows a physical behavior of the ship pressure in time. However differences can be noticed in terms of amount and features of the shipped water. These are partially due to the discretization used, *i.e.* with average size $\Delta x = 0.012L$ (L is the ship length).

This is too coarse to model the bulwark present on the physical model therefore the partial water reflection from the deck protection is not handled in the simulation. As a result the plunging phase occurring at the beginning of the water-on-deck is very limited in the numerical case. In the physical case the water-deck impact caused by the plunging is responsible for an increase of the water-front velocity toward the superstructure. The numerical results show instead a slower motion of the liquid. Another consequence of the bulwark lack in the numerical discretization is a quicker water-off-deck with respect to the experiments. The bottom-right plot of figure 3 examines the influence of the ramp function: some effects are still visible after four wave periods. They are localized in the ship-bow region and reduce elsewhere. The next steps of the research activity are: 1) to fully check the numerical convergence and 2) to introduce the strong-coupled DD strategy and verify its robustness and reliability. Numerical features of the developed DD strategy will be discussed at the conferences. Among the others, we mention: the use or less of an initial ramp function to implement the linear input data into the fully-nonlinear NS solver; the recovery of the linear solution by the DD strategy when linear seakeeping conditions are examined; the stability and convergence of the compound solver.

The present research activity is supported by the Centre for Ships and Ocean Structures (Ce-

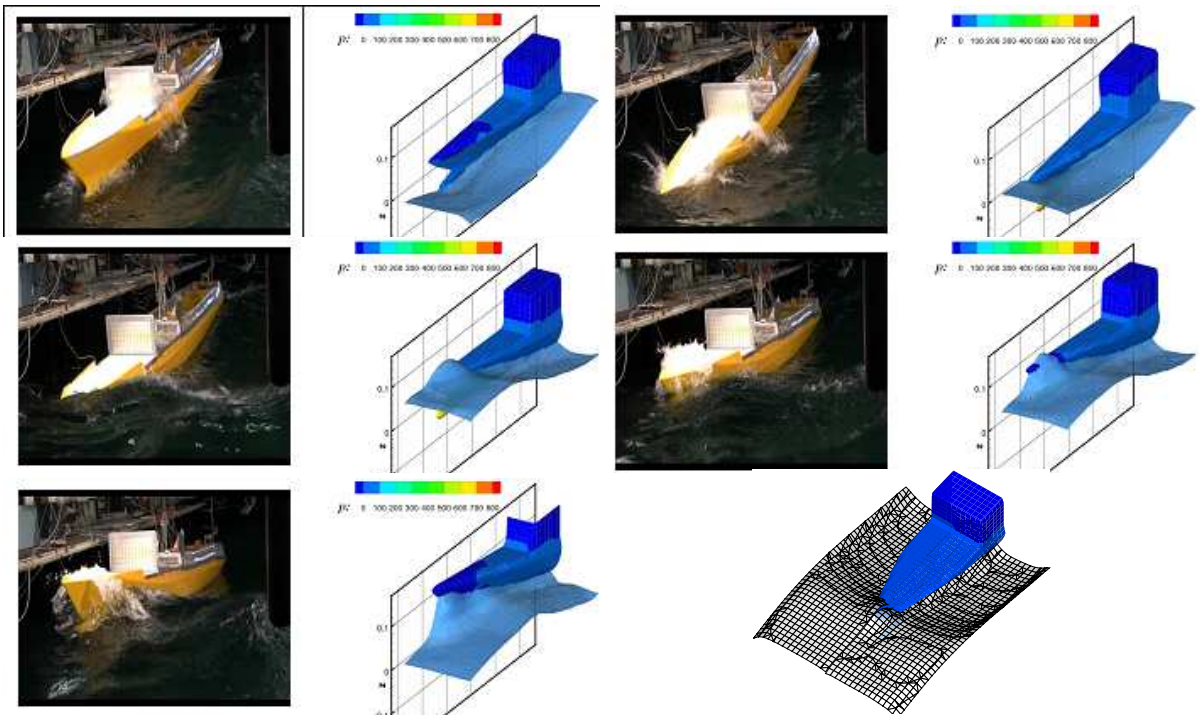

Figure 3: Water on deck caused by regular waves with $\lambda/L = 1.26$ and $kA = 0.22$ on the patrol-ship model at rest. Time increases from left to right and from top to bottom. Experimental (left) and numerical (right) flow evolution. The simulations provide both the free surface evolution and the pressure induced on the vessel. The simulations are performed with a ramp function of $0.25T$, T being the incident-wave period, and refer to $t > 4T$. Bottom-right plot: numerical solution with (left) and without (right) the ramp function at a time instant soon after the beginning of the water shipping.

SOS), NTNU, Trondheim, within the 'Violent Water-Vessel Interactions and Related Structural Loads' project.

References

Colicchio, G. (2004). *Violent disturbance and fragmentation of free surfaces*. Ph. D. thesis, School of Civil Engineering and the Environment, University of Southampton, Southampton.

Colicchio, G., M. Greco, and O. M. Faltinsen (2006). A BEM-Level Set Domain Decomposition Strategy for Nonlinear and Fragmented Interfacial Flows. *J. for Numerical Methods in Engineering*.

Colicchio, G., M. Greco, C. Lugni, and O. M. Faltinsen (2010). A 3D Navier-Stokes solver to investigate Water-On-Deck events within a Domain-Decomposition strategy. In *Proc. of* 25^{th} *Int. Workshop of Water Waves and Floating Bodies*, Harbin, China.

Enright, D., R. Fedkiw, J. Ferziger, and I. Michell (2002). A hybrid particle level-set method for improved interface capturing. *J. of Computational Physics 183*, 83–116.

Greco, M., B. Bouscasse, G. Colicchio, and C. Lugni (2009). Weakly-nonlinear seakeeping model: regular/irregular wave interaction with a ship without/with forward speed. In *Proc. of* 24^{th} *Int. Workshop of Water Waves and Floating Bodies*, Zelenogorsk, Russia.

Taghipour, R., T. Perez, and T. Moan (2008). Hybrid frequencytime domain models for dynamic response analysis of marine structrues. *Ocean Engineering*.

Using Automated Optimization Routines for Designing High Efficiency Nozzle Profiles.

Tobias Huuva and Magnus Pettersson, Berg Propulsion Technology AB
tobias.huuva@bergpropulsion.com

Introduction

Nozzles is today used in many different ships and vessels to increase thrust at low operational speed, e.g. in towing operations. Most vessels is using standard nozzle designs originating from the early 1930:s [1]. With the help of modern computational tools a number of new nozzle designs have been presented by various manufacturers, clamming highly improved efficiency as compared to the standard nozzles, especially as compared to the so called 19A nozzle. The 19A nozzle is the most commonly used profile in most vessels and it is suited for a large variety of applications.
Since the profile was developed for over 70 years ago and the fact that it is suited for several different applications are there possibilities to improve the profile, however it is not believed that the improvements are as great as has been reported for other designed profiles. To investigate how much efficiency can be gained by changing the profile and to investigate the influence of different parts of the nozzle an optimization study has been performed. Using the results from the investigation two different profiles has been designed based on the results from the optimization, manufacturing principles and on experience on nozzle propellers.
Two methods for automated CFD-simulations were developed, one using a 2D axisymmetric simulation model, with a simplistic model of the propeller, and one with 3D geometry model including the propeller geometry. The simulation methods use design of experiments, optimization algorithms and statistical methods to evaluate the effect of geometrical changes to the efficiency of the propeller and nozzle.
By comparing 2D and 3D results was it concluded that 3D models are necessary to give realistic trends.The optimizing of the performance of the nozzle-propeller system results in two nozzle designs, one for free run and one for bollard pull conditions. The nozzle geometries were compared with results from the 19A nozzle. For free running conditions the most important features of the profile is to keep the profile rather thin not to induce too much drag. The geometry at the diffuser part of the nozzle is very important. For bollard pull conditions, optimization of the nozzle profile leads to a nozzle of large outer diameter.

The automated 2D axis-symmetric model the propeller was simply defined as a line source with a pressure increase corresponding to a constant power on the propeller. The resulting geometries of the nozzles showed significant improvement of thrust compared to the reference modified 19A nozzle. These improvements were well in line with claims from other investigations showing over 10% improvement both in bollard pull and in free running. To verify the results a full 3D investigation was performed to investigate if any 3D effects have been lost in the 2D representation. In this very careful investigation it was found that the 2D model could not predict the separation point in the diffuser part because of the representation of the propeller through the line source. In the 3D model the actual blade is represented and the rotation is represented by multiple reference frame (MRF). To overcome this difficulty a new optimization loop was performed using the full 3D model instead of only a simplified 2D model. After some initial modification of the setup a large number of profiles was investigated using the automated optimization process. This investigation gave valuable information on important parameters in nozzle design and information about limits in the possibility to design nozzle profiles with much higher efficiency as compared to the 19A profile.

Geometric Representation

The system under study is the nozzle and propeller geometry, as seen in Figure 1. The flow conditions far from the propeller-nozzle system were assumed to be rotationally invariant, i.e. the influence of the ship hull and the surface was neglected. The propeller chosen for the simulations has a diameter of 2.65 m and the geometry was parameterized by morphing boxes in ANSA and the same parameterization was used for both the 2D model and the 3D model. The modification of the geometry is done by moving control points for the splines corresponding to rotation, scaling and translation operations of the splines, representing the nozzle profile.

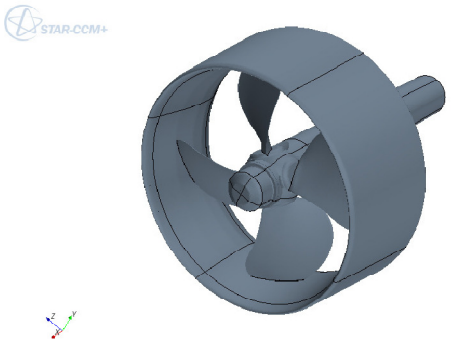

Figure 1. System under study, nozzle with propeller and shaftline.

Computational model

The material properties for the simulations are those for incompressible water at atmospheric pressure. Aspects of cavitation have not been accounted for. Turbulence is modeled by a high y+ SST model. Two fully automated CFD-simulations methods were developed and the first one was an axisymmetric 2D model with the propeller modeled as a fan surface producing a pressure increase as a function of the flow velocity. The method uses morphing techniques in the software ANSA for the 2D mesh and it uses FLUENT for the preprocessing, solving and postprocesing of the CFD model. Shell scripts were implemented to drive the CFD method in batch. The optimisation software modeFrontier was used to monitor the simulations and couple the geometry to algorithm for DOE, optimization and statistical post processing. As validation for the 2D model, 3D simulations of 19A nozzle and the nozzles resulting from the optimization simulations were performed. For validation simulations manual 3D CFD-techniques using the softwares ANSA and FLUENT was used. The 3D fully automated method was implemented by using the same morphing technology in ANSA as for the 2D model. The meshing, preprocessing, solving and post-processing was implemented in star-CCM. Shell scripts were implemented to drive the CFD-process in batch. The automated process was driven from within modeFrontier using Latin Hyper Cube DOEs and MOGA-II genetic algorithms to create the input parameters controlling the geometry of the nozzle.

Computational domain

For the 2D simulations the computational domain consisted of a bounding cylinder of 13.5 m in radius and 41 m in length. For the 3D simulations the bounding domain was smaller. The periodicity in geometry, i.e. four blades, was used to reduce the computational domain in the tangential direction. For the 3D free running nozzle optimization the computational domain was a quarter of a cylinder, with a 6 meter radius, extruded 3 m in front of the nozzle and 13 m behind the nozzle, as depicted in Figure 2.

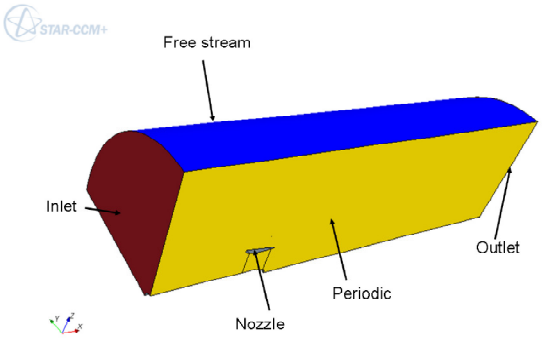

Figure 2. Domain used for the free-running condition.

It was found that using the same computational domain for the Bollard pull simulations resulted in divergences. The cause of the divergence was that the flow through the nozzle was mainly sucked from the outlet, producing *short circuit* between the turbulent nozzle jet and the nozzle inlet. The computational domain for the Bollard pull simulations was instead reconstructed as a quarter of a sphere, seen in Figure 3. The visualization of streamlines shows that a significant large portion of the flow through the propeller comes from the radial direction of the propeller. If the computational domain is to be cylindrical, very large computational domain is needed.

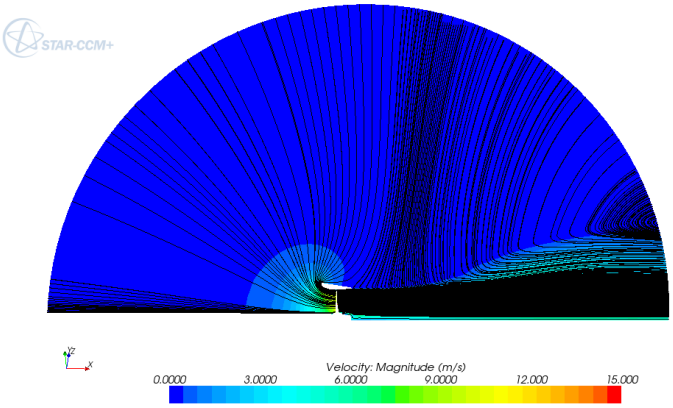

Figure 3. Domain used in the bollard pull condition.

Based on the conclusion from the 2D simulations an automated CFD-method that includes the propeller geometry was developed and used. The objective was to maximize the thrust on the propeller and nozzle while minimizing the power on the propeller. It was found that the total values of the three mentioned optimization parameters could be widely different when changing nozzle geometry. However by varying the rotation speed of the propeller it was concluded that a reasonable parameter to optimize is the total thrust/torque, where the total thrust is evaluated over both the propeller and nozzle and the torque is evaluated over the propeller at constant angular velocity. It was found that although changing the loads between the propeller and nozzle the efficiency or thrust/torque was more difficult to improve. For the 3D simulations two optimization loops were simulated, one for Bollard pull and one for Free running.

Mesh

For the 2D optimization studies the mesh consists of 10 boundary layers close to the nozzle. The mesh outside the boundary layer consists of mainly quadratic cells except in the vicinity of the nozzle were triangular cells were used. The mesh consist of about 70 000 cells. In 3D the mesh consist of a hexahedral trim mesh with 8 prism layers, which results in a y+ on the nozzle between 30 and 200. The mesh consisted of about 1.7 million volume cells for the free running cases and about 2.5 million for the Bollard pull simulations. The surface mesh size was about 5 cm. Figure 4 shows the surface mesh for the 19A profile and Figure 5 shows the volume mesh at a cross section through the propeller. Refinement boxes were used to increase the resolution in the wake of the nozzle and propeller.

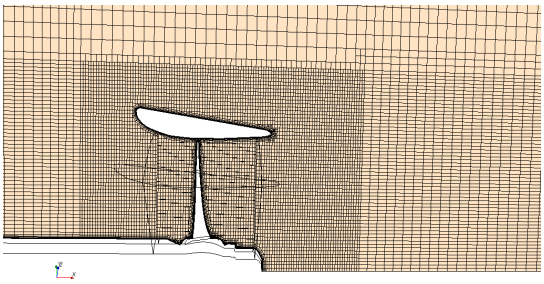

Figure 4. Cross-section of the mesh.

Boundary condition

For free running the boundary conditions used are velocity inlet using 6.3 m/s, i.e. 12.3 knots, which corresponds to about 14 knots ship speed. The outlet is treated as a static pressure outlet, the walls are treated as no slip and the blades are treated as stationary no slip inside a multiple frame of reference domain, which is rotating with 213 rpm. The boundary conditions for the bollard pull simulations were similar except for the inlet and outlet boundaries, which were substituted with a static pressure outlet/total pressure inlet at the bounding spherical surface.

Optimization

The algorithm used are Latin hypercube (LHC) for design of experiment (DOE) and genetic optimization algorithms (MOGA-II) to control changes of a parameterized geometry of the nozzle. The nozzle geometry is then analyzed using the automated CFD techniques, which handle meshing, solving and post processing of the results. The CFD results are then used as input for the optimization algorithm. In order to understand the response of the geometrical shape in the thrust, data from the simulations were also investigated using statistical tools, i.e. correlations, student t-test, scatter plots, parallel coordinate diagrams and analysis of meta-models such as polynomial fits and radial basis functions. For the 2D model the fan surface modeling the propeller was designed to give a certain power independent of the nozzle geometry. The total thrust evaluated over both the nozzle and the propeller was used as optimization parameter. For the 3D optimization method it was found that the main effect of increasing the thrust on the nozzle and propeller was to increase the momentum on the propeller. By changing the rotational speed in the simulations it was found that the force/momentum was reasonably constant. It was concluded that thrust/momentum could be used as the optimization variable to maximize.

The first optimization in 2D was performed varying all input parameters and the force on the nozzle and the propeller was calculated. Using these profiles gives a much higher efficiency as compared to the reference nozzle 19A. However when the nozzles was investigated in 3D it was found that the total thrust from the optimized nozzles was actually less as compared with the 19A nozzle due to heavy separation in the diffuser part.

Instead a fully automated CFD-simulation for 3D geometries was performed in three steps to limit the degrees of freedom. The first step was to investigate the thrust response for outer radius geometric parameters. The second step was performed optimizing efficiency, which for constant rotational speed for the propeller is proportional to thrust/torque, for free running using all parameters. The third step was performed by optimizing efficiency for bollard pull. This was performed using a design of experience (DOE) using the Latin hyper cube algorithm and analyzing the result using the statistical tools of correlation coefficients, student t-test, parallel coordinates, meta models by first and second order polynomials and radial basis functions. For the Free running optimization loop the leading edge and trailing edge length parameters were locked to the length of the 19A nozzle. The optimization was performed by using an initial LHC DOE using 26 geometries and then 11 subsequent generations of MOGA-II, resulting in a total of about 300 simulated geometries. The resulting geometry is seen in Figure 5. There is strong resemblance to the 19A profile, however there is tendency to a form a dolphin tale. The profile is also thin, which is due to the need of minimizing the drag component of force on the nozzle.

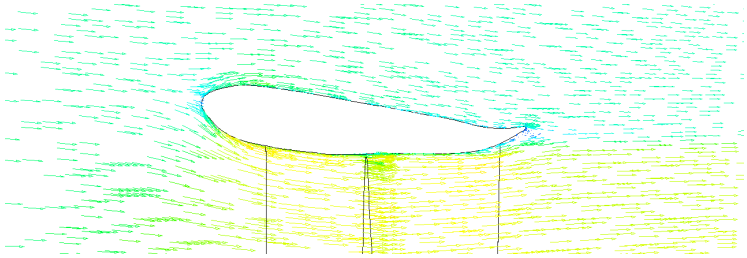

Figure 5. Free running profile after finalized DOE.

For the bollard pull optimization loop the leading edge and trailing edge length parameters were released with some limits. The optimization was performed by using an initial LHC DOE using 26 geometries and then 7 subsequent generations of MOGA-II, resulting in a total of about 200 simulated geometries. The profile of the resulting nozzle geometry is shown in Figure 6. There is strong resemblance to the 19A profile, however there is the outer diameter of the profile increases and there is no dolphin tale tendency.

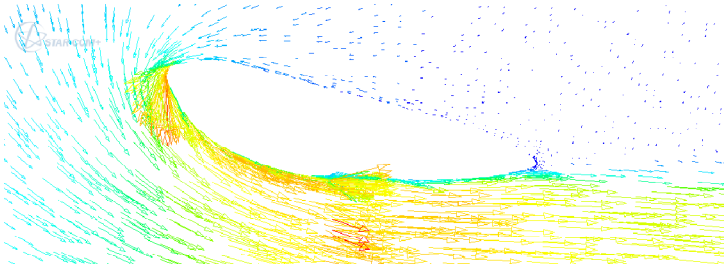

Figure 6. Bollard pull profile after finalized DOE.

For both profiles the cylindrical section, where the propeller blade is passing, has been extended and the diffuser part is initiated further aft. The reason for this is that the propeller slipstream is disturbing the flow and if the diffuser starts directly there is a greater risk of separation in the diffuser which will limit the performance of the nozzle significantly. The optimized profiles, together with knowledge learnt from the computations, can now be used to produce a number of profiles with high efficiency together with good producability. By analyzing the optimized profiles a high resemblance with the 19A is found, with some small distinctions. The high speed nozzle has a smaller frontal area, has a dolphin tale and has a longer cylindrical section as compared to the 19A profile. The bollard pull nozzle has a larger outer diameter, a longer sectional length and a longer cylindrical area as compared to the 19A nozzle. As many conical and cylindrical parts as possible is used design the nozzle since these are much easier to produce as compared to a general double bended surface. From the

optimization it is found that small changes in the detailed shape of the nozzle profile, i.e. going from a slightly double bended surface to a conical surface, has no or very little influence on the performance of the nozzle. The final nozzle profiles can be seen in figure 7.

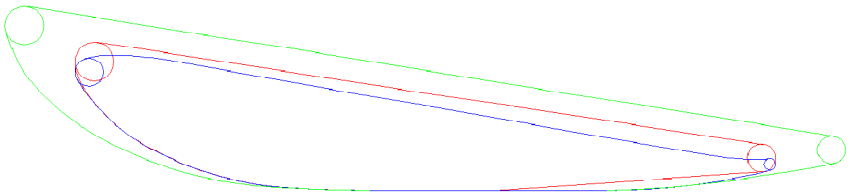

Figure 7. Final nozzle design, green bollard pull nozzle, blue high speed nozzle and red 19A nozzle

Conclusion

The work with automated CFD-simulations of nozzles and propellers has resulted in important understanding for new designs of nozzles optimized for free running and bollard pull conditions. The work of optimizing the performance of the nozzle-propeller system results in two designs of nozzles, one for free run and one for bollard pull conditions. The nozzle optimized for free run conditions improves the nozzle-propeller system by 2% in free run conditions and 2% in bollard pull conditions and the nozzle optimized for bollard pull conditions improves the thrust/torque with 5% in bollard pull and decreases performance with 1% during free run condition as compared with the 19A nozzle. It is concluded that without changing the propeller geometry the 19A nozzle has very good performance and the improvement of nozzle design is of the order of some percentage. For free running conditions the most important features of the profile is to keep the profile rather thin not to induce too much drag and the geometry at the diffuser part of the nozzle is very important.

In order to get realistic resulting trends from CFD-simulations it is important to include the 3D propeller geometry. This was concluded from using both a fully automated 2D axisymmetric simulation model and a 3D simulation model including propeller geometry. For simulations of bollard pull conditions it is effective to use a quarter of a sphere as boundary for the computational domain.

Acknowledgment

The authors would like to acknowledge Robert Moestam at FSDynamics for building the optimization routine and performing the computations.

References

[1] Charlton J. **2007**, *Marine Propellers and Propulsion*, Oxford : Butterworth-Heinemann.

Development of hybrid URANS-LES methods for flow simulation in the ship stern area

N. Kornev*, A. Taranov, E. Shchukin and L. Kleinsorge †
Chair of Modelling and Simulation, University of Rostock, 18057 Rostock, Germany

INTRODUCTION. Determination of the velocity field in the ship wake is one of the important problems of ship hydromechanics. Numerical simulation of the wake has attracted the attention of CFD experts for a long time. A substantial success has been achieved in this field in the last two decades. The averaged velocity field is predicted today with a high accuracy. Discrepancy between numerics and measurement is comparable with the rate of experimental data scattering. To get overview of the state of the art in this area, the reader is referred to contributions presented annually during the Gothenburg workshops [1]. An important feature of works done so far is the application of URANS (Unsteady Reynolds Averaged Navier Stokes) numerical technologies which are capable of capturing steady effects and large scale unsteadiness. Unfortunately, these techniques are not able to reproduce small and moderate flow oscillations due to large diffusivity which is an unavoidable feature of URANS closure models. These oscillations are caused by complicated vortex structures arisen due to flow separations on the hull and shedding of the boundary layer in the stern area. The time averaged vortex structure is well reproduced in URANS calculations what is confirmed by a good agreement between numerical simulations and measurement for mean velocities. Also, the time averaged fluctuation parameters like Reynolds stresses and the turbulent kinetic energy are predicted relatively well using advanced turbulent models such as the Reynolds stress models [2]. Therefore, the variances of fluctuations can be predicted properly but not the amplitudes and their spatial and temporal distributions. It can be a critical point for propeller design since flow, cavitation and thrust depend on the instantaneous spatial distributions of velocity in the incident flow. In present practical design methods the unsteady effects are partly taken into account. The velocity vector $\mathbf{U}$ at any point $\mathbf{x}$ on the propeller blade depends on the angular position of the blade ϑ which is the function of time, i.e. $\mathbf{U} = \mathbf{U}(\mathbf{x}, \vartheta(t))$. The time t is considered as the parameter. Unsteadiness of the propeller flow is purely due to rotation of the propeller blade through the non uniform time independent ("frozen") wake. The fact, that the incident flow can itself vary in time, with the other words, the fact, that the function $\mathbf{U}$ depends explicitly on time $\mathbf{U} = \mathbf{U}(\mathbf{x}, \vartheta(t), t)$ is usually neglected. This neglect can be considered as quite acceptable for ships with small and moderate block coefficients since the physical phenomena causing flow oscillations are not pronounced for such ships. However, the case of full-bottomed ships should be reconsidered. Because of disadvantages of URANS modeling mentioned above the most promising technology for these purposes is Large Eddy Simulation (LES) which is already widely used for engineering applications. Unfortunately, there exists a big difficulty which sufficiently restricts the LES application in ship hydromechanics. On the contrary to other engineering fields, typical Reynolds numbers in ship hydromechanics are very large even at model scales. The grid resolution necessary for a pure LES is huge what makes direct LES application impossible. A compromise solution is the application of hybrid URANS-LES methods with treatment of the near body flow region using URANS and LES simulation of far flow regions.

NUMERICAL METHOD. The hybrid method used in the present paper is based on the

* nikolai.kornev@uni-rostock.de † Chair of Shipbuilding, University of Rostock, 18057 Rostock, Germany

observation that the basic transport equation used in LES and RANS has the same form

$$\frac{\partial \overline{U}_i}{\partial t} + \frac{\partial (\overline{U}_i \overline{U}_j)}{\partial x_j} = -\frac{1}{\varrho}\frac{\partial \overline{p}^*}{\partial x_i} + \frac{\partial}{\partial x_j}\left[\overline{\tau_{ij}^l} + \overline{\tau_{ij}^t}\right]. \tag{1}$$

Here U_i are velocity components, ϱ is density, p^* is the pseudo pressure, x_i are coordinates, t is time and $\overline{\tau_{ij}^l}$ and $\overline{\tau_{ij}^t}$ are laminar and turbulent stresses respectively. The overline means the filtering in LES and Reynolds or ensemble averaging in URANS. Also the turbulent stresses are calculated in different ways in LES and URANS regions. The hybrid LES-URANS method presented here is a non-zonal approach which can be defined as the natural one. Switching between URANS and LES is performed depending on the ratio between the integral length scale L and the extended LES filter Δ. If the turbulent scale length L is larger than the extended filter Δ then the cell belongs to the LES region and vice versa:

$$\begin{cases} L > \Delta \rightarrow \quad LES \\ L < \Delta \rightarrow URANS \end{cases} \tag{2}$$

The integral length is calculated from the known formula of Kolmogorov and Prandtl with the correction factor 0.168 taken from [3]

$$L = 0.168\frac{k^{3/2}}{\varepsilon}, \tag{3}$$

where k is the turbulent kinetic energy and ε is the dissipation rate. The extended LES filter width Δ is calculated as $\Delta = \sqrt{d_{\max}^2 + \delta^2}$, where $d_{\max}$ is local maximum cell size $d_{\max} = \max(d_x, d_y, d_z)$ and $\delta = (\delta V)^{1/3}$ is the common filter width used in LES, where δV is the cell volume. This extended filter Δ takes the largest edges of the unstructured grid into account. This choice is especially efficient for very flat cells of the boundary layer.

We performed a series of methodic calculations selecting LES and URANS models with the best performance for the problem under consideration. Among them were linear and nonlinear $k-\varepsilon$, $k-\omega$ SST and $k\varepsilon v^2 f$ URANS models combined with the simple and dynamic Smagorinsky as well as with dynamic mixed LES closure models. The experience shows that the most satisfactory results are obtained using the URANS approach based on the $k\varepsilon v^2 f$ turbulent model of Durbin [4] and LES approach based on the Smagorinsky dynamic model. The turbulent stresses $\overline{\tau_{ij}^t}$ are calculated from the Boussinesq approach using the concept of the turbulent viscosity. The only difference between LES and URANS is the definition of the kinematic viscosity. Within LES the kinematic viscosity is considered as the sub-grid viscosity and calculated in accordance with the dynamic model of Smagorinsky: $\nu_{\mathrm{SGS}} = c_D(S_{ij})\Delta^2|S_{ij}|$, where S_{ij} is the strain velocity tensor $S_{ij} = 0.5(\nabla_i U_j + \nabla_j U_i)$ and c_D is the dynamic constant. In the URANS region the viscosity is calculated from the turbulent model of Durbin [4]: $\nu_t = \min(0.09k^2/\varepsilon, 0.22v^2 T_t)$, where v^2 is wall normal component of the stresses and T_t is the turbulent time $T_t = \max(k/\varepsilon, 6\sqrt{\nu/\varepsilon})$.

Fig. 1 illustrates typical distribution of URANS and LES zones in different ship frame sections. The URANS region is located close to the ship surface playing the role of a dynamic wall function. In areas of bilge vortices formation the boundary layer is shedding from the hull and penetrates into the outer flow part. Since the boundary layer is a fine scale flow the procedure (2) recognizes the bilge vortex formation zones as URANS ones. Far from the ship hull k and ε become small making the calculation of $k^{3/2}/\varepsilon$ quotients difficult. To avoid an irregular distribution of URANS and LES zones, the LES region is switched to URANS one if k is getting less than some threshold. This procedure has no influence on the ship flow parameters since it is used far from the area of primary interest.

This hybrid method has been incorporated in the open-source code OpenFOAM [5] based on the finite volume method. Numerical investigations were carried out on an unstructured 3D-grid containing 1.2×10^6 cells with $y_1^+ \approx 2-6$ in the wall region. This grid generated by

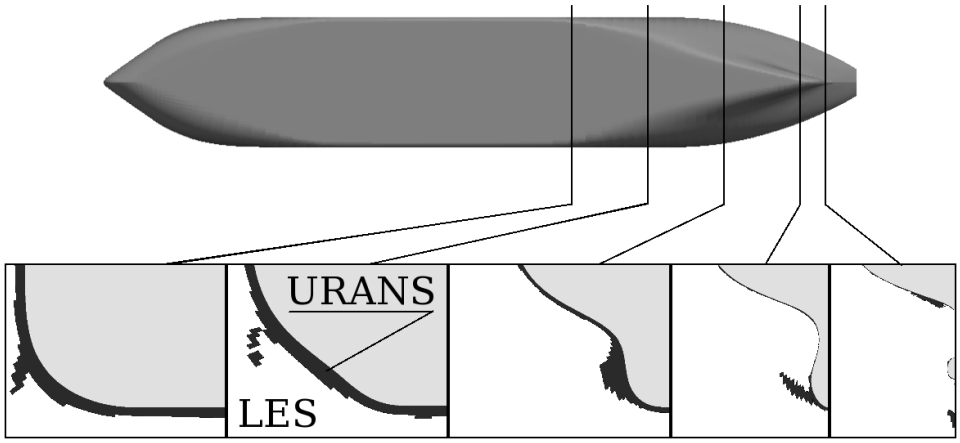

Figure 1: URANS (black) and LES (white) zones around the ship frames. Tanker KVLCC2 at $\mathrm{Re} = 4.6 \times 10^6$ and $\mathrm{Fn} = 0.142$.

the Ship Model Basin Potsdam (SVA Potsdam) proved to be an appropriate grid for RANS calculations. For space discretization, central differencing is used for all terms in the momentum equation whereas the Crank-Nicholson scheme is used for the time discretizations. Steady RANS solutions are used to initialize the flow in the computational domain. After a sufficiently long time period, as soon as the resolved flow attains a statistically steady state (typically it requires the ship way of $3-4$ lengths), the statistical analysis was performed to obtain time-averaged solutions. A typical time period for statistical averaging takes about $40-50$ seconds, which corresponds to $8-10$ lengths of the ship way.

RESULTS. The doubled model of the KRISO tanker KVLCC2 [6, 7] with the scale 1/58 is chosen for investigations since this is a well tried benchmark widely used in the shipbuilding community[1]. The model has length of 5.517 m, breadth of 1 m, draught of 0.359 m and block coefficient of 0.8098. Study of the wake was performed for the constant velocity of 1.047 m/s corresponding to the Reynolds number of 4.6×10^6. The Froude number is small ($\mathrm{Fn} = 0.142$) what makes it possible to neglect the water surface deformation effects.

Estimations of resolutions necessary for pure ship LES. Any exact determination of the necessary LES resolution is quite difficult. Estimations presented below are based on the idea that about eighty percent of the turbulent kinetic energy should be directly resolved and the rest is modelled in a properly resolved LES simulation. Implementation of this idea imply the knowledge of the Kolmogorov η and the integral length L scales which are used to draw the typical spectra of the full developed turbulence $E(k)$. The wave number k^* separating resolved and modelled turbulence is found from the condition $\int_{k^*}^{\infty} E(k)dk / \int_0^{\infty} E(k)dk \sim 0.2$. The maximum possible cell size is then $\Delta_{\max} = 2\pi/k^*$. The ratio $\lambda = \Delta_{\max}/\eta$ is then utilized as the scale parameter for grid generation. The scales L and η are found from known formulae $\eta = (\nu^3/\varepsilon)^{1/4}$ and $L = 0.168k^{3/2}/\varepsilon$ where the kinetic energy k and the dissipation rate ε are taken from RANS simulations using $k-\varepsilon$ linear model. Both lengths are changed in space what makes the grid generation procedure very complicated. To avoid cumbersome work which is not necessary for rough estimation purposes we assumed λ to be constant. We performed different calculations determining λ at two following points: i) point where L/η is maximum in the boundary layer and ii) point in the propeller disk where the vorticity ω is maximum in the region of the concentrated vortex structure. The latter is dictated by the wish to resolve the most important vortex flow structures most influencing the propeller operation. Since LES application is most required in the ship stern area only a part of the flow volume was meshed.

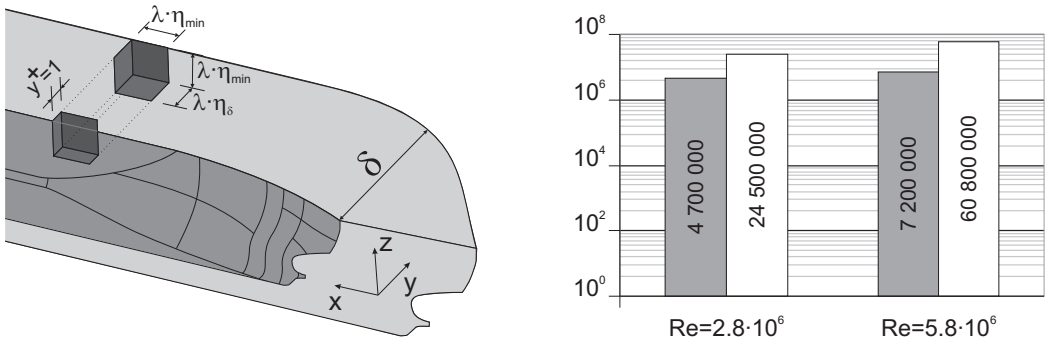

(a) (b)

Figure 2: Estimation of the resolution necessary for a pure LES.

It covers the boundary layer of the stern region starting from the end of the parallel midship section. The thickness of the meshed region was constant and equal to the maximum boundary layer thickness at the stern δ_{BL}. The grid for a pure LES is generated using the following algorithm. The minimum Kolmogorov length $\eta_{\min}$ is determined in the near wall region. The cell sizes in x and z directions along the wall are calculated by multiplication of $\eta_{\min}$ with the scale parameter λ. These sizes remain constant for all cells row in y direction which is normal to the ship surface (see Fig. 2(a)). The cells have at least two equal sizes what is desirable from the point of view of LES accuracy. The choice of the size in y direction is dictated by proper resolution of the boundary layer. Close to the wall this size is chosen from the condition $\Delta_w = \min(y_w, \eta_{\min})$. Since y_w is chosen as the ordinate where $y^+ = 1$ the first knots lay deeply in the viscous sublayer. The size in y direction at the upper border of the boundary layer is equal to $\Delta_\infty = \lambda\eta_\delta$, where η_δ is the Kolmogorov scale at $y = \delta_{BL}$. A simple grading is used in y direction between Δ_w and Δ_∞.

Results of estimations presented in Fig. 2(b) show that the required node numbers are ranging from $\sim$ 5 M to $\sim$ 25 M for $\mathrm{Re} = 2.8 \times 10^6$, and from $\sim$ 7 M to $\sim$ 60 M for $\mathrm{Re} = 5.8 \times 10^6$. The resolution estimations are scattered depending on the definition of λ. Therefore, they can be considered as very rough estimations. These estimations together with similar estimations from the non linear $k - \varepsilon$ model show that the LES grid should have the order of a few tens of millions of nodes. Nowadays the computations with hundred millions and even with a few billions of nodes are becoming available in the research community. However, a numerical study of engineering problems implies usually many computations which have to be performed within a reasonable time at moderate memory consumptions. In this sense, results of the present subsection demonstrate clearly that the pure LES remains invisible for ship applications. To get impression on the suitability of the present resolution estimation procedure it was applied for turbulent boundary layer (TBL) benchmark. First, we found that the pure LES with 1.0 M cells is quite accurate for prediction of velocity distribution, TBL thickness, TBL displacement thickness and wall shear stress. The present procedure predicted the necessary resolution around 0.5 M. Therefore, the estimations presented above are in no case any unrealistic over estimations rather than the estimations of the minimum resolution required for pure LES.

Validation. Before to start analyzing unsteady effects, the validation has been performed to show that the hybrid method predicts averaged flows with the accuracy which is not worse than that of RANS. Table 1 confirms that the hybrid method works well for ship resistance prediction. Both the overall resistance and resistance components ratio agree well with the KRISO (Korea research institute of ship and ocean engineering) measurement[6] and RANS.

Axial mean velocity field in the propeller plane for the KVLCC2 shown in Fig. 3(a) is compared with the experimental data of KRISO [7]. The axial velocity U_x is referred to the ship

	Resistance coefficient	Pressure resistance	Viscous resistance
KRISO Exp.	4.11×10^{-3}	15%	85%
RANS $k\varepsilon v^2 f$	4.00×10^{-3}	16%	84%
$k\omega$ SST SAS	3.80×10^{-3}	18%	82%
LES DMM	1.70×10^{-3}	81%	19%
Hybrid RANS LES	4.07×10^{-3}	17%	83%

Table 1: Results of the resistance prediction using different methods.

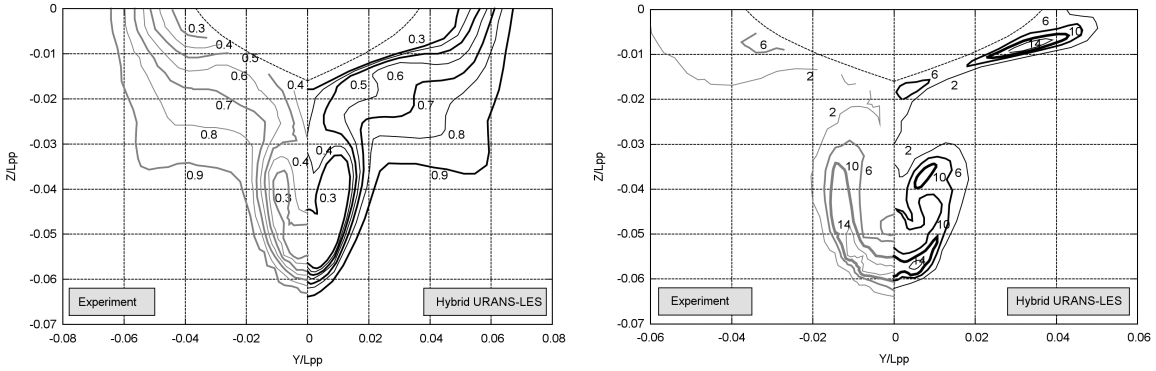

(a) (b)

Figure 3: Mean axial velocity field U_x/U_0 (a) and normalized Reynolds stress field $R_{xx} = \overline{U_x' U_x'}/U_0^2$ multiplied with 10^3 (b) in the propeller plane of the tanker KVLCC2 at Re $= 4.6 \times 10^6$ and Fn $= 0.142$.

model velocity U_0. The coordinates are referred to the length L_{pp} between perpendiculars of the ship model. The mean velocity field is very similar to the experimental one. The lines of the constant velocity have typical form and reflect the formation of a large longitudinal bilge vortex in the propeller disk. The second longitudinal vortex is formed near the water plane, but it has much smaller strength compared to the bilge one. Fig. 3(b) shows the Reynolds normal stress $\overline{U_x'^2}$ referred to U_0^2 in comparison with experimental data of KRISO. Topologically, the isolines are similar to those of the axial mean velocity shown in the Fig. 3(a). Again, the agreement between numerics and measurement can be considered as satisfactory.

Unsteady effects in the wake. The most important finding of this work is the observation of the strong unsteadiness of the velocity field in the wake which has still not be taken into account in modern engineering methods. Fig. 4 shows history of the axial velocity at points 3 ($r/R = 0.5$) and 4 ($r/R = 0.7$). The time averaged (mean) velocities are 0.1 and 0.24 at points 3 and 4 respectively. In reality the velocity is changed from -0.07 to 0.33 m/s at the point 3 and from 0.04 to 0.41 m/s at the point 4. Obviously, the estimations of the thrust and cavitation inception are quite different for velocities 0.24 and, say, 0.04 m/s. In the case $U_x = 0.04$ the trust is much larger and the cavitation is more probable.

It should be noted that the strong unsteadiness of the wake has been obtained only using the present hybrid method. URANS and SAS show good performance for the time averaged values. Unsteadiness predicted by these methods is either unrealistically weak (SAS) or even absent at all (various URANS models). Version of the detached eddy simulation approach DDES already implemented into OpenFOAM failed to predict the averaged velocity field properly.

CONCLUSION. LES is becoming an attractive tool for shipbuilding applications because

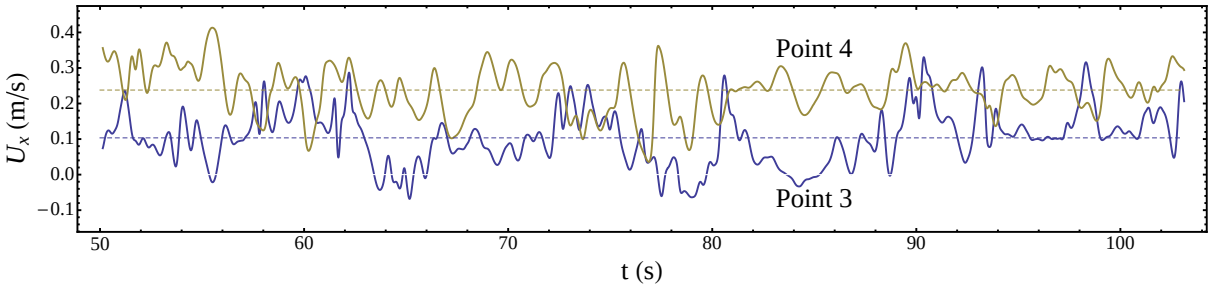

Figure 4: History of U_x at points 3 ($r/R = 0.5, \vartheta = 90^0$) and 4 ($r/R = 0.7, \vartheta = 90^0$). Dotted lines are time averaged values.

of its capability to resolve strong concentrated unsteady vortex structures. They play an important role in the interaction between propeller and ship hull with a large block coefficient. Study of the interaction problem is necessary to predict the overall propulsion, cavitation and vibration of the propeller and the hull. The estimations presented in this paper show that the pure LES demands a huge resolution what makes the LES application for shipbuilding purposes impractical even at small Re numbers for ship models. So far, the only reasonable solution is the application of hybrid methods. In this paper we presented a hybrid method based on the combination of the dynamic Smagorinsky SGS model (DSM) with $k\varepsilon v^2 f$ URANS approach. The method is applied to the calculation of the resistance and the wake flow of the tanker KVLCC2. Hybrid method provides very good results for the resistance. Also the fields of the mean axial velocity and the Reynolds stress R_{xx} agree well with the measurement in the propeller plane. Hybrid method predicts the unsteadiness of the wake flow. On the contrary, all URANS models including SAS as well as DES approach proved to be not capable reproducing unsteady character of the wake flow in the propeller disk at least on the relatively coarse grids used in this paper. Analysis shows that the instantaneous velocities deviate sufficiently from the mean values which are usually used as the estimated velocities in modern engineering methodologies. The results of the present study point out that the unsteadiness in the wake behind full ships can be very large and should be taken into account when propulsion and unsteady loadings are determined.

References

[1] Larsson L., Stern F., Bertram V., *Gothenburg 2000: A Workshop on Numerical Ship Hydrodynamics*, Chalmers University of Technology, Gothenburg, 2000.

[2] Kim S., Rhee S.H., *Assessment of eight turbulence models for a three-dimensional boundary layer involving crossflow and streamwise vortices*, Fluent Technical Notes **165**, 1-25 (2002).

[3] Schlichting H., *Boundary layer theory*, Springer, (2000).

[4] Durbin P.A., *Near-wall turbulence closure modeling without damping functions*, J. Theor. Comput. Fluid Dyn. **3**, 1–13 (1991).

[5] www.openfoam.com

[6] Kim W.J., Van S.H. and Kim D.H., *Measurement of flows around modern commercial ship models*, Exp. in Fluids **31**, 567–578 (2001).

[7] Lee S.J., Kim H.R., Kim W.J., and Van S.H., *Wind tunnel tests on flow characteristics of the KRISO* 3600 *TEU containership and* 300*K VLCC double-deck ship models*, J. Ship Res. **47**, 24–38 (2003).

Sheet Cavitation Model Implementation within a RANSE Solver

Jean-Marc LAURENS, Jean-Baptiste LEROUX, Benjamin PENGAM

ENSIETA, 2, rue François Verny, 29 806 BREST Cedex 09, France,

Jean-marc.laurens@ensieta.fr

In the VIRTUE program presented by F. Salvatore, [1], the developments of cavitation sheet model in Navier-Stokes solvers presented by all participants adopt multi-phase models based on a transport equation describing the generation and evolution of vapor content in the fluid. It implies that a transport equation is solved in addition to mass and momentum equations for the mixture of fluid. Some convincing results are reported but the required computing resources are still considered substantial. Furthermore, the use of a viscous two-phase flow solver still requires a cavitation model with some degrees of assumption and simplification. Salvatore, [1], also reminds that much faster simulations of the sheet cavitation are obtained with potential codes such as the ISEAN code of reference 2. BEM codes are using various methods of singularities in which the flow is deviated by sources and dipoles intensities. To avoid remeshing, the presence of the cavitation sheet is simulated by adjusting the singularities strengths. The differences between the models are essentially due to the assumptions concerning cavitation inception and closure. On the other hand, they are all assuming a slippery condition on the sheet cavitation surface.

These two types of developments are clearly separated since the cavitation sheet models are linked to the type of flow solver they use. A partial sheet cavitation model has recently been developed and implemented within potential flow codes in order to estimate the hydrodynamic forces of a propeller or a rudder working in an unsteady flow environment. The model described in [3], proposed that a relationship is established between the sheet cavitation geometry and the pressure distribution in subcavitating conditions. The model has been implemented within potential flow codes and has been successfully validated on two and three-dimensional foils. It is now proposed to study the feasibility of implementing this same cavitation model within a RANSE solver. Several stages are considered before a full implementation method is presented.

The model described in [3], uses the transpiration velocities technique in order to take the effect of partial sheet cavitation into account. In the potential flow codes, the transpiration velocities, v*, are equivalent to additional source strengths, σ*. When sources are used to impose a slippery condition at the surface of the obstacle, the implementation of the cavitation model in the potential flow codes is quite simple since it only requires the modification of the source strengths on the body surface where the cavity is attached. The additional strength of the sources causes a deviation of the slippery condition at the surface of the cavitation sheet. Once this technique has been adopted, the cavitation model consists of relating the physics of the cavitation phenomenon to the transpiration velocities. The model relates the transpiration velocity space derivative, $\frac{dv^*}{ds}$, to the difference between the subcavitating pressure P_{sub} and the water vapor pressure P_V, such as:

$$\frac{dv^*}{ds} = \frac{k}{\frac{1}{2}\rho.U.c}.\left[P_V - P_{sub}\right]$$

Where k is the linear slope coefficient, U and c are respectively the referent velocity and length (here the chord of the profile), P_V is the vapor pressure, and s is the curvilinear location

under the cavity. By using non-dimensional variables, the non-dimensional transpiration velocity $\tilde{v}^*$ is given by:

$$\tilde{v}^* = -k \int_{\tilde{s}_0}^{\tilde{s}} \left[C_p + \sigma_V \right] d\tilde{s}$$

Cp is the subcavitating pressure coefficient and σ_V is the cavitation number. v* is non-dimensionalized by U and s by c the chord of the profile, s_0 being the cavity detachment location. The cavity thickness t_c is directly associated with the transpiration velocity v* as follows:

$$\tilde{t}_c = \int_{s_0}^{s} \frac{\tilde{v}^*}{\tilde{v}_{sub}} d\tilde{s}; \quad \tilde{t}_c \geq 0,$$

v_{sub} is the subcavitating velocity. When v*<0, the transpiration velocity turns into an aspiration and the cavity ends when $\int v^* = 0$.

The model has been successfully validated by comparison with the 2D experimental results obtained by Leroux [4]. Since the case is sufficiently documented, it was decided to use it to test the implementation of the sheet cavitation model within a Navier-Stokes solver. The instrumented hydrofoil with pressure taps is a NACA66 (mod)–312 a=0.8 (relative maximum thickness 12% and maximum camber 2%) with a chord length of 150 mm. The hydrofoil is installed in the square test section (192mm × 192mm) of the cavitation tunnel of the Ecole Navale in Brest. Both the flow velocity and the pressure are controlled in the cavitation tunnel. The angle of attack of the hydrofoil is set to 6° and the Reynolds number, Re is about 7.5E5. The reference pressure variation capacity of the cavitation tunnel was used to set the cavitation number. The Cp distributions are given for the subcavitating foil and for three values of the cavitation number (1.495, 1.541, and 1.622).

First, the cavity geometry as computed by the cavitating potential flow code is imposed in the RANS simulation. A zero velocity boundary condition is set at the foil surface and a slippery boundary condition is set on the cavity surface. These boundary conditions are accepted to be consistent with all experimental observations. They are also comparable to the potential flow simulations since the viscous boundary layer is simulated also using transpiration velocities. The confinement within the cavitation tunnel is also present in both potential and RANSE simulations. Since high precision results are necessary, the generated meshes for the study are refined. They average 135,000 cells and the value of y+ is always smaller than one. All the computations were performed using second order schemes. The inlet turbulence intensity is set to 2% to be compliant with the turbulence intensity measured in the cavitation tunnel and RNG k-ε model is used.

The imposed cavity geometry simulations are presented together with the subcavitating case and compared with both the experimental results and the potential flow code simulations in Figure 1.

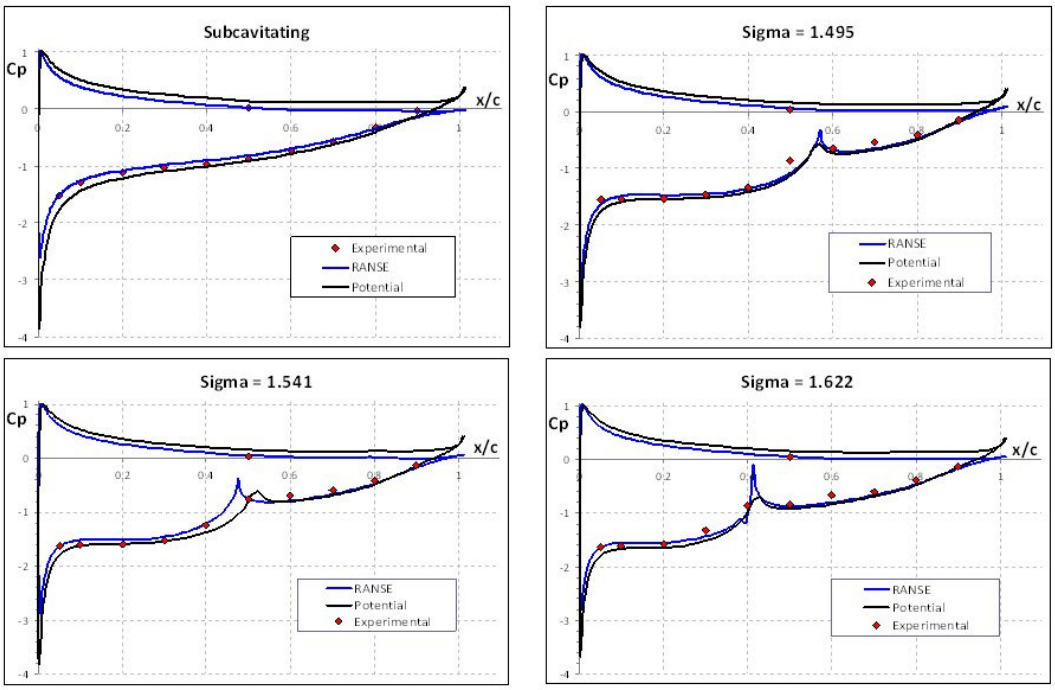

Figure 1 *Comparative Cp distributions between the experimental, the potential flow code and the RANSE simulations in cavitating and subcavitating regimes.*

These results prove that imposing the sheet cavitation geometry as computed by the BEM code does indeed produce good results.

However, the method is not very practical unless a steady state case is considered. The second stage consists in imposing the transpiration velocities as computed by the model implemented within the BEM code. The transpiration velocities, v*, area such as, $\int_{cavity} v^* = 0$, the mass balance is preserved. Although there is no change of phase, neither water nor vapor is generated or vanished. To use these transpiration velocities directly in RANSE simulations, the section of the profile underneath the cavity has to be declared with a velocity inlet. The VoF multiphase flow module is activated with water as phase 1 and vapor as phase 2. The VoF model relies on the fact that the two fluids are not interpenetrating. The two-phase flow interface is modeled by introducing the volume fraction variables α_1 and α_2. In each volume, the volume fractions of the two phases sum to unity. When the two phases are present within the same cell, the viscosity and the density are averaged according to volume fractions. The most convenient way to impose the transpiration velocities profile is to write a UDF (User's Defined Function) which will set the boundary condition. The three cavitation numbers cases were simulated using the same mesh refinement as in the previous section and the same statistical turbulence model was activated.

The obtained Cp distributions for the 3 cavitation number values are presented in Figure 2. The obtained cavity length is the same as previously but the shape of the Cp distribution has changed. The Cp's underneath the cavity now present a flat distribution even in the closure area. It is difficult to determine whether this behavior is closer to the physics since the error in the measurements would embed the two results.

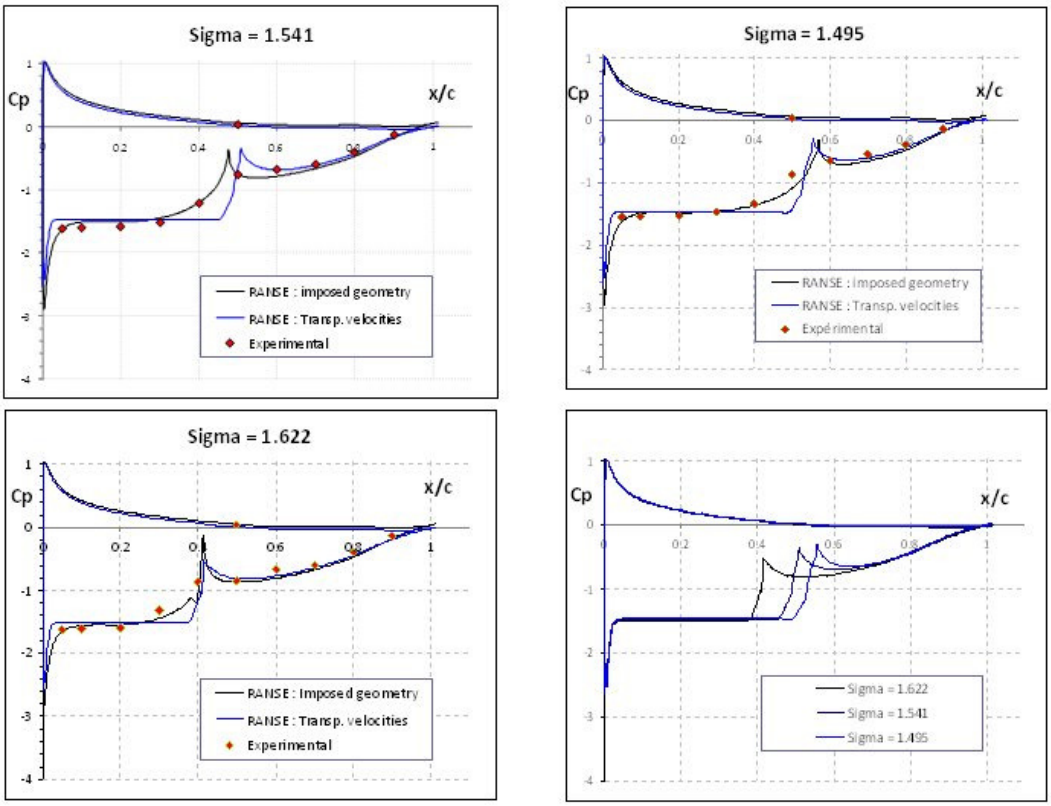

Figure 2 *Comparative Cp distributions between the experimental and the RANSE simulations with the sheet cavitation geometry imposed as described in stage 1 and with the imposed transpiration velocities as described in this section. The right graphic of the bottom row compares the results of the transpiration velocities technique in the RANSE simulations for the three different values of the cavitation number.*

These results prove that imposing the transpiration velocities as computed by the BEM code also produces good results. Furthermore, the method can be used to simulate a cavitating rudder in an unsteady state flow caused by the action of the propeller or a cavitating propeller in an unsteady state flow due to hydrostatic and/or a non-uniform upstream wake for instance. Using the procedure described in this section, a propeller presenting partial sheet cavitation can be simulated with a RANSE solver. It implies first that the full computation of the cavitating propeller is performed with the potential flow code. Then the maximum cavity extent is known and a velocity inlet boundary condition is set on this area of the body surface. The transpiration velocities computed by the potential flow code are known and stored against time for later use in the RANSE simulation. The procedure may appear laborious as it involves a full potential flow simulation but it would certainly be much faster than anything existing today to simulate the sheet cavitation with a RANSE solver.

Finally, the cavitation model can be used within the RANSE solver without the need of a potential flow code. The method simply consists of computing the transpiration velocities from the subcavitating Cp distribution obtained with the RANSE simulation instead of using the distribution obtained by the potential flow code. At present, the necessary iterations to compute k, the linear slope coefficient, are not yet programmed in a UDF and the converged value was taken from the cavitating potential flow code. The results presented in Figure 3 for σ_V = 1.622 are very encouraging since they show yet again, a slight improvement compared to the two previous methods. The main foreseen difficulty in the full implementation of the cavitation model within a RANSE solver is the fact that the cavity length is unknown unless it's been computed by the cavitating potential flow code before. The transpiration velocities have to be injected from the body surface declared as velocity inlet, the rest of the body surface

being declared as wall. Two approaches are possible: either there is a way to change the boundary condition type as the computation progress or everywhere on the body surface a cavitation sheet may be attached must be declared at velocity inlet. If no vapor injection occurs, it is equivalent to a slippery condition. Tests performed on the 2D cases presented here, proved that very little differences are observed in the recompression area and beyond. This second approach will therefore be taken as a first choice.

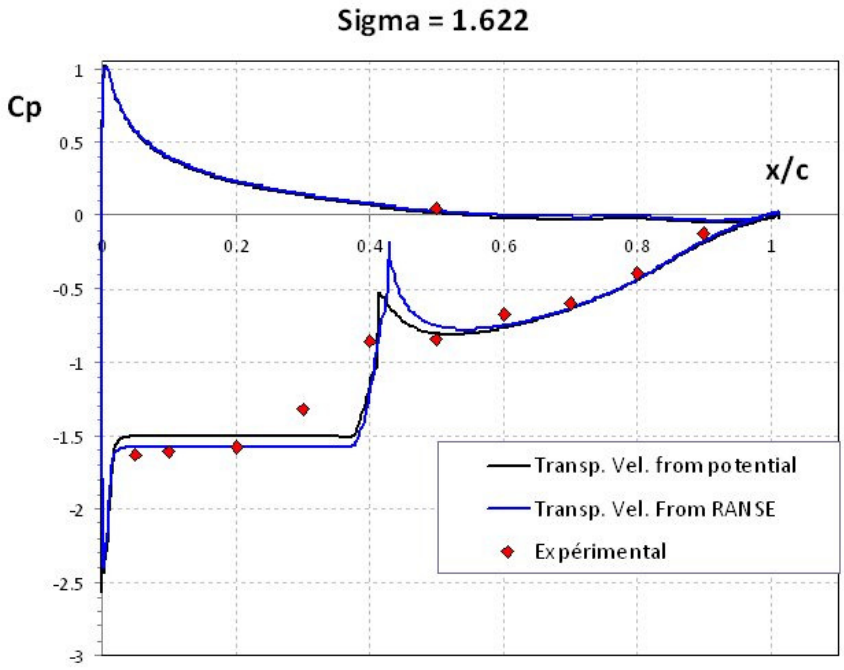

Figure 3. *Comparative Cp distributions between the experimental, and the RANSE simulations using the transpiration velocities technique. Two approaches are compared: 1) The transpiration velocities are directly taken from the potential flow simulation and 2) they are derived from the subcavitating Cp's distribution obtained by the RANSE simulation.*

As a conclusion, the feasibility of using the transpiration velocities technique to simulate sheet cavitation with a RANSE solver has been demonstrated. Imposing the cavity geometry with a slippery condition on its surface was only the first stage but it can be used for steady state cases. The transpiration velocities technique can be used directly in the RANSE simulations by activating the VoF module and by injecting water vapor normally to the surface of the solid. It is of course planned to proceed to a full implementation of the cavitation model in the RANSE solver. Nevertheless, the procedure consisting first of running the potential flow code to obtain the transpiration velocities to be injected underneath the cavity would certainly be much faster than anything existing today to simulate sheet cavitation with a RANSE solver. It is also planned to expand the cavitation model and its implementation to supercavitation. Since nothing artificial has to be done to satisfy the Kutta condition, the expansion to supercavitation into a RANSE solver appears simpler than into potential flow codes.

References

1. Salvatore, F., Streckwall, H., and van Terwisga, T. (2009). *Propeller cavitation modelling by cfd – results form the virtue 2008 Rome workshop*. Proceedings of SMP'09 the First International Symposium on Marine Propulsors, pages 362–371, Trondheim, Norway.

2. Salvatore, F., Testa, C., Ianniello, S. & Pereira, F. (2006). *Theoretical Modelling of Unsteady Cavitation and Induced Noise*. Proceedings of the Sixth International Symp. on Cavitation, CAV 2006, Wageningen, The Netherlands.

3. Phoemsapthawee, S.; Leroux J.-B.; Laurens J.-M.; (2009) ; *A Transpiration Velocities Based Sheet Cavitation Model*, Ship Technology Research. Vol. 56, no. 4, pp. 161-176. Sept.

4. Leroux, J.-B. (2003). *Étude expérimentale en tunnel hydrodynamique des instabilités de la cavitation par poche sur hydrofoil par la mesure spatio-temporelle du champ de pression pariétal*. PhD thesis, École Centrale de Nantes et Université de Nantes. Thèse de Doctorat.

Free-Surface CFD for Integrated Design of High-Speed Craft Stern Gear and Propeller

Simon G. Lewis[a,b;1], Marek Skrzynski[b], Stephen R. Turnock[a] and Alexander M. Wright[c]

a. Fluid Structure Interactions Research Group, School of Engineering Sciences, Highfield Campus, University of Southampton, Southampton, SO17 1BJ, UK.

b. CJR Propulsion Ltd. 70 -72 Quayside Road, Bitterne Manor, Southampton SO18 1AD, UK.

c. Wolfson Unit for Marine Technology and Industrial Aerodynamics. Building 15/A, University of Southampton, Highfield, Southampton SO17 1BJ, UK.

1. INTRODUCTION

CJR propulsion design and manufacture propellers and stern for luxury yachts. The current propeller design method assumes a uniform flow into the propeller. This assumption has significant errors, as the flow is affected by stern gear in front of the propeller in the flow as well as general hull performance. Propeller performance is currently calculated using an in house program based on a vortex lattice method (Szantyr, 1993). This investigation forms part of a project aiming to improve the prediction of the wake into the propeller in order to improve propeller design. This investigation presents a case study into the effect of the effect of the P bracket design on the propeller performance.

This work continues ongoing research into the CFD of high speed craft at the University of Southampton. Work has been carried out in the past on a improving the prediction of bodies impacting with water with the experiments in Lewis et al (2010) and the CFD simulation work by Lewis et al (2008).

2. CFD METHODOLOGY

The opensource CFD code, OpenFOAM version 1.6.x, is used to carry out the predictions. The main CFD parameters include:

- Transient free surface flow, using the interFoam solver. Typically 8 seconds simulation time. The solver varies the timestep ensuring that the maximum courant remains below 1.
- k-ε turbulence model. The initial value for the turbulent kinetic energy is 0.1 $m^2.s^{-2}$
- Mesh sizes from 400 000 to 5.7 million cells. The first mesh point away from the wall is of the order of 5mm, producing a y+ of the order of 200 with the finest mesh.
- Parallel simulations using from 4 to 32 processors.

The CFD simulation is set up with reference to WS Atkins (2002) and Ferziger and Perić (2002).
The hull is fixed in heave and trim. The trim is determined from trials data, and an iterative approach is used to determine the correct heave position, using the predicted lift and drag to compare with actual figures. The mesh dimensions are 100m x 20m x 20m, for a hull 22m long and with a beam of 6m.
The propeller wake is extracted from the results using the sample function. The velocities at 6 radial positions at 36 circumferential points around the propeller center are extracted. These are transformed into axial, radial and tangential velocities for input into the propeller code. The propeller codes uses a vortex lattice potenitial flow method which is quasi static, and solves the flow for every blade in every position. It also includes a cavitation prediction model.

[1] Email: S.G.Lewis@soton.ac.uk

3. P-BRACKET DESIGN STUDY

Three different P-brackets are analysed, as illustrated in figure 1. The proposed hypothesis is that angling the P-bracket away from the propeller will improve the flow into the propeller and increase propeller efficiency and performance. The current hull design uses a P-bracket angle of illustrated in figure 1(a), which is angled towards the propeller. During trials, the propeller designed for this yacht exhibited a tendency for corrosive cavitation, as well as a reduction in predicted thrust.

Two other P-bracket designs are simulated, and the flow into the propeller plane is used as an input into the vortex lattice code for predicting propeller performance. The P-brackets are classified by the angle of their trailing edge with the vertical. Figure 2 illustrates the numerical mesh around the stern gear. The mesh is generated using blockMesh and snappyHexMesh in OpenFOAM.

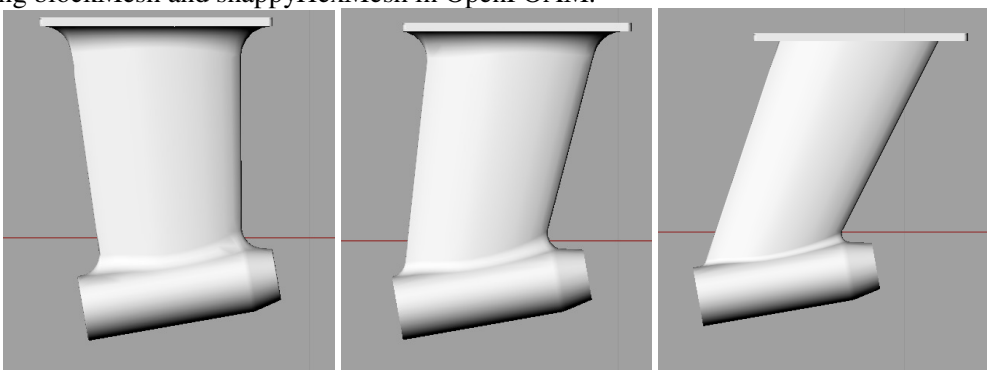

(a) -8º (b) 15º (c)26º

Figure 1: Different P-bracket designs.

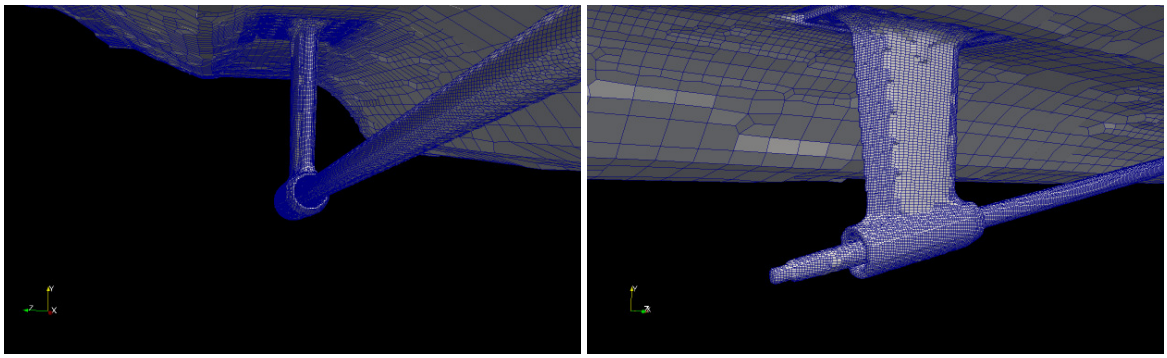

Figure 2: Numerical mesh showing P-bracket and propeller shaft.

Figures 3, 4 and 5 present contour plots of the flow velocity into the propeller plane for axial, vertical and horizontal crossflow respectively. The axial flow is reduced behind the P-bracket as shown in figure 3. This reduction in flow velocity is more severe with the -8º P-bracket compared with the 26º design. Figure 4 illustrates that there is an increased downward flow as the P-bracket is raked forward. Figure 5 demonstrates the horizontal crossflow velocity is reduced with the 26º P-bracket. The three components of the velocities are then used to predict the propeller performance for each design.

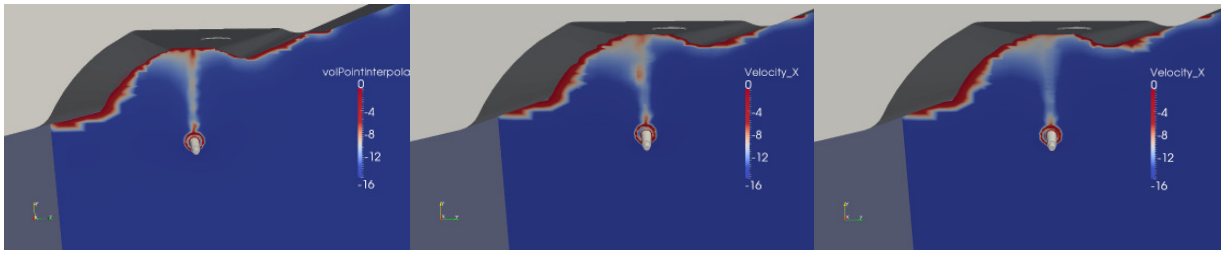

(a) -8º (b) 15º (c)26º

Figure 3: Effect of P-bracket design on axial flow.

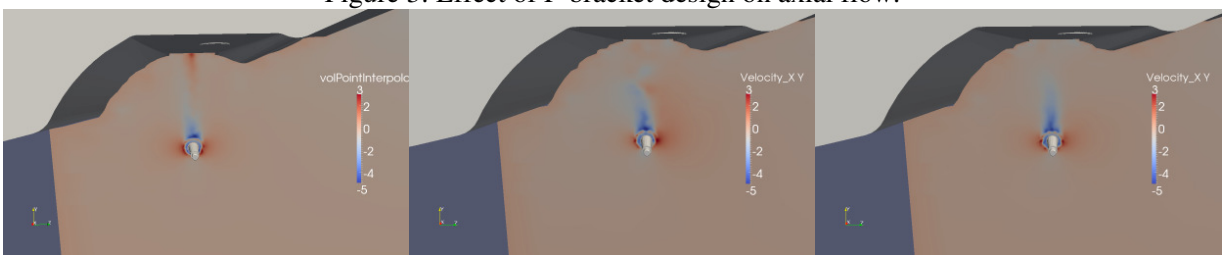

(a) -8º (b) 15º (c)26º

Figure 4: Effect of P-bracket on vertical flow

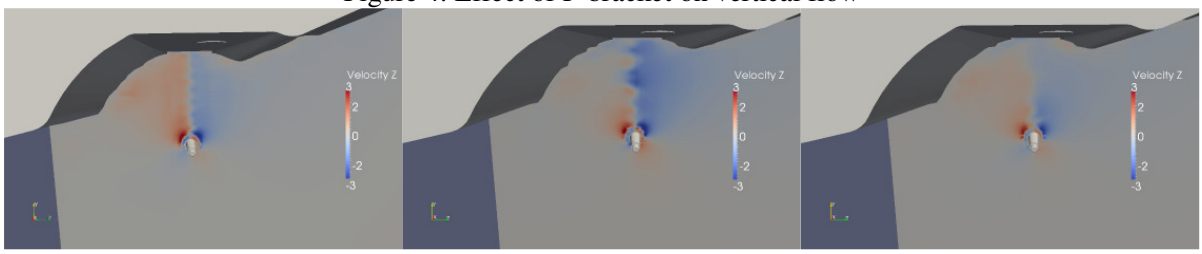

(a) -8º (b) 15º (c) 26º

Figure 5: Effect of P-bracket design on cross flow.

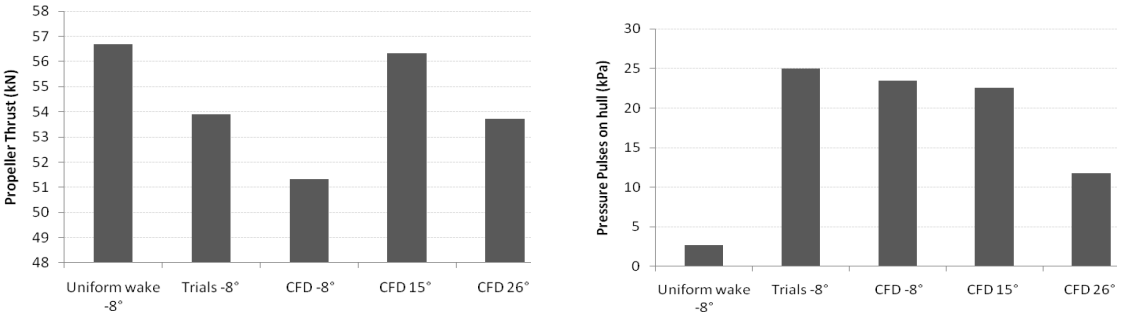

(a) Thrust (b) Pressure pulses on hull

Figure 6: Propeller predictions and trials data.

Figure 6(a) presents the propeller thrust predictions for each P-bracket design using the wake from the CFD simulation, the prediction for uniform flow into the propeller and the trials data. The thrust in the trials is lower than that predicted using the uniform wake. However the prediction for the -8º P-bracket expects an even lower thrust than the trials data suggests. This discrepancy in the results is due to the propeller operating at a higher revolution per minute at trials. This occurs as the propeller is providing less resistance to the engine than expected and is operating 'light'. The engine compensates by rotating faster than the design specification for the propeller. For the rest of analysis rated rpm of engine were used.

Figure 6(b) presents the pressure pulses on the hull due to the propeller. In a uniform wake, the pressure pulse is predicted to be negligible. The predicted pressure pulse using the CFD simulation correlates well

with the trials data. Adjusting the P-bracket angle from -8º to 26º has the effect of halving the predicted pressure pulses on the hull. The pressure pulse is partly dependant on the flow entering the propeller plane. In the case of the 26º P-bracket, the average velocity of the flow entering the propeller is less than the 15º and -8º designs, although the variation in the flow velocity around the azimuth of the propeller is also less. Figure 7(a) and (b) illustrates the variation in the axial flow into the propeller plane for the -8º and the 26º P-bracket respectively. Each curve represents a different non-dimensional radius from the propeller shaft, and the x-axis is the azimuth of the propeller, with 360º being the vertical line directly behind the P-bracket.

.

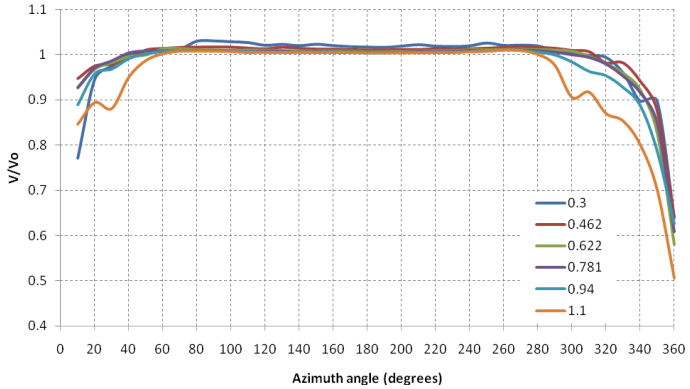

Figure 7(a): Axial flow through the propeller plane for various radial r/R positions on the propeller with the -8º P-bracket.

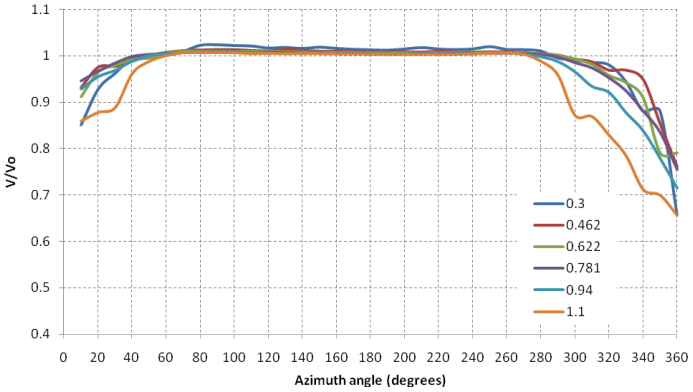

Figure 7(b): Axial flow through the propeller plane for various radial r/R positions on the propeller 26º P-bracket.

Figures 8 (a), (b) and (c) illustrate the predicted cavitation on the propeller as a result of using the uniform flow into the propeller, as well as taking the CFD wake prediction into account for two of the P-bracket designs. There is a significant increase in the amount of cavitation on the suction surface of the propeller blade. This is most important near the root of the blade, where minimal cavitation is predicted using the uniform flow model, compared to some cavitation predicted when using the CFD wake. This correlates well with the position of the actual corrosive cavitation experienced by the propeller blade, and is illustrated in figure 9. The cavitation can be reduced by tailoring the propeller design to the flow it experiences. Figure 8 (c) presents the cavitation predicted for a propeller optimized to the wake field behind the 26º P-bracket. The original propeller design is optimized using the uniform flow field.

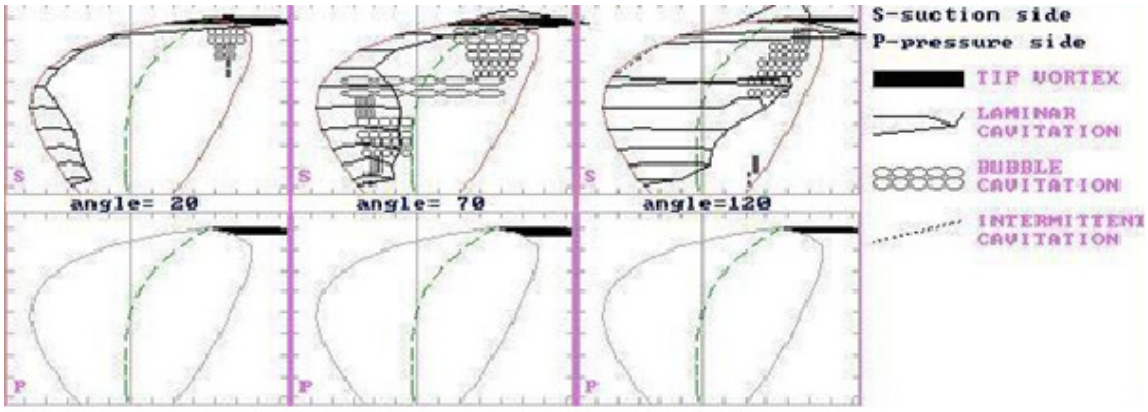

Figure 8 (a): Cavitation predicted with uniform wake into the propeller.

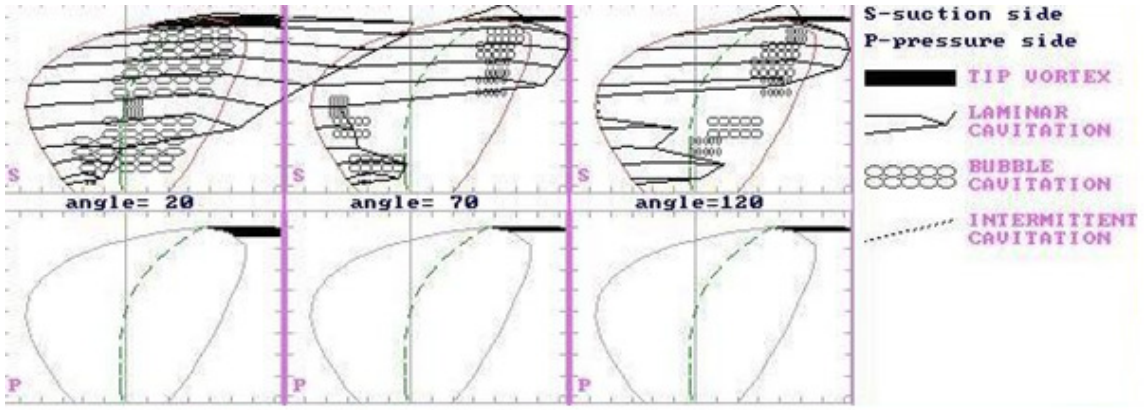

Figure 8 (b): Cavitation predicted with CFD wake into the propeller (-8º P-bracket).

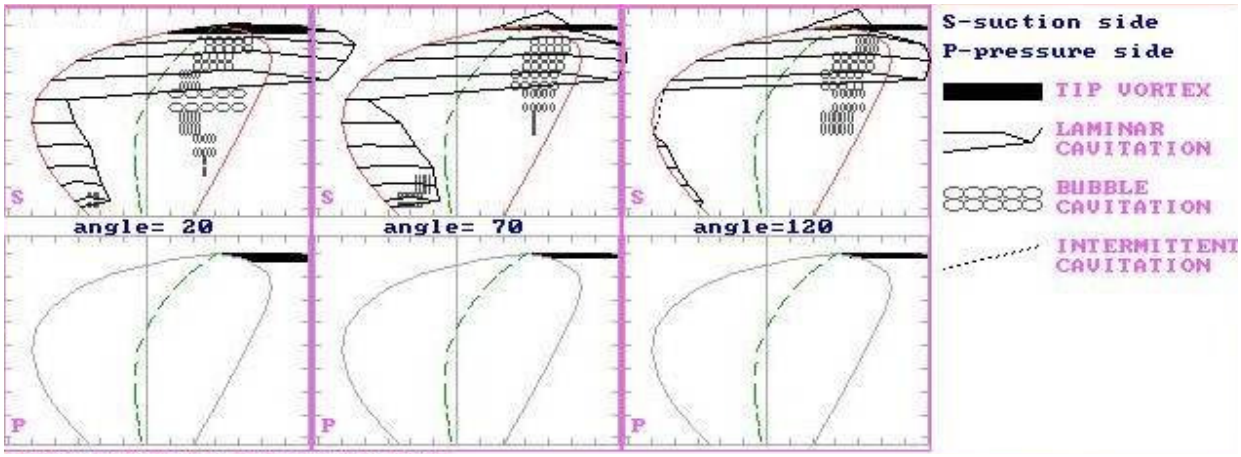

Figure 8 (c): Cavitation predicted with CFD wake into propeller optimised to the wake (26º P-bracket).

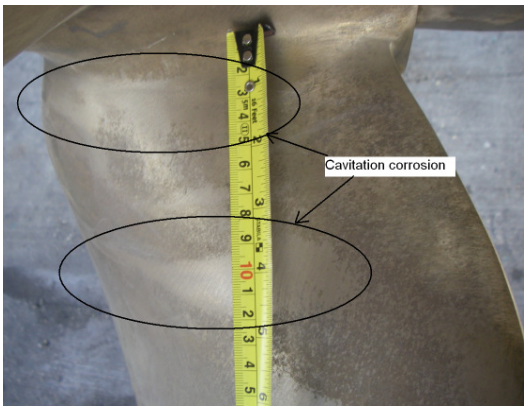

Figure 9: Cavitation corrosion near the propeller root.

4. CONCLUSIONS AND FUTURE WORK

The predictions correlate well with the available data from trials. Use of CFD to predict the wake flow into the propeller provides an improved cavitation prediction for the propeller blade, and these improved predictions closely match the actual cavitation found on the propeller.

The vertical angle of the P-bracket affects the flow into the propeller. Main advantages of angling the P-bracket away from the propeller (eg the 26º example) include:

- A cleaner flow into the propeller.
- Significant reduction in the predicted pressure pulses on the hull.
- Opportunity to design propeller matched to the wake (wake adapted design)
- Increase in propeller thrust and torque.
- Reduced cavitation.

Future work includes further validation of this method. The project is currently in an early phase, and further validation work needs to be carried out in order to improve the method. The flow out of the propeller plane needs to be incorporated back into the CFD simulation in order to allow the rudder design to be optimized.

ACKNOWLEDGEMENTS

This work is part funded by the Knowledge Transfer Partnership KTP007627 between the University of Southampton and CJR Propulsion Ltd.

REFERENCES

Ferziger J.H. and Perić M. (2002). Computational Methods for Fluid Dynamics. 3rd Edition. *Springer-Verlag.*

Lewis, S.G., Hudson, D.A. and Turnock, S.R. (2008) Improvement to body impact predictions using CFD through analysis of an unsteady boundary layer. In, 11th Numerical Towing Tank Symposium, Brest, France 07 - 09 Sep 2008. Brest, France, ENSIETA, 65-70.

Lewis, Simon G., Hudson, Dominic A., Turnock, Stephen R. and Taunton, Dominic J. (2010) Impact of a free-falling wedge with water: synchronized visualization, pressure and acceleration measurements. Fluid Dynamics Research, **42**, (3).

Szantyr J. (1993) The lifting Surface Program for Hydrodynamic analysis of marine propellers. Ship research and Design Centre CTO, Gdansk. Report No. RH-93/R-064.

WS Atkins (2002) MARNET-CFD Best Practice Guidelines for Marine Applications of CFD.

Combining CFD and Autonomic Control to Simulate Autonomous Surface Vessel Operation

Dimitrios Nikolakis,Nikolai Kornev, University of Rostock, Rostock/Germany,
dimitrios.nikolakis@uni-rostock.de
Daniel Schmode,Volker Bertram, FutureShip, Hamburg/Germany

The AGAPAS project shall develop a prototype of an unmanned surface vessel (USV) intended for rescue operations. The USV (rescue robot) shall find autonomously persons at sea with the help of Galileo satellite signals and support their rescue process. The following assumptions are made:

- The target person wears a life vest sending and receiving Galileo signals.
- The rescue robot is launched from a mother ship.
- The rescue robot has an autopilot to guide it toward the target person. The autopilot knows at all times the position of the target person and its own position.
- The target person is taken onboard the rescue robot via remote control from the mother ship.

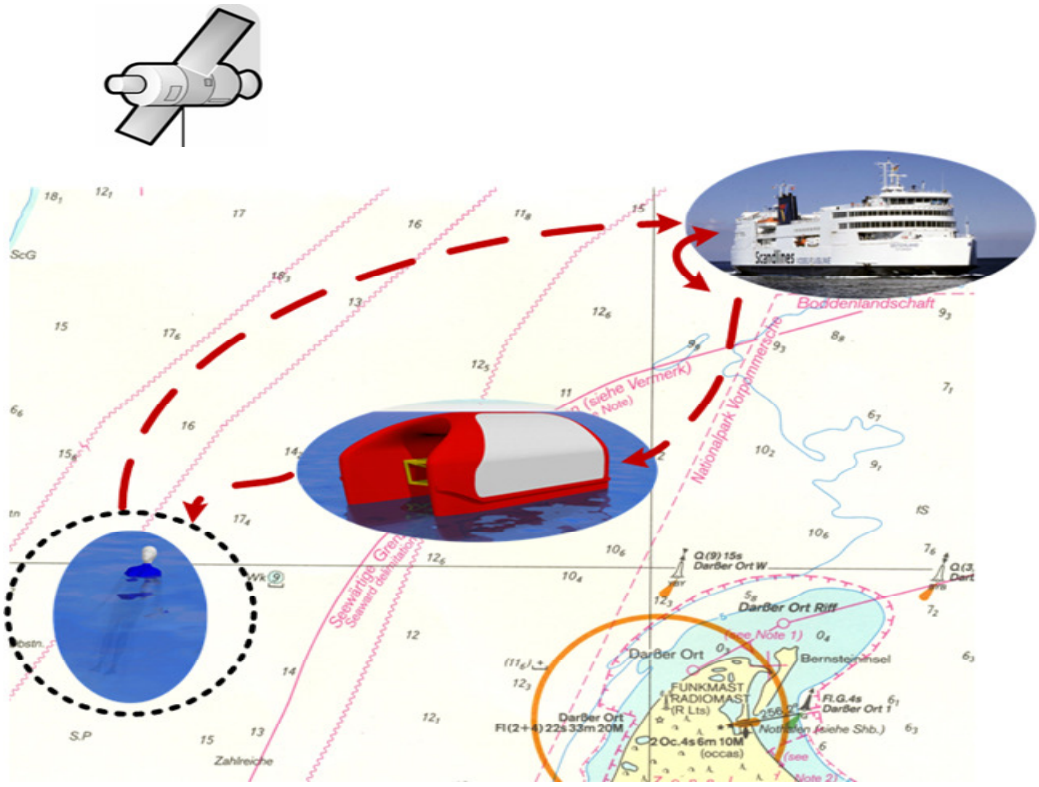

Fig.1: Schematic view of the salvage process

The University of Rostock is in charge of the work package developing the autopilot. During the development, simulations of manoeuvres served as input to optimize the autopilot algorithm. The manoeuvring simulations required basically two components:

1. A control module that processes position and heading of the rescue robot and generates control signals for propeller and rudder.
2. A manoeuvring module that uses Control module's signals of the control module to predict new position and heading of the vessel.

The two modules work in a loop until the recue robot has reached (within a given tolerance) the target person. In the following, we describe the hydrodynamic part within this task.

Fig.2 shows the rescue trajectory and the most important control parameters, which are not further discussed here, as the focus here is on the hydrodynamic part. We will describe the most important software module MANIS and OpenFOAM, Fig.3.

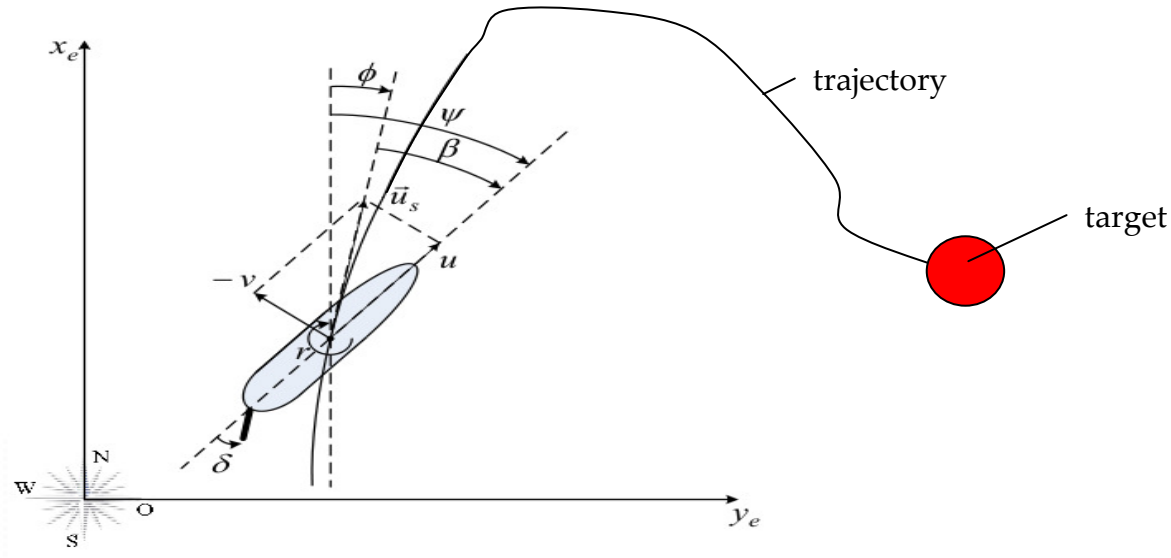

Fig.2: Schematic view of a rescue trajectory

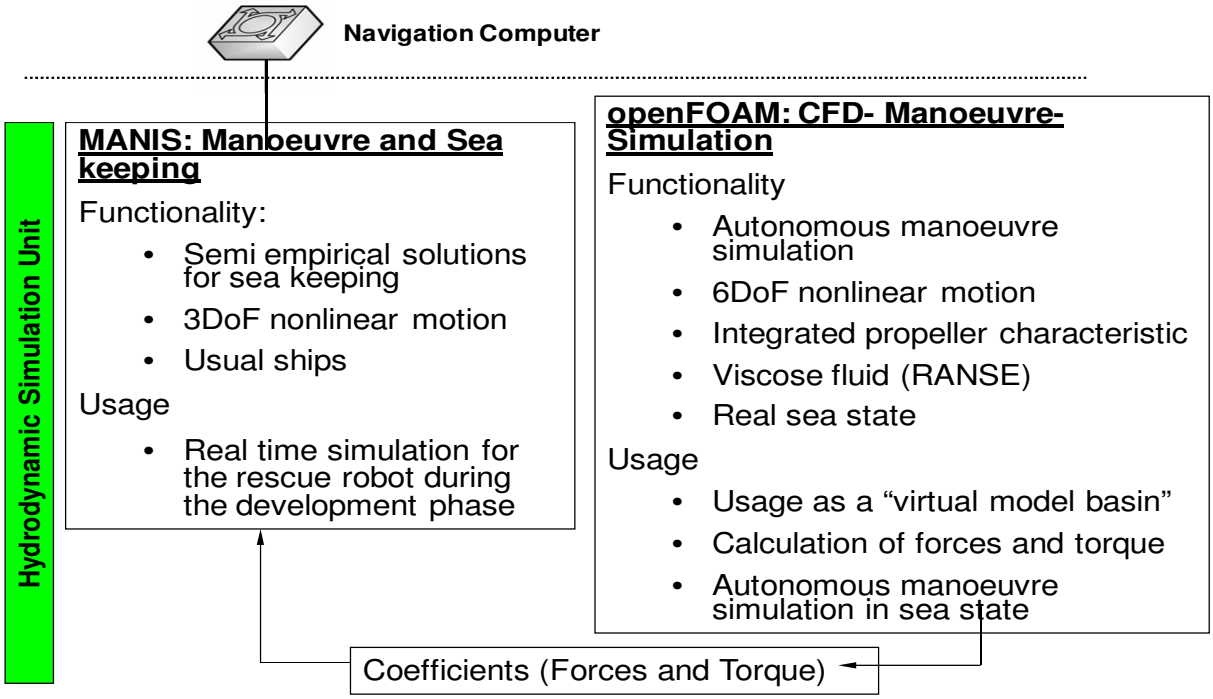

Fig.3: Components of hydrodynamic simulation

MANIS (Manoeuvring in Seaway) developed by Haase, Waltemath and Kornev is at the core of the autopilot (for details see [1]). It employs the control module and the input data from Galileo (position of target and position of rescue robot) to derive required settings for propellers and rudders for the fastest trajectory to the target. MANIS and the control module shall be fast enough to run in "real time". A nonlinear transient motion model in 3 degrees of freedom (DoF) (surge, sway, yaw) is solved using a Runge-Kutta integration. We assume a weak coupling between the roll motion and in-plane motions (sway, yaw). The hydrodynamic forces are computed using semi-empirical methods, following customary decomposition of the forces:

- Viscous forces are computed using a Krylov respectively SNAME method.
- The hydrodynamic added masses are estimated using empirical formulae.

- Damping forces are neglected. Due to the small ship width B, the nondimensional frequencies $\omega\sqrt{(B/(2g)}$ will be small as well.
- Exciting forces are considered with Krylov part and an empirical estimate for the ship-wave interaction part developed by the Krylov Institute.
- The propeller and rudder forces are added as governed by the PID controller.
- The interaction between two catamaran hulls is considered by another empirical correction.
- The wave length is assumed as much larger than the vessel length. Waves of short periods are neglected here.
- The draft is assumed to be small compared to the wave length. Thus the wave induced orbital velocity can be assumed as approximately constant over draft.
- Rudder angles are assumed to be small; hence there will be no stall (flow separation).
- The Reynolds number is assumed in excess of 10^6. This assumption may be questionable in long waves.

Irregular seas are represented by a Pierson-Moskowitz spectrum. The code extensively tested and validated with very good agreement against the model test results of the SIMMAN workshops, [1], [2]. The semi-empirical approach makes the method very rapid. Forces have been verified by CFD simulations using OpenFOAM.

OpenFOAM allows a very good capturing of the physics. A nonlinear transient motion model in 6 degrees of freedom (DoF) (surge, sway, yaw) is solved considering also free surface and viscous effects. Due to the high computational effort, this method is not suitable for real-time control of the autopilot. The approach is "simply" used to verify and adapt the faster semi-empirical approach. The CFD approach required had to meet some general functionalities:

1. RANSE solver
2. Free-surface capturing
3. Customary boundary conditions, such as no-slip walls, free-slip walls, open boundaries with specified pressure or velocity, non-reflecting boundaries, etc.
4. Capability for 6 DoF seakeeping simulation
5. Capability for manoeuvring simulation with prescribed (time dependent) propeller thrust and rudder angles.

At the time of development, there was no commercial code on the market that offered all these functionalities in a ready-made package. The AGAPAS team of the University of Rostock decided to base the required development on the open-source CFD-package OpenFOAM for the following reasons:

1. OpenFOAM offers maximum independence fort he future, as there are no licence fees and the university can add further functionalities as needed.
2. The university has already an OpenFOAM user group which is growing rapidly.
3. The poor documentation of OpenFOAM is compensated by a strong international user community with its own forums.

The strategic decision for OpenFOAM entails certain activities:

1. The missing functionalities (seakeeping 6 DoF simulation, manoeuvring) needs to be developed or sourced, and subsequently tested.
    a. The 6 DoF seakeeping module is supplied by FutureShip/Germanischer Lloyd.
    b. An additional extension is developed together with FutureShip. The extension allows adding several time-dependent external forces on the vessel. The external forces can be modified during the simulation following a prescribed formula or by a macro. This allows mimicking rudders and propellers, including the consideration of propeller characteristics. As a first approximation, these forces can be added to the equations of motions. This still neglects the interaction between ship and propulsion and approximates the propeller characteristics by simplified functions.
2. There is no support from a software vendor. This is compensated by planning a higher effort in the beginning, when expected bugs and problems will require trouble-shooting. Additional training time is then included in the budget.

3. The implementation is ensured by a suitable environment for research and development, testing and operative application.

OpenFOAM calculations were performed with these new functionalities. As a first step, a simple PD control strategy was tested with different coefficients. Fig.4 shows vessel trajectories starting at x=y=0 and the target at x=20 m and y=70 m. Thrust was kept constant and only the direction of the thrust controlled. The different trajectories represent different coefficients for the differential part d of the controller. d=0 represents a proportional controller.

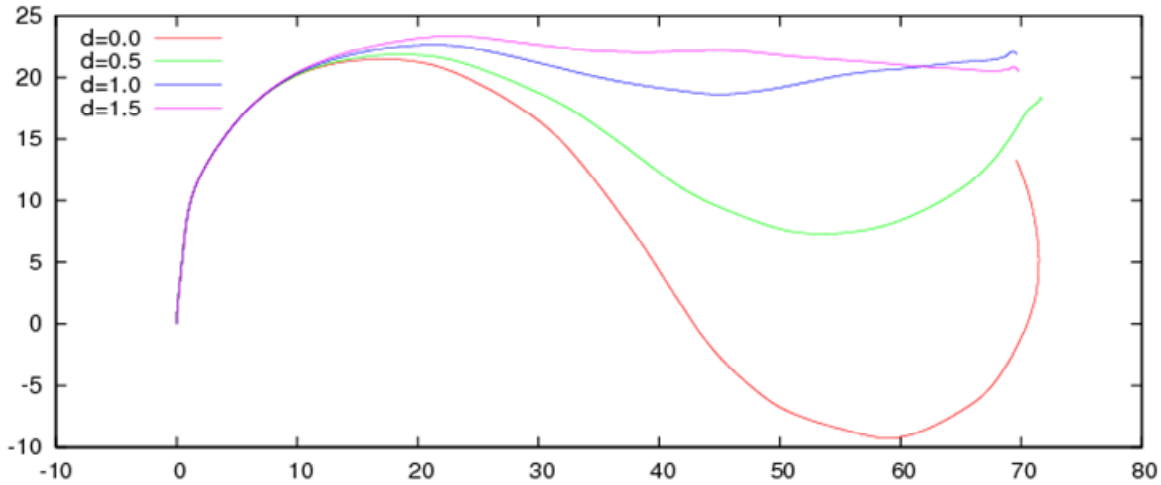

Fig.4: Vessel trajectories with variations of the differential control part

The time to reach a target is essential in rescue operations. Rescue operations were simulated using OpenFOAM, Fig.5. Table I lists the influence of thrust and sea state. The obtained times were compared to MANIS. The agreement is good.

Parameter	
target position (x,y)	(60, 200) [m]
Start of RR (x,y)	(0, 0)
Course Control	PD
Rotation velocity of Pod	8,5 °/ s
Max. pod angle	30°
Thrust = constant	300 N, 1250 N

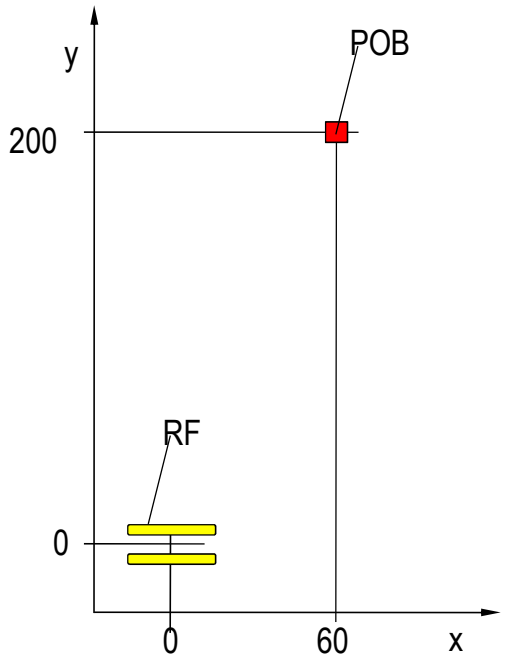

Fig.5: Parameters and initial condition for the rescue simulation; target = POB

Table I: Time to reach target POB

Time to reach the POB	Sea State 2	Sea State 4
Thrust = 1250 N	31 s	40 s
Thrust = 300 N	90 s	130 s

References

Haase, M.; Bronsart, R.; Kornev, N.; Nikolakis, D. (2010), *Simulation of the Dynamics of an Autonomously Acting Small Catamaran for Search and Rescue Process*; 8th IFAC Conf. (CAMS) 2010

Stern, F.; Agdrup, C. (2008), *SIMMAN 2008 - Workshop on Verification and Validation of Ship Manoeuvring Simulation Methods*, Workshop Proceedings, Copenhagen

Fluid-Structure Interaction using Free-Surface RANSE for Springing and Whipping

Jan Oberhagemann[*]
Ould el Moctar[†]

1 Abstract

We discuss excitation of the most relevant effects of fluid-structure interaction related to hull girder vibration of ships, whipping and springing. Benefits and challenges of using RANSE (Reynolds-Averaged Navier Stokes Equations) methods to approach the corresponding fluid dynamic problems are illustrated. Structure dynamic approaches for fluid-structure coupling with RANS are presented. Examples show a very good agreement of the applied methods with experimental data.

2 Introduction

Dimensioning of ship structures requires an appropriate knowledge of not only loads due to cargo loading, but seaway-induced loads as well. Dynamic structural responses due to hydrodynamic loading increase the stress level, compared to static load application. Neglecting structural flexibility and considering the ship to be rigid when computing seaway-induced loads has been common practice for a long time, for reasons of simplicity. Nowadays it has become more and more common sense that structural dynamics play an important role and cannot be neglected or simply be covered with rule-of-the-thumb safety factors.

However, the contribution of structure dynamic effects to the life-cycle loads extreme and fatigue loads, is still a controversial issue. Estimates range from “negligible” to “major” (50% and above). A lot of research activities focus on a more precise determination, including full scale measurements, model tests and numerical investigations.

Usually, two fundamental phenomenae are distinguished: Springing and Whipping. The former is described as a periodic resonant excitation of structural vibration, while the latter is a transient and decaying vibration caused by a single impact-like loading (i.e. slamming).

Both Springing and Whipping are effects of fluid-structure interaction. Not only does the fluid initiate structural vibration, but the vibration, which is an elastic displacement motion, in turn has an impact on the surrounding fluid flow and the fluid pressure. Numerical methods have to reflect this mutual interaction, hence we will present two-way coupling methods here.

Additionally, we will give a summary of our research activities on numerical methods. Besides describing developed tools and showing some interesting results, we will also name some open questions and highlight important issues.

3 Numerical Methods

A straight-forward and intuitive approach to fluid-structure interaction problems is to split the solution domain into a fluid domain and a structural domain, and solve both problems alternatingly. To achieve a consistent naming convention, we will refer to CFD (Computational Fluid Dynamics) and CSD (Computational Structure Dynamics), respectively. The fluid dynamic method is based on a finitve volume approach, while the structure dynamic methods use finite element approaches.

3.1 Free-Surface RANS Method

The CFD solver is the commercial RANS software COMET. Here we present a brief description of the implemented method; a more comprehensive description can be found in [4],[14].

The code solves the Reynolds-averaged Navier-Stokes (RANS) equations in their integral formulation on a discrete number of finite control volumes in the time domain with an iterative SIMPLE scheme. Spatial discretisation schemes are second-order Central Differencing (CDS) for the mass conservation equation or, in case of incompressible fluids, the pressure correction equation. The transport equation for the momentum is discretised with a blending of first order Upwind Differencing Scheme (UDS) and CDS.

A VoF implementation is used for free-surface flows. An additional transport equation for a scalar flow quantity Γ is introduced. Γ represents the volume ratio of two different fluids, in this case air and water. Fluid properties like density and molecular viscosity in each control volume are set according to the properties of the involved fluids and their filling ratio Γ, so the flow equations are solved for an effective fluid. The discretisation scheme is HRIC (High Resolution Interface Capturing), a blending of first and second order differencing schemes. HRIC accounts for the position of the free surface (Γ=0.5) and switches between different differencing schemes to minimize the number of cells with values of $\Gamma\,\varepsilon\,]0,1[$ in order to retain a sharp interface.

[*]jan.oberhagemann@uni-due.de, University of Duisburg-Essen
[†]ould.el-moctar@uni-due.de, University of Duisburg-Essen

3.2 Structure Dynamics Methods

All implemented structure dynamics methods are based on Finite Element (FE) approaches and solve a linear equation of motion of the nodal degrees of freedom (DoF) $\mathbf{u}$,

$$\mathbf{M\ddot{u}} + \mathbf{C\dot{u}} + \mathbf{Ku} = \mathbf{f}, \tag{1}$$

in the time domain. $\mathbf{M}$, $\mathbf{C}$ and $\mathbf{K}$ are the constant mass, damping and stiffness matrices, respectively, and $\mathbf{f}$ is the time-dependent vector of exciting forces.

3.2.1 Timoshenko Beam Approach

The methods implements a simple finite element beam representation of the hull girder with third-order elemental shape functions and two nodal degrees of freedom - displacement and rotation. This allows us to consider planar bending and shear deformation in the time domain according to the Timoshenko approach, including linearised planar shear deformation.

Elemental properties - mass, mass inertia, section area moment of inertia and effective shear area - are constant over the element length. Further linearisations are made with respect to the position of the neutral axis - it is assumed to be a straight line - and with respect to displacement and rotation (linear deformation approach). A derivation of the implemented method can be found in [10],[8].

The method is limited to planar bending modes, e.g. vertical or horizontal two-node or three-node bending.

3.2.2 Entire Finite Element Model Approach

As the name already implies, this method enables to consider a full finite element model of the ship, theoretically in any required depth of detail. Restrictions are a linear correlation of stress and strain, and the necessity to have geometrically similar surfaces of the structural and fluid dynamic representation (fluid-structure interface). Mass and stiffness matrix can be imported from any FE program in the open matrix market format, allowing to use arbitrary elemental shape functions.

Realistic complex structural elastic deformations, e.g. torsion including warping effects, and stresses at structural details can be captured with this method.

A major drawback of this method is the need to solve a large system of linear equations, limiting the practical application to relatively coarse FE models.

3.2.3 Modal Decomposition Approach

A good compromise between the very fast beam model approach and the ability of the entire finite element approach to cover even complex structural deformations is a modal decomposition approach [2]. Eigenmode analysis of the FE model yields the natural modes of the model and corresponding natural frequencies. Fluid dynamic loads are transformed to modal forces and applied to a selected number of natural modes. This allows to consider all modes of interest, yet results in a reduced and fast to solve system of equations. However, the method still requires a FE model of the ship.

3.3 Fluid-Structure Coupling

The coupling scheme between CFD and CSD solver is an implicit two-way coupling. In every time step, the solutions on both fluid and structure domain are found in an iterative way, where in each iteration an update of the fluid and structural solution is found alternatingly as well as an update of the nonlinear 6DoF motion state. To improve numerical stability and convergence, underrelaxation is applied to all solvers.

Fluid forces are communicated to the 6DoF and structure solvers through pressure and friction forces acting on the hull, and hull motions and deflections are communicated to the fluid solver by means of CFD grid deformations according to the instantaneous position and deflection. Finite Element nodal displacements are transformed to boundary face node displacements of the fluid grid. Internal grid node displacements are computed via a finite element representation of the fluid volume grid, or with simpler and faster approaches that utilize simplifying assumptions made in the particular FE methods.

Mass inertia forces due to gravity and translatory / rotary ship motions (and corresponding time derivates) act on the ship hull structure as well. According to the instantaneous motion state determined by the 6DoF solver, these inertia forces are passed to the CSD solver in every iteration. The combined overall sums of fluid and inertia forces and moments equal zero when the iterative solution scheme has converged. This is a crucial point since the FE model is not supported by any bearings, and non-zero sums of forces or moments might cause the deformations of the finite element model to drift during the simulation.

The described coupling technique implicitly accounts for the mutual influence of fluid and structure. Therefore, no modelling of hydrodynamic added mass and damping effects is necessary, as is the case in potential theory based methods. On the other hand, accurate results in terms of hydrodynamic damping require careful grid generation and appropriate grid resolution of the CFD mesh.

The implemented methods allow us to parallelize computations. We use domain decomposition for the CFD solution domain and the CFD grid deformation. The 6DoF and CSD solver are not parallelized and are run on every processor, as the corresponding small systems of equations can not be parallelized efficiently.

4 Excitation Mechanisms

The traditional distinction between Whipping and Springing is mainly based on a difference in excitation mechanisms:

- *Whipping* as a transient effect is characterized by an initial impact and a decay of vibration with time. The initial impact is caused by slamming events, i.e. pressure pulses during water entry of parts of the ship structure. Slamming typically occurs in heavy sea states in combination with large ship motion and acceleration amplitudes.

- *Springing*, in contrast, is a resonance phenomenon. Comparatively small amplitude periodic excitations cause a significant vibration level, when the excitation period is at or close to resonance.

Despite this clear distinction, full scale measurement time signals of stresses often exhibit characteristics of both springing and whipping. We will discuss this issue later on.

Various full scale measurements have indicated the importance of fundamental two-node vertical bending vibration, [7],[11],[12],[13], which usually corresponds to the lowest natural frequency . Although some ship types, e.g. container ships with large deck openings, typically have the lowest natural frequency corresponding to fundamental torsion, torsional vibration is of secondary interest for these ships as well.

4.1 Impulse Excitation

Slamming impacts are characterized by high peak pressures and a relatively short duration. While the absolute peak pressure is of less interest, impact duration and the integral pressure impulse - pressure integrated in space and time - are the key quantities to assess the significance of an impact.

Accurate determination of impact pressures is a challenging task for VoF-based free surface RANS methods, because the discontinuity of density at the free surface is represented by a continuos transition from one fluid to another within at least one finite volume and one time step. Spatial and temporal refinement can reduce the transition, but they cannot eliminate it. Additionally, refinement in space and time significantly increases computational costs. Figure 1 shows time series of pressure peaks at five sensor locations on a wedge during free-fall water impact model tests, compared to numerical results on very fine grids. In Figure 2, pressure peaks measured for a ship model in regular waves are compared with computational results. Spatial and temporal resolution in computations are less fine in this case.

Both figures show a good agreement of the overall slope, but the RANS method is unable to fully capture the pressure peak. Looking in more detail at exemplary impact peaks obtained for the ship model, figure ???, computations predict a longer peak duration, a significantly less steep initial increase of local pressure and less pronounced peaks. These observations clearly relate to the VoF method. Very fine resolution like in the first example allows a better capturing of local pressures, while a coarser resolution in space and / or time results in smeared and less pronounced peaks.

Another well-known but important observation is that even in regular waves the peak pressures strongly vary, in both experiments and simulation.

However, comparing integral impulses leads to more optimistic conclusions. Variations of time-integrated pressure pulses are small, and numerics and experiments result in very similar local pressure pulses. Of importance for global structural responses are pressure forces impulses acting on the whole impact area.

To estimate the effect of prolongated and less pronounced impulses on the structural response, figure 4 illustrates, for idealised impulse shapes, the dynamic response amplification ratio related to the impulse duration ratio (impulse duration divided by response period). Typical impact durations of severe bow or stern flare slamming are of the order $0.5\,s$ to $1.5\,s$, depending on the type and intensity of the slamming impact, [9]. Comparisons of numerical results and model tests have shown a good agreement here, see e.g. also [3].

This finding can be drawn from figure 1 as well: Numerics and experiments yield the same deceleration of the wedge, there is no time leg between pressure pulses at different locations.

4.2 Resonant Excitation

Simple resonant wave excitation occurs when the wave encounter period equals the natural frequency of particular interest. In general, this corresponds to the two-node vertical vibration mode. Periodic force fluctuations due to action of waves (Froude-Krylov) and ship (wave diffraction and radiation caused by ship motions) are the source of vibration. A vast amount of linear theory methods is able to predict this type of springing with good accuracy. Anyway, waves of appropriate length to cause linear springing are short, even for relatively fast ships with low natural periods, and thus small of amplitude and wave energy. Linear springing cannot satisfyingly explain observed springing vibration level.

Higher order springing excitation is still a controversial issue. Several authors (e.g. [6],[11],[13]) investigated a sum-frequency approach, where at least two wave components found in a seaway contribute to springing, when the sum of their encounter frequencies equals the fundamental hull girder frequency. Other theories focus on non-linear effects in waves in addition to linear theory Airy waves, and higher order changes of ship sectional buoyancy and added mass in waves.

To our knowledge, all higher order springing theories found in the literature are based on potential theory for hydrodynamic analysis, mostly using strip theory. We suggest to use RANS / finite volume methods to implicitly account for non-linearities in springing excitation.

5 Damping

Structural and hydrodynamic damping is of primary importance to predict maximum springing responses. Amplitudes in resonance conditions are directly linked to the overall damping. The range of excitation frequencies that cause significant springing depends on the damping as well - the higher the damping ratio, the smaller the response amplitude in resonance, but the broader the range of frequencies of interest.

Also for whipping the damping ratio is important since it determines the decay rate of the free vibration after the initial impact. Although the typically small damping does not affect the maximum whipping response amplitude, it determines the number of response cycles at certain amplitude levels.

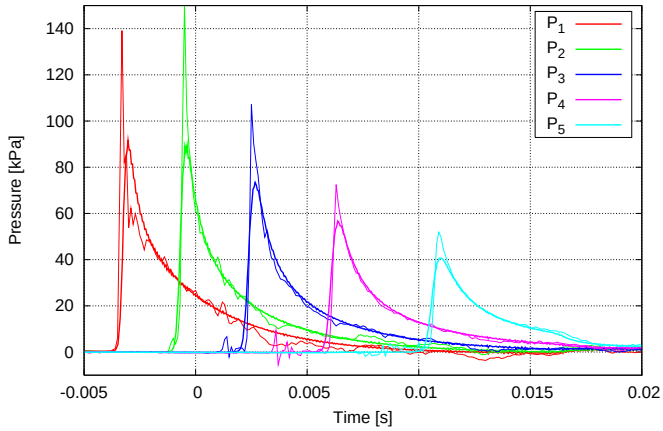

Fig. 1: Impact pressures during wedge free-fall water entry

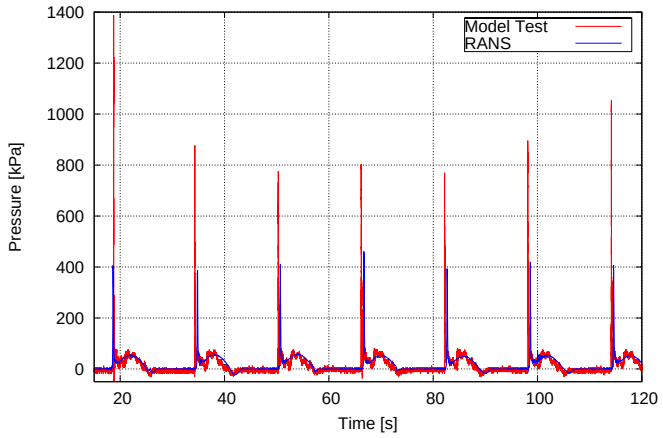

Fig. 2: Impact pressures in the stern region of a ship in regular waves

6 Combined Whipping and Springing

7 Conclusions

kommentare:

Plot noch mal neu machen, Zeitreihen unter /home/hk0440/RUN/EintauchVersuche/matthias/2D/testFall/reference

Plot noch mal neu machen, Zeitreihen unter ???

References

[1] Brunswig, J. & el Moctar, O.: Prediction of Ship Motions in Waves using RANSE. In: Proceedings of the 5th Numerical Towing Tank Symposium, Hamburg, 2004.

[2] Dilba, B.: Ein Verfahren zur Simulation von dreidimensionalen Strukturverformungen im Seegang mithilfe modaler Reduktion. Technical University of Hamburg-Harburg. Hamburg, 2008.

[3] El Moctar, O., Brunswig, J., Brehm, A. & Schellin, T.E.: Computations of Ship Motions in Waves and Slamming

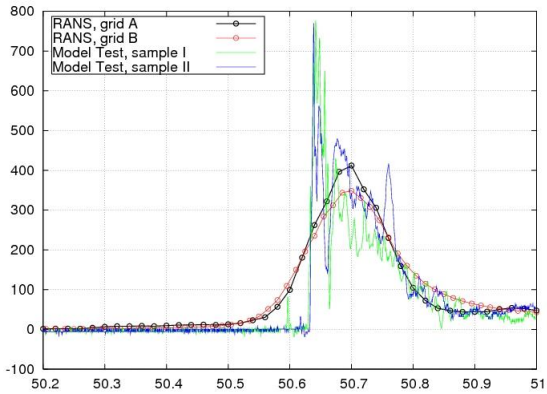

Fig. 3: Details of measured and computed pressure peaks

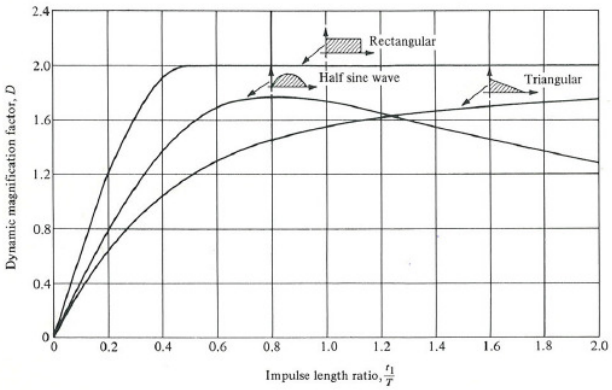

Fig. 4: Impulse shapes and duration and resulting dynamic amplification

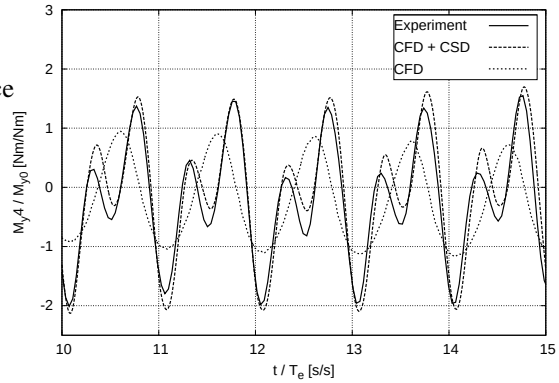

Fig. 5: Vertical Bending Moment of rigid versus elastic hull girder in higher order springing wave condition ($\omega_e = 2 \cdot \omega_n$)

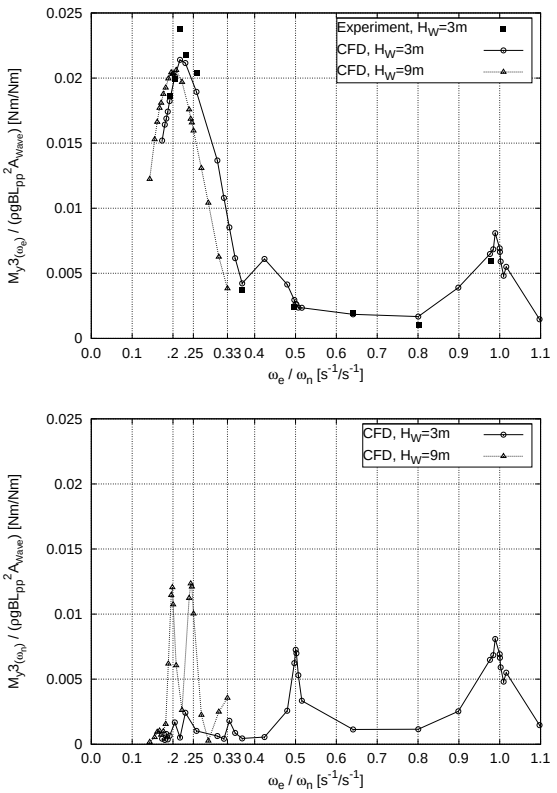

Fig. 6: Normalised vertical bending moment response at wave encounter frequency ω_e (top) and at two-node vibration frequency ω_n (bottom)

Loads for Fast Ships Using RANS. In: Proceedings of the International Conference on Fast Sea Transportation. St. Petersburg, 2005.

[4] Ferziger, J.H. & Periç, M.: Computational Methods for Fluid Dynamics. Springer, Berlin, 2002.

[5] Hong, S.Y.: Wave Induced Loads on Ships, Joint Industry Project II, First Year Model Test Report. Maritime and Ocean Engineering Research Institute, Seoul 2009.

[6] Jensen, J.J. & Pedersen, T.: Wave-Induced Bending Moments in Ships - A Quadratic Theory. Royal Institute of Naval Architects. London, 1978.

[7] Kahl, A. & Menzel, W.: Full-Scale Measurements on a PanMax Containership. ?????

[8] Oberhagemann, J.: A Numerical Method to Assess Effects of Whipping on Global Loads of Ships. Technical University of Hamburg-Harburg. Hamburg, 2006.

[9] Oberhagemann, J., el Moctar O. & Schellin, T.E.: Fluid-Structure Coupling to Assess Whipping Effects on Global Loads of a Large Containership. In: Proceedings of the 27th Symposium on Naval Hydrodynamics, Seoul, 2008.

[10] Söding, H.: Vibrationen von Schiffen I, Vorlesungsmanuskript Nr. 23, Institut für Schiffbau, Hamburg, 1987.

[11] Storhaug, G.: Experimental Investigation of Wave Induced Vibrations and their Effect on the Fatigue Loading of Ships. PhD thesis, Norwegian University of Science and Technology, Oslo, 2007.

[12] Storhaug, G., Vidic-Perunovic, J., Rüdinger, F., Holtsmark, G., Helmers, J.B. & Gu, X.: Springing / Whipping Response of a Large Ocean Going Vessel - A Comparison between Numerical Simulations an Full-Scale Measurements. In: Proceedings of Hydroelasticity in Marine Technology, Oxford, 2003.

[13] Vidic-Perunovic, J.: Springing Response due to Bidirectional Wave Excitation. PhD thesis, Technical University of Denmark. Lyngby, 2005.

[14] CD-Adapco: COMET User Manual 2.0. Nürnberg, 2002.

CFD Study on the Propeller-Hull-Interaction of Steerable Thrusters

Michael Palm, Dirk Jürgens, David Bendl
Voith Turbo Schneider Propulsion GmbH & Co. KG, Germany
michael.palm@voith.com

1. INTRODUCTION

Azimuth-steerable thrusters are widely used in the offshore industry for efficient dynamic positioning. Due to the thruster-hull and thruster-thruster interactions the installed propulsion system may experience severe efficiency losses at DP conditions.

To provide a better understanding of these phenomena the authors presented a study on the interaction effects for a semi-submersible drill rig at the Dynamic Positioning Conference 2008.[1] It was shown that for such a twin hull configuration an inclined rotational axis can to a large extend reduce the thrust losses. In Fig. 1 the pressure distribution on the second pontoon illustrates the differences in interaction losses due to different thruster inclinations.

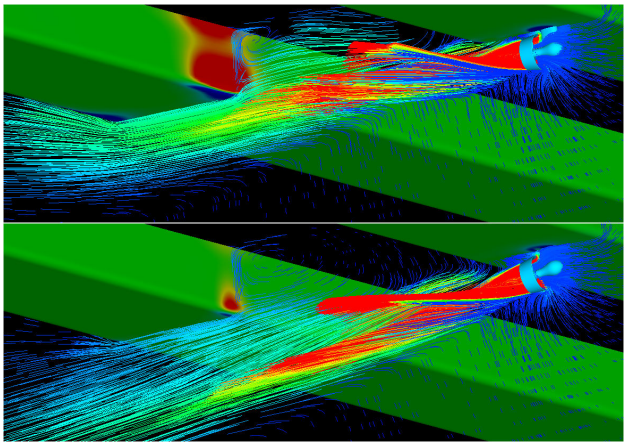

Fig. 1: Static pressure on second pontoon for 0° (top) and 8° axis tilt (bottom) on a twin hull configuration

In the current paper a CFD study is presented with the focus on a monohull vessel in order to detect possible benefits through axis tilting for this kind of ship class. Different thruster arrangements on a drill ship have been analysed to quantify the influence of thruster tilting with regard to interaction losses. The results for thrusters with gear-tilting are compared with a thruster that incorporates a horizontal propeller-axis and a tilted nozzle only.

The next section introduces briefly the solution method used. This is followed by sections describing the thruster and hull geometry and presenting the results of the CFD study. The final section summarizes the findings.

2. COMPUTATIONAL METHOD

All computations reported here are performed using the CFD software Comet. It is based on a finite-volume (FV) method and starts from conservation equations in integral form. With appropriate initial and boundary conditions and by means of a number of discrete approximations, an algebraic equation system solvable on a computer is obtained. First, the spatial solution domain is subdivided into a finite number of contiguous control volumes (CVs) which can be of an arbitrary polyhedral shape and are typically made smaller in regions of rapid variation of flow variables. The time interval of interest is also subdivided into time steps of appropriate size (not necessarily constant). The governing equations contain surface and volume integrals, as well as time and space derivatives. These are then approximated for each CV and time level using suitable approximations.

The flow is assumed to be governed by the Reynolds-averaged Navier-Stokes equations, in which turbulence effects are included via an eddy-viscosity model (k-ε or k-ω models are typically used). Thus, the continuity equation, three momentum component equations, and two equations for turbulence properties are solved. In addition, the space-conservation law must be satisfied because the CVs have to move and change their shape and location as the propeller starts to rotate. These equations are:

Mass conservation:

$$\frac{\mathrm{d}}{\mathrm{d}t}\int_V \rho \,\mathrm{d}V + \int_S \rho(\mathbf{v}-\mathbf{v}_\mathrm{b})\cdot\mathbf{n}\,\mathrm{d}S = 0$$

Momentum conservation:

$$\frac{\mathrm{d}}{\mathrm{d}t}\int_V \rho\mathbf{v}\,\mathrm{d}V + \int_S \rho\mathbf{v}(\mathbf{v}-\mathbf{v}_\mathrm{b})\cdot\mathbf{n}\,\mathrm{d}S = \int_S (\mathbf{T}-p\mathbf{I})\cdot\mathbf{n}\,\mathrm{d}S + \int_V \rho\mathbf{b}\,\mathrm{d}V$$

Generic transport equation for scalar quantities:

$$\frac{\mathrm{d}}{\mathrm{d}t}\int_V \rho\phi\,\mathrm{d}V + \int_S \rho\phi(\mathbf{v}-\mathbf{v}_\mathrm{b})\cdot\mathbf{n}\,\mathrm{d}S = \int_S \Gamma\nabla\phi\cdot\mathbf{n}\,\mathrm{d}S + \int_V \rho b_\phi\,\mathrm{d}V$$

Space-conservation law:

$$\frac{\mathrm{d}}{\mathrm{d}t}\int_V \mathrm{d}V - \int_S \mathbf{v}_\mathrm{b}\cdot\mathbf{n}\,\mathrm{d}S = 0$$

In these equations, ρ stands for fluid density, $\mathbf{v}$ is the fluid velocity vector and $\mathbf{v}_\mathrm{b}$ is the velocity of CV surface; $\mathbf{n}$ is the unit vector normal to CV surface whose area is S and volume V. $\mathbf{T}$ stands for the stress tensor (expressed in terms of velocity gradients and eddy viscosity), p is the

pressure, **I** is the unit tensor, ϕ stands for the scalar variable (k or ε or ω), Γ is the diffusivity coefficient, **b** is the vector of body forces per unit mass and b_ϕ represents sources or sinks of ϕ. Since the CV can move arbitrarily, velocity relative to CV surface appears in the convective flux terms, and the time derivative expresses the temporal change along the CV-path.

It is beyond the scope of this paper to go into all the details of the numerical solution method, so only a brief description is given here; details can be found in [2].

All integrals are approximated by midpoint rule, i.e. the value of the function to be integrated is first evaluated at the centre of the integration domain (CV face centres for surface integrals, CV centre for volume integrals, time level for time integrals) and then multiplied by the integration range (face area, cell volume, or time step). These approximations are of second-order accuracy, irrespective of the shape of the integration region (arbitrary polygons for surface integrals, arbitrary polyhedra for volume integrals). Since variable values are computed at CV centres, interpolation has to be used to compute values at face centres and linear interpolation is predominantly used. However, first-order upwind interpolation is sometimes blended with linear interpolation for stability reasons. In order to compute diffusive fluxes, gradients are also needed at cell faces, while some source terms in equations for turbulence quantities require gradients at CV centres. These are also computed from linear shape functions.

The solution of the Navier-Stokes equations is found by using a segregated iterative method, in which the linearised momentum component equations are solved first using prevailing pressure and mass fluxes through cell faces (inner iterations), followed by solving the pressure-correction equation derived from the continuity equation (SIMPLE-algorithm; see [2] for more details). Thereafter equations for volume fraction and turbulence quantities are solved; the sequence is repeated (outer iterations) until all non-linear and coupled equations are satisfied within a prescribed tolerance, after which the process advances to the next time level.

3. THRUSTER DESIGN

The thruster used in the current study is a Voith Radial Propeller (VRP) with an input power of 5500kW and a propeller diameter of 4.2m (Fig.2). This unit is equipped with a 98° bevel gear to implement the inclined rotational axis.
For comparison reasons all thruster arrangements on the drill ship have been simulated with the VRP at an 8° axis tilt and a rectangular radial propeller (RRP) with a horizontal rotational axis and nozzle inclination of 5°. All other geometrical features of the thruster have been left identical. Fig.3 shows both thruster configurations that have been used. The simulations were carried out at full scale.

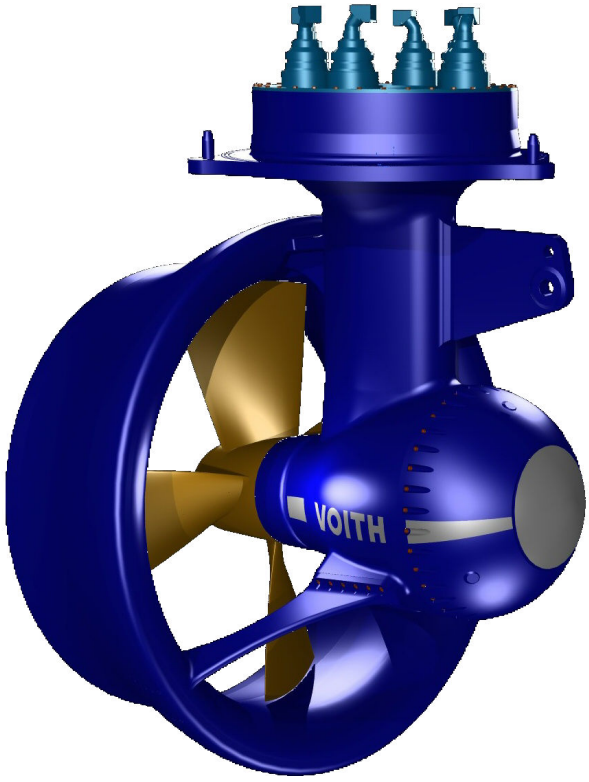

Fig. 2: Voith Radial Propeller 42-55

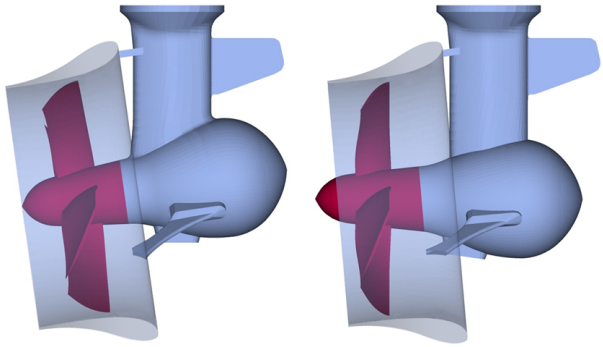

Fig. 3: VRP with 8° axis tilt (left) and RRP with 5° nozzle tilt (right)

The different nozzle and axis orientation lead to different performance characteristics. By adjusting the number of revolutions it was ensured, that both propellers generate the same amount of thrust.

4. INTERACTION LOSSES AT A SIMPLIFIED HULL SECTION

As a first step, the whole calculation setup was tested for plausibility at a simplified hull section with thrusters generating a transverse force. Fig. 4 shows the velocity field near the thruster and the resulting pressure distribution on the hull. As can be seen, the wake of the propeller interacts more pronouncedly with the hull in the RRP case. All computations have been carried out with a still standing vessel and an inflow velocity of zero.

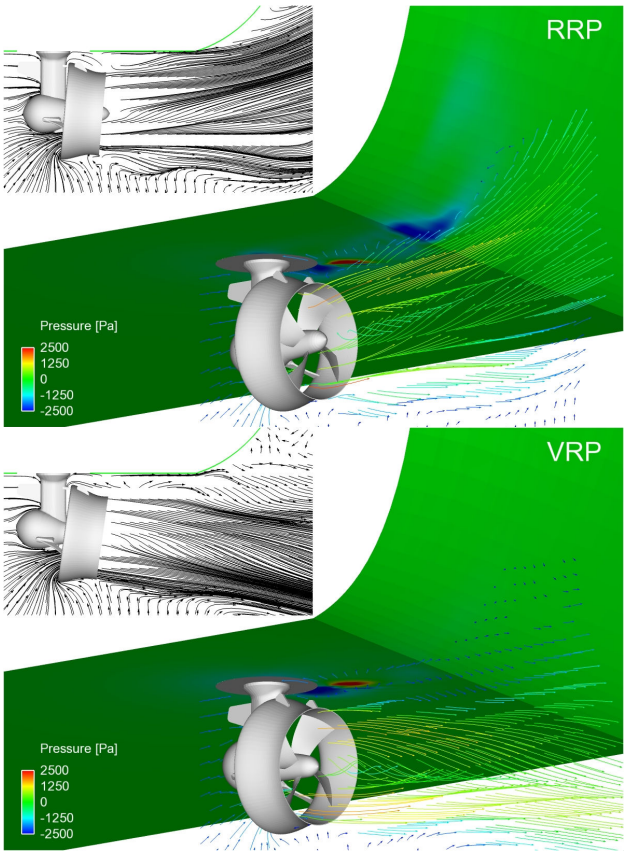

Fig. 4: pressure distribution on a hull section for the RRP (top) and VRP (bottom)

This is reflected through the region of lower static pressure in the area of the bilge radius.
This low pressure induces a force that opposes the nominal thrust direction of the propeller. As a result the effective thrust, which is meant to be the available force on the system hull-propeller, is decreased for the RRP.
While the thrust losses for the VRP amount to 1.2% they increase for the RRP to 4.2%.

5. DRILL SHIP DESIGN

The ship hull for this study was designed by Ulstein Sea of Solutions (Fig.5). The vessel has a length of 208m and a breadth of 32.2m. At an displacement of 42800t the draft amounts to 10.5m. The ship is equipped with six thrusters, three in the stern and three retractable types in the fore part.

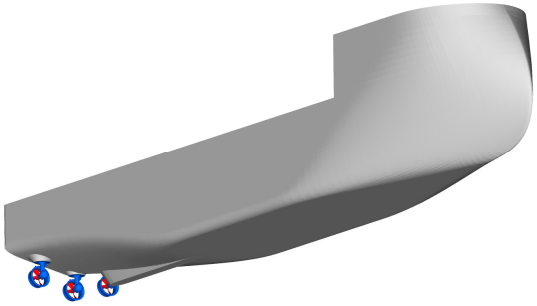

Fig. 5: hull lines by courtesy of Ulstein Sea of Solutions

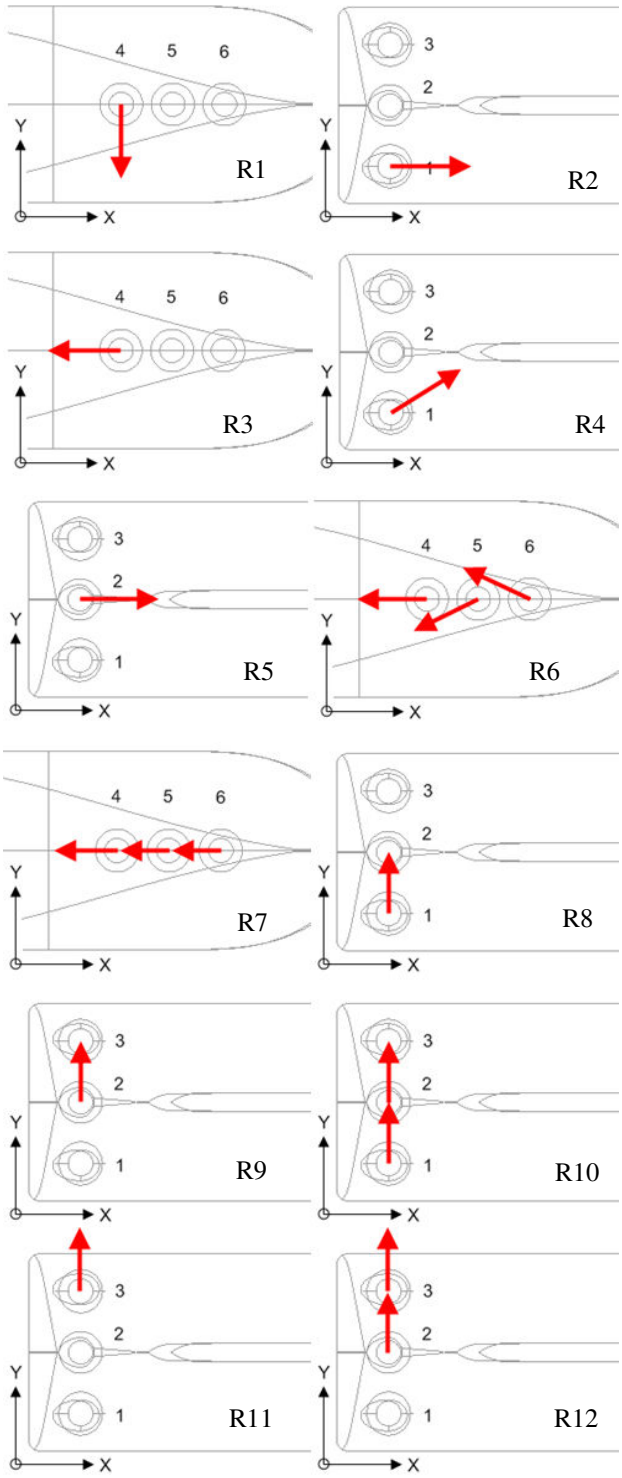

Fig. 6: investigated thruster configurations (arrows indicate wake direction)

In this study twelve different thruster arrangements were simulated. Fig.6 shows all configurations with the red arrows indicating the direction of the propeller wake. Although some thruster arrangements might be of academic nature due to lack of practical implementation, they have been investigated to cover a systematic range of different thruster-hull and thruster-thruster interaction incidents.

6. RESULTS

In the following section the results for all thruster configurations are presented and visualised for some selected cases. The denoted effective thrust for each configuration is defined as the total force acting on the system hull-thruster divided by the thrust of the propellers in each corresponding arrangement.
In the top part of Fig.7 the velocity field for arrangement R2 is shown, where the thrust is acting in sternwise direction. From the streamlines it can be concluded that the deflection ability of the inclined nozzle is somewhat limited compared to a fully inclined rotor axis.
The hull pressure in the lower part of Fig.7 indicates the unfavourable interactions which lead to an effective thrust of 91.8% for the RRP while the corresponding value for the VRP amounts to 96.1%.

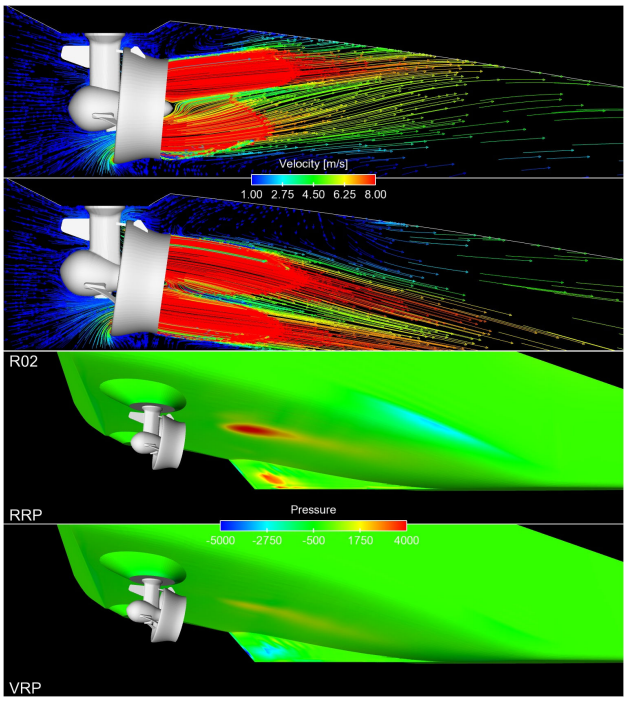

Fig. 7: velocity and pressure distribution for configuration R2 (RRP top, VRP bottom)

In case R6 the three bow thrusters are in focus. The two units near the bow have an azimuth angle of 35° towards the ships longitudinal axis.
The pressure distribution on the thrusters is depicted in Fig.8. In Fig.9 the velocity field illustrates the thruster-thruster interactions in this arrangement. In this case the effective thrust drops for the VRP to 89.6% and for the RRP to 83.8%. Due to the above-mentioned definition of the effective thrust, these values represent the losses due to hull-thruster interaction. An estimation of the thruster-thruster losses can be derived by comparison with configuration R3. Here the threefold thrust is approx. 22% higher than in R6. Comparing R6 with R7 the calculations show a thrust decrease for in-line arrangement in configuration R7 of approx. 37%.

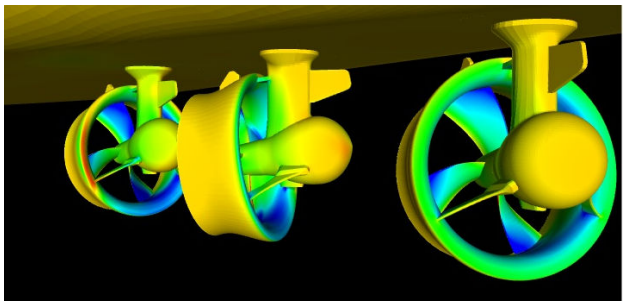

Fig. 8: velocity and pressure distribution for configuration R6

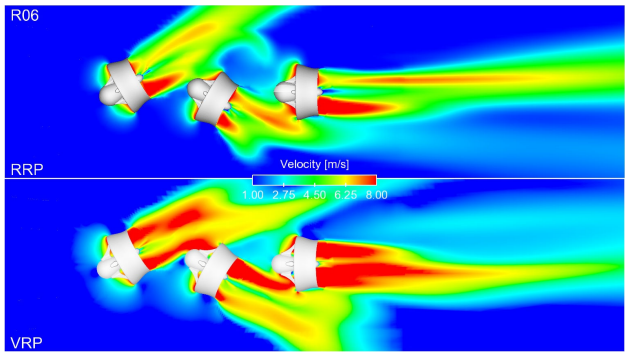

Fig. 9: velocity distribution for configuration R6

A configuration R8 that represents transverse thrust with the stern propellers is shown in Fig.10. Again an inclination of the rotor axis seems to be beneficial compared to a tilting of the nozzle only. The effective thrust decreases here to 76.8% for the VRP and to 60.7% for the RRP.

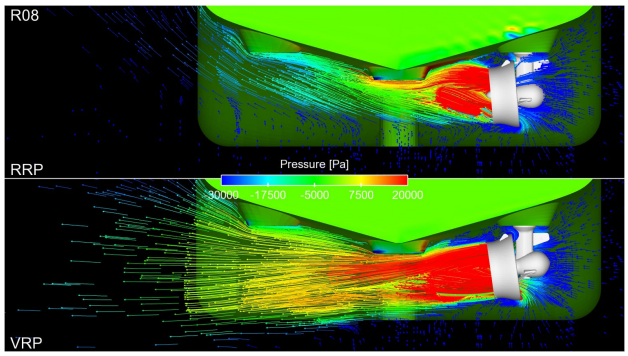

Fig. 10: velocity distribution for configuration R8

Activating also the centre thruster in addition to the starboard propeller leads to configuration R10. See Fig.11 for the velocity field. Here the effective thrust differences are of a similar magnitude compared to R8 giving a value of 89.0% for the VRP and 76.4% for the RRP.
Compared to the symmetrical arrangement of R12 where the port and the centre thruster are active (Fig.12), variant R10 produces 22% less thrust due to higher thruster-thruster losses. For R12, the effective thrust remains at a relatively high level of 94.8% for the VRP and 96.0% for the RRP evaluating the hull-thruster losses. Regarding the thruster-thruster losses, the variant

R12 generates 9% less thrust than the double value from configuration R9.

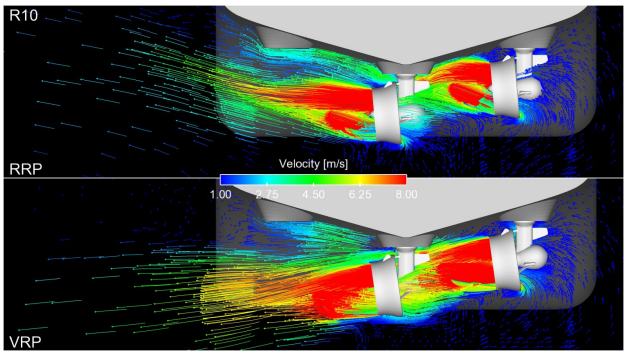

Fig. 11: velocity distribution for configuration R10

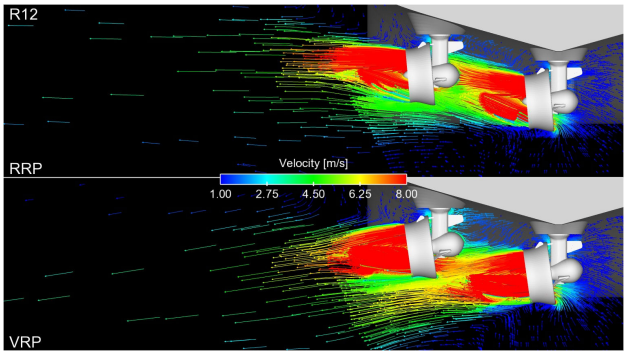

Fig. 12: velocity distribution for configuration R12

An overview on all investigated thruster arrangements is shown in Fig.13. The dark bars represent the effective thrust values for the VRP with 8° inclination while the bright bars indicate the corresponding values for the RRP with 5° nozzle tilt only.

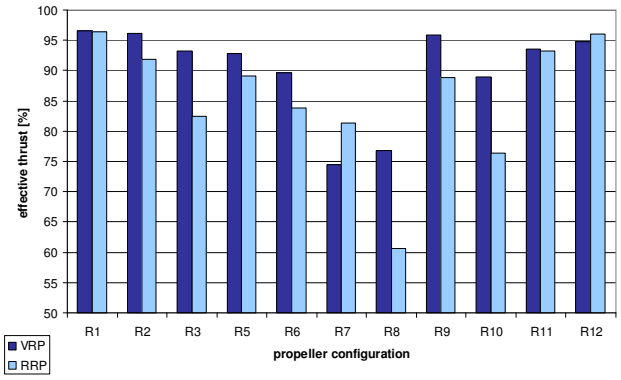

Fig. 13: effective thrust for different thruster arrangements

Configuration R4 was omitted from the diagram. Here the hull interaction led to very large hull forces that are directed almost perpendicular to the wake direction and therefore do not fit properly with the representation of the residual configurations. Fig.14 shows the flow pattern that makes the skeg act as a hydrofoil producing considerable lift forces.

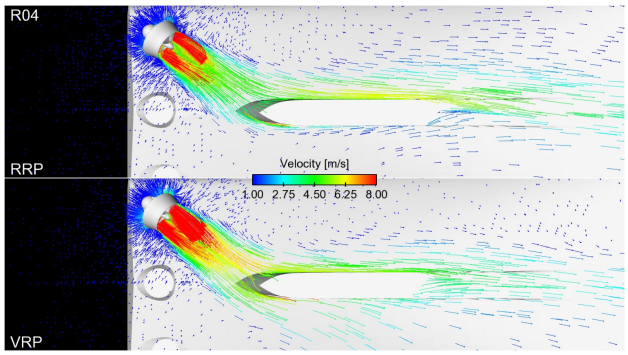

Fig. 14: velocity distribution for configuration R4

7. CONCLUSIONS

Except for variant R7, which corresponds to the in-line arrangement of the three bow thrusters and is avoided in practice anyhow, and variant R12 with only minor differences, all configurations have shown less thruster-hull or thruster-thruster interaction losses incorporating a 8° axis tilt.
As a result of the investigation, it can be concluded that tilting the axis by gear-tilt also offers advantages regarding the interaction effects for a monohull vessel.

8. REFERENCES

[1] D. Jürgens, M. Palm, A. Amelang, T. Moltrecht:
Design of Reliable Steerable Thrusters by Enhanced Numerical Methods and Full Scale Optimization of Thruster –Hull Interaction Using CFD
Dynamic Positioning Conference, Houston, 2008

[2] J. H. Ferziger, M. Perić:
Computational Methods for Fluid Dynamics
3rd ed., Springer, Berlin, 2003

Using Overlapping Mesh System to Develop a General Wavemaker

Roozbeh Panahi
Transportation Research Institute, Tehran, Iran, roozbeh_panahi@yahoo.com

Mehdi Shafieefar
Tarbiat Modares University, Tehran, Iran, shafiee@modares.ac.ir

INTRODUCTION

A Finite Volume (FV) approach has been introduced towards reaching virtual reality in hydrodynamics, although there is still a long distance. It handles free/forced motions of floating and/or submerged structures in the context of a viscous incompressible two-phase flow. The wave can also be generated here in the solver, using a Dirichelet boundary condition or a wavemaker of any type. Such an algorithm includes three major parts as well as coupling the pressure and the velocity fields, capturing the free surface and finally taking into account arbitrary motions of rigid structures. Therefore, a fractional step method is implemented to solve the flow field. A volume fraction transport equation is solved to capture the interface of two phases. After all, an overlapping mesh system is executed to simulate motions. Governing equations are reviewed in the next section. They have to be revised according to requirements in simulation of two-phase flow using FV discretisation in moving meshes. Then, discretisation of governing equations is briefly presented following by the solution of the Navier-Stokes equations. Some notes in an overlapping mesh with simple and novel solution to couple mesh components; especially in the case of a two-phase flow; are also included. Finally, regular and irregular waves are generated and motions of a structure are also recorded in the wave tank.

GOVERNING EQUATIONS

Differential equations which govern on encountered environment have to be revised according to FV discretisation, two phase simulation and mesh motions [1]. So, they will become as follows:

$$\frac{d}{dt}\int_V \rho_{eff}\, dV + \int_A \rho_{eff}\, \mathbf{u_{rel}}.\mathbf{n}\, dA = 0 \tag{1}$$

$$\frac{d}{dt}\int_V u_i\, dV + \int_A u_i\, (\mathbf{u_{rel}}.\mathbf{n})\, dA = -\int_A \frac{1}{\rho_{eff}} P n_i\, dA + \int_A \nu_{eff}\, \vec{\nabla} u_i.\mathbf{n}\, dA + \int_V g_i\, dV \tag{2}$$

$$\frac{d}{dt}\int_V \alpha\, dV + \int_A \alpha\, \mathbf{u_{rel}}.\mathbf{n}\, dA = 0 \tag{3}$$

where density and dynamic viscosity of the effective phase as a combination of phases volume fraction (α) is calculated as below:

$$\begin{aligned} \rho_{eff} &= \alpha\rho_1 + (1-\alpha)\rho_2 \\ \nu_{eff} &= \alpha\nu_1 + (1-\alpha)\nu_2 \end{aligned} \tag{4}$$

Also, $\mathbf{u_{rel}} = \mathbf{u} - \mathbf{u_m}$ is the fluid velocity vector $\mathbf{u}$ relative to the mesh velocity vector $\mathbf{u_m}$ and $\mathbf{n}$ represents a unit vector normal to a Control Volume (CV) face. u_i is the velocity component in the i Cartesian direction, P stands for the pressure, n_i is the i Cartesian direction component of $\mathbf{n}$ and g_i indicates the gravity component in this direction.

Movements of rigid bodies are also included in this study. They are calculated based on loads acting on the body, by solving the linear and angular momentum equations. Such loads can be raised from effects of flow field, body weight and probably external components. Rigid body motion equations are treated in a Global Coordinate System (GCS); a non-rotating, non-accelerating Newtonian reference system:

$$\sum \mathbf{F} = m\mathbf{a}_G \tag{5}$$

$$\sum \mathbf{M}_G = R I_G R^{-1} \vec{\alpha} + \vec{\omega} \times R I_G R^{-1} \vec{\omega} \tag{6}$$

where, in Eq.(5) $\mathbf{F}$ $[N]$ is the resultant force vector acting on the body. m $[kg]$ represents the mass of the body and $\mathbf{a}_G$ $\left[\frac{m}{s^2}\right]$ is the acceleration vector of the mass center of the body. Besides, in Eq.(6) $\mathbf{M}_G$ $[N.m]$ is the resultant moment vector at the mass center of the body and I_G $[kg.m^2]$ denotes the tensor of moment of inertia with respect to the mass center of the body. Additionally, $\vec{\omega}$ $\left[\frac{rad}{s}\right]$ is the angular velocity vector of the body and $\vec{\alpha}$ $\left[\frac{rad}{s^2}\right]$ corresponds to the angular acceleration vector of the body. R $[1]$ stands for the transformation matrix from the BCS to the GCS where the BCS; a Body-fixed Coordinate System; is set to be originated at the mass center of the body, while maintaining its orientation. The columns of R are the unit vectors x, y and z attached to the BCS. They can be expressed in terms of the Eulerian angles.

DISCRETISATION

Momentum conservation equations

The unsteady term can be replaced by the product of the value of the integrand at the CV center and the volume of the CV. The convection term is also discretised using the Gamma interpolation [2]. Besides, Piecewise Linear Interpolation (PLI) is implemented to deal with the spatial discretisation of the pressure term [3]. The diffusion term is treated by the over-relaxed interpolation [2] and finally, the gravity term is approximated as well as the unsteady term. Also, 1st order Euler implicit scheme is implemented for temporal discretisation of the unsteady term as well as the gravity term. 2nd order Crank-Nicholson is also used for convection and diffusion terms. About the pressure term, it has been discretised by 1st order explicit scheme in the momentum conservation equations.

Volume fraction transport equation

The spatial unsteady term is done similar to that of the momentum conservation equations. About its temporal discretisation, the first-order Euler implicit scheme is not a good option when wave generation and propagation are included. So, the 2nd order three-time-levels scheme which proposes a minimum level of diffusion, is used.
Also, the Compressive Interface Capturing Scheme for Arbitrary Meshes (CICSAM) [4] is applied for spatial discretisation of the convection term as well as Crank-Nicholson interpolation for its temporal discretisation according to an investigation conducted by the authors [5].

COUPLING OF THE PRESSURE AND THE VELOCITIS

To compute the pressure and the velocity fields, the fractional step method of Kim and Choi [4] is implemented by small modifications, as shown in Fig.1.

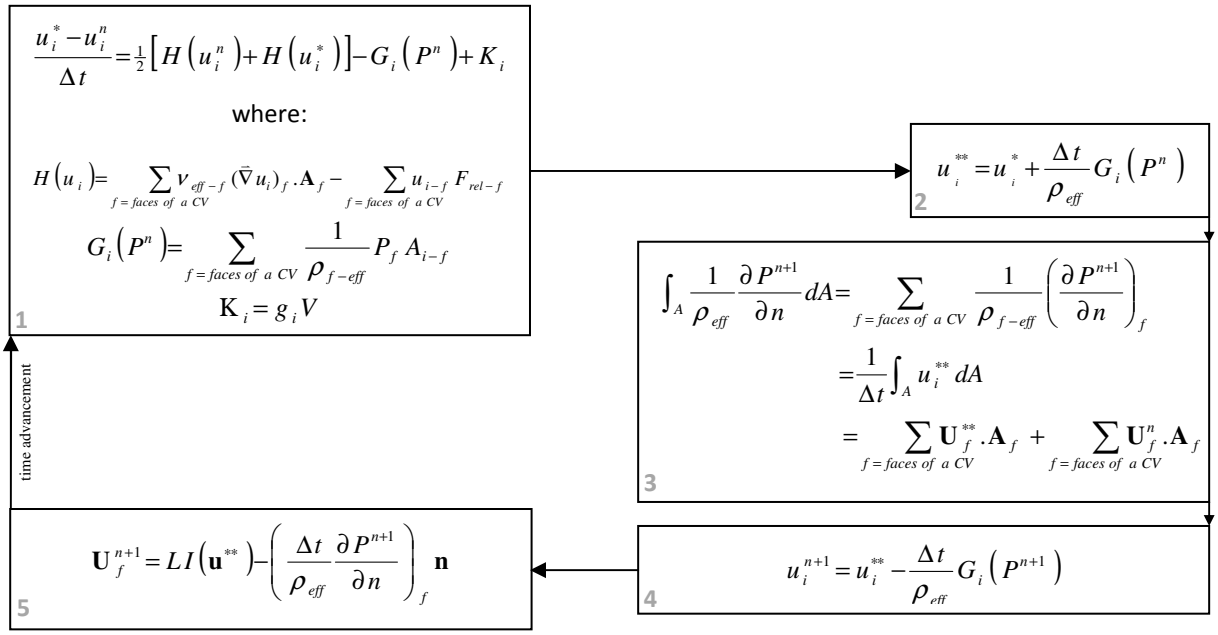

Fig.1 Coupling of the pressure and the velocities

OVERLAPPING MESH

As mentioned earlier, rigid body motions must be taken into account. Here, an overlapping mesh strategy; also known as chimera or overset mesh; is implemented among a wide variety of choices in this area such as re-mesh, deformable mesh and also Cartesian mesh. In this study, the overlapping mesh system consists of two or more mesh components: a stationary background mesh irrespective of motions and one or more moving boundary-fitted body-attached overset meshes, see Fig.2. Mesh components are not required to match in any especial way, but they have to overlap sufficiently to provide the means of coupling the solution on each of them.

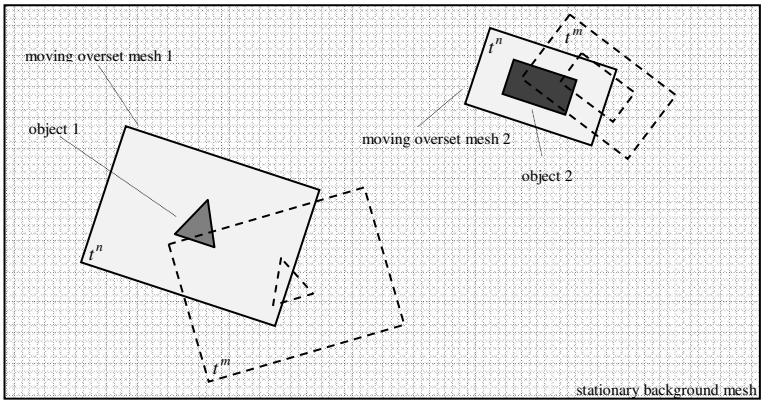

Fig.2 Overlapping mesh strategy; computational domain in two time steps

The overlapping mesh computation was performed firstly in 1981 to facilitate mesh generation in the case of complex boundaries [8]. It was later used to predict forced relative motions by Buning et al. [9] and also aerodynamic problems by Chen et al. [10]. It is just recently used in marine applications due to difficulties with an interfacial flow by Carrica et al. [11]. Using the overlapping mesh, flow variables have to be non/conservatively interpolated between the overlapped meshes to exchange the information. Numerical results show that neglecting the conservation accompanying with major simplicity in the algorithm is not an adverse assumption in encountered problems. However, the utilized overlapping mesh consists of three distinct steps which will be presented briefly in the following sub-sections.

Identification of CVs

When all mesh components necessary to appropriately cover the computational domain are generated, the next step is to identify the characteristic of all CVs according to their role in the solution process. They are among discretisation cells, interpolation cells or inactive cells. This job is accomplished using [12] is used in this study.

Coupling of mesh components

Here, a variable at an interpolation cell of a mesh component; identified in the previous step for both background and overset meshes; is obtained by interpolation of the variable from the overlapped mesh. The later mesh is called the donor mesh. Therefore, an interpolation stencil must be constructed for each interpolation cell of the considered mesh from CVs of the corresponding coincident mesh (donor mesh). A CV whose center is closest to the center of the interpolation cell (host cell) is the base of an interpolation stencil. Any additional cells on the donor mesh contributing to the interpolation formula come from the immediate neighborhood of the host cell. In the present study a neighbor-to-neighbor searching algorithm proposed by [13] is employed to accomplish the task of host searching. Then, a fully implicit algebraic equation for an interpolation cell is created as $\varphi_I = \varphi_H + \left(\bar{\nabla}\varphi\right)_H . \left(\mathbf{r}_I - \mathbf{r}_H\right)$ for variable φ which is velocity components, pressure and also volume fraction. Here, $\mathbf{r}$ indicates a vector connecting the origin to the interpolation (I) as well as the host (H) cell. Besides, φ_f appeared in calculation of $\left(\bar{\nabla}\varphi\right)_H$ is approximated using LI except in the case of pressure, where P_f is approximated using PLI [3]. Numerical results obviously show the efficiency of such a simple approach in complicated two-phase flows.

Solution of discrete equations

One can go back and forth between mesh components [14] or solve all mesh components simultaneously [12]. Using the former approach, information exchanging between meshes has a lag by an outer iteration and more iterations as well as stronger under-relaxation may be required to achieve a converged solution. In addition, to obtain a consistent pressure field in the entire domain, the reference pressure on each mesh component needs to be corrected in such a way that the pressure levels on all meshes are compatible with each other. Having all this in mind, the later approach is implemented in this study. Here, a global matrix has to be constructed including all cells of available meshes. The procedure includes preparing the equations in all meshes and then, renumbering the overset mesh by a simple shift as the total number of cells in the background mesh to assemble a global matrix.

Assume A and B as the background and the overset meshes, respectively. Equation for a discretisation cell (D) of A mesh is:

$$a_{D-A}\,\varphi_{D-A} = \sum_{ngb=neighbor\ CVs\ in\ \ A\ mesh} a_{ngb-A}\,\varphi_{ngb-A} + S_{D-A} \tag{7}$$

Equation for an interpolation cell (I) of A mesh (Eq. (4)) is also rearranged to represent a form similar to that of a discretisation cell based on its interpolation stencil on B mesh:

$$a_{I-A}\,\varphi_{I-A} = \sum_{ngb'=host\ cell\ and\ its\ neighbor\ CVs\ in\ B\ mesh} a_{ngb'-B}\,\varphi_{ngb'-B} + S_{I-A} \tag{8}$$

It is obvious that interpolation cells play an implicit rule in the solution procedure. Equation for an inactive cell (IA) of A mesh is prepared as well as $a_{IA-A}\,\varphi_{AI-A} = \varphi^{*}_{IA-A}$ where $a_{IA-A} = 1$ and φ^{*}_{IA-A} is the last known value of the inactive cell. After constructing analogous equations for *B* mesh, it is time to assemble the global matrix for variable φ using new continuous cell numbering.

NUMERICAL RESULTS

Wave generation by a Dirichelet boundary condition

For small amplitude waves, the velocities can be derived from the linear wave theory based on the potential flow. By assuming deep water, a zero-gradient boundary condition is used for all quantities except at the inlet where the velocity is conducted by a Dirichelet boundary condition of analytical velocities. Also, the numerical grid used to resolve the wave profile has 20 CVs per wavelength and 8 CVs in wave height. It must mentioned that using a numerical beach with gradually coarsen grids is very important to prevent probable wave reflection from the outlet boundary [15]. Small amplitude waves of an amplitude of a = 0.001 m and a circular frequency of $\omega = 17.73 s^{-1}$ have been generated first in the numerical tank. Fig.3 shows the comparison of wave profile between computation and the linear theory for one wavelength. As can be seen, the sinusoidal wave profile agrees very well with the analytical solution according to the linear wave theory. So, it has been shown that potential wave theory can be used in specifying the velocities at the inlet boundaries for wave generation in a numerical water tank with a satisfactory accuracy. However, attention has to be paid to the damping of wave amplitude in space and time during propagation of waves. Generally, the wave-damping factor can be influenced by (a): Grid resolution (the number of cells per wavelength and wave height) and (b): Temporal discretisation of the unsteady term of volume fraction transport equation. A small amplitude wave with a = 0.001 m and λ = 0.2 m has been generated here to show the effect of aforementioned parameters, see Fig.4.

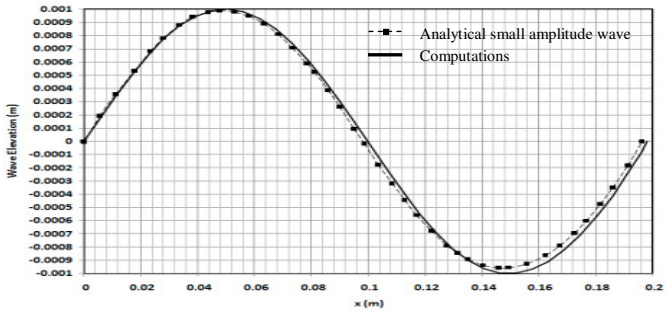

Fig.3 Wave profile comparison in one wavelength for a small amplitude linear wave

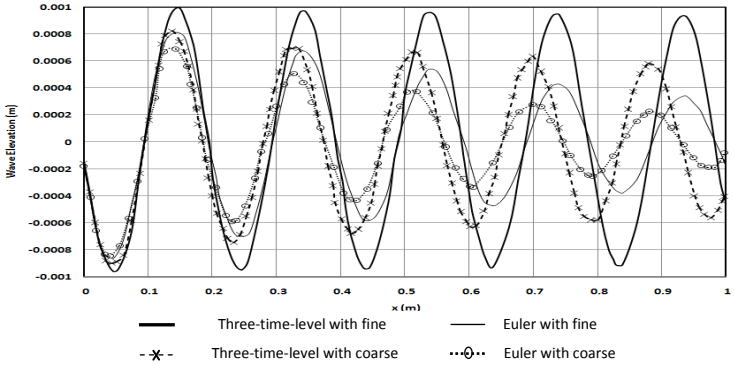

Fig.4 Effect of grid resolution and temporal discretisation on wave quality

The coarse grid used here has 10 cells per wavelength and 16 cells per wave height and the fine grid has doubled cells per wavelength. It can be observed that both grid refinement in the direction of wave propagation and the time integration scheme have strong influence on the damping factor. The result from the second-order three-time-level scheme and the fine grid seems to be rather satisfactory, but unacceptable results are produced by the coarse grid and the Euler time integration scheme. The first-order Euler scheme produces large numerical diffusion as expected, which is deteriorated if the gird is coarse.

Wave generation by a wedge-type wavemaker

Here, a plunger wavemaker [16] is simulated to validate the method in the case of a forced body motion, see Fig.5. The wedge has a sinusoidal vertical motion as $z=\sin(\sqrt{9.81}t)$ where the overset mesh also follows its motion. While, the background mesh remains stationary during the wave generation. No-slip and zero-gradient boundary conditions are applied for velocity and pressure as well as volume fraction at all boundaries, respectively. The computational domain includes an overset mesh of 16000 CVs with aforementioned vertical sinusoidal motion and a stationary background mesh of 75000 CVs. Besides, in order to minimize the reflection of the flow from the right wall of the wave tank, a damping zone is considered through the last $16d$ of its length, see Fig.5. Snapshots of the free surface are illustrated after the beginning of wavemaker harmonic motion in Fig.6. There is an approximately similar wave due to wedge motion after 75 s from the beginning of the wave generation. Besides, Fig.7 shows comparisons of the results with numerical data from the ISOPE Workshop [16] in the case of surface elevation. Fig.8 also shows calculated vertical force acting on the wedge in comparisons to other studies [16].

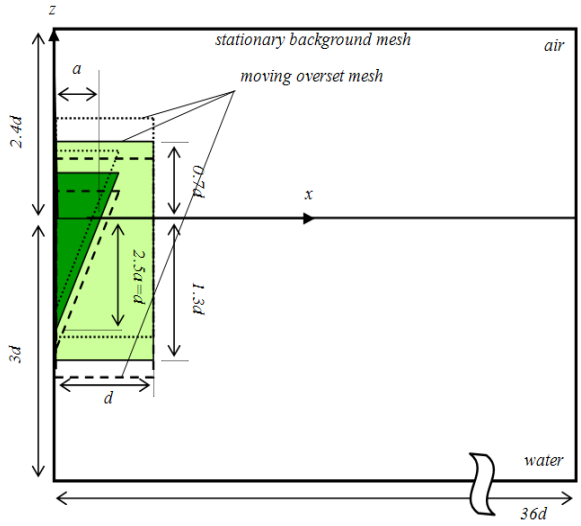

Fig.5 Schematic of plunger wavemaker; a=1m

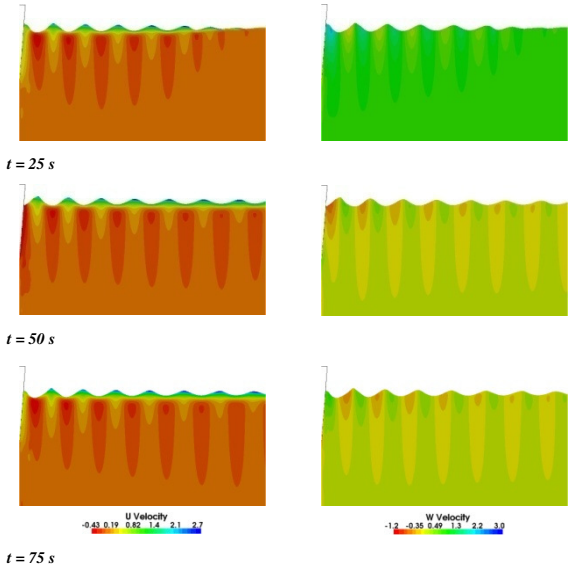

Fig.6 Free surface snapshots due to the vertical oscillations of the wedge in the first 58m of the tank; u and w velocities distribution is presented

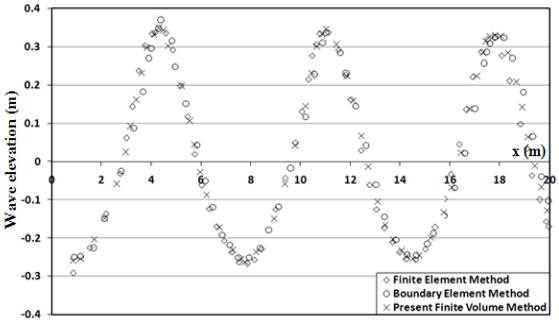

Fig.7 Free surface in the wave tank where wedge is at its mean position moving up; results of a FEM and a BEM simulations are extracted from ISOPE workshop[16]

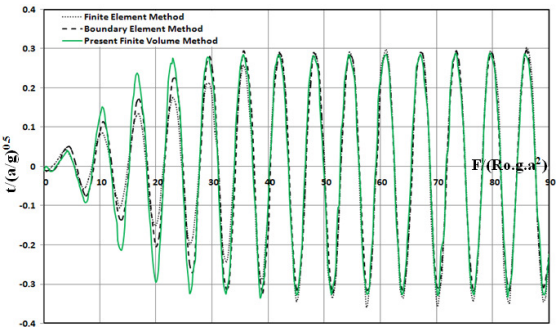

Fig.8 Heave force on the wedge

Wave generation by a flapping-type wavemaker

Here, regular wave is generated by a flapping-type wavemaker where the amplitude of its motion at the still water level is 15 mm with a period of 1.0 s and 3-DoF motions of a box are recorded, see Fig.9. The averaged density of the box is $680\frac{kg}{m^3}$. Boundary conditions are applied similar to those of the previous test case. However, surge motion of the box is typically presented in Fig.10 and compared to experimental data [17]. The agreement is satisfactory except at the initial stage, where small disturbances may exist in the experiment. Cell identity is typically shown in Fig.11 around the box at t=8*s*. It obviously shows the difference between cell sizes. A snapshot of the computational domain is also presented in Fig.12. More results such as other motions and discussions will be delivered when presenting the paper.

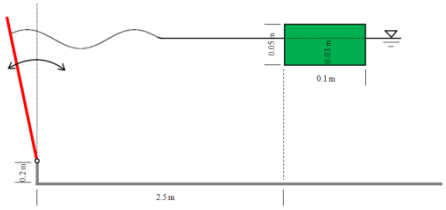

Fig.9 Schematic of box motions in a paddle-type wavemaker

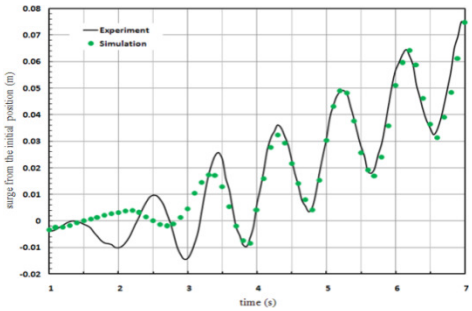

Fig.10 Surge motion of the box; comparison of simulation and experimental data [17]

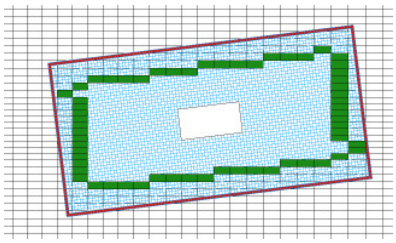

Fig.11 Cell Identity around the box at t= 8*s*
red: interpolation cell of overset mesh,
green: interpolation cell of background mesh

Fig.12 An snapshot of the computational domain at t= 8*s*

REFERENCES

1. R. Panahi, E. Jahanbakhsh and M.S. Seif, *Ocean Eng.* **36**, 256 (2009).
2. H. Jasak, *PhD Thesis*, University of London (1996).
3. E. Jahanbakhsh, R. Panahi and M.S. Seif, *Int. J. Numer. Meth. Heat Fluid Flow*, **17(4)**, 384 (2007).
4. O. Ubbink and R.I. Issa, *J. Comp. Phys.* **153(1)**, 26 (1999).
5. R. Panahi, E. Jahanbakhsh and M.S. Seif, *Iranian J. Sci. Tech.* **29(B6)**, 539 (2005).
6. D. Kim and H. Choi, *J. Comp. Phys.* **162(2)**,411 (2000).
7. R. Panahi, E. Jahanbakhsh and M.S. Seif, *Appl. Ocean Res.* **28(3)**, 171 (2006).
8. E.H. Atta, *AIAA Paper,* **81-0382** (1981).
9. P.G. Buning, T.C. Wong, A.D. Dilley and J.L. Pao, *AIAA Paper,* **2000-4009** (2000).
10. H.C. Chen, W.M. Lin, and W.Y. Hwang, *24th ONR Symp. Naval Hydrodynamics*, (2002).
11. M. Carrica, R.V. Wilson, R.W. Noack and F. Stern, *Comput. Fluid*, **36(9)**, 1415 (2007).
12. H. Hadzic, *PhD Thesis, Teschnichen Universitat Hamburg-Harburg,* (2005).
13. R. Löhner, *J. Comp. Phys.* **118(2)**,380 (1995).
14. D. Drakakis, J. Majewski, J. Rokichki and J. Zoltak, *Comput. Meth. Appl. Mech. Eng.* **190**, 5173 (2001).
15. J.C. Park and H. Miyata, *J. Soc. Naval. Arch. Japan,* **189**, 13(2001).
16. K. Tanizaw and A.H. Clément, *10th ISOPE Conf.* (2000).
17. Y. Xing-Kaeding, *PhD Thesis*, Teschnichen Universitat Hamburg-Harburg, (2004).

Computation of Scale Effects in Free-Surface Flows near a Ship's Transom

Auke van der Ploeg, A.v.d.Ploeg@MARIN.NL
Karl Chao, Chao@hsva.DE
Jochen Marzi, Marzi@hsva.DE
Jeroen Wackers, Jeroen.Wackers@ec-nantes.FR

1. Introduction

In the European project VIRTUE, an EC-funded project under the 6th Framework program, several participants have cooperated in carrying out research to advance the role of CFD in ship hydrodynamics and design [2]. One of the 5 work packages dealt with the computation of the steady flow around a ship hull in still water. A prominent theme in this work package was the improvement of the computation of free-surface viscous flow around the hull and the wave pattern and their scale effects. Strong improvements were obtained in the numerical accuracy, which was clearly demonstrated by the fact that in a VIRTUE workshop in 2007, in which participants were asked to submit computations of the viscous flow around a container ship, the 'Hamburg Test Case', two methods that differ in almost every respect gave very similar results as well in the computed wave patterns as in the wake fields, resistances and scale effects [3].

In this paper we focus on the computation of the viscous free-surface flow including scale effects for a more difficult test case: a container ship with a partly wetted transom. This wetted transom poses some extra challenges for a computational method: the transition between the wetted and dry regime and the details of the flow and the free surface (possible wave breaking) behind the wetted part of the transom are hard to capture. The challenge is to compute accurately the flow both on model scale and full scale. Scale effects near transoms can become very important when at full scale a smaller part of the transom is wetted than at model scale, since this can have a strong effect on the resistance.

We will present mutual comparisons of wave elevations computed by three free-surface RANS methods, together with a comparison with free-surface measurements at model scale. We will focus on the results and scale effects in the free surface near the transom. There are strong differences between the computational methods in the modelling of the viscous flow and the free surface, as well as in the iterative method. The question is whether or not we can get good agreement with measurements at model scale, and how well the computed scale effects are in common agreement.

2. Test case

The test case considered is the so-called Virtue Container Ship (VCS). Extensive experimental data at model scale for the wave heights at different drafts and speeds has been obtained by HSVA in two research projects. During the ABSS project [8] a new optical technique for the measurements of wave patterns in areas otherwise not accessible with standard wave probes has been developed. This technique has been applied to a number of test cases and was used also in the VIRTUE project to measure the wave elevation behind the stern of the VCS. The aim of the measurements was to supply quality measurements of the stern flow and wave elevation behind the stern of ships for different floating conditions, characterised by either a fully wetted or a free transom. The novel measurement technique featured a dedicated test rig supporting a set of line lasers in combination with a water spray curtain behind the transom of a ship model that was installed on the Towing Carriage. The stern wave at speed could be visualised in different positions. Photographs taken during runs were analysed with a dedicated image processing algorithm and translated into wave elevations behind the transom. A validation was performed with wave cuts besides the model which could also be measured using conventional wave probes. Figure 2.1 illustrates a set-up measuring 6 wave cuts behind the transom of the VCS.

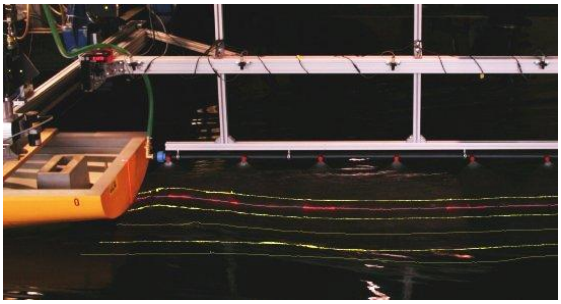

Fig. 2.1 *Optical Wave Measurements behind the transom of the VIRTUE container ship model.*

In this paper, we consider two static drafts: *T=11.3m* and *T=12.5m* and only one speed: 26 kts. No appendages and rudder have been taken into account, and computations addressed an unpropelled (towed) condition.

Computations for both model scale (1 : 29.1) and full scale were performed. The Reynolds number is $Rn = 1.85 \times 10^7$ for model scale and $Rn = 2.9 \times 10^9$ for full scale. The Froude number is *Fn=0.272*, and the ship's length is L_{PP}*=246.4m*, *B=32.2m*.

3. Computational methods

As mentioned before, we will compare the results of three different RANS methods: the ISIS-CFD flow solver [4], developed by EMN (Equipe Modélisation Numérique, i.e. CFD Department of the Fluid Mechanics Laboratory at Central Nantes), PARNASSOS [1], a RANS solver developed and used by MARIN and IST, and COMET used by HSVA.

The three methods use different computational approaches. PARNASSOS differs in almost every regard from the other two RANS methods:

1. Finite differences against finite volume.
2. Block-structured against unstructured grids.
3. No wall functions against wall functions.
4. Directly coupled versus pressure correction.

In addition, the approach for incorporating the free surface boundary conditions in PARNASSOS is completely different from what the other two methods, being steady instead of time-dependent. ISIS-CFD and COMET follow a time-dependent procedure, integrating the problem in time, starting from an initial condition, and continuing until a steady result is obtained. PARNASSOS uses the 'steady iterative formulation' [5, 6] which involves no time-dependent terms; neither in the momentum equations, nor in the free-surface boundary conditions. Furthermore, PARNASSOS uses a surface fitting approach whereas the other two methods use surface capturing, and in PARNASSOS we consider one-phase flow whereas the other two methods compute two-phase flow. More details about the RANS solvers PARNASSOS and ISIS-CFD, and about their free surface treatment and solution procedure can be found in [3].

In PARNASSOS, the one-equation turbulence model of Menter was used, where in ISIS-CFD Menter's two-equation k-omega SST model and in COMET RNG k-epsilon was used.

An important feature that has been used in ISIS-CFD is the adaptive grid refinement (see for example [7]. For the computations in this paper, refinement at the water surface location has been used, so one gets automatically more cells near the free surface, especially near steeper or breaking waves. An example of this refinement is shown in figure 3.1. The total number of cells in the grid used for ISIS-CFD was 3.8M for model scale, 4.9M for full scale.

PARNASSOS uses a 4-domains, block-structured grid, in which the total number of cells is 5.1M and 6.0M for, respectively, model and full scale. At the cross section near the transom a splitting of the grid is made, allowing to choose the grid topology well suited to a (partly) wetted transom. This is illustrated in Figure 3.2, in which the arrow indicates the position where the transom goes from wetted to dry.

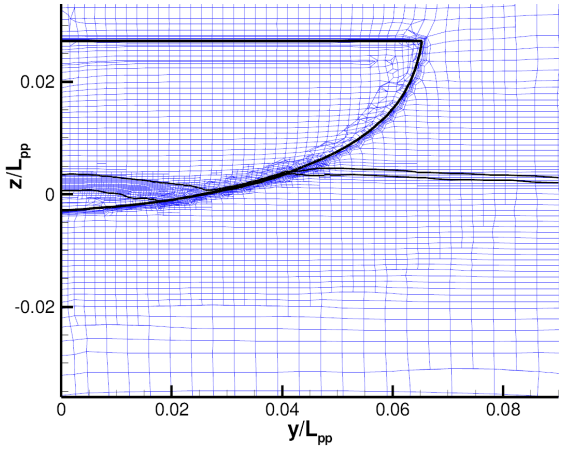

Fig. 3.1 *Cross-section, behind the transom, of a grid generated by ISIS-CFD using adaptive refinement. The limits of the water-air interface are shown in black. T=12.5m, model scale.*

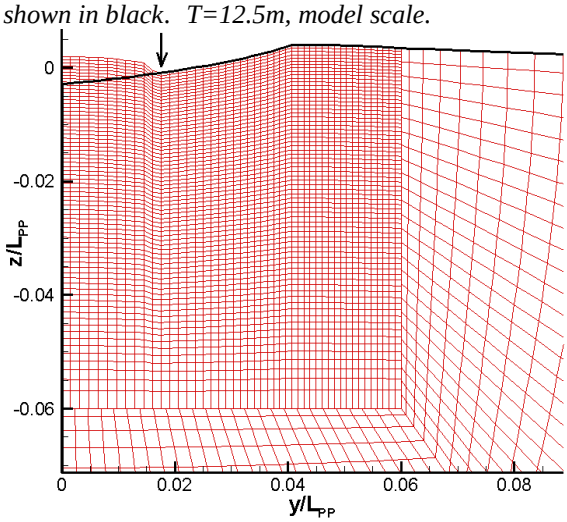

Fig. 3.2 Cross section of the grid used by PARNASSOS near the transom. T=12.5m, model scale. The black line indicates the transom edge.

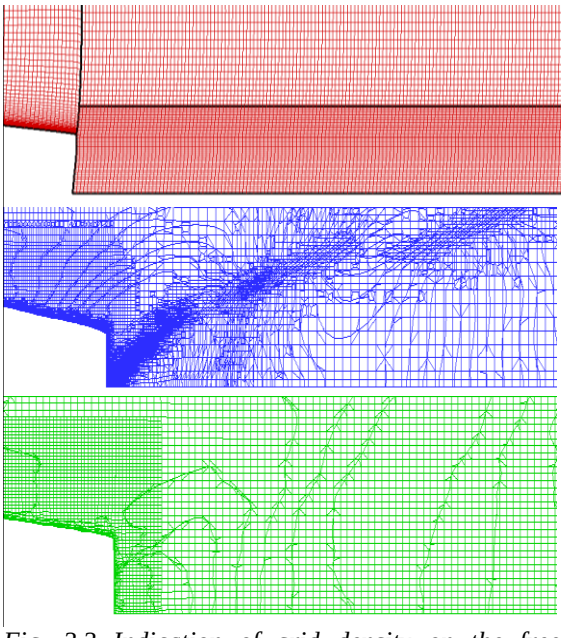

Fig. 3.3 Indication of grid density on the free surface near the transom. Top: PARNASSOS, middle: ISIS-CFD. Bottom: COMET.

The total number of cells used in the unstructured grid of COMET is 2.1M and 2.5M, for, respectively, model and full scale. Typical values for y^+ are 30 (model) and 300 (ship).
In order to give an indication of the grid resolution, Figure 3.3 shows the grid distribution on the free surface near the transom for the three codes. In the sequel of this paper, we will use the same colour coding as used in this figure for presenting the computed wave heights along wavecuts.

4. Computed and measured wave heights at model scale

T=11.3m
Figure 4.1 shows a comparison between measured wave heights and wave heights computed by PARNASSOS and ISIS-CFD for some wavecuts aft of the transom. The wave heights as computed by both codes are close to the measured wave heights. The difference between the computed results is less that the difference between measured and computed wave heights.

T=12.5m
An example of a comparison at model scale between computed and measured results for a wavecut near the ship is shown in Figure 4.2. In general we see good agreement between the computed and measured wave elevation. The amplitudes of the short diverging waves near x=-*0.3*L_{PP} are underestimated in COMET, overestimated in PARNASSOS, whereas ISIS-CFD shows better agreement with the measurements. This is probably caused by the adaptive grid refinement used in the latter.

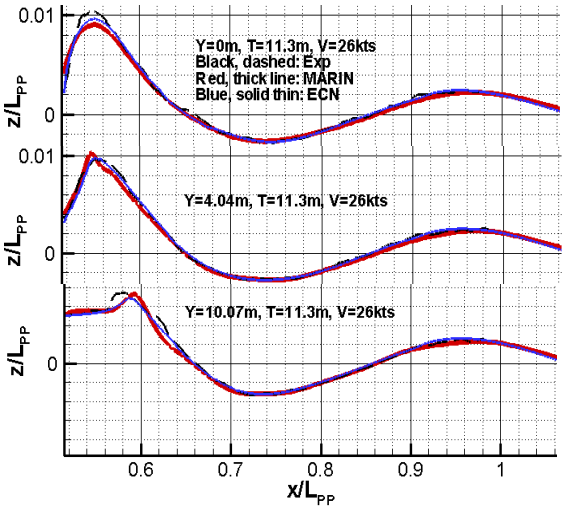

Fig. 4.1 Measured and computed wave heights for some wavecuts aft of the transom. T=11.3m.

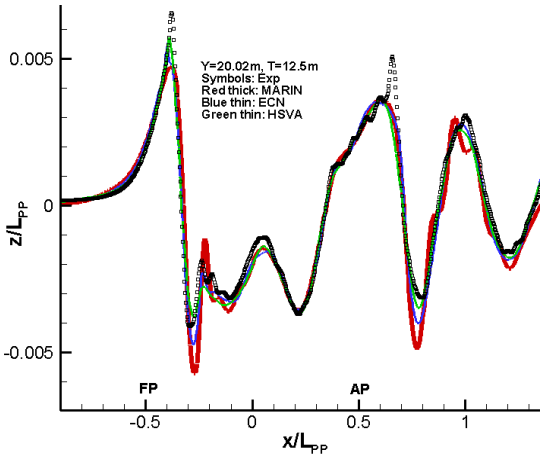

Fig. 4.2 Comparison of computed and measured wave heights for a wavecut near the ship. T=12.5m.

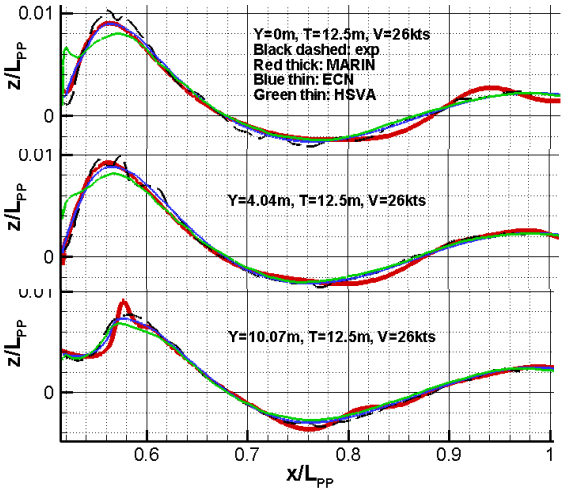

Fig. 4.3 Measured and computed wave heights for some wavecuts aft of the transom. T=12.5m

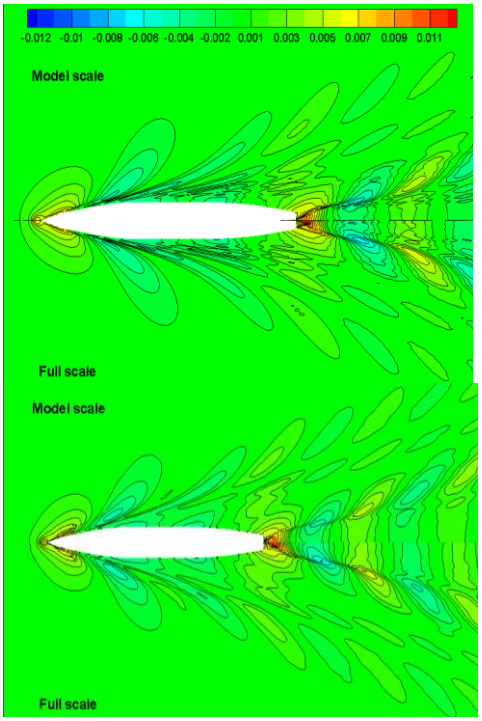

Fig. 5.1 Computed scale effect for T=11.3m. Top: PARNASSOS, bottom: ISIS-CFD.

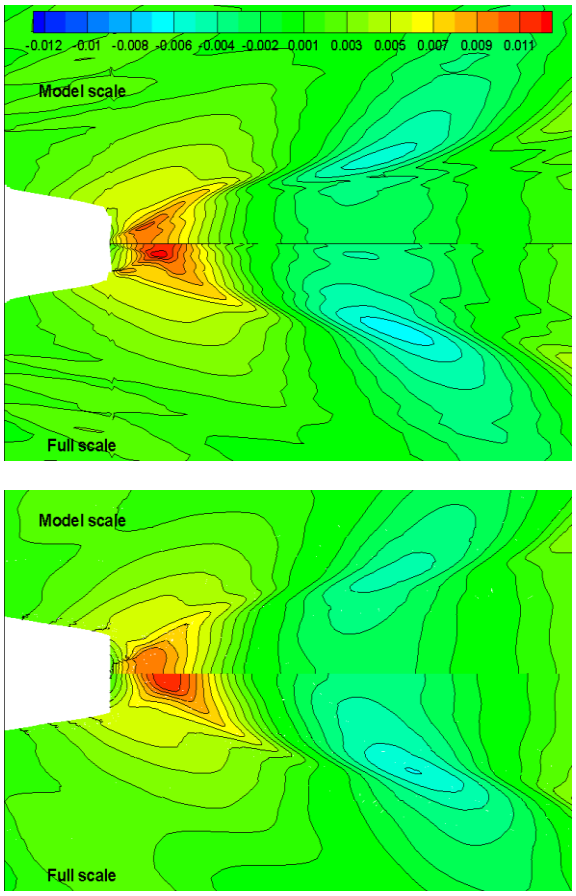

Fig. 5.2 Computed scale effects stern wave system for T=11.3m. Top: PARNASSOS, bottom: ISIS-CFD.

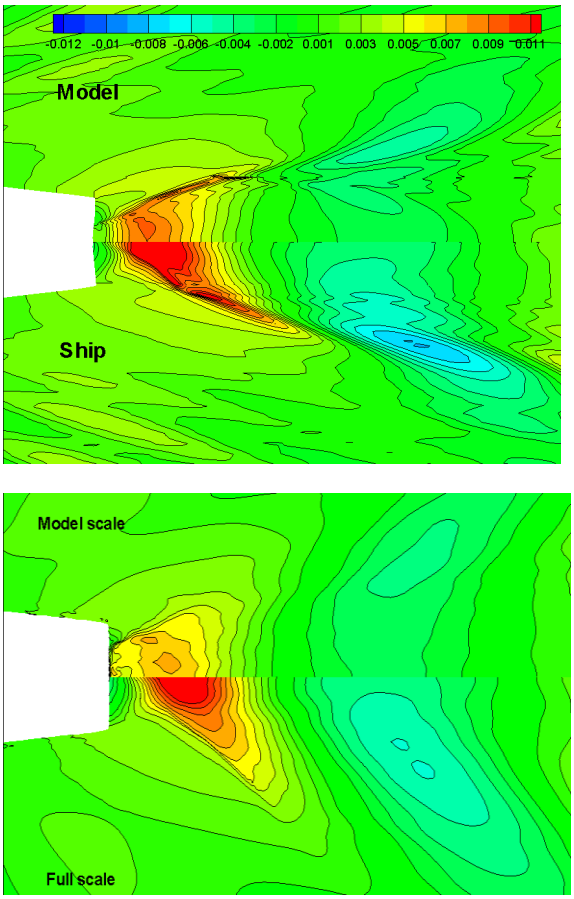

Fig. 5.4 Computed scale effects stern wave system for T=12.5m. Top: PARNASSOS. Bottom: COMET.

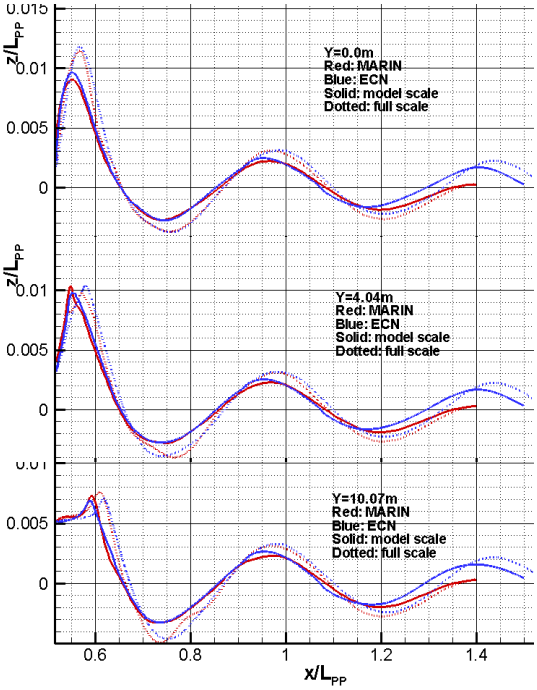

Fig. 5.3 Scale effects in wave heights behind the transom. PARNASSOS and ISIS-CFD. T=11.3m.

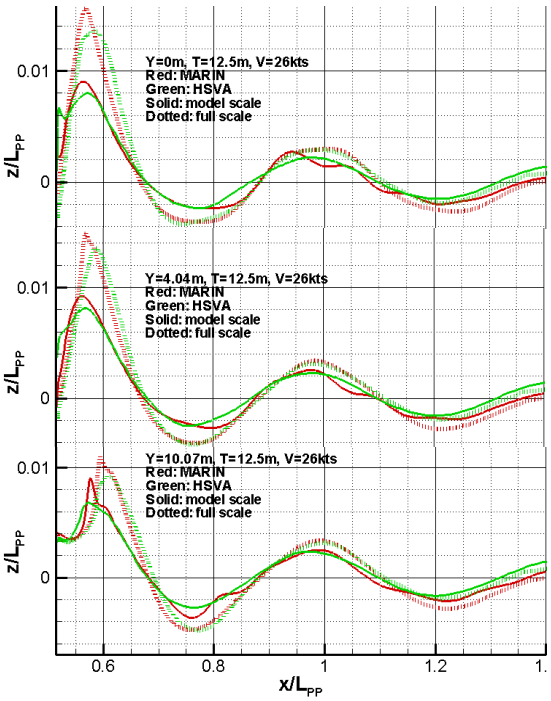

Fig. 5.5 Scale effects in wave heights behind the transom. PARNASSOS and COMET. T=12.5m.

Figure 4.3 shows a comparison between measured and computed results at the stern. There is in general good agreement, especially for *y=0m* and *y=4.04m*. Moreover, it appears again that the agreement between computed results is better than the agreement with measurements. PARNASSOS and ISIS-CFD compute almost exactly the same wave height and wavelength directly behind the transom, which are in excellent agreement with the measurements. For *y=0m* and *y=4.04m* there are some small oscillations in the measurements not present in the computations. PARNASSOS computes similar oscillations, but they are located at a larger distance from the symmetry plane (*y=10.07m*).

5 Scale effects

T=11.3m

A top view of the scale effects on the wave elevation for the smallest draft as computed by PARNASSOS and ISIS-CFD is shown in Figure 5.1. The computed scale effects are very similar. The main scale effects are limited to the stern wave system. Therefore, Figure 5.2 shows a close-up of the computed scale effects near the transom.

Figure 5.3 shows a direct comparison of the computed scale effects behind the transom at three different wavecuts. It appears that the wave amplitude for full scale is higher than at model scale, and the first wave top behind the transom shifts further downstream. These are similar scale effects as computed for the Hamburg test case [3].

T=12.5m

Figure 5.4 compares the scale effects near the transom as computed by PARNASSOS and COMET. Again we see that the computed scale effects are very similar, despite the completely different methods.

From Figs 5.3 and 5.5 it follows that for the larger draft the scale effect is significantly stronger than for the smaller draft. It appears that for *T=12.5m* the wave height at full scale is more than 60-70% higher than at model scale.

There is a clear scale effect on the part of the transom that is wetted. This is illustrated in Figure 5.6 which shows a top view of the axial water velocity component on the free surface. The negative velocities directly behind the transom at model scale are an indication that a large part of the transom is wetted. At full scale however, we do not get this indication. Also, in Figure 5.4, a small breaking wave is observed directly behind the transom in the model-scale results for both COMET and PARNASSOS; this wave delimits the wetted transom flow. At full scale, it has disappeared. This same phenomenon, though less pronounced, is seen in the ISIS-CFD results of Figure 5.2, for the *T=11.3m* case.

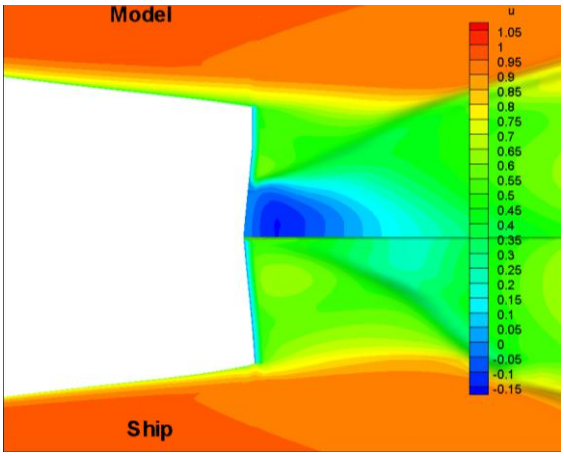

Fig. 5.6 Top view of scale effect in the water velocity near the transom. PARNASSOS. T=12.5m.

6 Conclusions and discussion

The good agreement with measurements and the strong similarity in the computed scale effects demonstrates that also for the more difficult case with a partly wetted transom, strong progress in free surface RANS methods has been achieved. Despite the big differences in the modelling of the viscous flow and the free surface, as well as in the iterative method, in many cases there is more mutual agreement between computed results than between computed and measured results. For example, the wetted part of the transom for the largest draft at model scale as computed by ISIS-CFD (Fig. 3.1) corresponds perfectly well with the PARNASSOS prediction (Fig. 3.2). This similarity in the computed results sustains the confidence in the computed scale effects.

For the Virtue Container Ship, the following scale effects were computed:

- Scale effects on the free surface are mainly restricted to the stern wave system.
- For both drafts, the transom is partly wetted at model scale. For the largest draft the transom is clearly wetted, for the smallest draft this is less clear. At full scale the transom is dry for both drafts.
- There is a clear increase (about 25% for the smallest draft and more than 60% for the largest draft) of the predicted stern wave amplitudes from model to full scale.
- The first wave top behind the transom shifts further downstream.

It appears that the adaptive grid refinement of ISIS-CFD, that is used to get automatically more grid points near the free surface, is very useful for increasing the resolution of steep and breaking waves. Also with the 4-domains block-structured grid used by PARNASSOS good results can be obtained. This grid topology is very well fitted to the local geometry of the transom and therefore allows for resolution in vertical direction along the

wetted part of the transom. However, care has to be taken not to choose the border of two domains too close to the symmetry plane.
COMET and ISIS-CFD have great flexibility in wetted-stern modeling. They can deal with very steep or even breaking waves. Of course, the free-surface fitting approach in PARNASSOS is less general, since the upper-boundary of the grid has to match the free surface estimate. However, the new 4-block structure proves very efficient and accurate for wetted-transom flow.
For this case with moderate breaking, all these different methods are shown to be successful.

ACKNOWLEDGEMENT

The research reported in this paper formed part of WP1 of the VIRTUE project, an Integrated Project in the 6th Framework Programme "Sustainable development, global change and ecosystems" under grant 516201 from the European Commission. This support is gratefully acknowledged.

References

1. Hoekstra, M., "*Numerical simulation of ship stern flows with a space-marching Navier Stokes method*", Thesis, Technical University of Delft, October 1999.
2. Marzi, J., "*VIRTUE - A European approach to developing the numerical towing tank*", RINA Marine CFD Conference, Southampton, 2008.
3. Van der Ploeg, A., Raven, H.C., Windt, J.W., Leroyer, A., Queutey, P., Deng, G.B., and Visonneau, M., "*Computations of free-surface viscous flows at model and full scale - a comparison of two different approaches"* , 27th Symp. Naval Hydrodynamics, Seoul, Oct. 2008.
4. Queutey, P. and Visonneau, M. "*An interface capturing method for free-surface hydro-dynamic flows*", Computers & Fluids, 36/9, pp. 1481—1510, 2007.
5. Raven, H.C., and Starke, A.R., "*Efficient methods to compute ship viscous flow with free surface*", 24th Symp. Naval Hydrodynamics, Fukuoka, Japan, 2002.
6. Raven, H.C., Van der Ploeg, A., and Starke, A.R., (2004), "*Computation of free-surface viscous flows at model and full scale by a steady iterative approach*", 25th Symp. Naval Hydrodynamics, St. John's, Canada, 2004
7. Wackers, J., Ait Said, K., Deng, G.B., Queutey, P., Visonneau, M., and Mizine, I., (2010), "*Adaptive grid refinement applied to RANS ship flow computation*", 28th Symp. Naval Hydrodynamics, Pasadena, California, 2010
8. ABSS: "Akkurate Berechnung der Strömung an einem Spiegelheck", German national research Project, funded by the Federal Ministry of Economics and Technology.

Multigrid Method in Free-Surface Flow Simulation

Mahdi Pourmostafa, Sharif University of Technology, mahdi_pourmostafa@alum.sharif.edu
Mohammad Saeed Seif, Sharif University of Technology, seif@sharif.edu

The application of CFD methods in engineering problems shows that for sufficient accuracy the mesh resolution has to be reasonably high. Conventional single-grid Navier–Stokes solvers suffer from poor convergence, particularly on fine grids. The computational effort varies nearly with the square of the number of grid points. This leads quickly to unacceptably large computing times for complex flow problems. Multigrid methods are then more efficient, having computation times directly proportional to the number of grid points. In this paper, the agglomeration multigrid is applied to speed up the convergence. This leads us to use fully unstructured grids. The fine grid is used to generate the coarse grids. The Navier-Stokes solver is based on fractional step method and the multigrid method is exerted on the pressure Poisson equation. The free surface is captured in a volume of fluid method. The two-phase interface is computed by solving a scalar transport equation for the volume fraction.

The governing conservation equations for unsteady, incompressible, Newtonian, multi-fluid flows are:

$$\frac{\partial u_i}{\partial t}+\frac{\partial u_i u_j}{\partial x_j}=-\frac{1}{\rho}\frac{\partial p}{\partial x_i}+\nu\frac{\partial^2 u_i}{\partial x_j \partial x_j}+g_i \tag{1}$$

$$\frac{\partial u_i}{\partial x_i}=0 \tag{2}$$

u is the velocity, P the pressure and g_i the gravitational acceleration. The mixture of fluid is considered as a single continuum. The local averaged density and viscosity (ρ and μ) are computed from the local distribution of the phase indicator:

$$\rho=\rho_1\alpha+\rho_2(1-\alpha)$$
$$\mu=\mu_1\alpha+\mu_2(1-\alpha) \tag{3}$$

The subscripts 1 and 2 denote the two fluids. The volume fraction α is advected as a Lagrangian invariant and has zero material derivative:

$$\frac{D\alpha}{Dt}=\frac{\partial\alpha}{\partial t}+u_j\frac{\partial\alpha}{\partial x_j}=0 \tag{4}$$

Using the continuity equation, the advection equation can be casted into the divergence form:

$$\frac{\partial\alpha}{\partial t}+\frac{\partial}{\partial x_j}(u_j\alpha)=0 \tag{5}$$

The Navier-Stokes equation is discretized in a second-order finite volume schemes. The diffusion term is discretized using over-relaxed interpolation [1]. In order to discretize the convection term, one needs fluid velocity at CV face where is calculated using Gamma interpolation scheme [1]. The Crank–Nicholson scheme is used for time discretization of diffusion and convection terms. The velocity and pressure field is coupled using fractional step method, [2]. In the same manner, the volume fraction transport Eq. (5) is discretized on the integration over the CVs and the time step, [2]. Simple interpolations (for computing the volume fraction on control volume faces) result in non-physical values. This leads to using a high-order composite interpolation. In this paper CICSAM* scheme is used [3].

After importing the fine grid to the code, one needs to generate coarse grids. The algorithm used in this paper is very similar to one Okomoto suggested [4]:
1- Select a starting vertex in fine grid (vertex 1 in Fig. 1).
2- Merge all the sharing volume of this vertex.
3- Select another vertex (vertex 2 in Fig. 1).

* Compressive Interface Capturing Scheme for Arbitrary Meshes

4- If one of the sharing volumes of this vertex is used in previous coarsening go to step 3, else go to 2 (in this step the vertex number 2 in Fig.1 is passed and vertex number 3 is selected for coarsening).

Sharing volume of a vertex: the volumes which that vertex is one of its nodes. After coarsening there can be more than one faces between each control volume. This requires the assumption of unstructured grids in computations. For better coarsening and efficient simulation, the vertexes should not be chosen by chance. So before the coarsening, a list of vertexes that have more sharing element must be made, and the coarsening should follow that list.

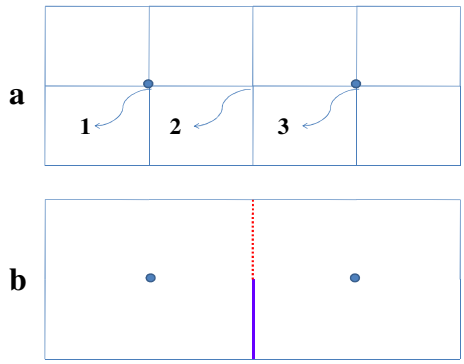

Fig.1: Fine grid (a) used to make coarse grid (b)

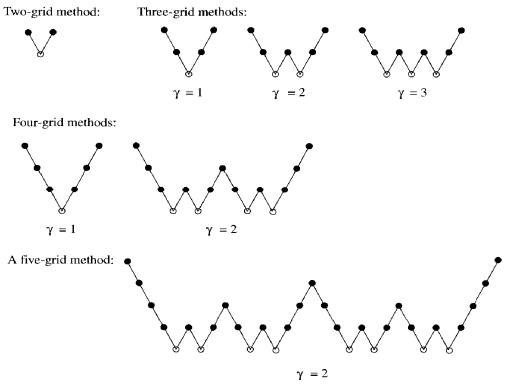

Fig.2: Structure of one multigrid cycle for different numbers of grids and different value of the cycle index γ [6]

The multigrid dampens the low-frequency error components. Two grid schemes were used. Consider a linear system of equation as *Ax=B*. The two schemes to solve this system are as follows [5]:

1- Relax on $A_1 x_1 = B_1$ on fine grid and find the approximate solution v_1 (Relax until the convergence rate decreases).

2- Compute the fine grid residual $r_1 = f_1 - A_1 v_1$ and restrict it to the coarse grid.

3- Solve $A_2 e_2 = r_2$ on coarse grid.

4- Prolong the coarse-grid error to the fine grid and correct the fine grid approximation $v_1 = v_1 + e_2$

5- Relax on $A_1 x_1 = B_1$ on fine grid with initial guess v_1.

The subscripts 1 and 2 denote fine and coarse grid, respectively. This algorithm could be extended on more grids and in different cycles. Fig.2 shows the structure of one iteration step (cycle) of a multigrid method with a few pictures. The cases $\gamma = 1$ (V-cycle) and $\gamma = 2$ (W cycle) are usually used. γ is cycle index [6].

The multigrid method also needs some operators to transfer data between the grids. The prolongation operator transfer a variable from a coarse grid to fine grid and the restriction operators transfer a variable from fine grid to coarse grid. Here, the operators introduced by Peric are used [7]:

Restriction operator: $$\phi_C = \frac{1}{N_f} \sum_{i=1}^{N_f} \left[\phi_{F_i} + \overrightarrow{(grad\,\phi)}_{F_i} . \overrightarrow{(r_C - r_{F_i})} \right] \quad (6)$$

Prolongation operator: $$\phi_{F_i} = \phi_C + \overrightarrow{(grad\,\phi)}_C . \overrightarrow{(r_{F_i} - r_C)} \quad (7)$$

In Eqs.(6) and (7), r is the cell center of control volumes, N_f the number of fine-grid Control Volume in one coarse-grid Control Volume. f and c denote the fine and coarse grid respectively. Fig.3 shows the operators clearly.

Based on algorithm described above, a numerical code was developed. Here, two applications are shown.

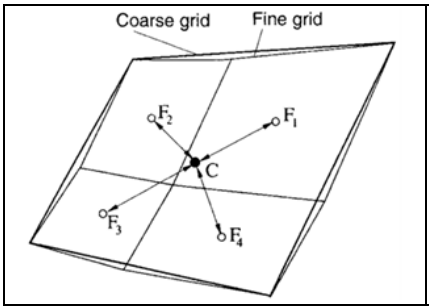

Fig.3: Transfer of variables from fine to coarse grid and vice-versa

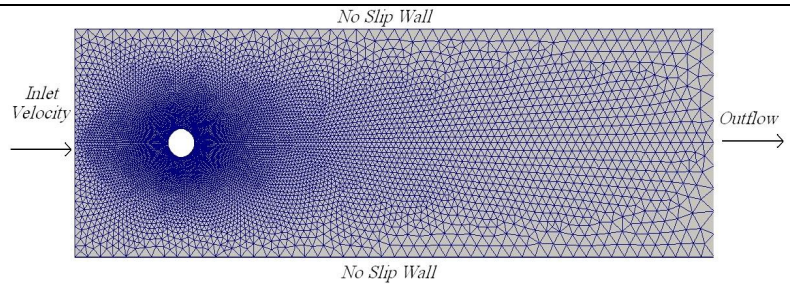

Fig.4: Fine grids for flow over a circular cylinder (17836 CVs)

The flow over a circular cylinder at $5000 > \mathrm{Re} > 40$ is a typical example of unsteady flow with vortex shedding. Fig.4 shows the geometry and the computational domain of problem. Calculation is performed at $\mathrm{Re} = u_0 D / \nu = 200$. Fig.5 shows the lift and drag coefficient versus time. These coefficients are compared with similar studies in Table 1. Our simulation is very similar to Rosenfield [8]. The vortex shedding of this simulation is illustrated in Fig. 6.

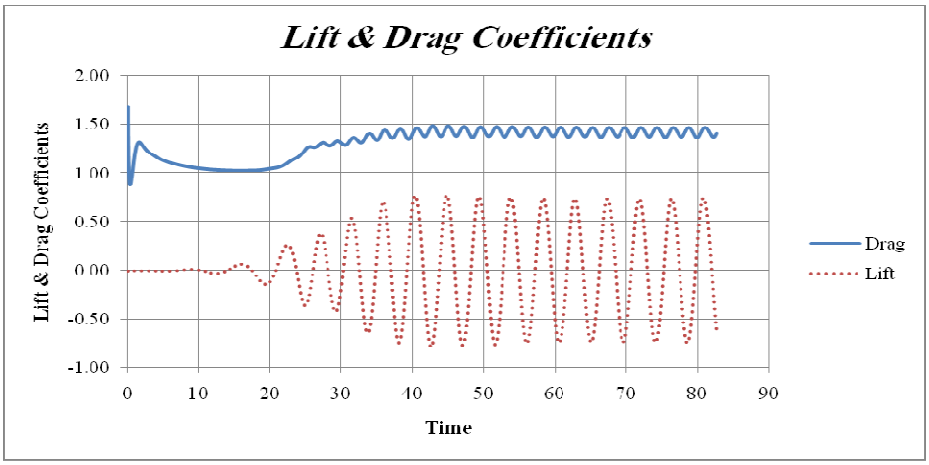

Fig.5: Lift and Drag Coefficient for flow over circular cylinder

Table 1: Comparison of results for flow over circular cylinder

References	Drag Coefficient	Lift Coefficient	Strouhal Number
Rosenfeld [8]	±0.69	1.46 ± 0.05	0.211
Miyake [9]	±0.67	1.34 ± 0.043	0.196
Liu [10]	±0.69	1.31 ± 0.049	0.192
Rogers [11]	±0.65	1.31 ± 0.049	0.185
Present study	**±0.71**	**1.42± 0.037**	**0.222**

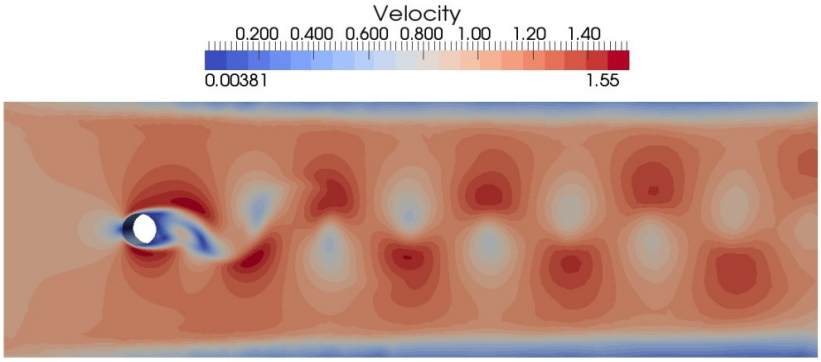

Fig.6: vortices contours plot for flow over circular cylinder

For the comparison of the V and W cycle and the selection of the cycle to simulate this test case, two parameters are considered. First, the residual reduction, plotted for two cycles, Fig.7; the residual is computed from Eq.(8). The second parameter is the time of simulation. For this purpose the problem simulated for 50 time steps with different cycles. The result shows in Table 2. Based on these two parameters the V cycle with 3 grids is chosen for simulation. Multigrid can increase the speed of simulation by more than 3 times.

$$\|e\|_2 = \frac{\left\{\sum_{g=1}^{n} e_g^2\right\}^{1/2}}{n} \tag{8}$$

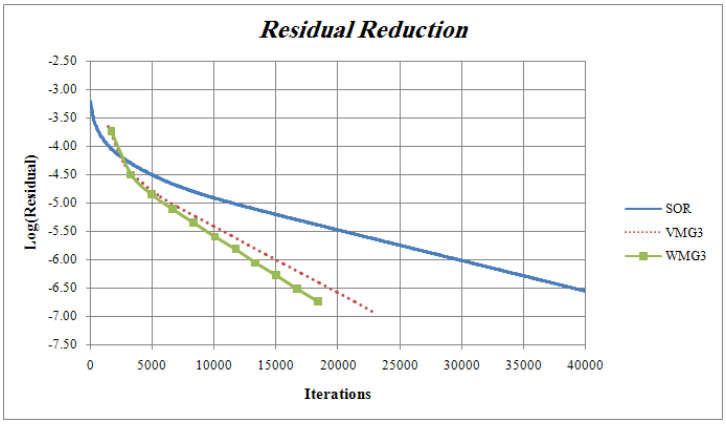

Fig 7: Residual reduction for the second time step

Table 2: Convergence features for flow over circular cylinder for 50 time steps

The method	CPU Time [s]	CPU speed-up Ratio
Single-grid	1927	1
3 grid V cycle	**599**	**3.22**
3 grid W cycle	600	3.21

The second test case is a moving barge, Fig.8, in calm water. We computed the barge with fixed trim and sinkage and then free to trim and sink. We compare with own model tests for V=0.807 m/s, [12]. The rigid-body motion equation is this problem is solved with the Navier-Stokes and fraction transport equation [2].

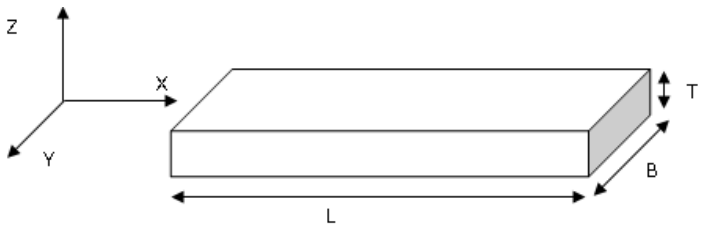

Fig.8: Barge: L=1.05 m, B=0.29 m, T = 0.025 m, C_B = 1, mass = 7.26 kg, I_{yy}=0.7 kgm^2, KG=0.025 m

Table 3: Comparison of barge resistance with experimental data, [12]

Method	**Resistance**	**Error**
Experimental	3.53 N	---
Numerical simulation in fix motion (single grid)	2.71 N	23.2%
Numerical simulation in 2-DOFmotion (single grid)	3.32 N	5.9%
Numerical simulation in fix motion (multigrid)	2.88 N	18.4%
Numerical simulation in 2-DOFmotion (multigrid)	3.41 N	3.4%

The resistance of the simulation for the two situations (fixed and 2-DOF) is compared with experimental data in Table 3. The 2-DOF results were more accurate than the fixed barge. Using multigrids increased the accuracy relative to single-grid simulation. Fig.9 shows the resistance history fir the 2-DOF case. After some oscillation the barge get constant trim and the resistance force becomes steady. The simulation for both motions was performed with multigrid method. The residual reduction for both of them is very similar. Fig.10 gives a sample diagram for 2-DOF.

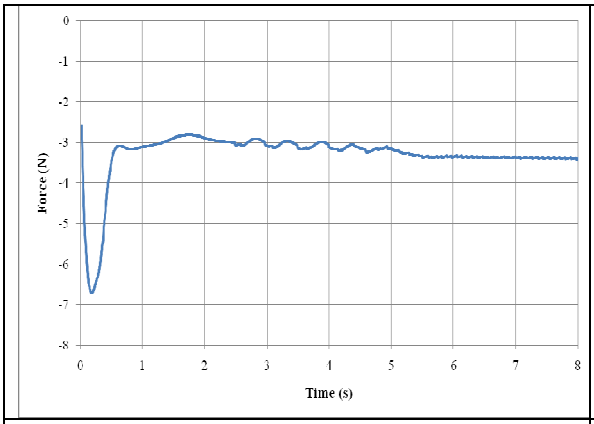

Fig.9: Resistance of the 2-DOF motion barge

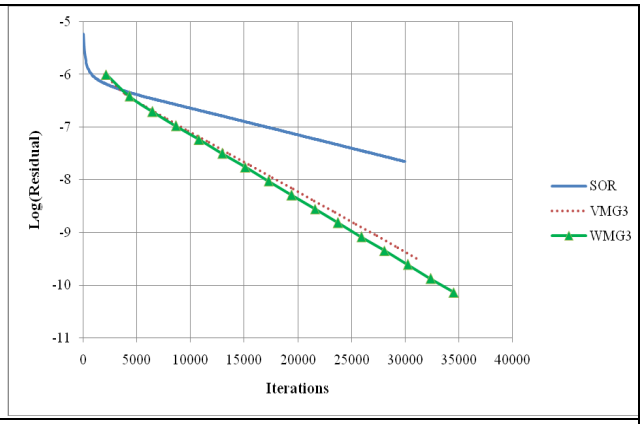

Fig.10: Residual reduction for 2-DOF motion barge in second time step

The simulation is done with all kind of cycles for 50 time steps and after that the W cycle with three grids level was chosen because of better speed, Table 4. The free surface near the barge is also compared with a photo of the model tests in Fig.11. Fig.12 shows the velocity contours in the domain which is based on numerical results.

Table 4: Convergence features for barge resistance for 50 time steps

The method	CPU Time [s]	CPU Speed-up Ratio
Single-grid (fix motion)	3877	1
3 grid V cycle (fix motion)	2772	1.40
3 grid W cycle (fix motion)	**2349**	**1.65**
Single-grid (2-DOF motion)	6038	1
3 grid V cycle (2-DOF motion)	4012	1.50
3 grid W cycle (2-DOF motion)	**3263**	**1.85**

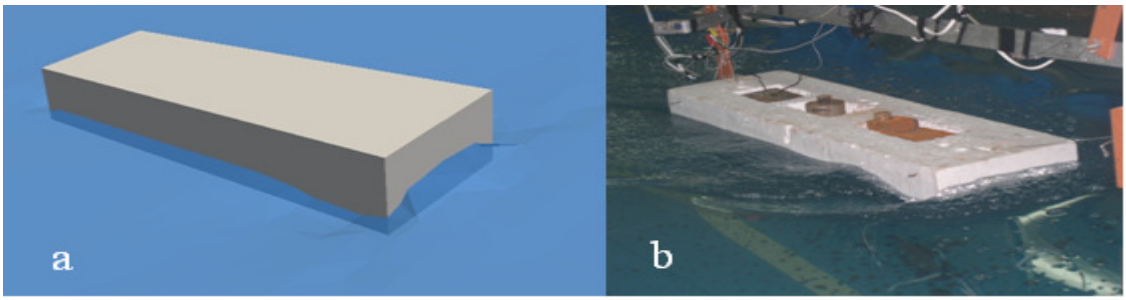

Fig 11: Free-surface deformation in front of barge: a: Simulation, b: Experiment [12]

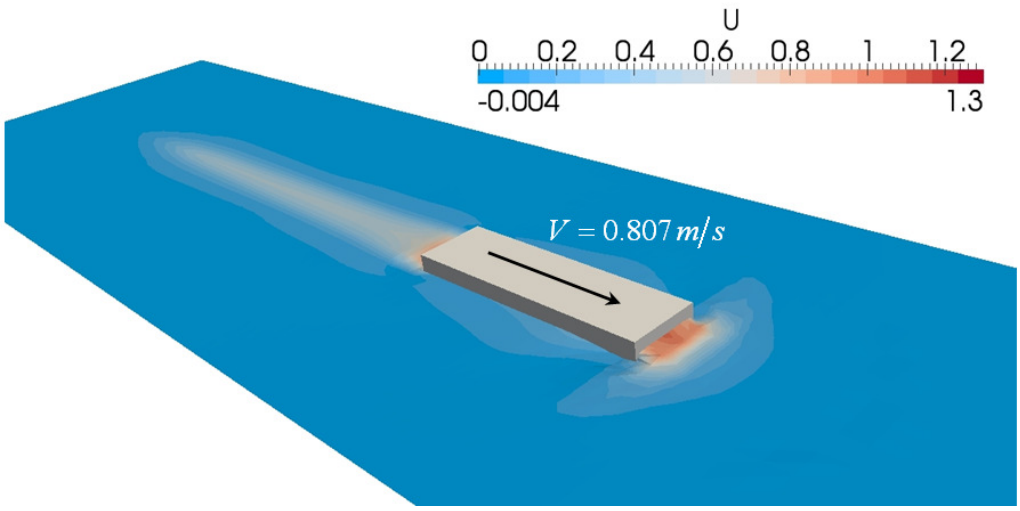

Fig 12: Velocity contours of barge

In seems that W cycles work better. This is because W cycle has more iteration on coarse grids which makes it more efficient. It also recommended using efficient number of grids. Use of large number of grids will not help always as the data transferring is also time consuming. So an efficient number of grids must selected.

[1] Jasak, H., (1996), *Error analysis and estimation for finite volume method with application to fluid flows*, PhD Thesis, University of London

[2] Panahi, R, Jahanbakhsh, E, Seif, M. (2009), *Toward simulation of 3D nonlinear high-speed vessels motion*. Ocean Engineering, 256-265.

[3] Ubbink, O., Issa, R.I. (1999), *A method for capturing sharp fluid interfaces on arbitrary meshes*, J. of Computational Physics, 153:26-50.

[4] Okamoto, N, Nakahashi, K, Obayashi S, (1998),"*A coarse generation algorithm for agglomeration multigrid method on unstructured grids*", *AIAA,* 980-77 japan

[5] Briggs, W, Henson, V, McCormick, S. (2000), "*A multigrid tutorial*", Siam

[6] Trottenberg, U, Oosterlee, C.W, Schuller, A, (2001), *Multigrid*, Academic Press

[7] Ferziger, J., Peric, M. (1996),"*Computational methods for fluid dynamics*", Springer Verlag.

[8] Rosenfeld M, Kwak D, Vinokur M. (1988), *A solution method for the unsteady and incompressible Navier–Stokes equations in generalized coordinate systems*. AIAA Paper 88-0718, 1988.

[9] Belov A, Martinelli L, Jameson A, (1995), *a new implicit algorithm with multigrid for unsteady incompressible flow calculations*. AIAA 95-0049

[10] Liu C, Zheng X, Sung CH. (1998), *preconditioned multigrid methods for unsteady incompressible flows*. J. Computational Physics; 139:35–57

[11] Rogers SE, Kwak D, (1990), *upwind differencing scheme for the time-accurate incompressible Navier–Stokes equations*. AIAA Journal; 28(2):253.

[12] Panahi, R, Jahanbakhsh, E, Seif, M. (2006), *Development of a VOF-fractional step solver for floating body motion simulation*. Applied Ocean Research, 171-181.

Unsteady Flow Simulations for Dynamically-Moving 2D and 3D Geometries by Unstructured Grid Based RANS Solver

Nobuaki SAKAMOTO † and Takanori HINO †

† National Maritime Research Institute, Mitaka, TOKYO 180-0004 JAPAN

sakamoto@nmri.go.jp, hino@nmri.go.jp

1. Introduction

Accurate prediction of ship motions with six degrees of freedom (6DOF) is one of the vital parts for evaluating ships' performance in terms of resistance/propulsion, maneuvering, and seakeeping. Specifically in a seakeeping field, major approaches to investigate ships' performance in waves have been tank tests and potential flow based computations. In addition to these approaches, Computational Fluid Dynamics (CFD) based on Unsteady Reynolds Averaged Navier-Stokes (URANS) equation has also become a powerful tool (ITTC 2008). Since URANS method takes viscous effect into account, several advantages over inviscid computations have been reported, for instance, it can estimate the hydrodynamic coefficients associated with roll decay of a square cylinder much better than traditional inviscid theory (Sarkar and Vassalos 2000).

Based on the backgrounds abovementioned, the major objective of the current research is to develop URANS solver with the capability of handling 6DOF ship motions in waves. National Maritime Research Institute (NMRI) has been developing unstructured grid based incompressible URANS solver SURF (Hino 1997). Implementing moving grid routine, equations of rigid-body motions and incident wave models to SURF are the three major tasks for the present development. This article is dedicated to validation of the first portion, and latter two items are on-going as separated efforts. Grid morphing technique (Hinatsu and Hino 2002) is introduced to SURF as a moving grid method. Several simulations are performed for 2D and 3D geometries with prescribed motions and the results are compared with the available reference data to validate the current dynamic grid morphing technique.

2. Computational Method

The governing equations are the continuity equation and URANS equation and they are solved in a relative-inertial coordinate system. These are non-dimensionalized by the fluid density ρ, the fluid kinematic viscosity ν, the characteristic length L_0, and the characteristic velocity U_0. Spatial discretization for the governing equations is accomplished using a cell-centered finite volume method with unstructured grids. For the use of artificial compressibility approach in the velocity-pressure coupling in unsteady flow calculations, pseudo time step τ is utilized in order to satisfy divergence-free condition at each physical time step t. In consequence, the equations to be solved are

$$\frac{\partial}{\partial t}\iiint_{V_i}\mathbf{q}\,dV+\frac{\partial}{\partial \tau}\iiint_{V_i}\mathbf{q}^*\,dV+\oint_{\partial V_i}\{(\mathbf{e}-\mathbf{e}^v)n_x+(\mathbf{f}-\mathbf{f}^v)n_y+(\mathbf{g}-\mathbf{g}^v)n_z\}dS=0 \quad (1)$$

where V_i is a control volume (= cell i), $[n_x, n_y, n_z]^T$ is the unit normal vector for each faces of a cell i, $\mathbf{q}$ and $\mathbf{q}^*$ are the flow variable vectors, $\mathbf{e}$, $\mathbf{f}$, $\mathbf{g}$ are the inviscid flux vectors and $\mathbf{e}^v$, $\mathbf{f}^v$, $\mathbf{g}^v$ are the viscous flux vectors described as

$$\mathbf{q}=[0,u,v,w]^T,\mathbf{q}^*=[p,u,v,w]^T \quad (2)$$

$$\mathbf{e}=\left[\beta u,u(u-u_g)+p,u(v-v_g),u(w-w_g)\right]^T \quad (3)$$

$$\mathbf{f}=\left[\beta v,v(u-u_g),v(v-v_g)+p,v(w-w_g)\right]^T \quad (4)$$

$$\mathbf{g}=\left[\beta w,w(u-u_g),w(v-v_g),w(w-w_g)+p\right]^T \quad (5)$$

$$\mathbf{e}^v=\left[0,\tau_{xx},\tau_{xy},\tau_{xz}\right]^T,\ \mathbf{f}^v=\left[0,\tau_{yx},\tau_{yy},\tau_{yz}\right]^T,\ \mathbf{g}^v=\left[0,\tau_{zx},\tau_{zy},\tau_{zz}\right]^T \quad (6)$$

In the inviscid flux vectors, β is the artificial compressibility parameter, and $[u_g, v_g, w_g]^T$ is the grid velocity which accounts for motions of the grid during a simulation. In the viscous flux vectors, shear stress is presented in a tensor-form as

$$\boldsymbol{\tau}_{ij} = \left(\frac{1}{R_n} + \nu_t\right)\left(\frac{\partial u_i}{\partial x_j} + \frac{\partial u_j}{\partial x_i}\right) \tag{7}$$

where R_n is the Reynolds number $(= U_0 L_0/\nu)$ and ν_t is the non-dimensional kinematic eddy viscosity. The ν_t is calculated by standard/modified Spalart-Allmaras one-quation turbulence model (Spalart and Allmaras 1994) for which its details and availabilities in ship hydrodynamics can be found in Hino (1995).

In Eq. (1), the inviscid fluxes are evaluated by the 2nd-order upwinding scheme based on the flux-difference splitting of Roe, and the viscous fluxes are evaluated by the 2nd-order central differencing scheme. Temporal discretization in Eq. (1) is accomplished using 2nd-order Euler backward differencing scheme in physical time t, and 1st-order Euler backward differencing scheme in pseudo-time τ.

Based on these discretization criteria in space and time, cell volume change in physical time is associated with the grid velocity U_g as

$$\frac{3V_i^{n+1} - 4V_i^n + V_i^{n-1}}{2\Delta t} + \sum_{faces}\left(-U_g^{n+1}\right) = 0 \tag{8}$$

$$U_g = u_g s_x + v_g s_y + w_g s_z \tag{9}$$

where Δt is the non-dimensional physical time increment, n is the physical time step index, and $[s_x, s_y, s_z]^T$ is a area vector for each faces of cell i.

The discretized equation is solved by the multi-color Symmetric Gauss-Seidel method (Sato et al. 2008). The pseudo-time iteration continues until the average residual is less than a threshold value or the iteration number reaches its preset value. The code is parallelized utilizing Open MP, and all the simulations presented in this article are carried out by a shared-memory type workstation with 8 CPU cores (Interl ® QuadCore 3.20GHz).

3. Simulation Design

3.1 Test cases

Table 1 summarizes the test cases in the present study. In Table 1, z_{max} and y_{max} are the maximum heave and sway amplitudes non-dimensionalized by chord-length and L_{pp}, respectively. ϕ_{max} is the maximum pitch amplitude in degrees. In all the cases the free surface is not taken into account.

Table 1 Test cases

#	Geometry	Prescribed motion	R_n	Validation data
1.1	2D NACA0012	Heave $(z_{max} = 0.1)$	3.0e6	Maida (1998)
1.2		Pitch $(\phi_{max} = 5deg)$		
2.1	6:1 prolate spheroid	Pitch $(\phi_{max} = 30deg)$	4.2e6	Wetzel and Simpson (1997) Rhee and Hino (2002)
3.1	KVLCC2	Sway $(y_{max} = 0.0688)$	1.94e6	Miyazaki et al. (2008)

For 2D NACA0012, heave/pitch motions are prescribed as

$$\begin{pmatrix} z \\ \phi \end{pmatrix} = f_{acc.} \cdot \begin{pmatrix} z_{max} \\ \phi_{max} \end{pmatrix} \cos(\omega \cdot n\Delta t) \quad \text{with} \quad \omega = 2.0, \Delta t = 0.0105 \tag{10}$$

where ω is the non-dimensional angular frequency, n is the physical time step index, and Δt is the non-dimensional physical time increment. Acceleration function $f_{acc.}$ is introduced which has a cubic

polynomial profile and allows objects accelerating smoothly in prescribed motions during a transient run. The center of pitch motion is located at a midchord.

For 6:1 prolate spheroid, a linear pitch-up motion is prescribed as

$$\phi = g_{acc.} \cdot \phi_{max} \cdot \frac{(n - n_{steady}) \cdot \Delta t}{11.0} \text{ with } g_{acc.} = \begin{cases} 0: n < n_{steady} \\ 1: n \geq n_{steady} \end{cases}, \ \Delta t = 0.005 \quad (11)$$

In this manner, the prolate spheroid starts pitching at n_{steady} time steps, and ϕ reaches ϕ_{max} in 11.0 non-dimensional time counted from the beginning of the pitching motion. The center of pitch motion is located at a midbody.

For KVLCC2, a sway motion is prescribed as

$$y = -f_{acc.} \cdot y_{max} \sin(\omega \cdot n\Delta t), \omega = 4.00753, \Delta t = 0.0043 \quad (12)$$

where the definitions of $f_{acc.}$, ω, n and Δt are the same as presented in Eq. (10).

3.2 Grids and boundary conditions

Figure 1 and Table 2 describe the overviews of the grids. All the grids are generated by Gridgen® with hyperbolic extrusion solver, and consist of hexahedra cells. In the present simulations, the movements of grids adjacent to the object are set to the same as the prescribed motion, while the grids adjacent to the outer boundary are always fixed spatially. Grids between the object and the outer boundary are moved in such a way that the movement is varied smoothly from the object to the outer boundary.

For the boundary conditions, inflow, outflow, far-field, symmetry and no-slip wall conditions are utilized. The grid velocities for the nodes on no-slip walls are calculated by 1st-order approximation based on prescribed motions of Eqs. (10), (11), (12) and Δt.

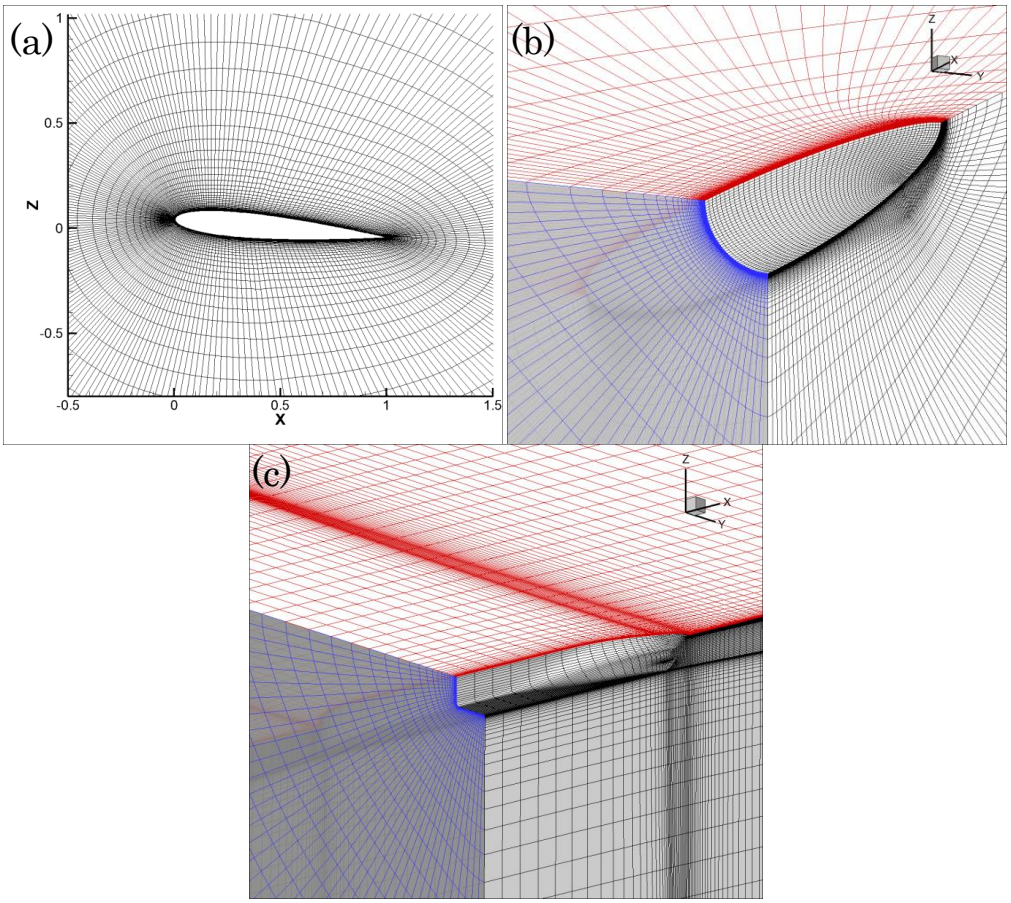

Fig. 1 Grid overviews: (a) 2D naca0012, (b) 6:1 prolate spheroid, (c) KVLCC2

Table 2 Grid details

Geometry	Topology	# of cells	Domain size	Min. spacing
2D NACA0012	O	42K	$-10.0 \leq x, z \leq 10.0$	4.0e-6
6:1 prolate spheroid	OO	0.27M (C)* 0.88M (F)**	$-25.0 \leq x, z \leq 25.0$ $-25.0 \leq y \leq 0.0$	3.2e-6
KVLCC2	OH	0.83M	$-2.0 \leq x \leq 2.5$ $-2.0 \leq y \leq 2.0$ $-2.0 \leq z \leq 0.0$	2.5e-6

*: Coarse grid, **: Fine grid (non-systematically refined from coarse grid)

4. Results and Discussions

4.1 2D NACA 0012 heave/pitch motions

Figure 2a presents the lift coefficient C_L acting on heaving/pitching 2D NACA 0012 in three non-dimensional motion periods. Figure 2b shows instantaneous contours of axial velocity at positive maximum amplitudes of heave/pitch motions. Turbulent simulations for both cases provide periodic response in C_L while the laminar simulations do not. In comparison to the reference data (Maida 1998) of both motions, turbulent simulation qualitatively shows better agreement in amplitude and phase of C_L than those from laminar simulation. This is reasonable in a sense that the reference data is computed by an inviscid panel method, i.e. no flow separation can be observed. As shown in Fig. 2b, the flow easily separates under laminar condition at the trailing edge of the airfoil which causes higher-order oscillation frequency and un-periodic response in C_L. When the turbulence model (modified SA model in this case) is activated, addition of eddy viscosity to the molecular viscosity enhances the viscous dissipation which prevents local flow at the trailing edge of the airfoil from separating, i.e. the local flow fields are expected to be similar to those of the reference data.

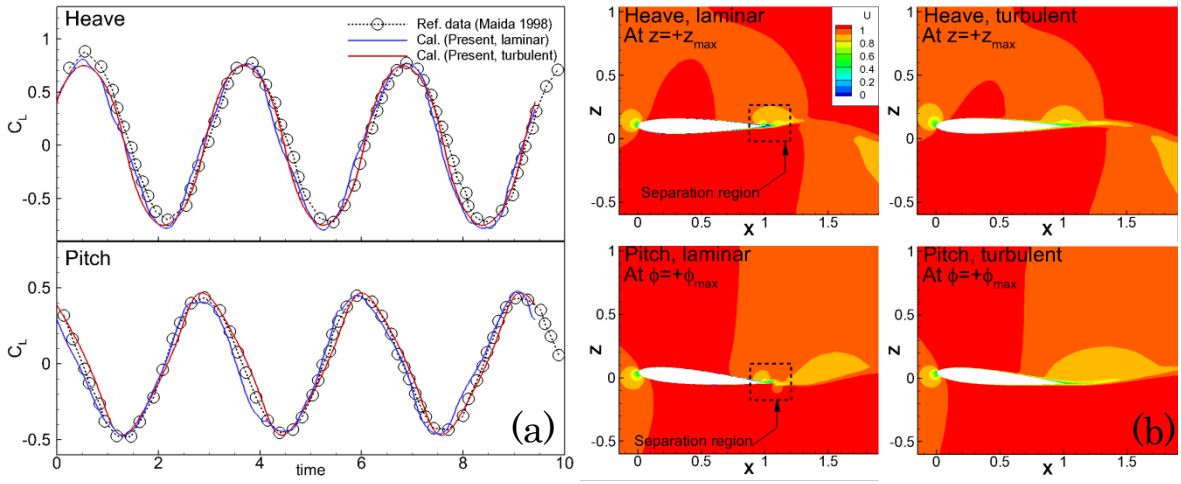

Fig. 2 2D NACA0012 heave/pitch motion: (a) lift coefficients, (b) instantaneous axial velocity

4.2 6:1 Prolate spheroid linear pitch-up motion

Figure 3a presents the normal force (C_N) and pitch moment (C_M) coefficients acting on 6:1 prolate spheroid under linear pitch-up motion around the midbody in 11 non-dimensional time. Figure 3b shows instantaneous contours of pressure at z-symmetry plane at three different pitch angles from 10deg to 30deg. When the standard SA model is utilized, the C_N shows excellent agreement to the experimental data (Wetzel and Simpson 1997) even for the result from relatively coarse grid over the entire range of pitch angle, while the amplitude of C_M is always larger than the experimental data. The modified SA model changes this trend, i.e. the C_N is smaller than the experimental data over the entire range of pitch angle and in the same level as the previous computational result (Rhee and Hino 2002), while the C_M at medium to large pitch angles agree better to the experimental data. It is conjectured that the current turbulence models are not capable of estimating separation regions on the spheroid surface accurately and thus the surface pressure is not well-estimated for its amount/distribution which

causes discrepancies in the C_N and C_M. Figure 3b clearly shows the massive flow separation at the leeward side of trailing edge due to the large cross flow as the pitch angle becomes larger.

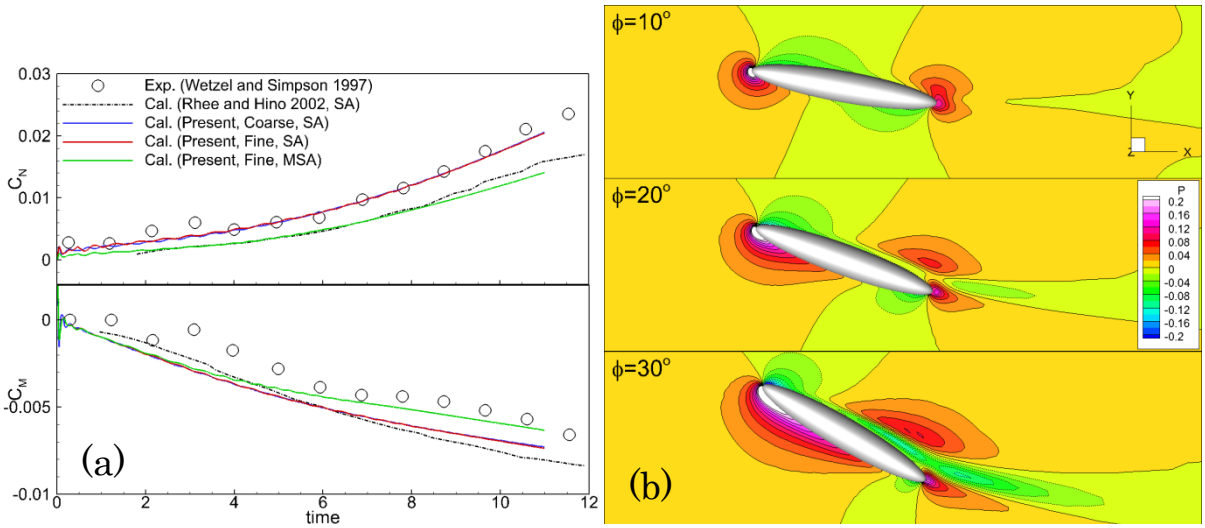

Fig. 3 6:1 prolate spheroid pitch-up motion: (a) normal force and pitching moment coefficients, (b) instantaneous pressure at z-symmetry plane in three different pitch angles

4.3 KVLCC2 pure sway motion

Figure 4a presents the lateral force (Y) and yaw moment (N) coefficients acting on KVLCC2 under pure sway motion in 1 non-dimensional sway motion period. Figure 4b shows the contours of axial vorticity in 10 cross sections from the bow to the stern at 4 successive PMM motion phases. The current computational results of Y and N agree quite well to the experimental data, although minor amplitude and phase differences are observed in both Y and N. The difference in Y and N associated with the turbulence models (i.e. SA vs MSA) is not that significant as was observed in the prolate spheroid case. Figure 4b shows the periodic deformation of the boundary layer at the port/starboard bilge and propeller plane associated with the imposed sway motion. Four vorticies can be identified which are very similar to the ESSO OSAKA tanker under static drift condition (Simonsen and Stern 2005), i.e. fore-body bilge vortex (FBV), bilge vortex (BV), aft-body bilge vortex (ABV) and aft-body side vortex (ASV). In their results these vortices are stationary, while in the current study they dynamically move due to the imposed sway motion.

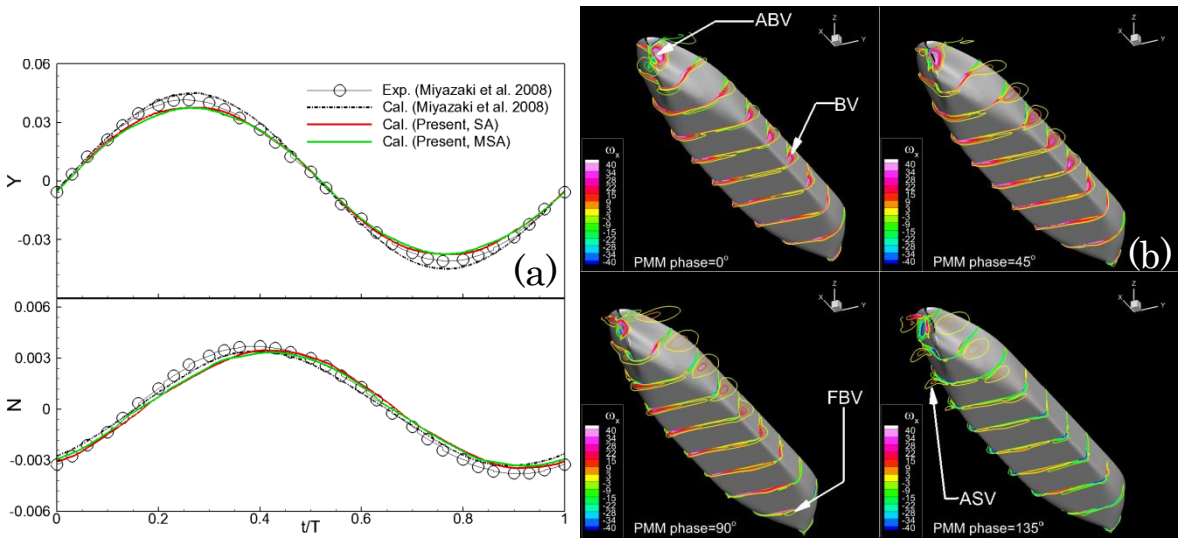

Fig. 4 KVLCC2 pure sway motion: (a) lateral force and yaw moment coefficients, (b) contour of axial vorticity at 10 cross sections in 4 successive PMM motion phases

5. Concluding Remarks

Unsteady flow simulations are carried out around 2D and 3D geometries with prescribed motions by unstructured grid based URANS solver SURF. The purpose of the present research is to validate the newly implemented grid morphing technique to SURF which is one of the most important portions to achieve the development of URANS solver with the capability of handling 6DOF ship motions in waves.

The overall results are encouraging in a sense that the computational results of hydrodynamic forces and moment coefficients generally agree well to the reference/experimental data. For a large amplitude motion, e.g. the prolate spheroid case, the use of Detached Eddy Simulation (DES) could contribute to improve the resolution of the local flow with massive separation (Kotapati-Apparao et al. 2003) which may results in the better estimation in the hydrodynamic forces and moment coefficients. It is also encouraging that the current CFD simulations are able to visualize the details of unsteady local flow around dynamically moving bodies. In consequence, the present grid morphing technique in SURF is confirmed to be promising in handling the dynamic ship motions, and the code is ready for the implementations of 6DOF equation of motions and wave models.

References

1. Hinatsu M. and Hino T., 2002, "Computation of viscous flows around a Wigley hull running in incident waves by use of unstructured grid method", Proc. The 12th International Offshore and Polar Engineering Conference and Exhibition, Kitakyushu, JAPAN.
2. Hino T., 1995, "Viscous flow computation around a ship using one-equation turbulence models", Journal of the Society of Naval Architects of Japan, Vol. 178, pp.9-22.
3. Hino T., 1997, "A 3D unstructured grid method for incompressible viscous flows", Journal of the Society of Naval Architects of Japan, Vol. 182, pp.9-15.
4. International Towing Tank Conference Seakeeping Committee, 2008, "Final report and recommendation to the 25th ITTC", Proc. The 25th International Towing Tank Conference - Vol. I, Fukuoka, JAPAN.
5. Kotapati-Apparao R.B., Squires K.D., and Forsythe J.R., 2003, "Prediction of a prolate spheroid undergoing a pitchup maneuver", AIAA 2003-0269, Aerospace Science Meeting 2003, Reno, Nevada, U.S.A.
6. Maida S., 1998, "A simplified panel method for unsteady propeller characteristics" (in Japanese), Ph.D. Thesis, Kyushu University, Fukuoka, JAPAN.
7. Miyazaki H., Ueno M., and Tsukada Y., 2008, "Numerical study of planar motion mechanism test (pure sway mode)", Proc. SIMMAN 2008 Workshop on Verification and Validation of Ship Manoeuvring Simulation Methods, Copenhagen, DENMARK.
8. Rhee S.H., and Hino T., 2002, "Numerical simulation of unsteady turbulent flow around maneuvering prolate spheroid", AIAA Journal, Vol. 40, No. 10, pp.2017-2026.
9. Sarkar T. and Vassalos D., 2000, "A RANS-based technique for simulation of the flow near a rolling cylinder at the free surface", Journal of Marine Science and Technology, Vol. 5, pp.66-77.
10. Sato Y., Takagi Y., and Hino T., 2008, "Parallelization of an unstructured multigrid Navier-Stokes solver for free-surface flow", Proc. The 22nd Computational Fluid Dynamics Symposium, Tokyo, JAPAN.
11. Spalart P.R. and Allmaras S.R., 1994, "A one-equation turbulence model for aerodynamics flows", La Rescherche Aerospatiale, No. 1, pp.5-21.
12. Simonsen C.D. and Stern F., 2005, "Flow pattern around an appended tanker hull form in simple maneuvering conditions", Computers and Fluids, Vol. 34, pp.169-198.
13. Wetzel T.G. and Simpson R.L., 1997, "Unsteady three-dimensional cross-flow separation measurements on a prolate spheroid undergoing time-dependent maneuvers", AIAA paper, 97-0618.

NUMERICAL INVESTIGATION OF THE INFLUENCE OF WATER DEPTH ON SHIP MANOEUVRING BEHAVIOUR

Jochen Schoop-Zipfel, Moustafa Abdel-Maksoud,Thomas Rung
Hamburg University of Technology
Institute for Fluiddynamics and Ship Theory
Email: jochen.schoop@tuhh.de

INTRODUCTION

To assess the manoeuvring behaviour of ships, traditionally model tests are carried out. Normally these tests are carried out in deep water condition. However, manoeuvring action mainly takes place in restricted waters like in estuary voyage. This situation will even intensify in future due to increasing ship sizes.

Former experimental investigations, e.g. [1] or [2], show that the water depth has a large influence on the manoeuvring behaviour. A substantial increase in turning diameter is shown in shallow water in comparison to deep water. This change in manoeuvring characteristics is very important from the viewpoint of ship safety, because high manoeuvring ability becomes important in shallow water, as in harbours or other restricted waterways.

In the present study, the manoeuvring behaviour is assessed with manoeuvring derivatives. Manoeuvring derivatives allow an efficient way to simulate arbitrary ship manoeuvers. The main effort lies in obtaining the derivatives. For the determination of the derivatives, captive model tests with a so-called Planar Motion Mechanism (PMM) can be carried out [3]. From the measured time histories of the hydrodynamic forces and moments acting on the model during properly selected captive motions, manoeuvring derivatives or hydrodynamic coefficients can be determined. Once the derivatives are obtained simulation of arbitrary manoeuvers is straightforward and very time-efficient.

Due to the increasing computational power of modern computers it is now possible to estimate the manoeuvring derivatives numerically [4]. [5] executed CFD calculations according to PMM tests. The free surface was neglected as well as trim and sinkage. With the procedure a very promising tool for the manoeuvring prediction has been shown.

NUMERICAL METHOD

The present flow simulations have been performed with *FreSCo*$^+$, the in-house RANSE code based on a finite volume technique for unstructured grids, [6]. The Reynolds averaged Navier Stokes Equation and additional transport equations are approximated in a fully conservative formulation. The equations are solved in a segregated manner. To satisfy the mass conservation a volume-specific SIMPLE pressure-correction scheme is implemented. To avoid decoupling of pressure and velocity a third order pressure smoothing along a route outlined by Rhie and Chow is employed, [7].

To close the equation system, the $k-\omega$ standard turbulence model is used.

A vital point for the accuracy of the results is the treatment of the propeller effect on the flow, [5]. It is possible to include a fully modelled propeller in the calculation domain, which would give a high accuracy of the flow and consequently of the acting forces. However, the necessary mesh refinement and time step result in very high computational cost. In the present study a 3D body force model based on momentum theory, developed in [7], is applied. In the propeller momentum theory the total thrust T_p can be derived from the velocity in front of the propeller plane v_A, the velocity behind it v_B and the mass flow through the propeller plane $\rho v_p A_p$.

The propeller side force Y_p is calculated by an empirical formula (Eqn. (1)) developed in [8].

$$Y_p = 0.0032 J \alpha^{0.095} \tag{1}$$

α is the inflow angle and J the advance coefficient of the propeller.

The unsteady motion of the ship is simulated by moving grid technique. The basis vectors in the transport equations don't change, so the relative velocities in the convective terms present the only changes.

OUTLINE OF EXECUTED CALCULATIONS

The aim of the calculations is to determine the manoeuvring derivatives of the ship hull in deep and in shallow water. The performed calculations are based on manoeuvring model tests. For the estimation of the damping derivatives as well as for the estimation of the rudder derivatives, steady calculations are conducted. To obtain the mass related

terms, unsteady calculations are performed. Three water depths are considered:

$h/D = \infty$
$h/D = 1.6$
$h/D = 1.2$

with h being the water depth and D being the ships draft.

To limit the complexity, the computation is performed for model scale. The free surface deformation as well as trim, sinkage and heel are neglected. The propeller is driven at the self propulsion point of the model in the initial condition of straight forward motion. The number of revolution is kept constant during all simulations.

For the steady calculations the rudder angle is varied between $\delta = -30°$ and $\delta = 30°$ in steps of $10°$. For each rudder angle five different drift velocities ($v' = -0.2; -0.1; 0.0; 0.1; 0.2$, with $v' = v/u_0$) and five different surge velocities ($u' = 0.6; 0.7; 0.8; 0.9; 1.0$, with $u' = u/u_0$) are chosen. The unsteady calculations are simulated according to Planar Motion Mechanism tests, i.e. pure yaw, pure sway and two combined sway-yaw motions, with

pure yaw:

$$r = \hat{r}cos(\omega t), \quad \text{with} \quad \hat{r}l/u_0 = 0.36 \tag{2}$$

pure sway:

$$v = \hat{v}cos(\omega t), \quad \text{with} \quad \hat{v}/u_0 = 0.19 \tag{3}$$

combined:

$$r = \hat{r}cos(\omega t), v = \hat{v}cos(\omega t) \quad \text{with} \quad \hat{v}/u_0 = 0.19 \tag{4}$$
$$\hat{r}l/u_0 = 0.24 \quad \text{and} \quad -0.24, \quad \text{respectively.}$$

$\hat{r}$ and $\hat{v}$ are the amplitudes of the yaw and the sway motion, respectively. In total, 63 steady calculations and four unsteady calculations are conducted for each water depth.

The performed calculations are identical on all three water depths. The same input parameters as ship speed are used. I.e. on all water depths the ship has the same initial Froude number.

The calculated forces are used to get the manoeuvring derivatives by means of least-squares fit and fourier transformation. A detailed description of the method followed to get the manoeuvring derivatives can be found in [9]. For the manoeuvring derivatives, i.e. the non-dimensional hydrodynamic forces and moments, the Abkowitz type mathematical model [10] is chosen.

Table 1. MAIN DIMENSIONS OF SERIE 60 SHIP.

Main Dimension	
L_{pp}	$182.884m$
L_{WL}	$185.947m$
B	$26.130m$
D	$10.452m$
c_B	0.7
Propeller	
D	$7.254m$
P/D at $r = 0.7$	1.012
A_E/A_O	0.500

$$X' = X'_0 + X'_{\dot{u}}\dot{u}' + X'_u\Delta u' + X'_{uu}\Delta u'^2 + X'_{uuu}\Delta u'^3 + X'_{vv}v'^2 + X'_{rr}r'^2 + X'_{\delta\delta}{\delta'_R}^2 + X'_{\delta\delta u}{\delta'_R}^2\Delta u + X'_{vr}v'r' + X'_{v\delta}v'\delta'_R \tag{5}$$

$$Y' = Y'_0 + Y'_{\dot{v}}\dot{v}' + Y'_{\dot{r}}\dot{r}' + Y'_u\Delta u' + Y'_{uu}\Delta u'^2 + Y'_v v' + Y'_{vvv}v'^3 + Y'_{vrr}v'r'^2 + Y'_{v\delta\delta}v'{\delta'_R}^2 + Y'_r r' + Y'_{rrr}r'^3 + Y'_\delta\delta'_R + Y'_{\delta\delta\delta}{\delta'_R}^3 + Y'_{\delta vv}\delta'_R v'^2 + Y'_{\delta u}\delta'_R\Delta u' + Y'_{\delta uu}\delta'_R\Delta u'^2 \tag{6}$$

$$N' = N'_0 + N'_{\dot{v}}\dot{v}' + N'_{\dot{r}}\dot{r}' + N'_u\Delta u' + N'_{uu}\Delta u'^2 + N'_v v' + N'_{vvv}v'^3 + N'_{v\delta\delta}v'{\delta'_R}^2 + N'_r r' + N'_{rrr}r'^3 + N'_\delta\delta'_R + N'_{\delta\delta\delta}{\delta'_R}^3 + N'_{\delta vv}\delta'_R v'^2 + N'_{\delta u}\delta'_R\Delta u' + N'_{\delta uu}\delta'_R\Delta u'^2 \tag{7}$$

Investigated Ship

The present investigation is done on a Serie 60 hull with $c_B = 0.7$. For this hull extensive results of model tests in deep water are available for validation, [11]. The main dimensions are shown in Tab. 1. The body plan of the hull is shown in Fig. 1.

The investigations are performed for a velocity of $u_0 = 16.5kn$ which results in a Froude number of $F_n = \frac{u_0}{\sqrt{gL_{pp}}} = 0.2$.

Numerical Grids

For each water depth a numerical grid is generated. All three grids have the same dimensions in the horizontal plane, i.e. one ship length in front of

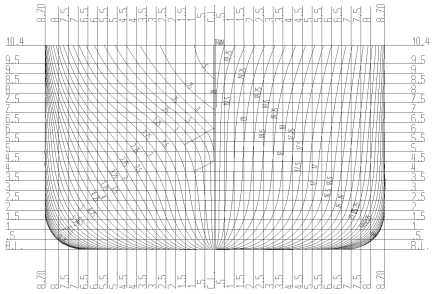

Figure 1. BODY PLAN OF SERIE 60 HULL.

the ship, two ship lengths to each side and four ship lengths behind the ship.

All grids are generated with Hexpress, a commercial automatic grid generator for complex geometries, which makes unstructured grids out of hexahedron elements.

First, calculations are performed in deep water. Here the distance between the ship bottom and the lower plane of the grid equals one ship length. In total, this grid contains 441,530 cells. For shallow water, with water depth being 1.6 and 1.2 times the ship draft, the generated grids contain 868,376 and 942,893 cells, respectively. In Fig. 2 the numerical grid for $h/D = \infty$ is shown.

The depth Froude number is $F_{nh} = \frac{u_0}{\sqrt{gh}} = 0.661$ for $h/D = 1.6$ and $F_{nh} = 0.764$ for $h/D = 1.2$.

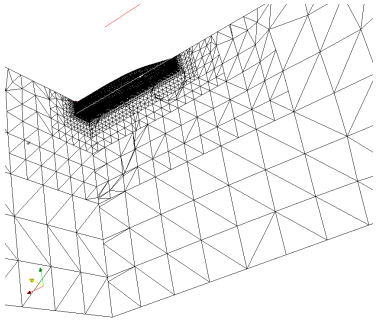

Figure 2. PART OF THE NUMERICAL GRID FOR $h/D = \infty$.

Boundary Conditions

- The upper plane, which is the free surface, is modelled as a symmetry plane. No velocity in normal direction to this plane is allowed. The tangential component is not constrained.
- At the plane behind the ship a fixed pressure is given.
- At the hull a no-slip wall boundary is set. To reduce the necessary amount of cells a high-R_n wall function is applied.
- At the plane in front of the ship and at the two side planes an inflow velocity is given. This velocity corresponds to the negative ship velocity.
- In the deep water case, the bottom is regarded as symmetry plane. In the two shallow water cases, a velocity analogue to the inflow is given.

VALIDATION

The calculated results of the deep water case are compared to experimental results of [11]. Figures 3 and 4 show the calculated forces in y- and in x-direction for different transverse and longitudinal velocities, respectively, plotted against the rudder angle.

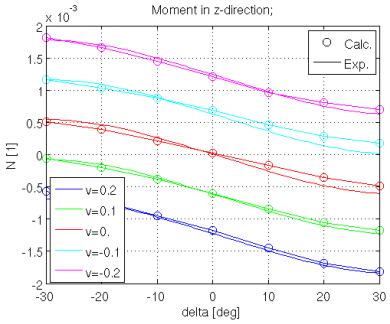

Figure 3. YAW MOMENT.

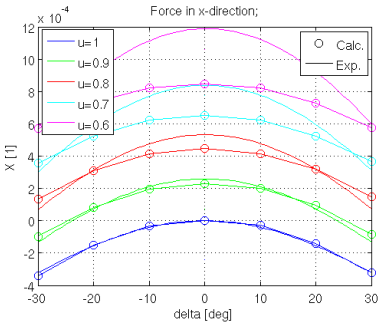

Figure 4. SURGE FORCE.

As can be seen in Fig. 3, the calculated yaw moments for different transverse velocities are in good agreement with the measured results. The same can be found for the sway force. However, the force in x-direction shows growing discrepancies for growing Δu, i.e. smaller surge velocities, see Fig. 4. Also sway force and yaw moment show increasing discrepancies for larger Δu. It appears, that the propeller effect is reflected wrong for propulsion points deviating from the self propulsion point. Also the neglected free-surface might have a considerable influence in this case.

The results of the unsteady pure-sway calculations show good agreement with the experimental results in [11], see Fig. 5. The calculated side forces due to pure yaw show some deviation in comparison with the measured values, Fig. 6.

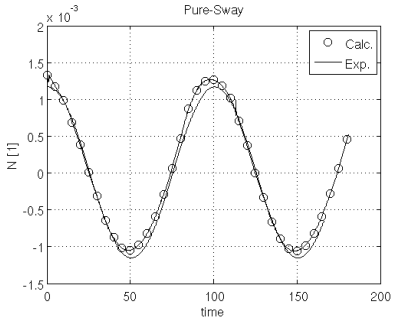

Figure 5. YAW MOMENT IN PURE-SWAY.

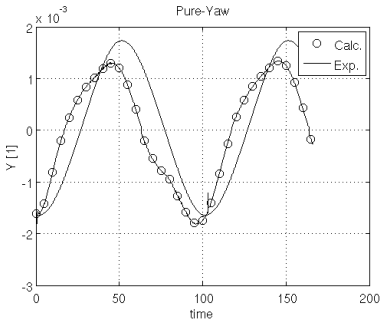

Figure 6. SWAY FORCE IN PURE-YAW.

By use of fourier transformation and method of least-squares the hydrodynamic derivatives of the hull are identified out of the calculated forces and moments. A set with 45 derivatives is obtained in this way for each water depth.

CALCULATIONS FOR DIFFERENT WATER DEPTHS

For the two shallow water cases much more calculation time is needed than in deep water. More iterations per time step and smaller time steps are necessary to reach convergence.

The calculations show that the forces and moment increase with decreasing water depth, especially for the forces pointing in the directions of the flow (i.e. X for variation in u and Y and N for variation in v), see Fig. 7 and Fig. 8.

The figures clarify that the forces are shifted parallel i.e. the hull force grows more than the rudder force. The rudder relatively looses influence.

The results obtained by the unsteady calculations show the same tendencies as those from the steady calculations, see Fig. 9 and Fig. 10.

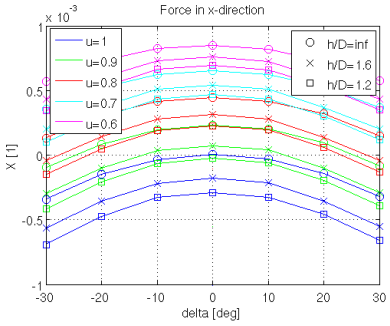

Figure 7. SURGE FORCE; DIFFERENT WATER DEPTHS.

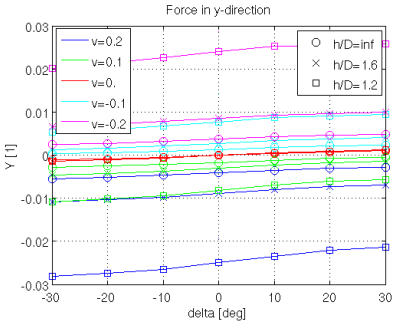

Figure 8. SWAY FORCE; DIFFERENT WATER DEPTHS.

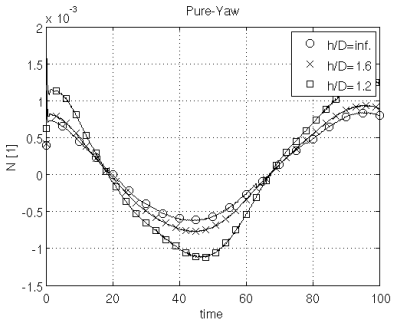

Figure 9. YAW MOMENT IN PURE-YAW; DIFFERENT WATER DEPTHS.

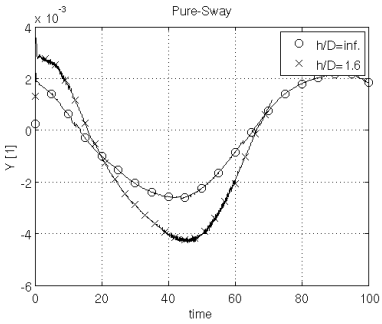

Figure 10. SWAY FORCE IN PURE-SWAY; DIFFERENT WATER DEPTHS.

Directional Stability

The manoeuvring derivatives obtained from the forces can be used to study the directional stabil-

ity. The stability condition is that $C > 0$, where C is the determinant of the damping matrix D of the linearized equation of motion, [12].

$$C = |D| = \begin{vmatrix} Y_v & Y_r - mU \\ N_v & N_r - mx_G U \end{vmatrix} \tag{8}$$

The stability indices for the different water depths are:

$$\begin{aligned} C &= -1.89 \cdot 10^{-4} \quad \text{for} \quad h/D = \infty \\ C &= 2.47 \cdot 10^{-6} \quad \text{for} \quad h/D = 1.6 \\ C &= 5.48 \cdot 10^{-4} \quad \text{for} \quad h/D = 1.2. \end{aligned}$$

The values of C indicate, that the ship is directional unstable in deep water. But the stability improves with decreasing water depth. However, the stability index is rather small in all cases i.e. the ship appears to be critically stable on all three water depths.

SIMULATION OF STANDARD MANOEUVERS

The sets of hydrodynamic derivatives obtained by the CFD calculations have been used to simulate standard manoeuvers on the different water depths.

For the simulation of manoeuvers the acting forces are calculated in discrete time steps. The known forces are used to calculate the accelerations. Via Runge-Kutta integration of the accelerations the velocities are obtained. The coordinates and the heading of the ship, respectively its track, are obtained by an Euler integration of the velocities. Also, the velocities are used in the next time step to get the acting forces. The method is able to handle four degrees of freedom, but in the present study only surge, sway and yaw are considered.

For different rudder angles turning circle manoeuvers are simulated, Fig. 11. Table 2 shows the characterisic parameters of the turning circles on the three different water depths. The numbers in brackets show the ratio of the values compared to the deep water results. In shallow water the turning circles become much larger than in deep water. The tactical diameter more than doubles on a waterdepth of $h/T = 1.2$ (increase by a factor of 2.3). However, the rate of turn just decreases averaged by 44%. Due to the decreased rate of turn, the resistance of the ship decreases in comparison to the deep water case. Subsequently the velocity reduction in longitudinal direction is smaller in both shallow water cases than in the deep water case. However, the velocity reduction for $h/D = 1.2$ is higher than for $h/D = 1.6$, see Tab. 2.

Figure 12 to 14 show the results of $10°/10°$ zigzag manoeuvers. The characteristic parameters of

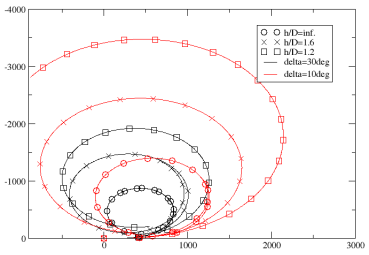

Figure 11. TURNING CIRCLE WITH POSITIVE RUDDER ANGLE.

Table 2. CHARACTERISTIC PARAMETER OF TURNING CIRCLE MANOEUVER

h/D	**Max. Advance**	**Tact. Diam.**	**rate of turn**	$\mathbf{u/u_0}$
–	m	m	deg/s	–
		$\delta = 10°$		
∞	1245	-1395	-0.5	0.69
1.6	1647 (1.32)	-2445 (1.75)	-0.37 (0.74)	0.92 (1.33)
1.2	2142 (1.72)	-3474 (2.50)	-0.24 (0.48)	0.85 (1.23)
		$\delta = 30°$		
∞	831	-871	-0.61	0.49
1.6	1006 (1.21)	-1472 (1.69)	-0.51 (0.84)	0.73 (1.49)
1.2	1256 (1.51)	-1920 (2.2)	-0.39 (0.64)	0.68 (1.39)

the manoeuvers and also for these of $20°/20°$ zigzag manoeuvers are listed in Tab. 3. The numbers in brackets are again the ratio of the absolute shallow water values and the deep water values. The table emphasises the results of the stability analysis. With decreasing water depth, the initial turning time is increasing while the yaw checking time is decreasing. I.e. the time until the ship is turning becomes larger and the time to stop the turning reduces for the water becoming more shallow.

Table 3. CHARACTERISTIC PARAMETER OF ZIG-ZAG MANOEUVER

h/D	**Init. Turn. Time**	**Yaw Check. Time**	**1st Oversh. Angle**	**2nd Oversh. Angle**
–	s	s	deg	deg
		$10°/10°$		
∞	56.3	43.9	7.76	24.24
1.6	65.0 (1.15)	23.5 (0.54)	3.90 (0.50)	16.12 (0.67)
1.2	76.4 (1.36)	21.0 (0.48)	2.48 (0.32)	3.70 (0.15)
		$20°/20°$		
∞	59.2	51.1	15.99	18.99
1.6	64.9 (1.10)	30.6 (0.60)	9.08 (0.57)	13.82 (0.73)
1.2	79.3 (1.34)	27.3 (0.53)	5.89 (0.37)	5.31 (0.28)

CONCLUSIONS

In shallow water the hull forces are much higher. The rudder forces increase less than the hull

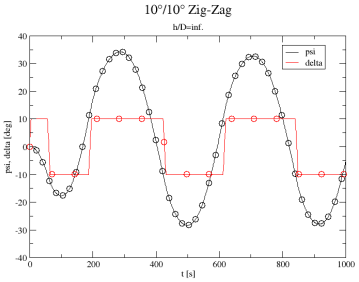

Figure 12.

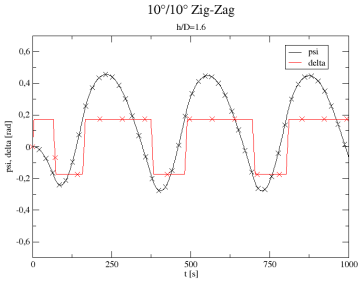

Figure 13.

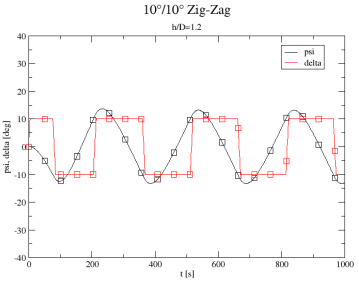

Figure 14.

forces. Due to the smaller ratio of rudder forces to hull forces, the rate of turn is less and the turning circles become much larger.

In the investigated case the directional stability of the hull improves on shallow water. Regarding the linear derivatives, Y_v increases most with decreasing water depth. Because N_v is increasing less, the point of attack of the force due to drift motion is moving amidships. This results in the improved directional stability.

The reduction of longitudinal velocity during turning is smaller in shallow water. This might lead to the critical situation, that the master estimates the turning behaviour wrong, and disregards the higher velocity and higher advance.

The longitudinal velocity has been chosen to be the same on all three water depths and is rather high in the shallow water cases. So a direct comparison between the water depths can be drawn. However, normally the ship speed is reduced on shallow water.

In the present paper, free-surface as well as trim and sinkage are neglected. Further calculations should be conducted with these effects taken into account. Especially in shallow water there should be a large dependence on these parameters.

ACKNOWLEDGMENT

The authors are grateful to Prof. Cura Hochbaum, TU Berlin, for his kind assistance and advices.

REFERENCES

[1] Crane, C., 1979. “Maneuvering trials of a 278,000-dwt tanker in shallow and deep waters”. *SNAME Trans.,* ***87***, pp. 251–283.

[2] Steele, B. N., and Wood, R. J., 1971. Shallow water manoeuvring using a conventional and a rotating cylinder rudder - a comparison with deep water performance. Tech. rep., National Physical Laboratory.

[3] ITTC, 2008. Testing and extrapolation methods manoeuvrability captive model test procedures. ITTC – Recommended Procedures and Guidelines.

[4] Committee, T. M., ed., 2008. Proceedings of 25th ITTC, Vol. 1. Final Report and Recommendations to the 25th ITTC.

[5] Hochbaum, C., 2008. “Manoeuvring prediction for two tankers based on rans simulations”. In SIMMAN 2008 - Workshop on Verification and Validation of Ship Manoeuvring Simulation Methods.

[6] Rung, T., Wöckner, K., Manzke, M., Stück, A., Brunswig, J., and Ulrich, C., 2009. “Challenges and perspectives for maritime cfd applications”. *Jahrbuch der Schiffbautechnischen Gesellschaft,* ***103***.

[7] Manzke, M., 2008. “Numerical simulation of unsteady body motion in turbulent flow”. Master’s thesis, Hamburg University of Technology.

[8] Moctar, O. M. E., 2001. “Numerische Berechnung von Strömungskräften beim Manövrieren von Schiffen”. PhD thesis, TU Hamburg-Harburg. (in German).

[9] Oltmann, P., and Wolff, K., 1976. “”Computerized Planar Motion Carriage” Anlagenbeschreibung und erste Betriebserfahrungen”. *Jahrbuch der Schiffbautechnischen Gesellschaft,* ***70***, pp. 414–441. (in German).

[10] Abkowitz, M. A., 1964. *Lectures on Ship Hydrodynamics - Steering and Manoeuvrability*. Danish Technical Press, Lyngby, Denmark.

[11] Wolff, K., 1981. Ermittlung der Manövriereigenschaften fünf repräsentativer Schiffstypen mit Hilfe von CPMC-Modellversuchen. Tech. rep., Institut für Schiffbau der Universität Hamburg. (in German).

[12] Faltinsen, O. M., 2005. *Hydrodynamics of High-Speed Marine Vehicles*. Cambridge University Press.

Using CFD for simulation of ships with different fuel saving rudder-propeller devices

Claus D. Simonsen, Christian Klimt Nielsen and Zdravko Kishev
FORCE Technology, Denmark, cds@force.dk

Introduction

FORCE Technology, Grontmij | Carl Bro and Rolls Royce in Denmark are involved in a joint project under DCMT (Danish Centre for Maritime Technology). The goal of the project is to test and demonstrate the capabilities of RANS in connection with flow simulations for different rudder and propeller configurations. Focus is on a complete CFD model for hull, propeller and appendages, which can account for the mutual interaction between the components when the flow field is calculated. In RANS, propellers can be modeled by body-forces as in [1], but in the present work the real propeller geometry is modeled using the same approach as outlined in [2]. In the present work different rudder-propeller configurations are evaluated behind a 180m bulk carrier in order to study how different configurations influence the ship performance for a given speed at the ships self-propulsion point. In addition to the combined hull-propeller calculation, both propeller and hull are simulated in an open water and a resistance test setup, respectively. In order to check the performance of the CFD model, the calculated results are compared with experimental data measured in FORCE Technology's towing tank. All meshing and flow simulation are conducted with Star-CCM+ provided by CD-adapco.

Numerical method

The computations are performed with the Reynolds Averaged Navier-Stokes (RANS) solver StarCCM+ from CD-adapco. The code solves the RANS and continuity equations on integral form on a unstructured mesh by means of the finite volume technique. Both steady state and transient calculations are considered. For the steady state calculations the temporal discretization is based on a first order Euler difference, while a second order difference is used for transient calculations. Spatial discretization is performed with second order schemes for both convective and viscous terms. The pressure and the velocities are coupled by means of the SIMPLE method. Closure of the Reynolds stress problem is achieved by means of the isotropic blended k-ε/k-ω SST turbulence model with an all Y^+ wall treatment. The rotating propeller is treated in different ways. For open water calculations the propeller inflow is uniform, so the moving reference frame approach is applied, i.e. the blade velocity is set on the propeller blades and centripetal effects are included in additional source terms in the momentum equations. For the propeller rotating behind the ship, a rigid body approach is applied. The free surface is modeled with the two phase volume of fluid technique (VOF). Further details about the code can be found in [3].

Basic ship configuration

The study is carried out for the 180m Diamond 34 Bulk Carrier from Grontmij | Carl Bro, Figure 1. The "as built" configuration, i.e. ship with original rudder and propeller, is considered as base case. Later in the study, the rudder and propeller are changed. The computations are done in model scale using a scale of 1:23.73. The main particulars and propeller data for the base configuration are shown in Table 1. Finally, one model speed condition was chosen for all configurations namely 1.479 m/s (14 knots full scale) corresponding to a Froude number of 0.173.

L_{pp}	[m]	7.449
B	[m]	1.264
T	[m]	0.411
S	[m^2]	15.533
C_B	[-]	0.80
D_P	[m]	0.236
Z	[no. of blades]	4
$P/D_{0.7}$	[-]	0.839

Table 1: Hull and propeller data.

Figure 1: 180m bulk carrier.

Rudder propeller configurations

In addition to the "as built" rudder-propeller configuration for the Diamond 34 vessel, the so-called PROMAS solution designed by Rolls Royce is considered. The goal of the project is to see if the CFD model can capture the effect of changing rudder-propeller configuration and learn more about the background for the effects. In Figure 2, the original rudder propeller configuration is shown together with the PROMAS configuration.

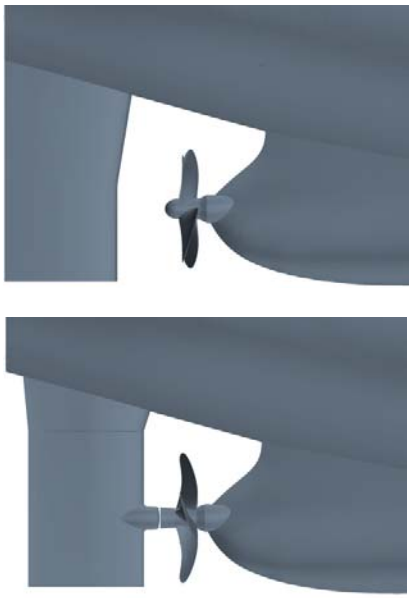

Figure 2: Upper: Original design (Base case). Lower: PROMAS design

The PROMAS geometry was fitted to the Diamond 34 by Rolls Royce. The design was based on basic geometric information and wake field measurements previously done on the vessel [4]. When compared to the "as built" version several differences are seen for the PROMAS configuration compared to the original one:

- The leading edge of the rudder is closer to the propeller
- The propeller geometry is different
- There is a rudder bulb on the PROMAS rudder plus a hub fairing

The rudder on the PROMAS comes with a very mild asymmetry, since the leading edge is slightly twisted to meet the propeller swirl. The original rudder is straight and symmetric. The PROMAS propeller differs from the original one by having a smaller diameter and a smaller pitch ratio, Table 2.

D_P	[m]	0.228
Z	[no. of blades]	4
$P/D_{0.7}$	[-]	0.777

Table 2: Main propeller characteristics for the PROMAS propeller – model scale

In order to study the possible effect of the different elements of the PROMAS device, two additional rudder configurations were made based on the PROMAS rudder: An asymmetric rudder without bulb and a symmetric rudder without bulb. So, in total 5 different rudder-propeller configurations are considered.

Case	Propeller	Rudder
1	Original	Original (O)
2	PROMAS	Asymmetric rudder with bulb (A+B)
3	PROMAS	Symmetric rudder without bulb (S)
4	PROMAS	Asymmetric rudder without bulb (As)
5	Original	Symmetric rudder without bulb (S)

Table 3: Propeller and rudder configurations.

For all 5 cases standard resistance and self-propulsion tests were made in FORCE Technology's towing tank. The results and conclusions from all tests are documented in [5], and all comparisons between computational results (CFD) and measurements (EFD) presented in the following are based on this data set.

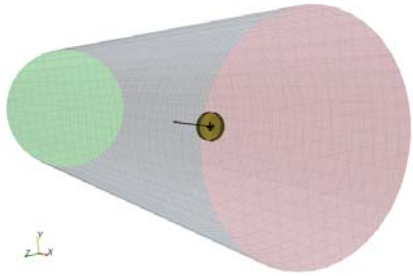

Figure 3: Computational grid for open water propeller.

Computational meshes

Concerning the grid, the computations are performed with unstructured grids generated in Star-CCM+. Both hull, rudder and propeller are modeled with a trimmed mesh, which is a hexa-dominant polyhedral mesh. Since the propeller is running behind the ship, both sides of the hull are considered instead of exploiting the centre plane symmetry. The grids are shown in Figure 3 to Figure 5. The near wall spacing of the grids on no-slip surfaces are in the range from $y^+ \approx 1$ to $y^+ \approx 30$.

Figure 4: Computational grid on hull.

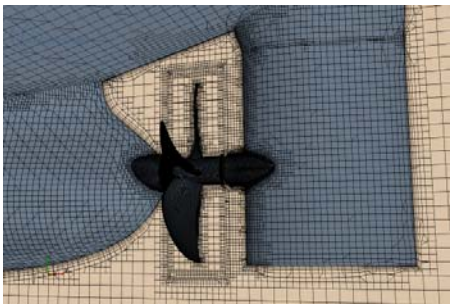

Figure 5: Computational grid on hull and PROMAS propeller.

Results for open water propeller calculation

The open water simulation was carried out at the same running conditions as used in the experimental set up at FORCE Technology. The propeller was set up in a large cylindrical domain, with a local smaller cylinder around it. The flow solver was run in steady mode and the rotation of the propeller was accounted for by using moving reference frame approach. The approach works fine in open water, where the propeller sees a completely uniform inflow field.

Like in the experiment the computed thrust and torque on the propeller were converted into the dimensionless thrust coefficient K_T, torque coefficient K_Q and the open water efficiency η_0. The advance ratio J and the three coefficients are defined as

$$J = \frac{U_a}{nD}$$

where U_a is the speed of advance, n is the propeller revolution rate and D is the propeller diameter.

The thrust coefficient K_T and torque coefficient K_Q are defined as

$$K_T = \frac{T}{\rho n^2 D^4} \qquad K_Q = \frac{Q}{\rho n^2 D^5}$$

where T and Q are the measured thrust and torque, respectively. ρ is the density of water.

The propeller efficiency is defined as

$$\eta_0 = \frac{J}{2\pi}\frac{K_T}{K_Q}$$

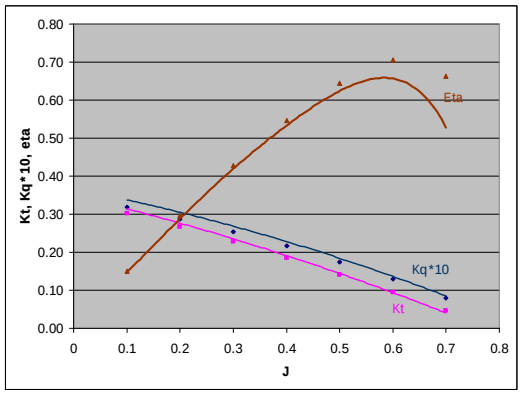

Figure 6: Open water results - Original propeller

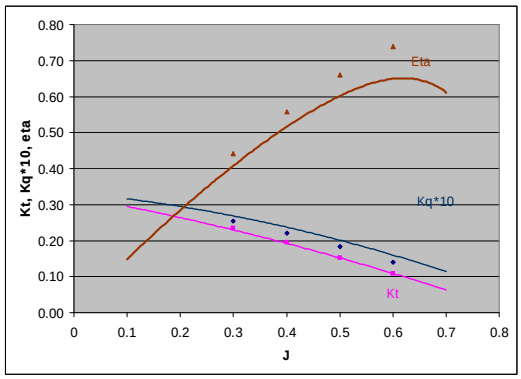

Figure 7: Open water results – PROMAS propeller

Figure 6 and Figure 7 show the calculated open water curves (marked wit points) together with the measured curves (full lines) [5]. The figures show that in the range from close to bollard pull condition (J=0.1) to the vessels point of operation (around J=0.5), the CFD results match the measurements relatively well, with the thrust being close to the measured values and the torque being reasonably close to the measured values. For both propellers a tendency for the torque to be under predicted is noticed.

Results for hull with appendages

The numerical appended hull model without propeller was tested in a resistance test setup, where the model was positioned and locked according to measured dynamic sinkage and trim. The considered model speed was 1.479m/s. (14kn full scale), corresponding to a Froude number of 0.173. The calculation was performed for the Diamond 34 configuration with its original rudder.

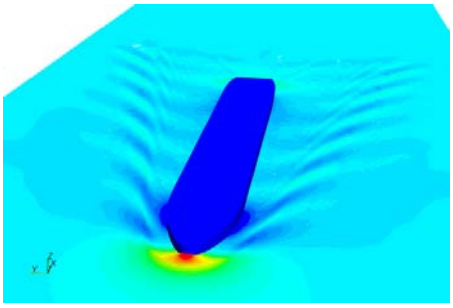

Figure 8: Calculated free surface elevation.

Comparison between the calculated and the measured resistance is given in Table 4, where quite good agreement between calculation and measurement is achieved.

$R_{M,CFD}$	$R_{M,EFD}$	Deviation
56.24 N	56.97 N	1.30%

Table 4: Bare hull resistance in model scale CFD versus EFD

With respect to the field quantities no measured data is available for comparison. However the results can briefly be summarized as follows:
1) High pressure occurs in the bow region where the flow is slowed down and the bow wave is formed due to stagnation.
2) The pressure decreases around the shoulders, where the flow is accelerated to get around and below the hull.
3) Further downstream the pressure recovers and basically constant flow properties along the prismatic section of the hull are seen.
4) At the aft shoulders, i.e. the region where the hull form start to narrow in towards the stern and the water starts to flow into the wake region, the pressure decreases again.
5) The pressure increases again in the stern region and formation of the wake field with lower velocities are seen. The pressure field is not shown here.
Figure 8 shows the calculated wave elevations around the ship and reveals a typical Kelvin wave pattern. Finally, Figure 9 shows the calculated nominal wake field behind the ship at a cross section located at the propeller plane. It is seen that the wake field is not symmetric with respect to centre plane, which is probably due to the dynamic behaviour of the flow around the stern. The geometry and mesh were made by reflection around the centre plane, so the mesh is perfectly symmetric.

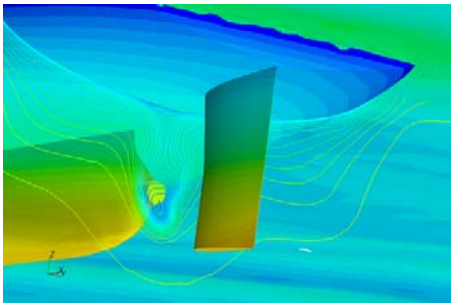

Figure 9: Calculated wake field.

Results for combined rudder-propeller-hull configuration

After propeller and hull have been investigated separately a combined model is made. In the present case the propellers rotational number was taken from measurements, as this part of the investigation would be to validate the model's ability to predict T and Q for a given propeller revolutions, n, and not to solve the problem of finding n at the self-propulsion point.

Flow field observations

In the combined model some general flow features that can be observed these are presented in the sections below. Due to the limitations of the present paper only a few configurations have been chosen as example.

Propeller pressure distribution

In the figures below, the pressure distribution is shown for suction and pressure sides of the propeller in the configuration with the PROMAS propeller and a symmetric rudder.

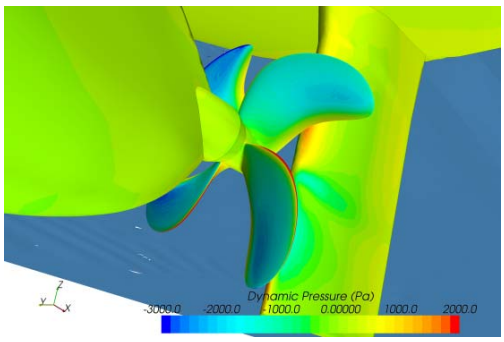

Figure 10: Port side, suction side

First it is seen how the propeller is working harder (higher negative dynamic pressure on suction side) in areas where the surrounding fluid has to be accelerated the most, namely where the propeller blade passes the uppermost low speed region around the 12 o'clock position, Figure 10. The closer one gets the hull surface, the slower the fluid will be, due to the presence

of the hull boundary layer and the "shadow" from the skeg.

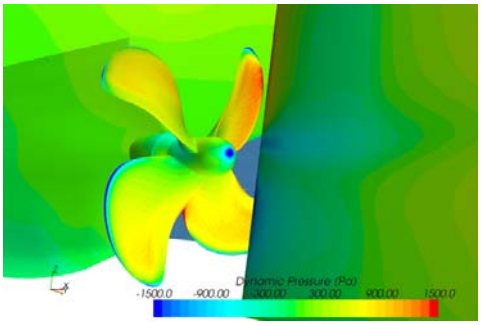

Figure 11: Port side, pressure side.

On the pressure side, Figure 11, the same effect is noticed – higher pressure as the propeller blade rotates through the low velocity zone. Finally, the load on the blade also reflects the cross flow direction in the wake, i.e. the load reflects whether the blade moves downwards or upwards through the wake.

When comparing the suction and pressure sides, it is noticed how both leading and trailing edges experience very high pressure gradients (across the edges) at the middle section of the blade. Obviously it is important, but also difficult, to resolve these very small pressure jumps across these edges, in order to predict especially the propeller torque Q.

Finally, a low pressure region is seen to be located at the tip of the hub, which is due to rotating propeller producing a hub vortex downstream of the propeller.

Hub vortex

Figure 12 and Figure 13 illustrates how streamlines released from the propeller and travel downstream for two different propeller-rudder configurations. It is seen how the hub vortex is modified by the hub/bulb geometry of the PROMAS configuration.

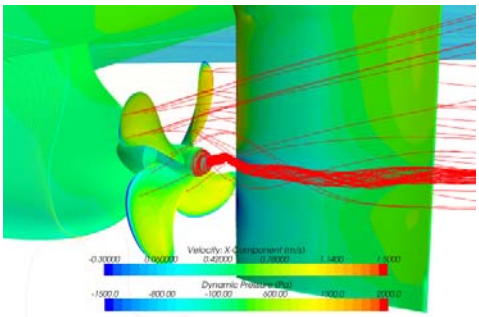

Figure 12: Streamlines released from propeller. PROMAS propeller and symmetric rudder.

The vortex originating from the faired hub is significantly reduced compared to the case with the 'free' hub. This indicates that the vorticity and hence the loss of rotational energy is less for PROMAS compared to the other case.

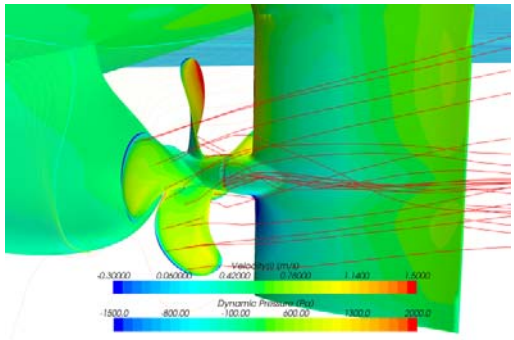

Figure 13: Streamlines released from propeller. PROMAS propeller and symmetric rudder with bulb.

Rudder load distribution

From the figures below it is seen how the propeller induced flow is affecting the pressure distribution over the rudder, as a typical 'anti-symmetric' pattern of high and low pressure areas are present at the leading edge corresponding to the propeller induced flow reaching the rudder.

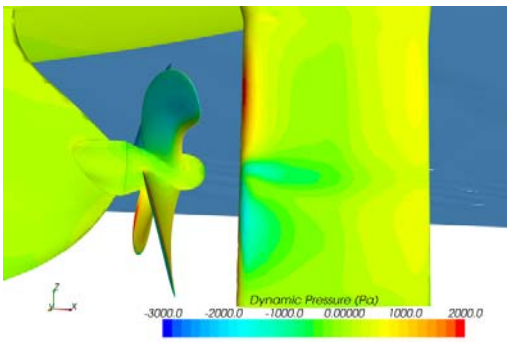

Figure 14: Port side rudder pressure

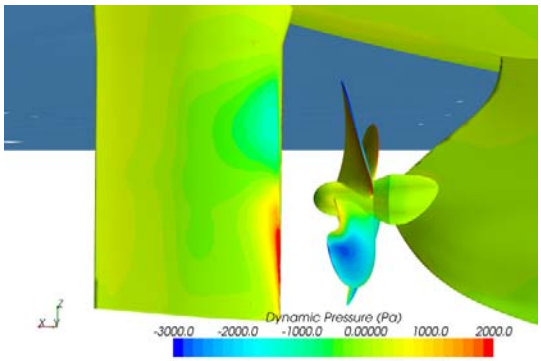

Figure 15: Starboard rudder pressure

Also it is seen how the low pressure connected to the hub vortex, *Figure 12*, creates a signature along the port side of the rudder.

Propeller forces and moments

In Table 5, the deviations between model scale CFD and measurement are.

Case	Propeller	Rudder	T	Q
1	Original	O	0.63%	2.98%
2	PROMAS	A+B	-4.53%	-5.28%
3	PROMAS	S	-2.84%	-4.66%
4	PROMAS	As	-4.03%	-4.87%
5	Original	S	2.66%	3.53%

Table 5: Deviations between CFD and EFD results for thrust and torque for the 5 cases.

For the configurations with the original propeller, CFD is seen to over predict Q, and for the configurations with PROMAS propeller the CFD is seen to under predict Q. This trend is somewhat different from the open water results, where the Q values of both the PROMAS propeller and the original propeller were under predicted by the CFD method.

For T, the CFD calculations are seen to under predict the thrust in cases that use the PROMAS propeller by a margin in the order 3-5%. This is a somewhat larger deviation range compared to the open water calculations, where the deviations in K_T were very small (<1% around the working point).
The predicted T values for the original propeller configurations are over predicted within a range of 1-3%, which is in reasonable agreement with open water results.

The different trends could be due to different propeller resolutions between configurations. This is being investigated further. However, to summarize, the results show that the method does capture the overall values of Q and T within a range of 5%.

Concluding remarks

In the present work RANS CFD has been used to perform numerical open water, resistance and self propulsion tests.

The numerical open water tests show that thrust and torque coefficient are predicted fairly well. Though, a tendency for under prediction of Q is noted.

The numerical resistance test with the appended hull is in good agreement with measurements, showing a deviation of about 1%.

The self propulsion tests are performed with the propeller revolutions obtained at the model tests. The flow field is investigated by evaluating the dynamic pressure on the hull, rudder and propeller. Here it is observed how the load on the propeller blade is influenced by the wake and evidently high pressure gradients are observed at both the leading and trailing edges. It can clearly be seen that the rotating propeller gives an asymmetric load distribution on the rudder. Finally, streamlines are released to illustrate the flow around the hub and the rudder and it is shown that the hub vortex can be reduced by adding a fairing piece between hub and rudder as done in PROMAS concept.

Regarding propeller forces and moments in the behind the ship condition it is generally seen that the CFD model can predict the thrust and torque within about 5%. It must though be noted that the thrust and torque is over predicted with the original propeller and under predicted with the PROMAS propeller. There is some incoherence between thrust and torque predicted in the open water and in the behind ship condition, which could be explained by different grid resolutions.

Future activities

There are primarily two topics for future work: one is to estimate the power consumption so the CFD model can be used to quantify which configuration is the most energy efficient. The other is to find the self propulsion point using CFD, so numerical self propulsion tests can be conducted. Finally, grid sensitivity should be investigated.

Acknowledgements

This research is sponsored in parts by The Danish Maritime Foundation through DCMT.

References

[1] *Simonsen, C.D. and Stern, F., "RANS maneuvering simulation of Esso Osaka with rudder and a body-force propeller," J. of Ship Research, Vol 49, No. 2, June 2005*
[2] *Simonsen, C.D. and Carstens, R., "RANS simulation of the flow around a ship appended with rudder, ice fins and rotating propeller," proceedings from NuTTS08, Brest France, 2008*
[3] *StarCCM+ Users manual*
[4] *FORCE Technology report no. 107-26802 (Confidential)*
[5] *FORCE Technology report no. 107-24345.08-1B (Confidential)*

Propeller Optimisation in behind Condition considering Sheet Cavitation

Florian Vesting (florian.vesting@chalmers.se), **Daniel Knutsson** (daniel.knutsson@chalmers.se),
Rickard Bensow (rickard.bensow@chalmers.se), **Lars Larsson** (lars.larsson@chalmers.se)

Department of Shipping and Marine Technology, Chalmers University of Technology,
SE 412 96 Gothenburg, Sweden

Introduction

Whenever a ship is in motion, the momentum induces pressure and velocity fluctuations in the wake. Consequently, a propeller operating behind a ship, experiences a non-uniform flow field with high velocity gradients. Depending on the operation conditions, by means of rotational speed or submergence of the propeller, the local absolute pressure drops below the vapor pressure and a phase change can be observed. This phenomenon is commonly known as cavitation. These cavities grow and collapse extremely rapidly which cause vibration, noise and on occasion erosion. However, cavitation has always been a major concern for the propeller design and a common philosophy has been to avoid cavitation within the range of operating condition. Nevertheless, for high performance propeller this is no longer possible and the presence of cavitation needs to be accepted and considered in design.

Investigations of cavitating flows are of interest in many scientific and technical problems and can be observed in many flow situations. The process itself is physically utmost complex while the flow is highly non-linear and multi-phase. The problem of cavitation on a foil is well known but still very complex and it becomes even more complex on a ship propeller. Computations of viscous flow on realistic configurations require efficient methods and high grid resolution computation. The computational demand makes it certainly not feasible for practical design tasks. To obtain information about cavitation at an early design stage, potential flow methods still play an important role due to their computational efficiency, which makes them attractive to use in optimisation based propeller design. In ship hydrodynamics it is considered standard procedure to utilize potential flow codes for the propeller in a given wake complemented by experiments. For systematic variant studies, the potential flow based methods gives reasonable accuracy for low computational time before further experimental work commences. However, considering the interaction effects between the propeller and the hull has only fairly recently been feasible, and has not to our knowledge been performed considering a cavitating propeller.

The work presented in this paper, follows up a presented work of Han and Bark (2006) and Han and Larsson (2006). Han presented a cavitating propeller optimized in a given wake, to maximize the efficiency and minimize the propeller-induced pressure fluctuations, by tuning the propeller-blade geometry. Moreover, a near optimum propeller and an off-design propeller were optimized behind a ship at full scale by minimizing the delivered power for a certain speed. Thus as a logical consequence, the aim of this work is the automatic optimization of a propeller geometry under consideration of the cavitating properties in conditions behind a ship. By considering the delivered thrust as an equality constraint, span-wise distribution parameter curves for pitch ratio, chord length ratio, camber ratio and skew are changed to create geometry variation. For the presented investigation, the revolution speed, number of blades and the diameter as well as the ships speed are fixed constants, mimicking the work of Han and Bark (2006). The objective is to minimize the pressure pulses and maximize the propeller efficiency for a 170 meters container vessel with a fixed pitch off-design propeller.

The ship wake is iteratively computed utilizing a Navier-Stokes solver (SHIPFLOW´s Chapman) and updated with the body forces from a potential flow solver representing the propeller geometry (MPUF3A of University of Texas). Han and Larsson (2006) showed the validation of the computed wake from Chapman and the result of the presented grid density study are applied in the present work. In addition, numerical results for the initial design are evaluated with the propellers performance from experiments in the cavitation tunnel. The geometry variation and constraints-, parameters- and objectives-management is controlled by the FRIENDSHIP-SYSTEMS Framework. The built-in multi-objective evolutionary algorithm is utilized.

References

Bertram, V. (2000),
Practical Ship Hydrodynamics. Oxford: Butterworth-Heinemann.

Han, K.-J., Bark, G., Larsson, L., & Regnström, B. (2006)
A Procedure for Optimizing Cavitating Propeller Blades in a Given Wake. Ship Technology Research .

Han, K.-J., Larsson, L., & Regnström, B. (2006)
Numerical optimization of the propeller behind aa ship hull at full scale. 26th Symposium on Naval Hydrodynamics. Rome.

Lee, H., and Spyros, K. (2001)
Modelling of Unsteady Blade Sheet and Developed Tip VortexCavitation. International Symposium on Cavitation.

Lee, H., Gu, H., Kakar, K. and Kinnas, S. (2010)
MPUF user´s manual and documentation

Mishima, S. (1996)
Design of Cavitationg Propeller Blades in Non-Uniform Flow by numerical Optimization. Ph.D thesis, Messachussets Institute of Technology.

Tensor-based grid refinement criteria for ship flow simulation

Jeroen Wackers, Ganbo Deng and Michel Visonneau
Laboratoire de Mecanique des Fluides, Ecole Centrale de Nantes
CNRS-UMR 6598, 44321 Nantes Cedex 3, France
Jeroen.Wackers@ec-nantes.fr

1 Introduction

Adaptive grid refinement is a technique for efficiently solving flow problems by locally dividing the cells of a coarse original grid into smaller cells, thus increasing precision in regions where this is needed. Adaptive grid refinement methods have been developed since the 1970s, they are currently entering the industrial practice for the case of single-fluid flow. However, grid refinement for hydrodynamic flow applications has started being developed only recently.

The main particularity of ship flow simulation is, that many different physical types of flow may need to be resolved. Accurate resolution of wave fields requires different grids than aft-body and propeller-plane flow simulations. For grid refinement, this means that the refinement criterion (which is that part of the refinement algorithm that, based on the flow solution, decides where the grid should be refined) must be different for different flow problems. So for a grid refinement method that is generally applicable for ship flow simulations, it is of the highest importance that the refinement criteria can be easily exchanged.

Such an adaptive grid refinement method has been developed for ISIS-CFD [4], the unstructured finite-volume flow solver created by EMN (CFD Department of the Fluid Mechanics Laboratory). The method is integrated in the flow solver and entirely parallelised, including automatic redistribution of the grid over the processors. During a flow computation, the refinement procedure is called repeatedly. In such a call, first the refinement criterion is calculated, then the grid is refined based on this criterion. For steady flow, the refinement procedure converges: once the grid is correctly refined according to the criterion, further calls to the procedure no longer cause any changes. Details of the algorithm can be found in [5, 6], its use for unsteady flow is described in [7].

The ISIS-CFD flow solver can be used for many types of flow problems arising in ship flow simulation, so the above requirement holds for our refinement algorithm: different refinement criteria must be implemented and it must be easy to exchange these criteria. Therefore, refinement based on 3×3 symmetric tensors has recently been implemented in the code. This allows the specification of cell sizes that are anisotropic in all directions and therefore, maximum flexibility in the control of grid refinement. Due to its generality, many types of refinement criteria can be implemented in this framework.

This paper describes the tensor-based refinement. It starts with a comparison between isotropic and directional refinement, for which tensor-based criteria are natural (section 2). Then, in section 3 the principle of tensor-based refinement is explained and it is shown why it can be used for the implementation of highly different refinement criteria. Section 4 gives an example of a refinement criterion, based on the Hessian of the pressure. In section 5 this criterion is applied to the double-model flow around the KVLCC2 tanker. The paper ends with a conclusion.

2 Directional and isotropic refinement

The simplest grid refinement methods are isotropic: when a cell is refined, it is divided in all its directions (a rectangle is divided in four, a hexahedron in eight, etc.) The resulting small cells have the same shape as the original cell. Directional refinement is more flexible, but more difficult to implement; here, cells may be refined in all directions at once, or in one direction only. Thus, not only the cell sizes, but also their aspect ratios may be changed during refinement.

While directional refinement is more difficult to implement, it is essential for our type of grid refinement. Isotropic grid refinement is very costly in three dimensions, since every refinement of a cell means a division in eight (for a hexahedron). Thus, creating very fine cells to accurately resolve a local flow phenomenon becomes almost impossible. However, if we can profit from flow features that require a fine grid in only one direction (notably, the water surface!) by refining the grid in that direction only, then we can greatly reduce the number of cells required and thus, we can resolve finer flow details.

A second reason for directional refinement is, that we base our refinement on unstructured hexahedral original grids (see figure 1). In these grids, cells of completely different aspect ratios lie side by side. Therefore, when refining, we need to control the size of the fine cells in all their directions independently, otherwise we may get cells that have good, smoothly varying sizes in one direction, but wild changes from fine to coarse and back to fine in another. Isotropic refinement is not enough to prevent this. Therefore, for our type of grid refinement, directional refinement is the mandatory choice.

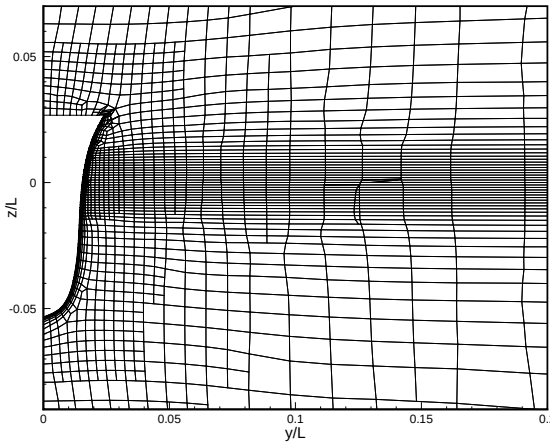

Figure 1: Cut through an unstructured hexahedral mesh.

3 Tensor refinement criteria

For directional refinement, a way is needed to specify different cell sizes in different directions. The use of metric tensors as refinement criteria is such a way. This technique was first developed for the generation and refinement of unstructured tetrahedral meshes [1, 2]. It is also an extremely useful and flexible framework for the refinement of our unstructured hexahedral meshes. This section describes first how the method works (section 3.1), then how it can be used to implement highly different refinement criteria (section 3.2).

3.1 Metric tensors

For tensor-based refinement, the refinement criterion in each cell is a 3×3 symmetric positive definite matrix C_i. This matrix is seen as a geometric transformation tensor, which maps a cell Ω_i in the physical space Ω onto a cell $\tilde{\Omega}_i$ in the modified space $\tilde{\Omega}$. Directional refinement is then applied to the cells to create a grid which, in the *modified* space, has the same size for all cells in all directions. The result in the real space Ω is an anisotropic, locally refined grid.

The refinement of the cells is decided as follows. Let the criterion tensors C_i in each cell be known (they are computed, in some way, from the flow solution, see the following sections). Then compute, in each hexahedral cell, the cell size vectors $\mathbf{d}_{j,i}$ ($j = 1, \ldots, 3$), which are the vectors between the opposing face centres in the three cell directions. Next, compute the modified sizes as:

$$\tilde{\mathbf{d}}_{j,i} = C_i \mathbf{d}_{j,i}. \tag{1}$$

Finally, decide to refine a cell in the direction j when this size exceeds a given, constant threshold value T_r:

$$\|\tilde{\mathbf{d}}_{j,i}\| \geq T_r. \tag{2}$$

The tensors C_i are direct specifications of the desired cell sizes: in a converged refined grid, the cell sizes are inversely proportional to the magnitude of the C_i. As a consequence, the C_i should be a function of the flow field only, they may not depend on the cell sizes themselves. This is the complete opposite of many refinement decision strategies for isotropic refinement, where the criterion is a local error estimation that varies with the grid size and the goal of the refinement is to obtain the same criterion value in all the cells. This procedure is intrinsically isotropic: it indicates which cells are to be refined, but not in which direction to refine them. Therefore, the tensor-based refinement is a more natural procedure for directional refinement.

3.2 Different types of criteria

An advantage of tensor-based refinement for ship flow simulation is, that nearly all types of refinement criteria can be formulated in terms of metric tensors. Therefore, it is possible to implement all these criteria without changing the decision process or the refinement procedure itself. This greatly increases the flexibility of the method.

Scalar criteria In many cases, refinement is to be based on a scalar quantity c_i in each cell. For example, in [6] refinement is performed according to the magnitude of the pressure gradient. While a scalar criterion can only specify isotropic refinement, it is still useful to combine these criteria with the directional refinement procedure, for the cases where the *original* grid is non-isotropic. In these cases, a good isotropic refined grid can never be obtained without directional refinement.

In the context of tensor-based refinement, scalar criteria are obtained with diagonal matrices that are created by first computing the scalar criterion c_i and then multiplying with the 3×3 identity matrix:

$$C_i = \mathcal{I}_3 c_i. \tag{3}$$

Vector criteria Criteria in vector form are used to specify refinement in one direction only. The direction of the vector $\mathbf{c}_i$ in each cell is the desired direction of refinement, its magnitude indicates the desired cell size. An important example for hydrodynamic flow is the refinement around the water surface for surface-capturing flow solvers (like ISIS-CFD). As these solvers model the surface with an equation for the discontinuous volume fraction of the water, the accurate capturing of the surface requires small cells in the direction normal to the surface. The surface is often horizontal in most of the domain and therefore aligned with the grid, so efficient refinement can be obtained by refining only in the normal direction of the surface. See [5, 6, 7] for further explanation and examples.

In tensor form, the vector criteria are implemented as matrices having only one non-zero eigenvalue, associated with the direction of the vector. In the directions normal to the vector, the eigenvalues are zero. This leads to a desired grid size of infinity in these directions. As a consequence, the grid is not refined in these directions, the original cell sizes are kept.

The tensors C_i are computed as follows (with $\otimes$ representing the tensor product):

$$C_i = \mathbf{c}_i \otimes \mathbf{c}_i. \tag{4}$$

Tensor criteria In the case where the refinement criterion is already a symmetric tensor, it can be used directly. This is, of course, the most powerful way of using the technique and generally the only one that appears in the literature. One possible manipulation to the criterion may be needed for tensors that, while symmetric, are not positive definite. In that case, it is enough to recompute C_i with the same eigenvectors as the original tensor, but with the absolute values of its eigenvalues.

4 Pressure Hessian criterion

In the next section, an example of a grid refinement study will be presented. For this study, the refinement is based on the Hessian matrix of second spatial derivatives of the pressure p:

$$\mathcal{H}_i = \begin{bmatrix} (p_i)_{xx} & (p_i)_{xy} & (p_i)_{xz} \\ (p_i)_{xy} & (p_i)_{yy} & (p_i)_{yz} \\ (p_i)_{xz} & (p_i)_{yz} & (p_i)_{zz} \end{bmatrix}. \tag{5}$$

This matrix is often used as the basis for the construction of tetrahedral meshes [1, 2]. For finite-element methods, the reason for this choice is, that the element interpolation errors are proportional to this matrix; this argument is sometimes used to motivate its use for finite-volume methods as well. As the interpolation errors are proportional to $\mathcal{H}$ times the grid size squared, the equi-distribution of the interpolation errors leads to the criterion:

$$C_i = (\mathcal{H}_i)^{\frac{1}{2}}, \tag{6}$$

where $(\mathcal{H}_i)^{\frac{1}{2}}$ has the same eigenvectors as $\mathcal{H}_i$ and eigenvalues that are the square roots of those of $\mathcal{H}_i$ (in absolute value).

The reason for choosing the pressure as the basis of the criterion concerns the boundary layers. As the required cell sizes in the boundary layer of a ship are well known, it is our idea that the user should generate these cells in the original grid and that the boundary layer should only be automatically refined where the outside flow dictates this. Since the pressure stays more or less constant over the thickness of the boundary layer, while the velocity components have high gradients, this idea implies that the pressure is the better choice as a refinement criterion.

5 KVLCC2 test

To investigate the behaviour of the Hessian criterion, we shall compute the double-model flow around the KVLCC2 tanker at model scale, $Re = 6.4 \cdot 10^6$ (see [3]). We will focus on the computed drag and the flow in the propeller plane. For grid refinement, this is a particularly hard case, as there are no dominating flow features (like a free surface, or flow singularities) that clearly demand refinement; to get good accuracy, grid refinement has to be applied all around the ship hull. So to prevent the grid from becoming too large, an effective refinement criterion is needed.

To study the Hessian criterion for this case, a systematic variation of the threshold T_r is carried out between $T_r = 0.14$ and $T_r = 0.01$, for situations where the maximum number of refinements of the cells (the g̈enerations)̈ is limited to 1, 2 or 3. The threshold is the main control for the grid refinement: for lower T_r, cells will be refined

over a larger area. Limiting the number of generations mostly has an influence on the regions near the ship hull where the flow gradients are largest: there, the maximum resolution becomes limited.

Figure 2 shows an example of the surface mesh for the refined grid with $T_r = 0.04$ and two generations maximum. The refinement is concentrated in the regions near the bow and the stern. Both directional and isotropic refinement is observed, the criterion creates smooth transitions between the isotropic zones and the directional refinement close to the bow, in front of the bow, and in the wake. In these regions, the directional refinement clearly helps to reduce the total number of refined cells.

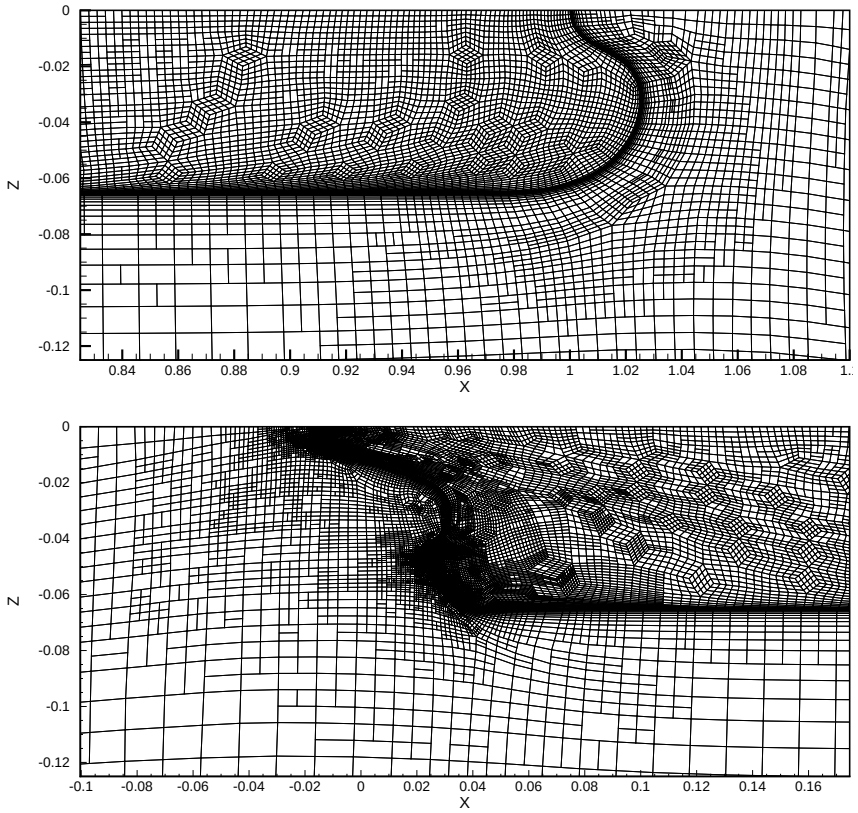

Figure 2: Surface grid on the hull and in the Y-symmetry plane for the KVLCC2 with $T_r = 0.04$ and maximum 2 generations. Bow region (top) and stern region (bottom).

Figure 3 shows the mesh and the axial velocity in the propeller plane. Here, the influence of T_r and the maximum number of generations can be seen. Varying the threshold for the same number of generations (figures (a), (b) and (c)) changes the grid in the entire propeller region, with the finest grid in the propeller disk region where the flow derivatives are highest. Varying the maximum number of generations for a given threshold (figures (b), (d) and (e)) mostly changes the grid in this disk. For max. three generations, the structure of the propeller disk flow can be clearly seen in the grid. The flow field can be compared with the experimental result of figure 4.

Finally, we study the convergence of two global quantities: the drag coefficient $C_T = F_x/(\frac{1}{2}\rho U^2 S)$, where $S = 0.2655$ for the non-dimensional ship, and the 'wake factor', the integral of the axial velocity over the propeller disk centered at [0.0175 0.0 -0.0469] and with outer and inner radius 0.0154 and 0.0024. The curves are converging smoothly, which means that the refinement criterion is not noisy: different threshold values produce grids that form a logical sequence. The correspondence with experiments is reasonable.

Mostly, the figures underline the importance of limiting the number of generations. While one generation is not enough for accuracy, going from two to three generations does not change the accuracy much, it only increases the number of cells. Probably, for three generations, the refinement is concentrated some local regions where very high derivatives appear, but whose influence on the overall flow is limited.

6 Conclusion

Tensor-criterion based grid refinement has been presented for ship flow applications. This approach is natural for directional refinement, which is mandatory for refinement of three-dimensional meshes. We have shown how this approach can be used to implement scalar-, vector-, and tensor criteria, which makes it flexible for the use on different types of ship flow. A test using a pressure Hessian based criterion for double-model flow computation

a) T_r = 0.08, max 2 generations.

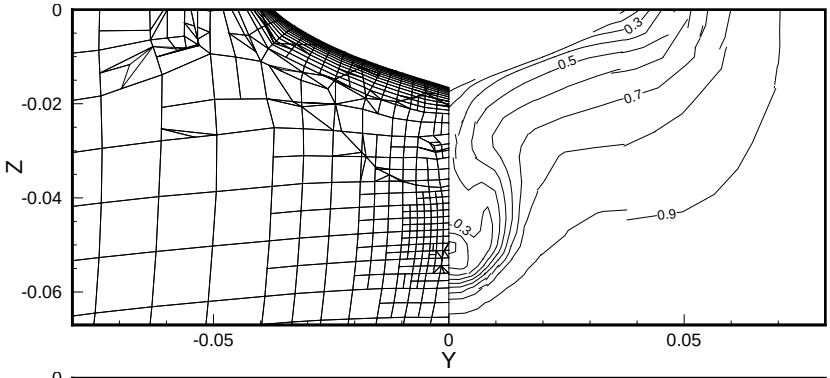

b) T_r = 0.04, max 2 generations.

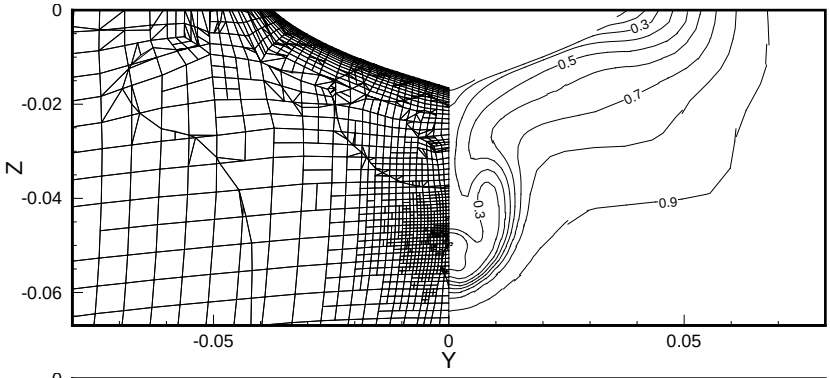

c) T_r = 0.02, max 2 generations.

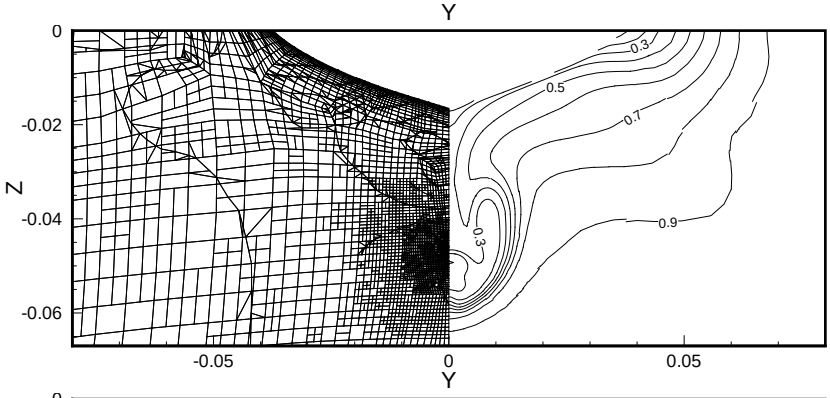

d) T_r = 0.04, max 1 generation.

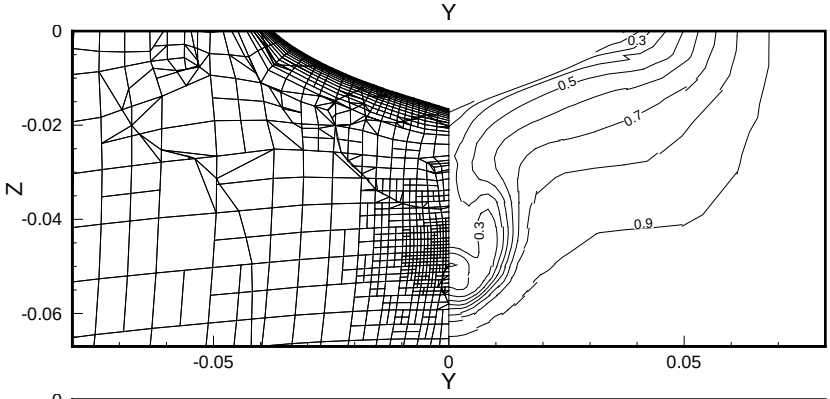

e) T_r = 0.04, max 3 generations.

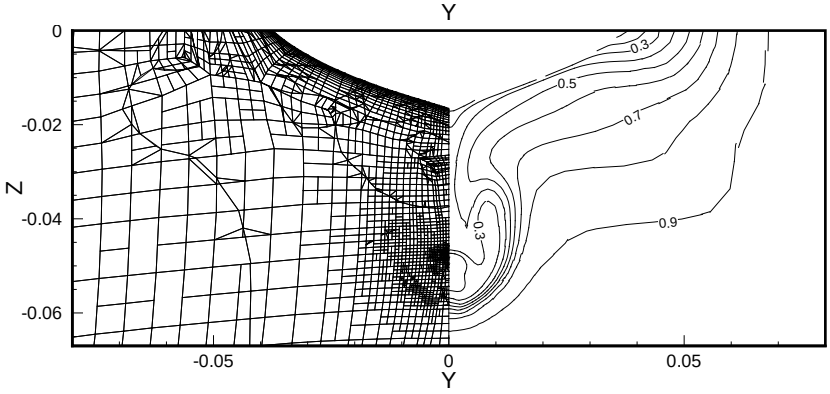

Figure 3: Mesh and axial velocity in the propeller plane X = 0.0175, for the KVLCC2.

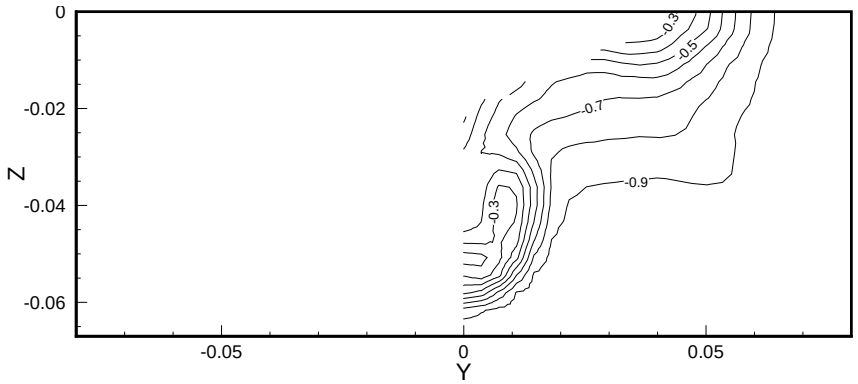

Figure 4: Axial velocity (experimental) for the KVLCC2.

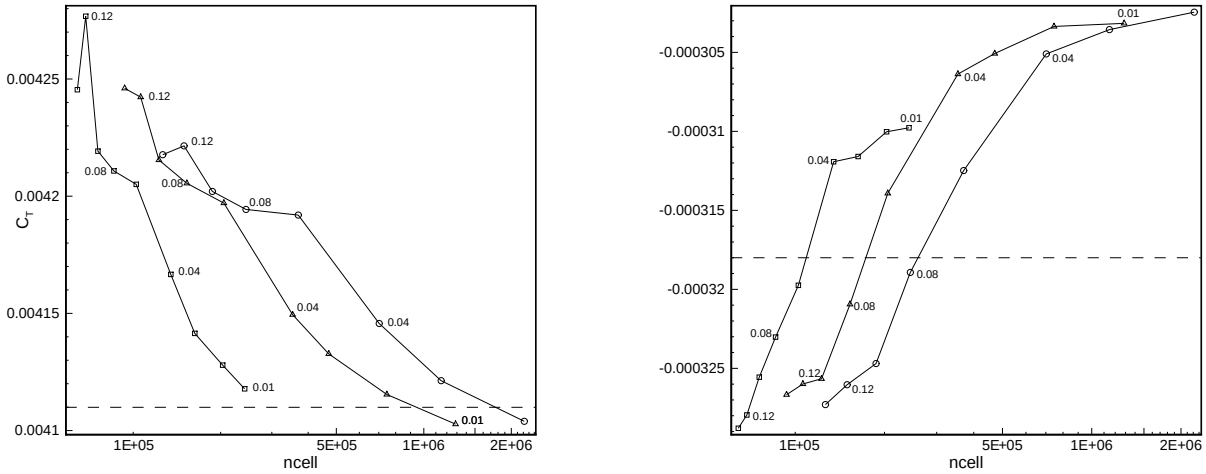

(a) Drag coefficient.

(b) Wake factor.

Figure 5: Convergence of global quantities for the KVLCC2. □: 1 generation, △: 2 generations, ○: 3 generations. The thresholds used are T_r = 0.14, 0.12, 0.10, 0.08, 0.06, 0.04, 0.03, 0.02, and 0.01 (except for 3 generations). The dashed lines indicate experimental values.

shows, that the directional refinement is consistently producing good, smooth grids. However, in order to get good accuracy with a limited number of cells, a delicate balance between the refinement threshold and the maximum allowed number of generations must be found.

References

[1] F. Alauzet and A. Loseille. High-order sonic boom modeling based on adaptive methods. *J. Comp. Phys.*, **229**(3), 561–593 (2010).

[2] P.-L. George and H. Borouchaki, Delaunay Triangulation and Meshing: Application to Finite Elements, *Hermes* (1998).

[3] L. Larsson, F. Stern, and V. Bertram (eds.), Gothenburg 2000, A Workshop on Numerical Ship Hydrodynamics, *Chalmers University*, Gothenburg (2000).

[4] P. Queutey and M. Visonneau. An interface capturing method for free-surface hydrodynamic flows. *Computers & Fluids*, **36**(9), 1481–1510 (2007).

[5] J. Wackers and M. Visonneau. Adaptive grid refinement for ISIS-CFD. In *Proceedings of the 10th Numerical Towing Tank Symposium (NuTTS '08)*, Landéda, France (2008).

[6] J. Wackers, Z. Ali, and M. Visonneau. Adaptive grid refinement for hydrodynamic flow simulation. *Ship Technology Research*, **56**(4), 154–160 (2009).

[7] J. Wackers, P. Queutey, and M. Visonneau. Adaptive grid refinement for unsteady ship flow and ship motion simulation. In *Proceedings of the 11th Numerical Towing Tank Symposium (NuTTS '09)*, Cortona, Italy (2009).

CFD Simulation of Orifice Flow for the Flooding of Damaged Ships

Christian D Wood, Dominic A Hudson, Mingyi Tan

Fluid Structure Interactions Research Group,
School of Engineering Sciences,
University of Southampton, UK.
Email: C.D.Wood@soton.ac.uk

1 Introduction

The aim of this research is to investigate parameters that affect the behaviour of a damaged ship and also to assess the ability of RANS codes to accurately model the physical processes occurring in the flooding of a damaged ship. Initially, the flooding of a damaged ship has been divided into smaller components to assess the accuracy of the predictions for these flow-fields when validated against experiment or other simulation methods. These components are:

1. Violent floodwater motions
2. Modelling a seaway
3. Compartment flooding rates
4. Rigid body motions

These phenomena require models that include viscous effects and violent free surface behaviour, both external and internal to the damaged ship. The surrounding sea-state and resulting ship motions also require simulation. Whilst each of these phenomena may, separately, be non-linear in their behaviour the interaction between them further complicates analysis. It was shown in Smith et al (2007) that large structural loads can occur due to interaction between the ship motions and the ingress and egress of floodwater. Damage size affects the frequency and amplitude of floodwater oscillation compared to wave oscillation and for certain conditions this can lead to maximum floodwater being present as a wave trough passes amidships. When the ship length is equal to the wave length this can increase hull girder loads significantly. Full simulation of this condition requires accurate simulation of flooding rates into the ship.

Typical state of the art flooding models use Torricelli's formula (equation 1) to calculate flooding rates using a constant coefficient of discharge (de Kat, et al., 2002).

$$Q = C_d A_0 \sqrt{2gh}, \tag{1}$$

where, C_d is the discharge coefficient, with typical values between 0.6-0.8, A_0 is the area of the hole, g is gravitational acceleration and h is the height difference between the internal and external water levels. Based on Bernoulli's theorem, turbulence and viscosity effects are included in this equation using a C_d which is independent of damage size or shape. It is believed this assumption could potentially over-simplify the problem to an extent where the calculated flooding rates are in error.

Other research in the area of discharge co-efficient and orifice flow comes from a variety of sources. The majority of this work has come from the field of civil engineering for hydraulics, pipe systems, manifolds and spargers (Werth, et al., 2005) and also from research into flow around standard orifice plates in the aerospace industry (Ganiev, et al., 2008). These studies indicate that discharge coefficient is affected by orifice size, particularly in relation to the size of the structure around the orifice. In work involving spargers, where water vents from an orifice, the parameter of interest is the ratio of the orifice area to the area of the pipe; this could potentially be of interest in this study. In almost every case the problems of interest are steady and whilst it does look into orifice size, the effect of orifice shape has largely been ignored.

There is the potential to improve the fidelity of these models through research into the behaviour of C_d for a variety of parameters. This can be achieved either by the application of Reynolds Averaged Navier-Stokes

equations (RANS) solvers which have the ability to resolve violent free surface problems and naturally include non-linear effects (Hadzic, et al., 2005), by experiment, or by a combination of the two. This paper will look solely at the numerical computations.

This paper reports numerical results obtained for prediction of floodwater flow rates through a variety of damage geometries. This is part of a wider research project into the fluid loads and motions experienced by a damaged ship. In the present study, the fluid flow is predicted using the commercial CFD code Star CCM+, details for which are available in (CD-Adapco, 2009). It is based on the finite volume method and can accommodate any type of grid and is therefore capable of being applied to complex geometries. Coupling of the pressure and velocity fields is by the SIMPLE method, the air and water phases are modelled using VoF (Volume of Fluids) and enhanced using the HRIC (High Resolution Interface Capturing) scheme which allows a sharper interface whilst also allowing wave breaking.

2 Physical problem

The problem investigated here is that of transient flooding of a compartment. The compartment in this case is a cylinder, placed on its end into the water, where the damage is located on the flat edge that is immersed; the other cylinder end is open to the atmosphere. The cylinder external dimensions are 200mm diameter with 10mm wall thickness. The depth of the orifice on the external side is 0.26m. The case begins with the water level on the level with the external side of the damage. The schematic in Figure 1 depicts the problem layout.

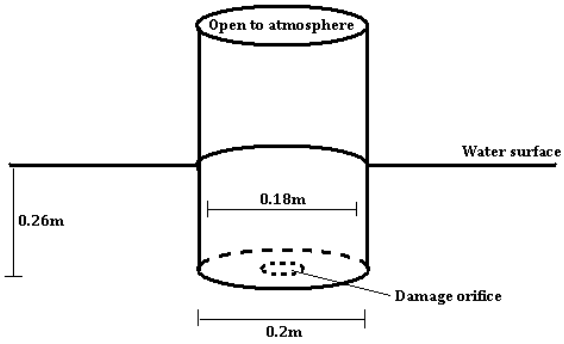

Figure 1 - Schematic of transient compartment flooding problem

The flow features common in this case are highly unsteady and turbulent. As soon as the damage orifice appears a jet of floodwater emerges and upon landing the fluid motions are violent, involving air entrapment and jetting. As the flooding continues and a base layer of water is present, a vena contracta will form where a ring vortex will form just downstream of the edges of the damage orifice. Many of these features would be lost through modelling using potential flow and therefore unsteady RANS will be applied.

3 Methodology

3.1 Governing equations of fluid motion

The finite volume method for incompressible viscous flows is derived in detail in Ferziger et al. (2002). A brief description will be shown here. Starting point is the conservation equations for mass, momentum and generic scalar quantities, shown here in their integral form.

$$\frac{d}{dt}\int_V \rho \mathrm{d}V + \int_S \rho \boldsymbol{v}\cdot\boldsymbol{n}\mathrm{d}S = 0 \tag{2}$$

$$\frac{d}{dt}\int_V \rho\varphi \mathrm{d}V + \int_S \rho\varphi\boldsymbol{v}\cdot\boldsymbol{n}\mathrm{d}S = \int_S \Gamma\nabla\varphi\cdot\mathbf{n}\mathrm{d}S + \int_V \rho b_\varphi \mathrm{d}V \tag{3}$$

Where ρ is fluid density, V is the control volume bounded by closed surface S, $\boldsymbol{v}$ is the velocity vector, t is time, Γ is the diffusion co-efficient and b_φ is the volumetric source of scalar quantity φ, p is the pressure, $\boldsymbol{n}$ is the unit

normal vector to the surface facing outwards. Turbulence is modelled using a k-ε type turbulence model, which modifies the calculation of the viscous stress tensor with the addition of turbulent eddy viscosity (μ_t); calculated locally as a function of turbulence kinetic energy k and dissipation $\boldsymbol{\varepsilon}$. Further detail is also available in Ferziger et al (2002). The interface capturing method is VoF used with HRIC scheme, details available in CD-Adapco (2009), which is used to simulate the free surface. This creates an additional transport equation to solve for the volume fraction c (4). Both liquid and gas phases are modelled, c is set to 1 for water and 0 for air. This way these two fluids are treated as a single fluid and its properties vary according to the local volume fraction, an example is shown for density in (5) where subscript l is for the liquid phase and g the gas phase.

$$\frac{d}{dt}\int_V c\mathrm{d}V + \int_S c\boldsymbol{v}\cdot\boldsymbol{n}\mathrm{d}S = 0 \tag{4}$$

$$\rho = \rho_l c + \rho_g(1-c) \tag{5}$$

Surface tension at the interface is treated as a body force that is a function of volume fraction c. This is through the addition of a continuum surface force (CSF). The CSF model uses a smoothed field of c to define a vector normal to the free surface. The expression of surface tension force (F_{st}) is shown in (6), where σ is the surface tension co-efficient and κ is the curvature of the free surface interface.

$$F_{st} = \int_V \sigma\kappa\nabla c\mathrm{d}V, \qquad \kappa = -\nabla\cdot\left(\frac{\nabla c}{|\nabla c|}\right) \tag{6}$$

3.2 Numerical scheme

The domain of interest is divided up into a finite number of control volumes with the use of an unstructured grid. In the centre of each of these cells there lies a computational point for which the known quantities are specified and unknown properties are computed. The above equations are applied to each computational point and then discretized, which results in one algebraic equation for each control volume; importantly these equations are dependent on both the properties from previous time steps and the control volumes in close proximity. The equation is of the form as shown in (7), where n_j is the number of cell faces around cell of interest P_0; b_{p0} is the source terms and contributions from boundary faces.

$$a_{P0}\varphi_{P0} + \sum_{j=1}^{n_j} a_{Pj}\varphi_{Pj} = b_{P0} \tag{7}$$

In order to calculate the pressure field and couple it to the velocity field, the SIMPLE method is used, which is described in Ferziger et al (2002). Equation (7) is used to calculate each of the variables, but due to the non-linear nature of the equations, the linearised system of equations is solved by iterative methods; also known as inner iterations. A segregated algorithm is then used to achieve the solution for each time step and advance.

4 Compartment Flooding

4.1 Domain

To assess whether there is a dependency of the discharge coefficient (C_d) on damage orifice geometry and location, the physical model as described in section 2 will be used as a testing case. The case is a 3D problem, comparable to any generic side shell damage. The cylinder is 0.5m long and 0.2m in external diameter with a wall thickness of 0.01m. The external domain is 0.5m in diameter and 0.35m in height. Outside of the compartment the water level is effectively 0.26m high, whilst inside the compartment the water is at 0m. The damage shape, location and size are varied.

The grid set-up is as shown in Figure 2. The mesh is refined around the damage opening and cell size grows slowly outward toward the pressure outlet boundaries. The initial study has been performed on a Dell Vostro laptop with dual core Intel Centrino 2.4Ghz processors and 3Gb of RAM. The discretised domain contains ~64,000-109,000 control volumes, where smaller elements are required around the smaller damage orifices, the largest cells being 0.05m and refined to 0.01m-0.005m around the damage orifice, values obtained from a grid dependency study for a 2D case (Wood, et al., 2009). This initial investigation comprises 9 cases; 3 different shapes (circle, square and rectangle) and 3 different orifice areas (0.00503m^2, 0.00283m^2 and 0.00126m^2).

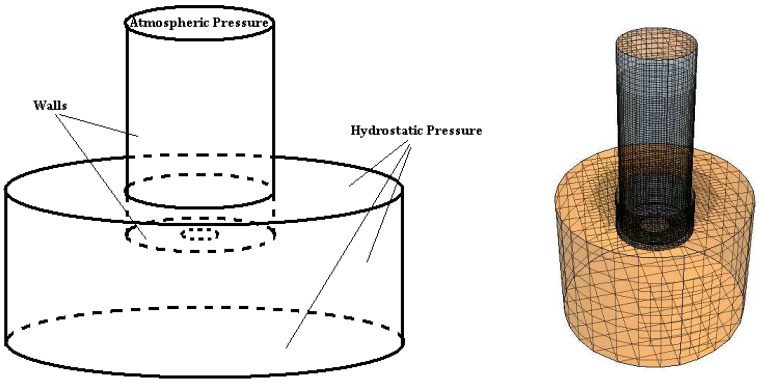

Figure 2 - Domain setup (left) and grid (right)

4.2 Boundary Conditions

The domain setup in Figure 2 gives an indication of the boundary condition set up. The cylinder walls both externally and internally are modelled as no-slip wall boundaries. The top of the cylinder is a pressure outlet effectively open to the atmosphere. Boundaries external to the cylinder are placed under the effective external water level of the problem, this reduces the need to resolve the free surface in areas not of interest in this case. These boundaries are modelled as pressure outlets and hydrostatic pressure in accordance with the actual depth of the problem is prescribed.

4.3 Simulation

A Eulerian multiphase model is used and the two phases are water and air. The density of these fluids was set as ρ_w=998.2 kgm^{-3} and ρ_a=1.225 kgm^{-3}, respectively. Atmospheric pressure was set to 101325 Pa and gravity prescribed in the vertical direction at -9.81 ms^{-2}. Initialisation of the domain in Star CCM+ is achieved using field functions which define volume fraction and hydrostatic pressure in the 3D domain.

Time step is set to 0.01s with the use of second order temporal discretisation as per the 2D study in Wood, et al., (2009). Careful attention has been given to the convergence levels in the first time step, where the continuity residual is required to reach 1x10^{-4} before progressing to the next time step, typically required just over 100 inner iterations. The importance of this is demonstrated in Figure 3 from the investigation into the 2D flooding case. Inadequate convergence results in the formation of a non-symmetric jet. Subsequent time steps typically require only 10-40 inner iterations to reach continuity residual convergence targets.

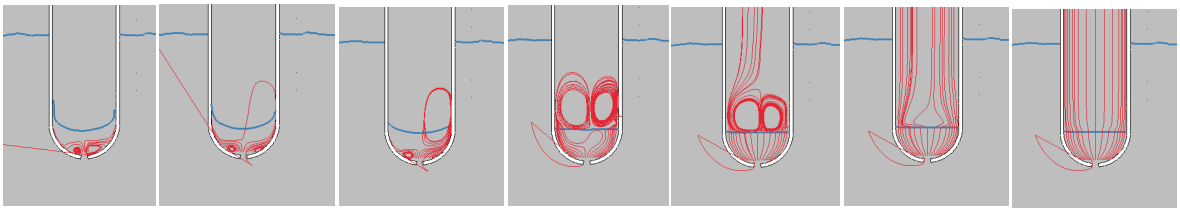

Figure 3 - Snapshots during first time step by continuity convergence level, from left to right; 2x10^{-2}, 3x10^{-2}, 8x10^{-3}, 2x10^{-3}, 7x10^{-4} and 2x10^{-4}.

4.4 Results

The time to flood for each case was recorded. This was determined by the velocity at the damage orifice reducing to zero. For the cases with a larger damage orifice, there is a small overshoot as a result of the momentum of the floodwater ingress, however as the area is constant, this method still reflects the differences caused by the shape of the orifice. Results are shown in Table 1, where the average flow rate is calculated from the time taken to flood a known volume. From the average flow rate the average discharge coefficient is found using equation (1).

Table 1 – Calculated discharge coefficient for varying damage geometries.

Damage Area (m^2)	Shape	Time to flood (s)	Average flow rate ($m^3 s^{-1}$)	Average Discharge Coefficient
5.03E-03	Circle	1.51	0.006740901	0.677
5.03E-03	Square	1.46	0.006971754	0.700
5.03E-03	Rectangle	1.41	0.007218979	**0.725**
2.83E-03	Circle	3.19	0.003190834	0.570
2.83E-03	Square	3.43	0.002967569	0.530
2.83E-03	Rectangle	3.35	0.003038436	0.543
1.26E-03	Circle	7.25	0.001403967	0.564
1.26E-03	Square	9.04	0.001125969	**0.452**
1.26E-03	Rectangle	8.14	0.001250462	0.502

The results show a large difference in the average discharge coefficient, both with respect to shape and to size. These differences are more obvious in the extreme cases of large damage and of small damage. For constant area the largest difference is for the smallest orifice areas, giving rise to a difference in discharge coefficient of 0.112. This corresponds to more than a 10% difference in the rates compared to the inviscid solution (eg. C_d=1). The dominant feature of this flow field is that of the initial jet and the vena contracta. The vena contracta is a contraction in the streamtube downstream of the damage orifice. The shape and strength of which appear to be affected by the shape of the orifice and the proximity of the damage orifice edges to the wall of the cylinder. The larger damage cases show give rise to larger discharge co-efficients, this is as a result of the hampered formation of the streamtube contraction due to interference from the cylinder wall; the smaller cases have a far more developed vena contracta; in the case shown in Figure 4, two contra-rotating vortices have formed which have resulted in a lower discharge co-efficient.

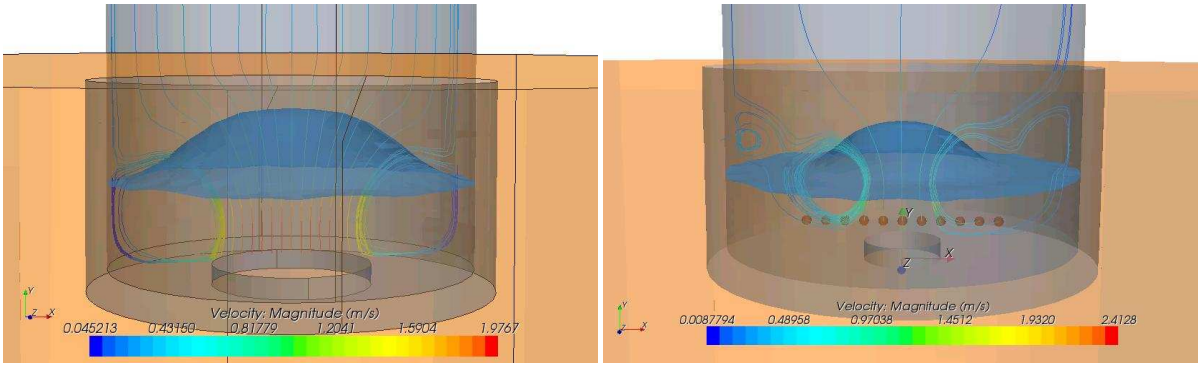

Figure 4 – Two flooding cases where free surface and streamlines of constant velocity are shown: Large circular damage case showing a vortex ring constrained by the compartment geometry (left) Small circular damage with vortex rings and vena contracta (right)

The sudden release of even this modest head of pressure will still give rise to a jet formation and collapse within the damage compartment. The collapse of the jet temporarily results in disruption to the vortices formed and affects the flow rates. This can be seen in the form of perturbations in the orifice velocity in Figure 5 in between 0s and 1s. The subsequent gradient of the line has only a very small curvature, therefore could be reasonably approximated using a straight line; using the example in Figure 5 gives a gradient of -0.44335ms^{-2}. A

continuation of this work is being performed which shall investigate this phenomena for a much larger variety of parameters and using grids of a higher resolution.

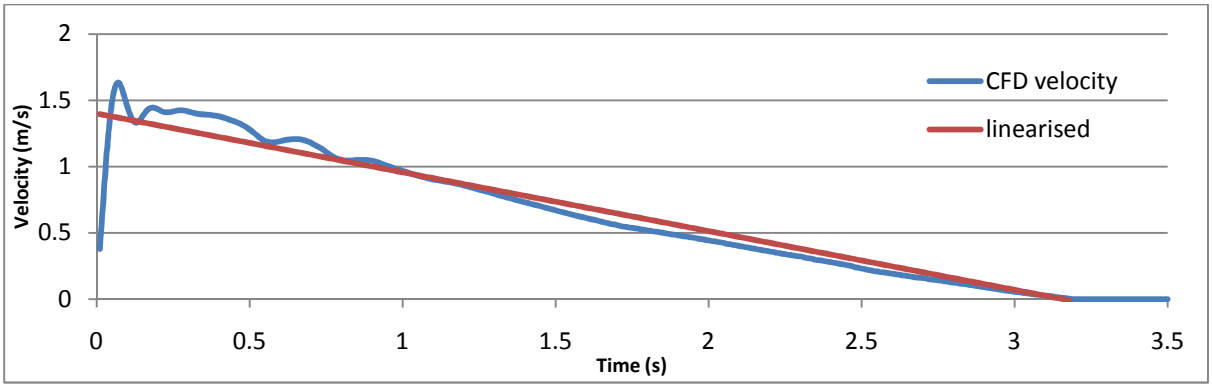

Figure 5 - Graph of maximum orifice velocity for medium circle damage

5 Conclusions

The results presented in this paper indicate that the widely used assumption of using a constant coefficient of discharge for orifice flow is incorrect. As would be expected the largest differences attributable to the change in shape of the damage are from the case of constant minimum area, as this has the least influence from the cylinder walls. This effect is demonstrated where for constant area the circular damage case floods almost 25% quicker than the square damage case.

The parameters that appear to affect the discharge coefficient are; the orifice size in relation to the size of the compartment and the proximity of the orifice edges to the cylinder wall. The aspect ratio also appears to play a factor although to what extent is unknown as there are only two variations in this study.

In response to the findings in this initial study, cases of a higher fidelity are being run on the University of Southampton's Iridis 3 computing cluster. The cluster has 1024 nodes, each with 8 processing cores, linked with infiniband connections. A detailed grid size, time step dependency study and turbulence model survey will be performed and validated against experimental measurements.

6 References

CD-Adapco Star CCM+ v4.06.011 Help. - 2009.

de Kat J O and Peters A J Model Experiments and Simulations of a Damaged Frigate, Proceedings of the 10th International Conference of the International Maritime Association of the Mediterranean. - Crete : IMAM '02, 2002.

Ferziger J H and Peric M Computational Methods for Fluid Dynamics, Springer-Verlag, 2002. - 3 : p. 423.

Ganiev R.I. [et al.] Choice of a turbulence grid and model to calculate the discharge coefficient of the standard orifice plate, Russian Aeronautics, Allerton Press Inc, 2008. - 4 : Vol. 51. - pp. 377-381.

Hadzic I [et al.] Computation of flow-induced motion of floating bodies, Applied Mathematical Modelling. - 2005. - Vol. 29. - pp. 1196-1210.

Smith T W P, Drake K R and Rusling S Investigation of the variation of loads experienced by a damaged ship in waves, Advancements in Marine Structures: Proceedings of Marstruct 2007. - Glasgow, 2007.

Werth D.E., Khan A.A. and Gregg W.B. Experimental study of wall curvature and bypass flow effects on orifice discharge coefficients, Experiments in Fluids. - 2005. - 39. - pp. 483-489.

Wood C.D., Hudson D.A. and Tan M. Numerical Simulation of Compartment Flooding for Damaged Ships, Proceedings of the 12th Numerical Towing Tank Symposium. - Cortona, 2009.

CFD Analysis of a Duct's Effectiveness for Model Scale and Full Scale

Tobias Zorn, Justus Heimann, Volker Bertram, FutureShip, Hamburg & Potsdam/Germany
{tobias.zorn,justus.heimann,volker.bertram}@GL-group.com

Rising fuel prices and stricter regulations on emissions drive a quest for more fuel efficient ships that is reminiscent of the 1970s, when after the first oil shock a plethora of fuel saving devices was investigated. Examples are Schneekluth ducts (wake equalizing ducts), Grim vane wheel, Grothues spoilers, or asymmetric aftbodies, *Schneekluth and Bertram (1998).* Many of the "propulsion improving devices" of the 1970s are now again under debate. More than a generation later, we start basically again from scratch. The original reports on efficiency gains are often incomplete and invariably based on model tests. We know that model tests violate scaling laws in the aftbody, changing boundary layers and propeller rpm and/or loading. Model tests with "empirical scaling" were the only option in the 1970s. The progress in CFD allows today much better insight into full-scale flows involving propulsion improving devices, allowing better scaling from model to full scale conditions, hence better quantitative predictions of the efficiency gains, but also into the physical mechanism allowing better insight into why gains are achieved or not. *Ok (2004,2005)* presented CFD studies for a Schneekluth nozzle for a public-domain tanker geometry, the E3 tanker. Contrary to common belief, he found that the nozzle did not improve the flow at full scale but was actually harmful. His work triggered a controversial debate. However, there is large consensus that the effectiveness of propulsion improving devices depends on the individual flow conditions, thus the hull and propeller designs. Showing the ineffectiveness of a device for one ship allows only the conclusion that the device is not always effective. For other devices or other ships, case by case analyses are recommended. Intrigued by Ok's work, and stimulated by the rising interest in these devices, we decided to conduct our own study. In particular, the study was performed to shed some light on the following issues:

- Check whether an upstream nozzle improves the wake field of a bulker in model and full scale; assess the importance of scaling effects
- Assess improvement (if any) for the propulsion case (with propeller) for model scale and full scale
- Assess the appropriate level of the model for hull optimization purposes; in particular, assess whether the wake field ("resistance test") suffices or whether the propeller needs to be taken into account ("propulsion test"). A numerical resistance test is much faster than a numerical propulsion test.

We created a typical tanker geometry using parametric modeling within the Friendship Framework. Main dimensions and block coefficient are representative for a large crude oil carrier. These ships operate at Froude numbers around 0.14 to 0.16 at fully loaded condition. The propellers are well submerged and the waves are small. Therefore we felt justified in conducting the study without free-surface modeling. From sketches and public-domain photos, we created a so-called Hitachi Zosen duct, again using the framework. The choice of duct was somewhat arbitrary and does not reflect any prejudice in favor or against any of the other duct types promoted in the market (e.g. Schneekluth nozzles, Mewis ducts, Sumitomo Integrated Lammeren Duct, Mitsui Integrated Ducted Propeller, etc, etc). Neither was the chosen nozzle tuned or optimized for the given geometry. The results of the study are thus by nature indicative only.

We used the RANSE solver Star-CCM+ for our study. For solution method is based on conservation equations in integral form with appropriate initial and boundary conditions. The solution domain is subdivided into a finite number of control volumes which can be of an arbitrary polyhedral shape and are typically locally refined in regions of rapid variation of flow variables. The time interval of interest is also subdivided into time steps of appropriate size. The governing equations contain surface and volume integrals, as well as time and space derivatives. These are approximated for each control volume and time level using finite-difference approximations, leading to an algebraic equation system. Turbulence effects are included via an eddy-viscosity model. Thus, the continuity equation, momentum equation, and two equations for turbulence properties are solved. All integrals are approximated by midpoint rule, i.e. the value of the function to be integrated is evaluated at the centre of the integration domain (control volume face centres for surface integrals, control volume centre for volume inte-

grals, time level for time integrals) and then multiplied by the integration range (face area, cell volume, or time step, respectively). These approximations are of second-order accuracy for smooth functions, irrespective of the shape of the integration region (arbitrary polygons for surface integrals and arbitrary polyhedra for volume integrals). Since variable values are computed at control volume centres, interpolation has to be used to compute values at face centres. The convective fluxes are computed with second-order linear reconstruction using upwind TVD-limited gradients. In order to compute diffusive fluxes, gradients are also needed at cell faces, while some source terms in equations for turbulence quantities require gradients at control volume centres. These are computed from linear shape functions. The solution of the Navier-Stokes equations is accomplished in a segregated iterative method, in which the linearised momentum component equations are solved first using prevailing pressure and mass fluxes through cell faces (inner iterations), followed by solving the pressure-correction equation derived from the continuity equation (SIMPLE algorithm). Thereafter equations for species transport and turbulence quantities are solved. The sequence is repeated (outer iterations) until all equations are satisfied within a prescribed tolerance, after which the process advances to the next time level. Further details of the numerical solution method can be found in Muzaferija and Perić (1999) and Ferziger and Perić (2003).

The grids used predominantly hexahedral cells and were automatically generated, also for the propeller. The same refinement levels were used for all simulations to allow comparison of results. Meshing parameters were kept same for the case with and without nozzle. For cases with propeller, a real rotating propeller behind the ship was used (moving mesh simulation). The mesh around the ship and the mesh of the propeller were dynamically connected using the sliding interface technique, allowing the rotation of the entire propeller mesh. For this purpose, the propeller mesh had a form of circular cylinder with the axis coinciding with the propeller axis. Free-surface effects were neglected to shorten simulation time. Constant propeller speed (fixed rpm) was imposed. The propeller rpm was scaled between model and full scale using Reynolds similarity. For cases without propeller, steady state simulations were used. For cases with propeller, the time step was varied, starting with large time steps to let the flow develop around the hull. At the end, small time steps were used to capture the details of the flow around the propeller and duct. The grids used:

- 3.7 million cells for the ship without propeller, an without nozzle, steady case
- 8.5 million cells for the ship without propeller, with nozzle, steady case
- 2.6 million cells for the ship with propeller, without duct, unsteady case
- 6.6. million cells for the ship with propeller, with duct, unsteady case

The unsteady “propulsion test” required coarser grids to compensate for the higher computational effort for unsteady computations. The same numbers of cells and topologies were used for model and full scale, but in full scale the cells were clustered more towards the hull surface for full scale.

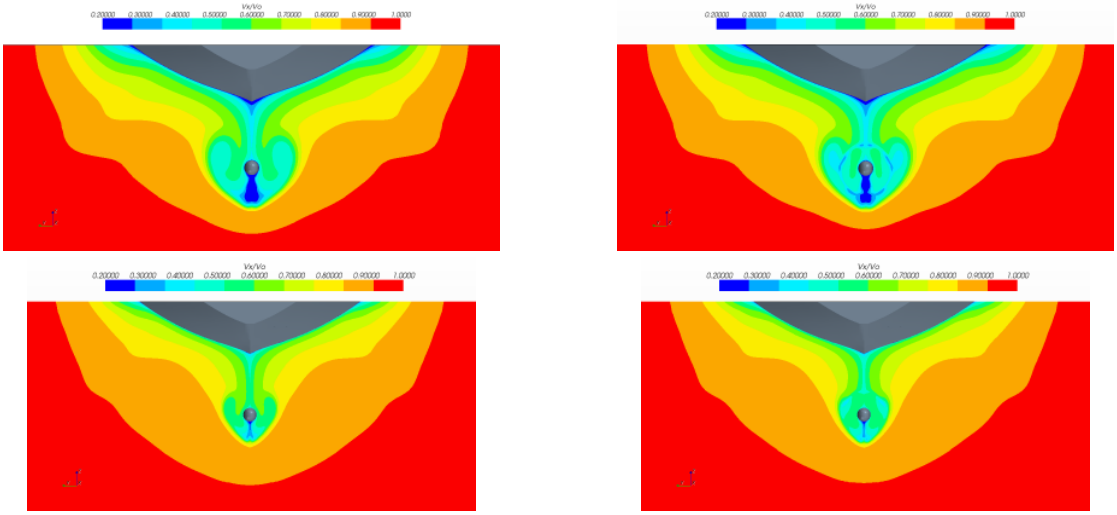

Fig.1: Wake field in the propeller plane for “resistance cse”;
model scale (top) and full scale (bottom); without duct (left) and with duct (right)

For the “resistance case”, the duct improved the wake filed for model and full scale, Fig.1. Equalizing the wake field seems to work better for full scale Rn. For full-scale Reynolds number Rn and model scale Rn, the duct produced thrust. Comparing net forces, benefit for full-scale Rn was 0.5 %. For model scale Rn, 1.2 % drag reduction was achieved, i.e. the duct was working slightly better for model scale.

For the “propulsion case”, the duct clearly changes the wake field for model and full scale, Fig.2. The flow is accelerated through nozzle. Especially for full Rn flow field is more equalized. Compared to wake field without propeller, the flow separation zone is much smaller. The duct increases resistance somewhat: 0.5% in full scale, 0.7% in model. However, the thrust increases also by 1.5% for model and full scale. Thus there is 1% benefit in full scale for the duct. This is a bit disappointing and hardly measurable during sea trials. Redesign of aft hull lines would offer more potential for improvement. For a retrofit, the nozzle should be optimized to achieve higher savings.

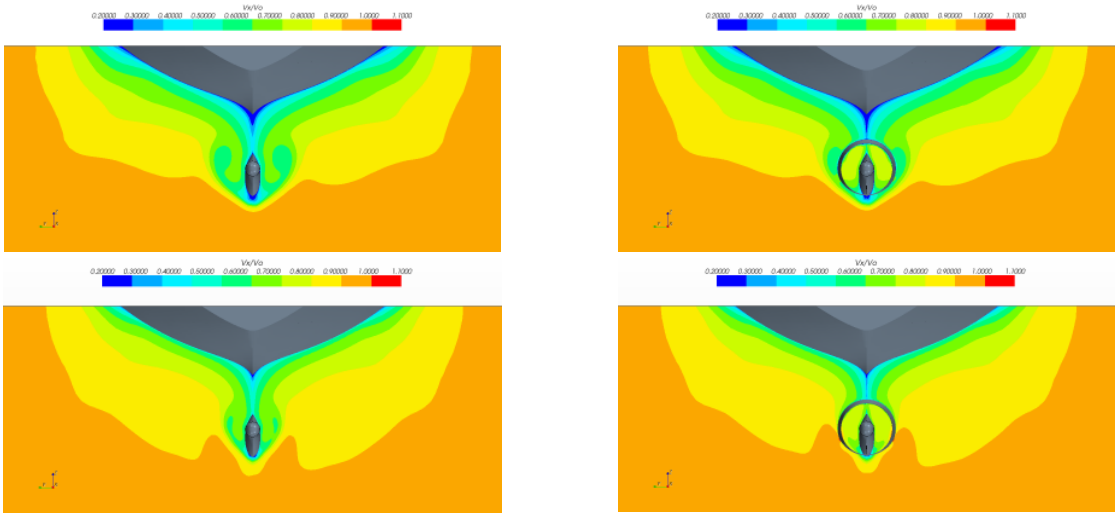

Fig.2: Wake field in the propeller plane for “propulsion case”
model scale (top) and full scale (bottom); without duct (left) and with duct (right)

Streaklines showed separation near the propeller, with comparable flow patterns in model and full scale, Fig.3. The duct improves the previous downward flow near the propeller to a more horizontal flow. The large separation zone at the rear of the ship is not improved by the duct. Here, modifications of the aft hull lines are recommended.

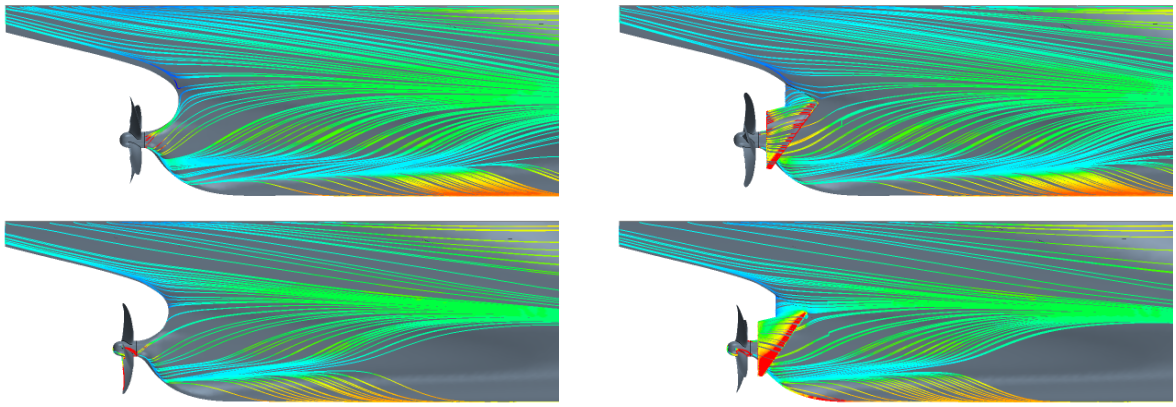

Fig.3: Streaklines (Wall Shear Stress Streamlines) for “propulsion case”
model scale (top) and full scale (bottom); without duct (left) and with duct (right)

In conclusion:

- The duct is working, but gives only very small improvement.
- Simulations with and without propeller show the same trends; this needs further investigation.
- Model and full scale Rn flow show the same trends, but the flow fields differ in some areas.
- The duct needs optimization to give significant improvements.
- For a newbuilding, a redesign of aft hull lines is probably more effective than the duct.

References

FERZIGER, J.H.; PERIĆ, M. (2003), *Computational Methods for Fluid Dynamics*, 3rd Ed., Springer

MUZAFERIJA, S.; PERIĆ, M. (1999), *Computation of free surface flows using interface-tracking and interface-capturing methods*, Nonlinear Water Wave Interaction, pp.59-100, WIT Press

OK, J.P. (2004), *Numerical investigation of scale effects of the wake-equalizing duct,* 7th Numerical Towing Tank Symposium (NuTTS), Hamburg
http://www.uni-due.de/imperia/md/content/ist/nutts_07_2004_hamburg_scan.pdf

OK, J.P. (2005), *Numerical investigation of scale effects of a wake-equalizing duct*, Ship Technology Research 52, pp.34-53.

SCHNEKLUTH, H.; BERTRAM, V. (1998), *Ship Design for Efficiency and Economy,* Butterworth & Heinemann, Oxford.